

Nucleon Structure from Neutrino Interactions in an Iron Target  
with a Study of the Singlet Quark Distribution

Thesis by

David Brian MacFarlane

In Partial Fulfillment of the Requirements  
for the Degree of  
Doctor of Philosophy

California Institute of Technology  
Pasadena, California

1984  
(Submitted October 6, 1983)

## Acknowledgements

The work described below represents a culmination of efforts by many people. Through the attentions of F.Sciulli and M.Shaevitz, this author has been guided through the intricacies of analyzing and understanding a major physics experiment. The size of the task of obtaining structure functions was beyond my abilities alone. It is a pleasure to acknowledge M.Purohit as a friend and fellow traveler through these mysteries. Other contributors to this analysis include R.Blair, D.Novikoff and P.Auchincloss. I wish to thank B.Messner for his advice and guidance.

Only a small part of an experiment is the analysis. The design, construction and running of Fermilab experiment E616 was the achievement of physicists from Caltech, Fermilab, Rochester and Rockeller. Our success was possible only through the support of the technical staff at Fermilab.

I wish to thank M.Barnett, D.Duke and D.Owens for graciously supplying programs which fit QCD predictions to the  $Q^2$  evolution of structure functions, and for assisting in the understanding of the theory.

Midway through my tenure at Caltech, unexpected complications set in. In this connection, I would like to thank D.Hitlin for stepping into the breach. The hospitality and support of the Nevis staff played an important part in the completion of this work.

Financial support for these efforts has been provided by Caltech, the U.S. Department of Energy and National Science Foundation, and the Natural Sciences and Engineering Research Council of Canada.

My parents have in no small way been responsible for instilling the curiosity which continues to motivate me. Finally, I would like to thank my wife, Kathy, for her support and sacrifice over the past few years, and her willingness to share in future adventures.

## Abstract

Nucleon structure functions have been extracted from a large sample of neutrino and anti-neutrino inclusive charged-current events. These data were obtained over the period from June, 1979 through January, 1980, using the Lab E detector in the N30 dichromatic beam at Fermilab (experiment E616).

The use of the narrow-band beam made possible flux normalized cross section and structure function measurements. Neutrinos were obtained from sign and momentum selected pions and kaons produced from 400GeV primary protons. Details of the methods used to monitor and determine properties of the secondary beam are provided. The flux of neutrinos at the detector was calculated from this knowledge.

The Lab E detector performed the function of neutrino target, as well as measuring final state properties of the events. Hadron energy was measured using calorimetry. Spark chambers interspersed throughout the target and following toroidal spectrometer were used to sample the position of the outgoing muon. From these measurements, the muon angle and momentum could be determined. The procedure used for reconstructing physics variables from detector measurements is presented with estimates of systematic errors.

The methods used to extract structure functions from the data are detailed. An analysis of sources of systematic error on these results is made. A comparison of our results for  $F_2$  is made with other measurements from both neutrino and charged lepton scattering. Differences in overall normalization and in the  $x$  dependence of the structure function are found. The mean square quark charge rule from the quark-parton model is confirmed at the 10% level. Quantum Chromodynamics (QCD) predicts a pattern of scaling violations in  $F_2$  which is observed in our results. This has been quantified by making fits to the data using numerical integration of the Altarelli-Parisi equations. The value of  $\Lambda_{\overline{\text{MS}}}$ , the QCD scale parameter, is found to be  $340 \pm 100 \pm 60 \text{MeV}$  with an additional uncertainty of  $\pm 50 \text{MeV}$  due to the unknown form of the gluon distribution.

to Kath

# Contents

	Page
<b>Chapter 1. Introduction</b> . . . . .	<b>1</b>
1.1 The Neutrino and the Weak Force . . . . .	1
1.2 The Quark-Parton Model and Neutrino Scattering . . . . .	4
1.3 Structure Functions and QCD . . . . .	9
1.4 Outline of Presentation . . . . .	11
<b>Chapter 2. Neutrino Source</b> . . . . .	<b>13</b>
2.1 Dichromatic Beam . . . . .	14
2.2 Total Intensity Monitors . . . . .	16
2.2.1 Calibration . . . . .	16
2.2.2 Systematic flux errors . . . . .	18
2.3 Beam Composition . . . . .	19
2.3.1 Čerenkov counter for E616 . . . . .	19
2.3.2 Diffraction effects in a finite length counter . . . . .	22
2.3.3 Backgrounds . . . . .	23
2.3.4 Analysis of pressure curves . . . . .	25
2.3.5 Mean momenta and widths . . . . .	26
2.4 Beam Dispersion and Steering . . . . .	27
2.5 Beam Monte Carlo . . . . .	27
2.5.1 Wide-band background . . . . .	29

---

Chapter 3. Neutrino Detector . . . . .	30
3.1 Scintillation Counters . . . . .	31
3.2 Spark Chambers . . . . .	33
3.3 Data Acquisition . . . . .	35
3.4 Triggers . . . . .	36
3.4.1 Livetime . . . . .	39
Chapter 4. Event Analysis . . . . .	40
4.1 Hadron Energy Determination . . . . .	40
4.1.1 Counter gain monitoring . . . . .	41
4.1.2 Counter mapping . . . . .	42
4.1.3 Calibration of hadron energy . . . . .	45
4.2 Muon Parameters . . . . .	47
4.2.1 Target track . . . . .	47
4.2.2 Toroid track . . . . .	47
4.2.3 Event scanning . . . . .	51
4.2.4 Muon deep-inelastic scatters . . . . .	51
4.2.5 Best fit to muon angle . . . . .	52
4.3 Cuts . . . . .	53
4.3.1 Monitor and steering cuts . . . . .	53
4.3.2 Cosmic-ray cuts . . . . .	54
4.3.3 Geometric and fiducial cuts . . . . .	54
4.3.4 Acceptance calculation . . . . .	55
4.3.5 Kinematic cuts . . . . .	57
4.4 Tests of the Data . . . . .	58
4.4.1 Trigger efficiencies . . . . .	58
4.4.2 Calibration check . . . . .	60
4.4.3 Separation of pion and kaon neutrino events . . . . .	62

---

Chapter 5. Extraction of Structure Functions . . . . .	63
5.1 Total Cross Sections . . . . .	63
5.2 Weighted Event Method for $F_2$ and $xF_3$ . . . . .	66
5.2.1 Corrections to isoscalar cross section . . . . .	69
5.2.2 Model of $F_2$ and $xF_3$ for integrations . . . . .	74
5.2.3 Quadrature technique . . . . .	78
5.2.4 Resolution smearing corrections . . . . .	79
5.3 Flux Smoothing Procedure . . . . .	83
5.4 Alternative Extraction Method . . . . .	87
5.5 Results for $F_2$ and $xF_3$ with Fixed $R$ . . . . .	88
5.6 Systematic Errors . . . . .	93
5.7 Extraction of $R$ . . . . .	96
5.7.1 Results for $R = \sigma_L/\sigma_T$ . . . . .	97
Chapter 6. Quark-Parton Model and QCD Results . . . . .	100
6.1 Comparisons with Existing Neutrino Results . . . . .	100
6.2 Mean Square Quark Charge Test . . . . .	112
6.3 Gross-Llewellyn Smith Sum Rule . . . . .	122
6.4 QCD Formalism . . . . .	124
6.5 QCD Fits . . . . .	130
6.5.1 $F_2$ analysis . . . . .	132
6.5.2 Comparison with results from other experiments . . . . .	138
6.5.3 $F_2$ analysis with $\bar{q}$ . . . . .	138
6.5.4 $xF_3$ analysis . . . . .	142
6.5.5 Comments on $R$ . . . . .	143
6.6 Conclusions and the Future . . . . .	145

---

Appendix A. List of Collaborators on E616 . . . . .	148
Appendix B. Target Counter Maps . . . . .	150
Appendix C. Hadron Calibration . . . . .	154
Appendix D. Multiple Scattering Error Matrix . . . . .	156
Appendix E. Quark Model Predictions for Cross Sections . . . . .	158
Appendix F. Characteristics of Binned Data . . . . .	162
List of References . . . . .	167

# Introduction

Herein is described a scattering experiment in the tradition of Rutherford's probing of atomic structure with alpha particles: the determination of nucleon structure through neutrino deep-inelastic scattering. The neutrino, interacting via the weak force, scatters off constituent partons of the nucleon, providing information both about the nature and properties of those constituents, and the forces which hold the nucleon together. We treat the neutrino probe as a known quantity, and analyze the scattering data in terms of the leading theory of nucleon structure, Quantum Chromodynamics (QCD). Quarks and gluons are not directly observable, but this experiment provides a means of making basic tests of the consequences of their existence.

## 1.1 The Neutrino and the Weak Force

In 1931 Pauli hypothesized [Pa33] the existence of a near massless neutral half-integral spin object, later called the neutrino, to explain the apparent violation in nuclear  $\beta$ -decay of the fundamental conservation laws of energy and angular momentum. However, it was not until 1956 that a neutral member of the lepton family ( $\bar{\nu}_e$ ) was actually observed [Re59] in interactions with matter. Implementing ideas of Pontecorvo [Po59] and Schwartz [Sc60], the first neutrino beams were built at the AGS at Brookhaven (1961) and the PS at CERN (1963) [Pe69]. The weak interaction could then be studied at high energies and  $Q^2$ .

Like these original efforts, the present neutrino beams at Fermilab and the SPS at CERN are obtained from the weak decay of pions and kaons. The difficulty has always been in determining neutrino flux. The high energy, momentum selected (narrow-band) beam used in this experiment, with its sophisticated monitoring systems, represents a culmination to date of efforts to minimize systematic errors in determining fluxes. In parallel, the bubble chambers and simple counter detectors of the first experiments have evolved into large volume, precision detectors, such as that located in Lab E.

Assumptions are made about the properties of the neutrino probe and the description of its interaction with matter, consistent with present world data. As a neutral spin  $\frac{1}{2}$  lepton,

the neutrino partakes of neither the strong nor the electromagnetic forces in interacting with matter. The experimental evidence at present indicates that the three types of charged lepton ( $e^-$ ,  $\mu^-$ ,  $\tau^-$ ) and associated neutrino ( $\nu_e, \nu_\mu, \nu_\tau$ ), are distinguished by three separately conserved, additive conservation numbers, ( $L_e, L_\mu, L_\tau$ ) [Co73]. Neutrino rest masses are known to be less than  $46 \text{ eV}/c^2$ ,  $520 \text{ keV}/c^2$  and  $250 \text{ MeV}/c^2$  respectively for the  $\nu_e, \nu_\mu$  and  $\nu_\tau$  [Ro82].

The limit on muon neutrino mass is well below the point where it could kinematically affect charged current scattering results. However, finite neutrino masses, coupled with a violation of lepton number conservation, could result in spontaneous transitions of muon neutrinos into neutrinos of another type [Po67]. These transitions would cause the superposition of a characteristic oscillatory behavior on the normal dichromatic flux spectrum. No compelling evidence exists for such a phenomenon at the neutrino energies and distance to source involved in this experiment [Ha83]. Therefore, neutrino oscillations are not considered in this analysis.

Soon after Pauli proposed the existence of the neutrino, Fermi [Fe34] suggested, in analogy with QED, an empirical form of the weak lagrangian to describe  $\beta$ -decay:

$$L_W = \frac{G}{\sqrt{2}} j_H^\dagger j_e \quad (1.1)$$

where the two currents,  $j_e$  and  $j_H^\dagger$ , can be written in terms of fields,  $\psi$ :

$$\begin{aligned} j_e &= \bar{\psi}_e \gamma^\alpha \psi_{\nu_e} \\ j_H^\dagger &= \bar{\psi}_p \gamma_\alpha \psi_n \end{aligned} \quad (1.2)$$

The prediction [Le56] and discovery [Wu57] of parity violation in weak interactions led to a more general form of the lagrangian, containing both scalar and pseudo-scalar products of currents [Fe58]. The lepton currents took on the familiar (V-A) form:

$$\begin{aligned} j_e &= \bar{\psi}_e \gamma^\alpha (1 + \gamma^5) \psi_{\nu_e} \\ j_e &= \bar{\psi}_\mu \gamma^\alpha (1 + \gamma^5) \psi_{\nu_\mu} \end{aligned} \quad (1.3)$$

The hadronic current, reflecting the complicated structure of the nucleon, was written as a linear combination of vector and axial-vector terms:

$$j_H^\dagger = V_H^\dagger + A_H^\dagger = \bar{\psi}_p \gamma^\alpha (1 + c\gamma^5) \psi_n \quad (1.4)$$

The operators  $a(\bar{a}) = \frac{1}{2}(1 \pm \gamma^5)$  project out left-handed (positive helicity), and right-handed (negative helicity) neutrinos and anti-neutrinos respectively. The form of the lagrangian summarizes the observed feature of the weak interactions, namely that to the extent that lepton masses can be neglected, only left-handed fermions and right-handed anti-fermions interact.

The analogy with QED is completed by the current standard theory of weak interactions, due to Weinberg and Salam [We67, Sa68]. The weak and electromagnetic forces are

mediated by four vector bosons,  $W^\pm$ ,  $W^0$  and  $B^0$ . The underlying  $SU(2) \times U(1)$  symmetry is spontaneously broken, resulting in the three massive vector bosons ( $W^\pm, Z^0$ ) of the weak interaction and the massless photon. The (V-A) character of the charged current is preserved in the theory. The only modification to the pointlike behavior expressed in equation 1.1 is to include the propagator effect. The coupling becomes  $G = G_F / (1 + Q^2/M_W^2)$ , where  $M_W$  is the mass of the exchanged boson.

Consider first the scattering process,  $\nu_\mu e^- \rightarrow \mu^- \nu_e$ , as a prototype of the weak interaction. Let  $(k, k')$  and  $(p, p')$  be the initial and final state four-vectors of the  $(\nu_\mu, \mu)$  and  $(e, \nu_e)$  respectively. From the weak lagrangian (1.1), the cross section can be shown to be:

$$\frac{d\sigma^{\nu_\mu e}}{d\Omega' dE'} = \frac{G^2}{(2\pi)^2} \frac{E'}{E} L_{\mu\nu}^{[\mu]} L_{[e]}^{\mu\nu} \quad (1.5)$$

where

$$\begin{aligned} L_{\mu\nu}^{[\mu]} &= k_\mu k'_\nu + k'_\mu k_\nu - g_{\mu\nu} k \cdot k' \pm i\epsilon_{\mu\nu\alpha\beta} k^\alpha k'^\beta \\ L_{\mu\nu}^{[e]} &= p_\mu p'_\nu + p'_\mu p_\nu - g_{\mu\nu} p \cdot p' \pm i\epsilon_{\mu\nu\alpha\beta} p^\alpha p'^\beta \end{aligned} \quad (1.6)$$

The tensors,  $L_{\mu\nu}$ , are products of weak coupling spin factors,  $\gamma^\mu(1 + \gamma^5)$ , sandwiched between spinors for initial and final states. Neglecting masses, this reduces in the centre-of-mass to:

$$\frac{d\sigma^{\nu_\mu e}}{d \cos \theta^*} = \frac{G^2 s}{2\pi} \quad (1.7)$$

where  $\theta^*$  is the centre-of-mass angle between the incoming  $\nu_\mu$  and the outgoing  $\mu^-$ . Two observations should be made. First, the cross section rises linearly with the square of the centre-of-mass energy,  $s$ , a consequence of the pointlike nature of the weak interaction at distance scales  $Q^2 \ll M_W^2$ . Second, in the centre-of-mass, the left-handed spin of the  $\nu_\mu$  and  $e^-$  result in a total angular momentum of 0; hence, the cross section is isotropic.

Consider next the inclusive process studied in this experiment,  $\nu_\mu(\bar{\nu}_\mu) N \rightarrow \mu^\mp X$ . In analogy to the  $\nu_\mu e$  case above, the cross section is given by:

$$\frac{d\sigma^{\nu(\bar{\nu})}}{d\Omega' dE'} = \frac{G^2}{(2\pi)^2} \frac{E'}{E} L_{\mu\nu}^{[\mu(\bar{\mu})]} W^{\mu\nu} \quad (1.8)$$

The tensor  $W^{\mu\nu}$  describes the hadronic part of the interaction schematically shown in figure 1.1. The nucleon, unlike the pointlike electron, has a structure on the distance scales probed by the weak interaction. In its most general form, the hadronic tensor can be written in terms of three unknown functions of  $x$  and  $Q^2$ :

$$W_{\mu\nu} = \frac{g_{\mu\nu}}{M} F_1(x, Q^2) + \frac{p_\mu p_\nu}{M^2 \nu} F_2(x, Q^2) - i\epsilon_{\mu\nu\alpha\beta} \frac{p^\alpha p^\beta}{2M^2 \nu} F_3(x, Q^2) \quad (1.9)$$

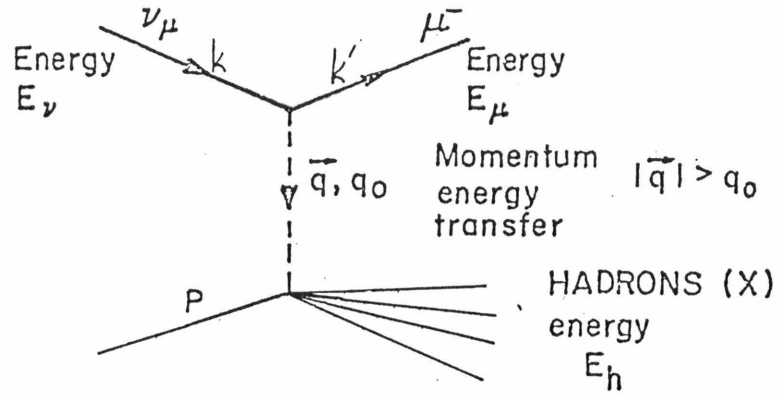


Figure 1.1 Neutrino charged current event

Terms which will yield contributions of the order of lepton masses in the cross section are neglected. These same unknown functions then parametrize the differential cross section:

$$\frac{d\sigma^{\nu(\bar{\nu})}}{dx dy} = \frac{G^2 ME}{\pi} \left\{ \left( 1 - y - \frac{Mxy}{2E} \right) F_2^{\nu(\bar{\nu})}(x, Q^2) + \frac{y^2}{2} 2xF_1^{\nu(\bar{\nu})}(x, Q^2) \right. \\ \left. \pm y \left( 1 - \frac{y}{2} \right) xF_3^{\nu(\bar{\nu})}(x, Q^2) \right\} \quad (1.10)$$

This is also commonly written in terms of  $R = \sigma_L/\sigma_T$ , where:

$$R(x, Q^2) = \left( 1 + \frac{Q^2}{\nu^2} \right) \frac{F_2(x, Q^2)}{2xF_1(x, Q^2)} - 1 \quad (1.11)$$

It can be shown that  $R$  is a measure of the non-spin  $\frac{1}{2}$  component of the nucleon [Cl79]. These functions:  $2xF_1$ ,  $F_2$  and  $xF_3$ , describe the structure of the nucleon and are the quantities to be measured in this experiment.

## 1.2 The Quark-Parton Model and Neutrino Scattering

Originally, the existence of quarks was inferred from the periodicity of hadron spectroscopy [Ge64, Zw64]. Such structure could arise if mesons and baryons were composed of some underlying triplet of objects:  $u$ ,  $d$  and  $s$  quarks. Mesons represent combinations of  $q\bar{q}$ , while

baryons are three quark states:  $qqq$ . The original scheme has subsequently been enlarged to include c and b quarks, with an expected sixth quark, t. These additional quarks provide an explanation for the absence of strangeness changing neutral currents (the GIM mechanism [Gl70]), and the narrow vector meson resonances ( $\psi$  [Au74a,Au74b] and  $\Upsilon$  [He77]). Despite extensive search, with one possible exception [La77,La78,La81], no free quarks have been observed [Jo77,Ly80]. However, existence may be indirectly inferred from the properties of deep-inelastic lepton scattering.

Flavour	u	d	s	c
Isospin	1/2	1/2	0	0
$I_3$	1/2	-1/2	0	0
Charge	2/3	-1/3	-1/3	2/3
Baryon number	1/3	1/3	1/3	1/3
Strangeness	0	0	-1	0
Charm	0	0	0	1

Table 1.1 Properties of quarks

The standard model posits the form of the weak current for quarks to be (V-A) analogous to the leptonic current. Quarks appear in left-handed doublets of weak isospin:  $(u,d)_L$ ,  $(c,s)_L$  and  $(t,b)_L$ , and right-handed singlets. However, the eigenstates of the weak lagrangian are not the mass eigenstates. This leads to the complication of a mixing matrix, as suggested by Cabibbo [Ca63]:

$$\begin{aligned}
 j_\mu = & \cos \theta_c \bar{u} \gamma_\mu (1 - \gamma_5) d \\
 & + \sin \theta_c \bar{u} \gamma_\mu (1 - \gamma_5) s \\
 & - \sin \theta_c \bar{c} \gamma_\mu (1 - \gamma_5) d \\
 & + \cos \theta_c \bar{c} \gamma_\mu (1 - \gamma_5) s
 \end{aligned} \tag{1.12}$$

The matrix has been generalized by Kobayashi-Maskawa [Ko73] to the present situation of six (supposed) quarks.

Using this form for the hadronic current, centre-of-mass cross sections (table 1.2) can be calculated for free quarks. Scattering of a (left-handed) neutrino from a (left-handed) quark, having net angular momentum 0, is isotropic. Scattering of a (left-handed) neutrino from a (right-handed) anti-quark, having net angular momentum 1, exhibits a  $((1 + \cos \theta^*)/2)^2$  distribution.

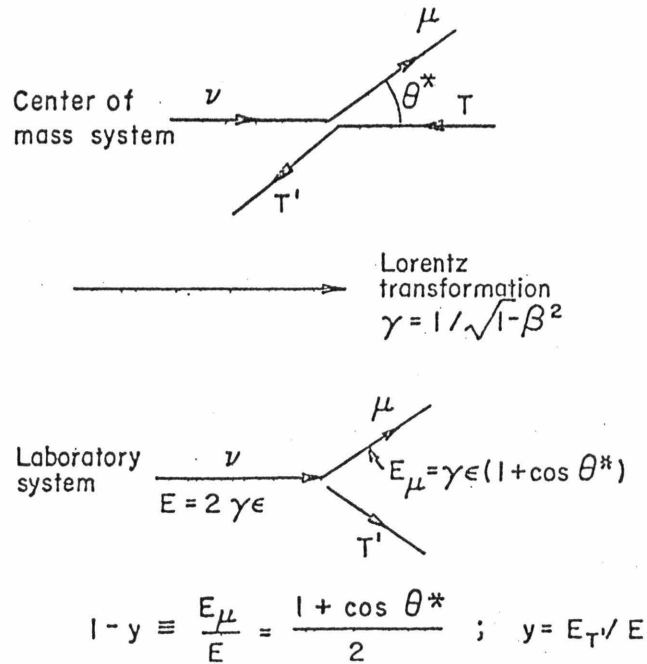
	$\frac{d\sigma}{d \cos \theta^*}$	$\frac{d\sigma}{y}$
$\nu_\mu d, \bar{\nu}_\mu \bar{d}$	$\frac{G^2 s}{2\pi}$	$\frac{G^2 s}{\pi}$
$\bar{\nu}_\mu u, \nu_\mu \bar{u}$	$\frac{G^2 s}{2\pi} \left( \frac{1 + \cos \theta^*}{2} \right)^2$	$\frac{G^2 s}{\pi} (1 - y)^2$

Table 1.2 Free quark cross sections

At high energies where we may neglect masses, the centre-of-mass angle can be related to a measurable quantity in the lab frame, the inelasticity  $y = 1 - E_\mu/E_\nu$ , where  $E_\nu$  is the incident neutrino energy,  $E_\mu$  the outgoing muon energy. Referring to figure 1.2, it can be seen that

$$1 - y = \frac{1 + \cos \theta^*}{2} \quad (1.13)$$

The free-quark cross sections expressed in terms of  $y$  are listed in the second column of table 1.2.

Figure 1.2 Connection between  $y$  and centre-of-mass scattering angle

Within the nucleon, the quarks are not free. Suppose that in the frame of the neutrino-quark system, the struck quark carries a fraction,  $\xi$ , of the total proton momentum. Then the energy dependence of the free quark cross sections (table 1.2) are modified to the extent that  $s_{\nu q} = \xi s$ :

$$\frac{d\sigma}{dy} = \left( \frac{d\sigma}{dy} \right)_{free} \xi \rho(\xi) d\xi \quad (1.14)$$

The probability of finding a quark with fractional momenta between  $\xi$  and  $\xi + d\xi$  is given by  $\rho(\xi) d\xi$ .

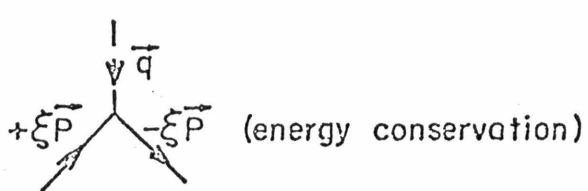
The fractional momentum,  $\xi$ , can be related to measurable quantities. In the quark-parton model [Fe69,Bj69] it is assumed that the struck quark is quasi-free: that is, a near massless, pointlike object, with limited transverse momentum. Effectively, other quarks in the nucleon can be ignored on the distance scale of the weak interaction. Consider the boson and quark in the frame where the boson has zero energy, as shown in figure 1.3. A simple consideration of energy-momentum balance shows that

$$\xi = x = \frac{-q^2}{2P \cdot q} = \frac{-q^2}{2M\nu} \quad (1.15)$$

where  $\nu = E_\nu - E_\mu$ ,  $Q^2 = -q^2 = 2E_\nu E_\mu (1 - \cos \theta_\mu)$ , and  $\theta_\mu$  is the angle the outgoing muon makes relative to the incident neutrino.

$$\text{Transferred} \begin{cases} \text{energy} & q_0 = E_\nu - E_\mu \\ \text{momentum} & \vec{q} = \vec{P}_\nu - \vec{P}_\mu \\ \text{invariant} & q^2 = q_0^2 - |\vec{q}|^2 < 0 \end{cases}$$
  

Frame with  $q_0 = 0$



$$\vec{q} = -2\xi \vec{P} \quad (\text{momentum conservation})$$

$$|\vec{q}|^2 = -2\xi \vec{P} \cdot \vec{q}$$

$$-q^2 = 2\xi P \cdot q$$

Figure 1.3 Connection between the scaling variable  $x$  and measurable quantities

Within the limits of the impulse approximation, cross sections for the nucleon can be constructed from quark and anti-quark momentum densities,  $q(x) = x\rho(x)$ :

$$\begin{aligned}\frac{d^2\sigma^\nu}{dx dy} &= \frac{G^2 ME}{\pi} \left\{ q^\nu(x) + \bar{q}^\nu(x)(1-y)^2 \right\} \\ \frac{d^2\sigma^{\bar{\nu}}}{dx dy} &= \frac{G^2 ME}{\pi} \left\{ q^{\bar{\nu}}(x)(1-y)^2 + \bar{q}^{\bar{\nu}}(x) \right\}\end{aligned}\quad (1.16)$$

Neglect for the moment small corrections due to expected differences between the strange and charm sea in the nucleon. Defining:

$$\begin{aligned}q^\nu(x) &= q^{\bar{\nu}}(x) = u(x) + d(x) + s(x) + c(x) \\ \bar{q}^\nu(x) &= \bar{q}^{\bar{\nu}}(x) = \bar{u}(x) + \bar{d}(x) + \bar{s}(x) + \bar{c}(x)\end{aligned}\quad (1.17)$$

the cross sections become:

$$\begin{aligned}\frac{d^2\sigma^\nu}{dx dy} &= \frac{G^2 ME}{\pi} \left\{ (q(x) + \bar{q}(x)) \frac{(1 + (1-y)^2)}{2} + (q(x) - \bar{q}(x)) \frac{(1 - (1-y)^2)}{2} \right\} \\ \frac{d^2\sigma^{\bar{\nu}}}{dx dy} &= \frac{G^2 ME}{\pi} \left\{ (q(x) + \bar{q}(x)) \frac{(1 + (1-y)^2)}{2} - (q(x) - \bar{q}(x)) \frac{(1 - (1-y)^2)}{2} \right\}\end{aligned}\quad (1.18)$$

This quark-parton model calculation can be compared with the general expression for the cross section (1.10). The connection with the standard structure functions is clearly:

$$\begin{aligned}R &= 0 \quad \text{or} \quad 2xF_1(x) = F_2(x) \\ F_2(x) &= F_2^\nu(x) = F_2^{\bar{\nu}}(x) = q(x) + \bar{q}(x) \\ xF_3(x) &= xF_3^\nu(x) = xF_3^{\bar{\nu}}(x) = q(x) - \bar{q}(x)\end{aligned}\quad (1.19)$$

In the quark-parton model, the structure functions scale with  $x$  [Fe69,Bj69]. Furthermore, the Callen-Gross relation [Ca69],  $2xF_1(x) = F_2(x)$ , is satisfied unless the nucleon is hypothesized to contain interacting, non-spin  $\frac{1}{2}$  objects.

A number of quark counting rules can be derived using the quark model. For example, the Gross-Llewellyn-Smith (GLS) sum rule [Gr69] predicts that:

$$\int_0^1 F_3(x) dx = 3 \quad (1.20)$$

where 3 is the number of valence quarks. This can be tested using our results for  $xF_3$ . Quark-parton predictions can also be made for charged lepton scattering by replacing the weak with the electromagnetic lagrangian in the calculations outlined above. The result obtained reflects

the coupling to quark electric rather than weak charge:

$$\begin{aligned} F_2^{l\pm}(x) &= \frac{5}{18}(q(x) + \bar{q}(x)) \\ &= \frac{5}{18}F_2(x) \end{aligned} \tag{1.21}$$

A comparison of our result for  $F_2$  with that measured from charged lepton scattering can test this prediction.

### 1.3 Structure Functions and QCD

Deviations from this simple scaling model are expected. The finite mass of the nucleon introduces scale breaking effects on the order of  $M_N^2/Q^2$ . Thus, structure functions should scale not with  $x$ , but with:

$$\xi = \frac{2x}{1 + \sqrt{1 + 4M_N^2 x^2/Q^2}} \tag{1.22}$$

[Ge76a,Ge76b]. The intrinsic transverse momenta ( $k_T^2$ ) of quarks within the nucleon also introduces terms which fall like  $1/Q^2$ . The quark-parton model predicts [Fe72] that:

$$R = \frac{4(k_T^2 + M_N^2 \pm \Delta)}{Q^2} \tag{1.23}$$

Finally, Quantum Chromodynamics (QCD), the leading theory of strong interactions, predicts logarithmic scaling violations [Al82].

In the language of perturbative QCD, coloured exchange fields, called gluons, bind quarks together to form hadrons. The interactions between quarks and gluons is described by a running coupling constant, which to lowest order is:

$$\alpha_s(Q^2) = \frac{4\pi}{(11 - 2N_f/3) \ln Q^2/\Lambda^2} \tag{1.24}$$

where  $N_f$  is the number of quark flavours. Unlike QED, the coupling  $\alpha_s(Q^2) \rightarrow 0$  as  $Q^2 \rightarrow \infty$ , a phenomenon referred to as asymptotic freedom. The treatment of the struck quark in the quark-parton model as a quasi-free object is essentially correct. However, as the nucleon is probed with higher  $Q^2$ , and hence over smaller distance scales, the struck quarks are resolved into quark plus gluon, and gluons into a quark plus anti-quark pairs or two gluons.

The Altarelli-Parisi equations [Al77] quantify these statements. A set of splitting functions,  $P_{ij}(z)$ , describe the probability of finding a parton  $i$  inside a parton  $j$ , with a fraction,  $z = x_i/x_j$ , of the parent momentum. QCD is unable to predict the form of the quark distribution functions at a given  $Q^2$ , since that would involve excursions into the low  $Q^2$ , non-perturbative regime of the theory. Instead, the evolution of quark densities as a function

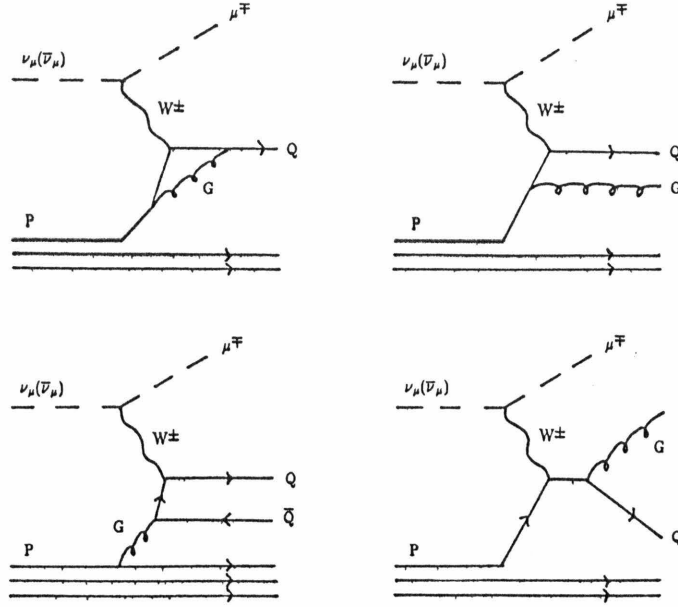


Figure 1.4 Higher order QCD corrections to pointlike cross section of  $Q^2$  is predicted by a set of differential equations using these splitting functions:

$$\begin{aligned}
 Q^2 \frac{d}{dQ^2} \frac{F_2(x, Q^2)}{x} &= \frac{\alpha_s(Q^2)}{2\pi} \left\{ P_{qq}(x) \otimes \frac{F_2(x, Q^2)}{x} + 2N_f P_{qG}(x) \otimes \frac{G(x, Q^2)}{x} \right\} \\
 Q^2 \frac{d}{dQ^2} \frac{G(x, Q^2)}{x} &= \frac{\alpha_s(Q^2)}{2\pi} \left\{ P_{Gq}(x) \otimes \frac{F_2(x, Q^2)}{x} + P_{GG}(x) \otimes \frac{G(x, Q^2)}{x} \right\} \\
 Q^2 \frac{d}{dQ^2} F_3(x, Q^2) &= \frac{\alpha_s(Q^2)}{2\pi} P_{qq}(x) \otimes F_3(x, Q^2)
 \end{aligned} \tag{1.25}$$

where

$$f \otimes g = \int_x^1 \frac{dz}{z} f(z) g\left(\frac{x}{z}\right) \tag{1.26}$$

Here,  $G(x, Q^2)$  is the momentum distribution of gluons in the nucleon. Valence quarks radiate gluons and move from large to small  $x$ . Sea quarks at small  $x$  result from gluon pair production. Therefore, with increasing  $Q^2$ , we expect a decrease in the number of quarks at large  $x$ , and an increase at small  $x$ . The validity of the theory in describing nucleon structure can be confirmed by observation of this predicted pattern of logarithmic scaling violations, parametrized by the single constant  $\Lambda$ .

Perturbative QCD also predicts a finite value for  $R(x, Q^2)$ , which falls off sharply with  $x$ , and exhibits the usual logarithmic  $Q^2$  dependence [Fi78]. Although difficult to measure, this experiment can address the question of the value of  $R(x, Q^2)$ , particularly at small  $x$ .

## 1.4 Outline of Presentation

Experimental particle physics is a collaborative effort, and the data set described here is part of ongoing work by physicists from Caltech (now Columbia), Fermilab, Rochester and Rockefeller. The group has had a long history of involvement in neutrino physics, beginning with the first generation of neutrino detectors at Fermilab [Ba75a-b, Ba76b, Ba77a-d, Ba78a, Mc78]. The present detector, located in Lab E, represents a substantial upgrade, in terms of fiducial volume, over early detectors. Results from an engineering run of the detector in the summer of 1978 have been presented [Le81]. Between June, 1979 and January, 1980 a high statistics sample of neutrino and anti-neutrino charged current events were obtained in a run known as Fermilab experiment E616. Total cross sections and  $y$ -distributions from E616 were the subject of a Caltech thesis by R.Blair [Bl82, Bl83a].

Here we will examine results of an effort to extract structure functions from this same data set, and a confrontation of those results with some of the predictions of the quark-parton model and QCD described above. In addressing this task, the subject has been divided in the following manner: Chapter 2 examines the dichromatic beam line, the source of neutrinos for the experiment, Chapter 3 describes the Lab E detector, Chapter 4 presents details of the analysis required to convert raw experimental data into physics variables, Chapter 5 details the techniques used to extract structure functions from the charged current sample, and finally Chapter 6 covers various tests of our structure function results in the light of predictions by the

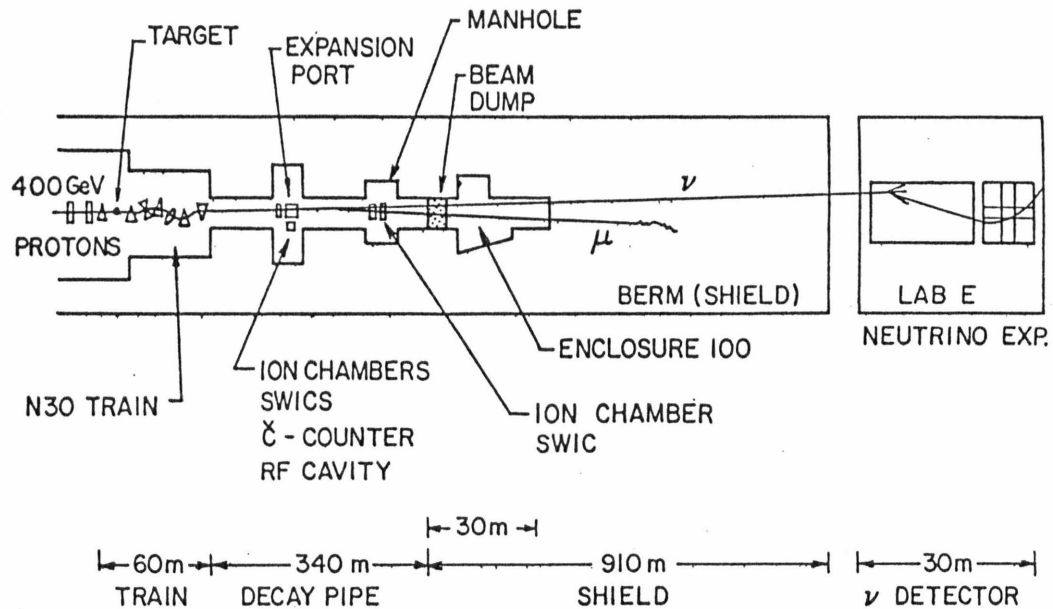


Figure 1.5 Layout of the neutrino area at Fermilab

quark model and QCD. In general, the material covered in the first three chapters represents an outline for the purpose of completeness. Details can be found in the Caltech theses of J.Lee [Le81], or R.Blair [Bl82]. Also in the literature are more extensive accounts of the beam monitoring system [Bl83b], diffraction in the Čerenkov counter [Bo83b], and the Lab E detector [Ba78b].

Work by the group continues. During the spring of 1981, neutrino data were taken simultaneously in detectors located in the Wonder building and Lab E, in a search for evidence of neutrino oscillations [Ha83]. An upgrade of the Lab E detector is under way, converting from spark chambers to drift chambers, in anticipation of running at the Tevatron. The increased  $Q^2$  range obtained with such high energy neutrinos should make possible a definitive determination of  $\Lambda$ , the QCD interaction scale [Bl80].

## Neutrino Source

Measurement of the logarithmic scaling violations of structure functions requires a large sample of neutrino and anti-neutrino events over a wide range of high  $Q^2$ . Furthermore, systematic errors on flux calculations should be minimized. Definitive tests of quark model predictions, which depend on absolute normalization of structure functions, also require precision flux measurements. The source of neutrinos in this experiment, the dichromatic beam line at Fermilab, fulfills these requirements.

The principal decay mode of charged pions and kaons is the two body decay into  $\mu^\pm$  and  $\nu_\mu(\bar{\nu}_\mu)$ . If some fraction of the particles in a high energy beam of pions and kaons is allowed to decay, a flux of high energy neutrinos and muons is obtained. Muons can be removed by range-out in material, leaving a neutrino beam.

The kinematics of two body decays results in a simple correspondence between neutrino energy,  $E_\nu$ , and the decay angle,  $\theta_\nu$ , that the neutrino makes with the parent particle:

$$E_\nu = \frac{1 - (\mu/m_s)^2}{1 + (\gamma\theta_\nu)^2} E_s \quad (2.1)$$

$$\gamma = E_s/m_s$$

where  $m_s$  and  $E_s$  are the mass and energy of the parent particle, and  $\mu$  is the muon mass. In a detector a distance  $z$  downstream of the decay point, and at a radius  $r = z \tan \theta_\nu$ , the population of neutrinos from pion and kaon decay will be clearly distinguishable by energy. For example, at  $\theta_\nu = 0^\circ$ , neutrinos from pion decay have an energy  $0.43E_s$ , whereas those from kaon decay have energy  $0.95E_s$ . The banding of neutrino events from pion and kaon decay in energy versus radius plots is characteristic of the dichromatic beam.

The degree to which this simple relationship is complicated is a reflection of the disorder of the secondary beam producing the neutrinos, and the necessarily extended length of the decay region. The flux of a real beam, with small angular dispersion and momentum bite, will deviate little from that calculated for an ideal beam. The problem of determining the composition of the secondary beam is also much simplified under these conditions. The design of the Fermilab dichromatic beam represents a reasonable compromise between the

requirements of large neutrino flux and small systematic errors in the calculation of that same flux [Ed76a,Ed76b,St78].

## 2.1 Dichromatic Beam

Primary protons from the main ring at 400GeV/c interacted in a 12in BeO target (about one collision length) to produce hadrons. The resulting secondary beam of pions, kaons and protons was sign and momentum selected by bending the particles with a dipole magnet and accepting only those particles passing through a momentum defining slit. This is analogous to how one would pick out one wavelength of light from a white source, using a prism and slit arrangement. The particular momentum selected could be controlled by changing the current of the dipole-bending magnet. Data were taken at nominal secondary momenta of 250, 200, 168, 140, and 120GeV/c, for both positive (neutrino) and negative (anti-neutrino) polarities.

The function of collimating the beam before entry into the decay pipe was accomplished by a point-to-parallel system of quadrupole magnets. A quadrupole focusing in the horizontal (defocusing in the vertical), followed by a second quadrupole focusing in the vertical (defocusing in the horizontal) may be likened to a lens of optical systems. In this case, particles emerging from the target, at the focus, entered the decay pipe with small angular divergence. The dipole and quadrupole magnets, termed the N-30 train, sat on a series of carts which could be moved into and out of the beamline. Table 2.1 summarizes the characteristics of the secondary beam.

Primary proton energy	400Gev
Intensity	$10^{12}$ to $2 \times 10^{13}$
Target	12in BeO
Targeting angles	
Horizontal	11.96mr
Vertical	1.125mr
Solid angle acceptance	$11.5\mu sr$
Momentum acceptance	$\pm 9\%$
Angular divergence of secondary beam	
Horizontal	$\pm .15mr$
Vertical	$\pm .20mr$
Secondary momentum	50 to 300GeV/c

Table 2.1 Summary of characteristics of the dichromatic beam

The design of the N-30 train also addressed the problem of contaminating decays of hadrons into neutrinos before the momentum slit. At no point before the final bend did the beam point toward the Lab E apparatus. Targeting was at an angle of 12mr, and there were bends in both vertical and horizontal planes as shown in figure 2.1 to accomplish this end.

Decays which did intercept the detector were from wide angle secondaries, or at large angles. Hence the wide-band flux was small and peaked at low energies.

Collimated secondaries pass into a 350m evacuated decay pipe where pions and kaons decayed. A secondary dump, 6.5m of steel and aluminum, absorbed the hadrons which failed to decay by the end of the decay pipe. There followed 930m of earth and steel berm before Lab E, shielding to stop muons produced in secondary decays.

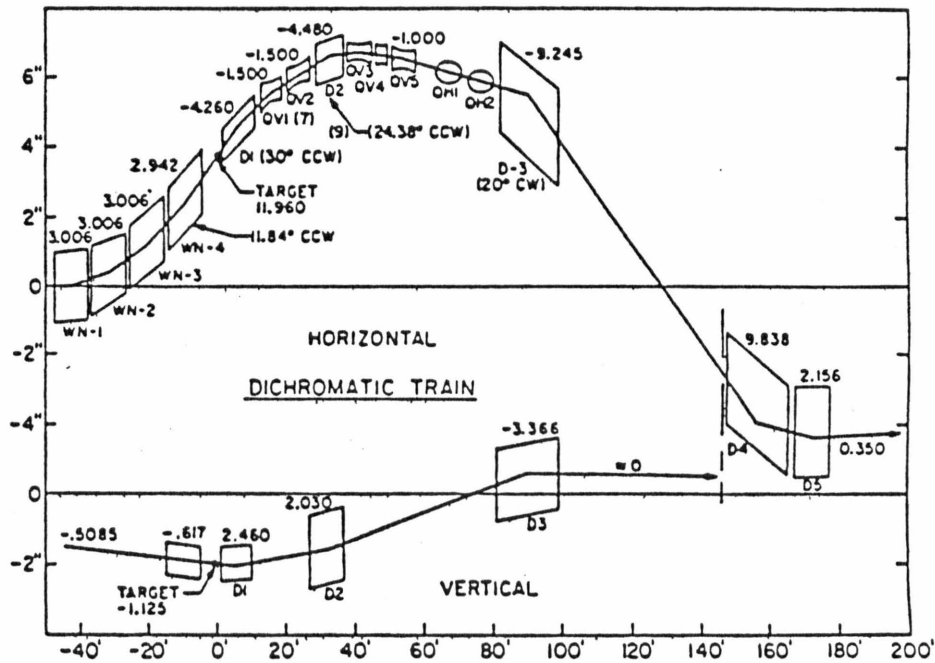


Figure 2.1

Layout of the N-30 dichromatic train showing magnet elements and the central momentum ray

The calculation of neutrino fluxes required a knowledge of (1) the number of incident pions and kaons for a given period of running, and (2) characteristics of the beam such as mean momenta, momentum spread, and beam dispersion. The first task was further broken down into (1a) a measurement of particle fractions using a Čerenkov counter, and (1b) a total flux measurement using ionization chambers. Monitors were therefore of two varieties: those which measured beam characteristics, and those which continuously monitored total secondary flux.

Various devices to accomplish these tasks were distributed along the N-30 train, and at two locations in the decay pipe: the expansion port and the target manhole, respectively 136m and 290m downstream of the last bend (see figure 1.5).

## 2.2 Total Intensity Monitors

The flux of primary protons was monitored using a beam current transformer (BCT). An attempt was made to do the same with the secondary beam, but this proved impossible due to the large number of beam-associated muons passing through the toroid aluminum. Instead, the primary flux monitors for the secondary beam were ionization chambers located in the expansion port and the target manhole. A typical ion chamber consisted of thin foils separated by 0.5in fibreglass spacers, the gap filled with gaseous helium. Electrons released by the passage of ionizing radiation were collected without multiplication, and the total charge digitized.

### 2.2.1 Calibration

The amount of charge produced per secondary passing through an ion chamber, the absolute calibration of the device, was determined in several ways. The most direct measurement was made using a beam of sufficiently low intensity to allow comparison of the ion chamber response with conventional counting using scintillator. This of course required that the chamber and its electronic readout be linear over beam intensity changes of the order of  $10^5$ , in order to extrapolate to operating intensities. Comprehensive measurements were made in a secondary beam in the Meson area at Fermilab (M-2 line), after preliminary studies in the Neutrino hadron beam (N-5 line). A special chamber with ceramic spacers was used in order that the small signal levels produced in a low intensity beam not be swamped by noise. During the course of this investigation, it was observed that the calibration of the chamber differed for mesons and protons. Heavily ionizing slow alphas and protons are produced by interactions in the upstream window of the chamber, and contribute significantly to the signal. The observed difference of 6.2% can be traced to the difference in absorption cross sections for protons and mesons. The absolute calibration was determined to be  $3.38 \pm .05 \times 10^{-18}$  Coulombs/meson and  $3.63 \pm .06 \times 10^{-18}$  Coulombs/proton.

The ion chambers were also calibrated by comparison with flux as measured by  $\text{Na}^{24}$  production in copper foils. This method was used with the ion chambers in situ, using 200GeV/c primary protons passed through the train with the target removed. Intensity extrapolations to normal beam conditions were of the order of  $10^2$ . However, the precision of the foil measurements were limited to  $\pm 5\%$ , by uncertainties in foil thickness, and the acceptance of the gamma-ray detector used to measure the  $\text{Na}^{24}$  content of the irradiated foils. Also, an accurate determination of the production cross section,  $p+\text{Cu}\rightarrow\text{Na}^{24}+X$ , was of course necessary. Using the CERN measurement for the production cross section,  $3.83 \pm .07\text{mb}$ , the resulting calibration was  $3.38 \pm .10 \times 10^{-18}$  Coulombs/proton. A separate determination of this production cross section was made using the neuhall toroid (BCT), a device which could easily be calibrated with a current loop. The result,  $3.91 \pm .20\text{mb}$ , agreed with the CERN cross section measurement, and yields an ion chamber calibration of  $3.45 \pm .22 \times 10^{-18}$  Coulombs/proton.

A second total intensity monitor, an RF cavity, was located in the beam during much of the running. This device, tuned to the RF frequency of the main ring accelerating cavities (53.1Mhz), was sensitive to the electric field across the cavity gap at that frequency. An output

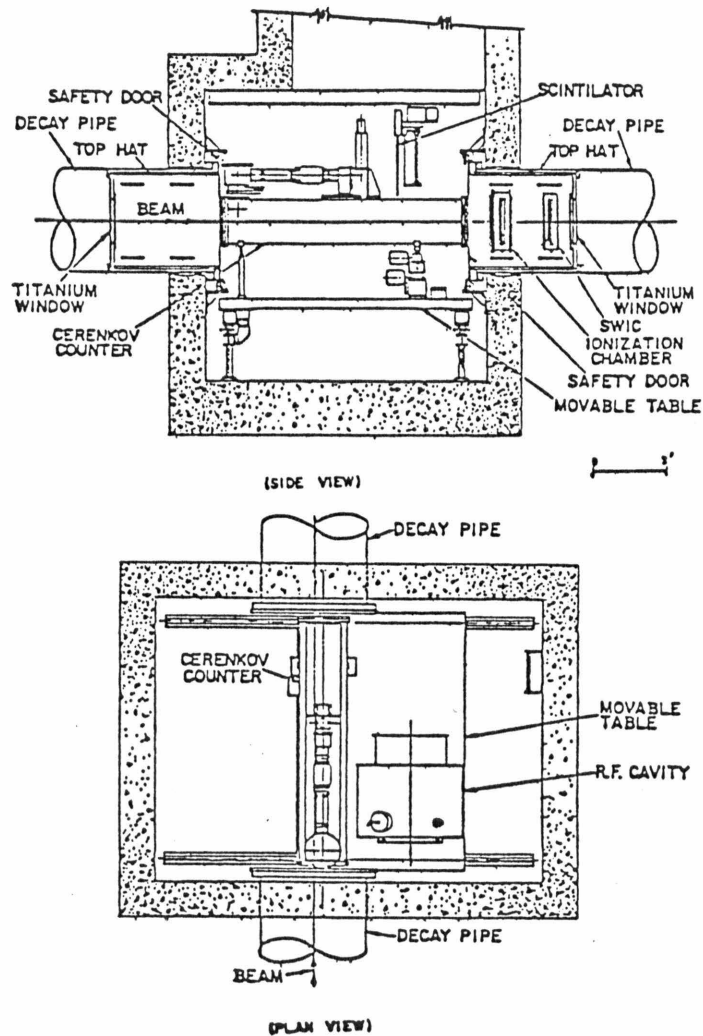
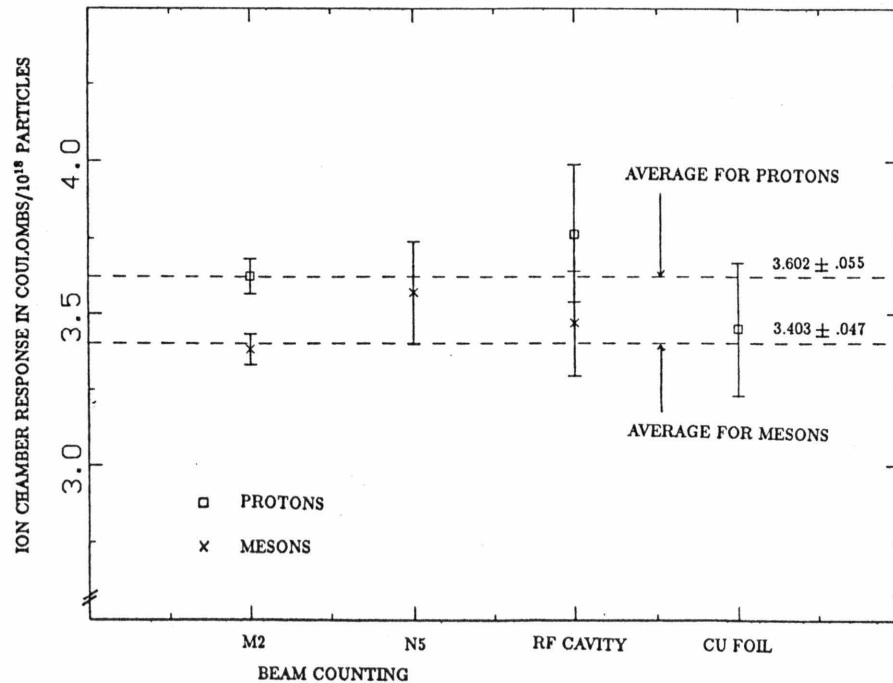


Figure 2.2 Layout of monitor devices in the Expansion Port

proportional to the number of beam particles passing through the cavity was produced. The calibration of the device could be determined from cavity properties. Unfortunately, the RF cavity response exhibited a not-understood 5% setting-to-setting dependence in comparison with ion chamber measurements. The errors on the RF cavity determination of the ion chamber calibration have been increased to accommodate this problem. The measured value for the calibration was  $3.47 \pm .17 \times 10^{-18}$  Coulombs/meson and  $3.76 \pm .22 \times 10^{-18}$  Coulombs/proton. Since the measurement can be made in a full intensity beam, this would be an area for fruitful effort in the future.

The agreement among the various methods was excellent, and the average result for the ion chamber calibration was:  $3.623 \pm .055 \times 10^{-18}$  Coulombs/meson and  $3.403 \pm .047 \times 10^{-18}$  Coulombs/proton. The foil calibration using the CERN production cross section measurement was not included in this average. All other measurements are internal to this experiment and therefore the source of systematic errors are well understood. The much smaller error assigned to the CERN cross section measurement is not understood in the light of our own attempts to measure the same number.



*Figure 2.9*

A comparison of the results of various techniques for calibrating the ion chambers

### 2.2.2 Systematic flux errors

In general, at any given time during the running, several ion chambers were used to measure secondary flux. Comparisons of the response of different ion chambers, or of ion chambers and the BCT, exhibited fluctuations of  $\pm 2\%$  for neutrinos and  $\pm 5\%$  for anti-neutrinos. Since the foil calibration measurement was made during neutrino running, the response of the ion chambers before and after calibration could have deviated by as much as 2% from the average running condition. Combined with a measurement uncertainty of 1% on the calibration measurement itself, a correlated 2.5% normalization error was therefore assigned to the secondary flux measurements. During the transition from anti-neutrino to neutrino running,

the response of the ion chambers changed by as much as 3%. An additional uncorrelated 3% uncertainty was assigned to the normalization of the anti-neutrino data.

In an oversight, the temperature of the gas circulated through the ion chambers was not directly monitored during the run—only temperature in the expansion port. The maximum variation in this temperature was  $\pm 5^\circ\text{C}$  about the mean. The ion chamber response depended on the gas density: hence, fluctuations relative to absolute zero were important. The uncertainty introduced by temperature was taken to be 1%, uncorrelated for neutrinos and anti-neutrinos.

### 2.3 Beam Composition

Measurements of beam composition were made using an integrating Čerenkov counter which could be moved into the beam in the expansion port. Before examining the characteristics of the actual device, consider first the case of a monoenergetic, well collimated beam of particles passing through a counter of length,  $L \rightarrow \infty$ , filled with helium at pressure  $P$ . If such particles have mass  $m_s$ , and momentum  $p_s$ , Čerenkov light is emitted at a fixed angle  $\theta_c$  with respect to the beam, where:

$$\theta_c^2 = 2\kappa P - \left(\frac{m_s}{p_s}\right)^2 \quad (2.2)$$

The constant  $\kappa$  parametrizes the pressure dependence of the index of refraction of the helium radiator:  $n = 1 + \kappa P$ . The intensity,  $I_c$ , of emitted light is given by:

$$\frac{dI_c}{d\lambda} = 2\pi\alpha L \left(\frac{1}{\lambda_2^2} - \frac{1}{\lambda_1^2}\right) \sin^2 \theta_c \quad (2.3)$$

where  $\lambda_1$  and  $\lambda_2$  are the wavelength limits of the photon detector.

Light is collected by the counter for angles in the interval  $\theta_0 \pm \delta\theta$ . This corresponds to a pressure interval of:

$$P_{\pm} = \frac{1}{2\kappa} \left( (\theta_0 \pm \delta\theta)^2 + \left(\frac{m_s}{p_s}\right)^2 \right) \quad (2.4)$$

A beam composed of pions, kaons and protons, with three distinct masses, would produce as a function of gas pressure in the counter three distinct bands of observable Čerenkov light separated by regions of zero response. The integral of light intensity in each band is proportional to the number of traversing particles of a given species; hence, such pressure curves could be used to determine particle composition of the beam.

#### 2.3.1 Čerenkov counter for E616

The Čerenkov counter used in this experiment is shown in figure 2.4. A parabolic mirror, with 120in focal length, collected and focused Čerenkov light along a double bend optical path onto an iris, which passed light with angles  $0.85 \pm 0.15\text{mr}$  with respect to the

beam axis. Such light was then focused onto a simple three-stage RCA phototube (CPM). The phototube response was found to be linear to better than 1% over the useful output range. Likewise the pressure gauge (CPR) was checked in the manner described in the thesis of J.Lee [Le81], and found to be linear at the 0.5% level.

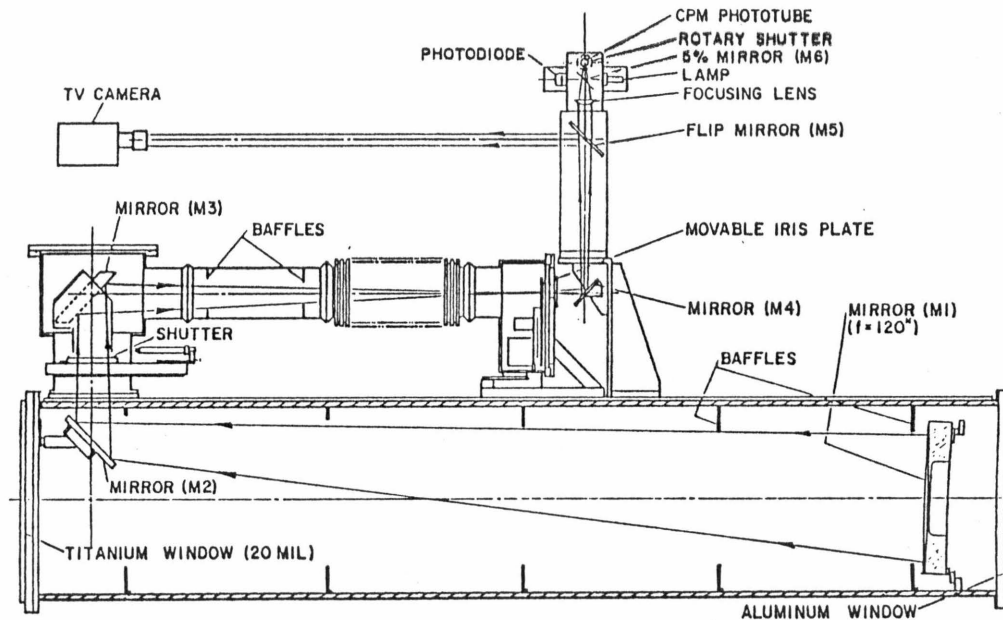
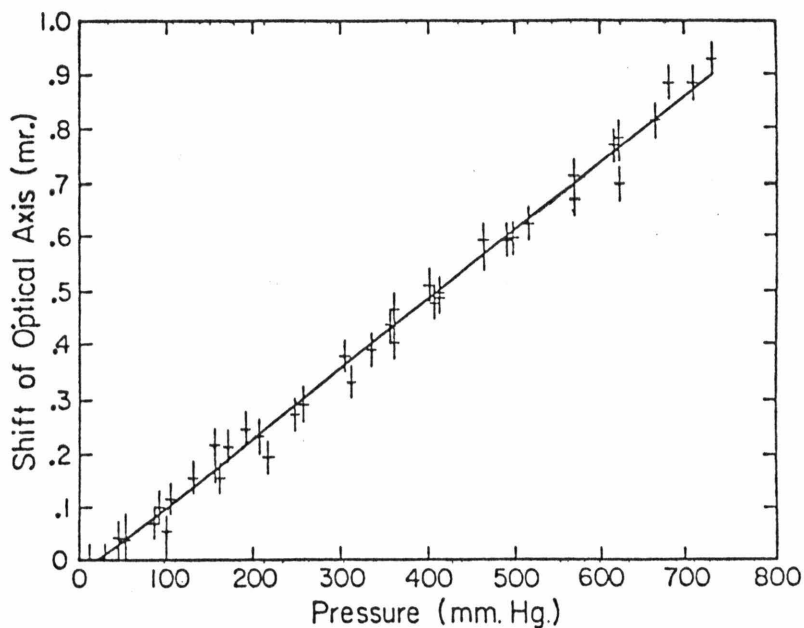


Figure 2.4 Schematic diagram of the Čerenkov counter used for E616

The procedure used to obtain a Čerenkov pressure curve was a two-step process. First, the axis of the counter was aligned with the secondary beam direction. This was accomplished at pressures just above the pion peak, by studying the variation of the counter response with respect to rotations about two directions perpendicular to the beam. Proper alignment was achieved when a circular image was produced at the iris plane. The counter was then evacuated and phototube response recorded each beam cycle (12s), with pressure incremented by a fixed volume of helium between cycles. In a typical curve (figure 2.8), the peaks due to pions, kaons and protons are clearly separated.

It was discovered after completion of the data run for E616 that the optical alignment of the counter shifted with pressure, due to mechanical instability. The shift as a function of gas pressure has been measured and found to be both linear and quite reproducible, as shown in figure 2.5. The correction was of course only significant for kaons and protons, since as noted the counter was always aligned at pressures just above the pion peak. However, the error introduced in all cases was small compared with other sources.

In a real secondary beam, such as the Fermilab dichromatic beam, a number of effects



*Figure 2.5 Čerenkov misalignment with pressure*

contribute to the broadening of the distinct bands of response of the ideal case described above: (1) beam divergence, (2) finite momentum spread, (3) diffraction in a finite length counter, (4) chromatic dispersion, due to variation of the index of refraction with wavelength, and (5) optical aberrations, negligible. Table 2.2 illustrates the level of contribution of each of these sources to the width of the pressure peaks. In general, the momentum spread dominated the width of kaons and protons, while diffraction dominated the peak widths of low mass particles such as pions, electrons and muons. In fact, diffraction resulted in an overlap of pion and proton contributions under the kaon signal. The procedure used to extract the particle fractions was necessarily more complicated than the simple area law.

The effect of beam dispersion was minimized by adjusting the position of the iris so that the optical system focuses not from infinity, but from a point on the N-30 train near the target, some 205m upstream. The effective dispersion was reduced to the size of the beam emerging from the target as seen from this distance, less than 0.1mr.

Source	$\Delta\theta_\pi$ mr	$\Delta P_\pi$ mmHg	$\Delta\theta_K$ mr	$\Delta P_K$ mmHg	$\Delta\theta_p$ mr	$\Delta P_p$ mmHg
Iris width	0.15	2.9	0.15	2.9	0.15	2.9
Beam angular dispersion	0.18	3.6	0.18	3.6	0.18	3.6
Beam momentum bite	0.05	1.0	0.60	14.	2.20	50.
Chromatic aberration	0.01	0.2	0.01	0.2	0.01	0.2
Diffraction	0.26	5.0	0.26	5.0	0.26	5.0

Table 2.2

Contributions to the smearing of Čerenkov peaks in a 200GeV/c secondary beam. For  $\theta_o = 0.85m\tau$ , the pion, kaon and proton peaks are at 14.1mmHg, 78.5mmHg and 211.1mmHg respectively.

### 2.3.2 Diffraction effects in a finite length counter

Small Čerenkov angles and short counter lengths were quite satisfactory in the integrating Čerenkov counter used in this experiment. Roughly  $5 \times 10^{-3}$  photoelectrons per particle were observed, but the large number ( $10^{10}$ ) of traversing particles resulted in a more than adequate signal. However, the short length did result in observable diffraction effects. For a counter of length  $L$ , the intensity of observed light is actually:

$$\frac{dI_c}{d\lambda d \cos \theta} = \frac{2\pi\alpha}{\lambda} \left(\frac{L}{\lambda}\right)^2 \left(\frac{\sin \psi}{\psi}\right)^2 \sin^2 \theta \quad (2.5)$$

where

$$\begin{aligned} \psi &= \frac{\pi L}{\lambda} \left(\frac{1}{n\beta} - \cos \theta\right) \\ &\approx \frac{\pi L}{2\lambda} \left(\left(\frac{m_s}{p_s}\right)^2 + \theta^2 - 2\kappa P\right) \end{aligned} \quad (2.6)$$

The width at the first node  $\psi = \pi$ , gives the diffraction entry shown in table 2.2. It is important to note that diffraction broadening results in contributions of intensity at all angles, including those below Čerenkov threshold. A finite response at zero pressure is predicted, a phenomenon commonly referred to as transition radiation.

The validity of the diffraction formula has been confirmed in two ways. Čerenkov pressure curves were taken with monoenergetic 200GeV/c primary protons: a beam brought through the N-30 train with target out, and with 0.1mr angular divergence. Therefore, diffraction effects dominated the width of the proton pressure peak. As can be seen from figure 2.6, the prediction of the diffraction formula conformed to observation for over three orders of magnitude of

intensity variation. The additional backgrounds in this figure can be accounted for in terms of light scattering from dust particles on mirrors in the counter, and effects of interactions in material in the beam upstream of the counter.

Secondly, the diffraction formula predicts without free parameters the level of response observed at zero pressure in the Čerenkov counter, for pressure curves taken with typical secondary beams of the experiment. Figure 2.7 shows both the measured and predicted ratio of zero pressure intensity to intensity integrated over electron and pion peaks. Again agreement was excellent.

### 2.3.3 Backgrounds

Three backgrounds had to be subtracted from Čerenkov pressure curves before analyzing beam content. The first was light produced outside the helium radiator. This was measured as a function of pressure, by periodically recording along with the normal Čerenkov signal, the phototube response when optically isolated from the helium radiator by a shutter. This background has already been removed in figure 2.8.

Interactions of particles with material in the beam, namely the vacuum window on the decay pipe and the counter front window, result in a wide spectrum of lower energy high angle particles. Such particles were a source of diffuse Čerenkov light, and produced a tail on the

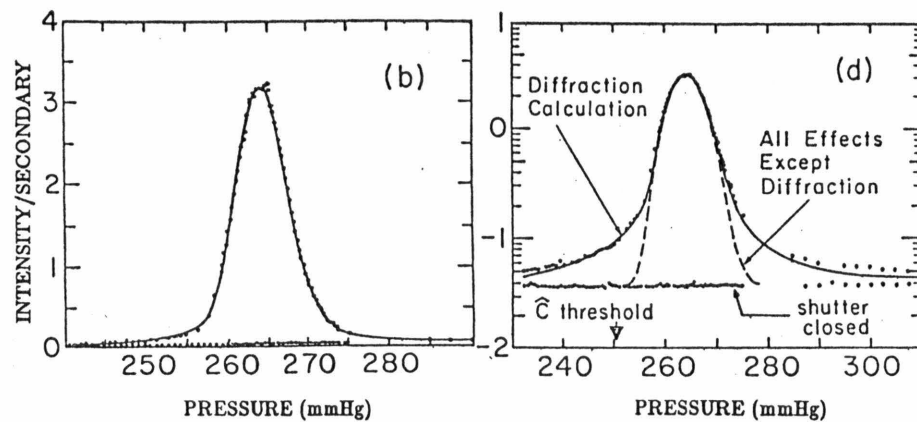


Figure 2.6 Pressure curve for 200 GeV/c protons

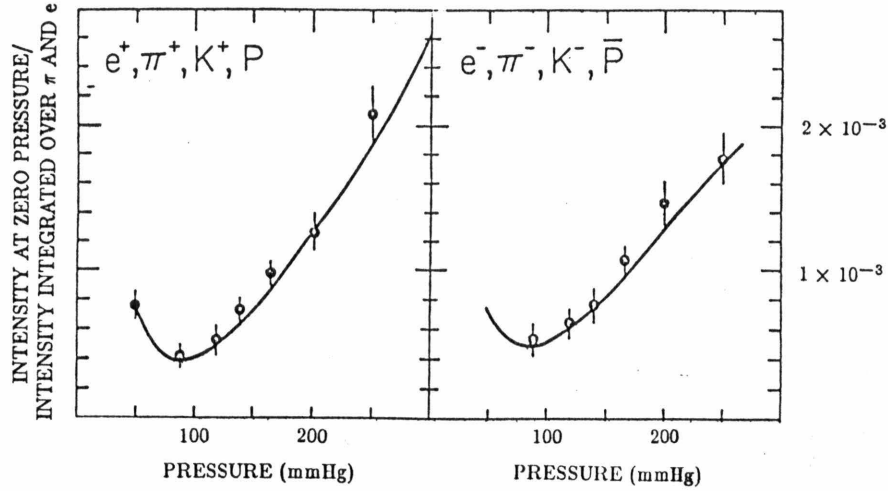


Figure 2.7 Zero pressure background and predictions

high pressure (low momentum) side of particle peaks. This effect was studied by putting further material in front of the counter, and observing the changes in pressure curves. In making the background subtraction, the differences were scaled by the inverse ratio of interaction lengths with and without additional material. Background curves were taken with 200GeV/c primary protons, and at the  $-120\text{GeV}/c$  and  $-250\text{GeV}/c$  settings of the secondary beam. The form of the subtraction was interpolated to the other settings.

The scattering of light from walls, baffles and particularly dust particles on mirror surfaces was an additional source of diffuse background. Two approaches have been used to remove this background. The material subtracted 200GeV/c proton pressure curve provided the pressure dependence of the background. If it is assumed that the form is momentum independent, contributions could be summed for each point in a particle peak. Amplitude adjustments of up to 10% were made in order to match the observed Čerenkov levels well beyond the proton peak, since the amount of dust on mirrors was time dependent. A second method used was to parametrize the background by:

$$I_{LS} = \begin{cases} \alpha + \beta\theta^2 & \theta \leq 4.5\text{mr} \\ \alpha + \gamma\theta^2 & \theta > 4.5\text{mr} \end{cases} \quad (2.7)$$

where  $\alpha$ ,  $\beta$  and  $\gamma$  are free constants to be fit. The change in slope at  $\theta = 4.5\text{mr}$  was empirical, in that it seemed to best fit the data. The final particle fractions were the average of the results

obtained using the two techniques; the difference was taken as a measure of the error due to uncertainties in the light scattering subtraction.

### 2.3.4 Analysis of pressure curves

Diffraction effects resulted in a significant contribution by pions and protons to the kaon peak, as noted above. Furthermore, the area rule breaks down unless integration is carried out over the entire diffraction peak, stretching below zero pressure for pions. A monte carlo, incorporating the correct Čerenkov intensity formula (2.5), was used to predict counter response functions for pions, kaons and protons. These response functions were then fit to pressure curves, after background subtraction. Free parameters were: (1) particle fractions, mean momenta and peak widths for each of the three species, and possibly (2) parameters  $\alpha$ ,  $\beta$  and  $\gamma$  for the light scattering background. A typical fit is shown in figure 2.8, and the values obtained for the particle fractions are listed in table 2.3.

In addition to pions, kaons and protons, the beam contained a small component of electrons and products from the secondary decays such as muons. Electrons were produced by neutral pion decay and gamma conversion in the production target. Measurements were

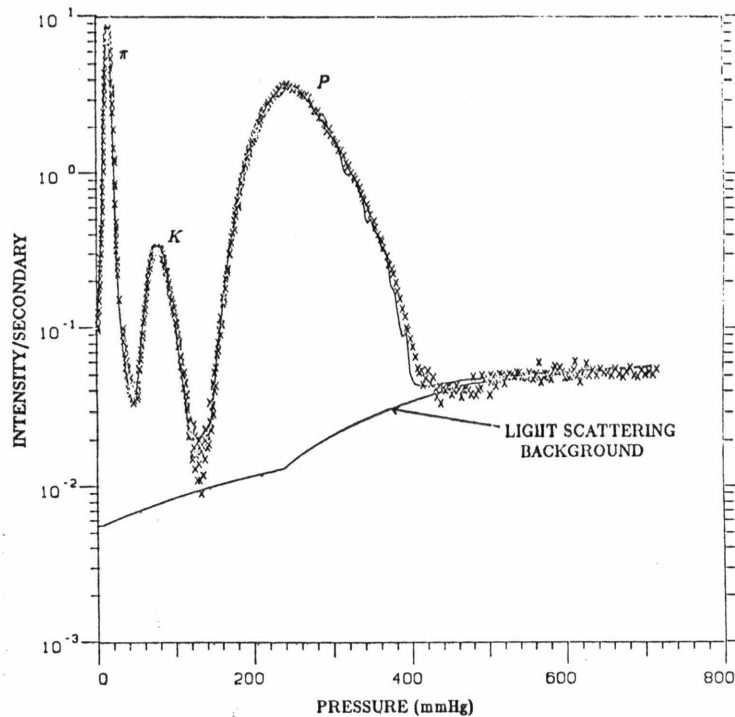


Figure 2.8

Pressure curve for 200 GeV/c secondary showing backgrounds and contribution from the three particle types

Setting	e/ $\pi$ +e	$\pi$ /Total	K/Total	P/Total
+120	.029 $\pm$ .002	.5243 $\pm$ .0205	.0470 $\pm$ .0029	.4220 $\pm$ .0219
+140	.020 $\pm$ .003	.4214 $\pm$ .0136	.0427 $\pm$ .0022	.5300 $\pm$ .0148
+168	.011 $\pm$ .003	.3115 $\pm$ .0115	.0349 $\pm$ .0016	.6520 $\pm$ .0127
+200	.006 $\pm$ .003	.1918 $\pm$ .0067	.0240 $\pm$ .0012	.7830 $\pm$ .0075
+250	.003 $\pm$ .002	.0771 $\pm$ .0026	.0115 $\pm$ .0007	.9110 $\pm$ .0030
-120	.065 $\pm$ .008	.8733 $\pm$ .0097	.0516 $\pm$ .0028	.0128 $\pm$ .0099
-140	.052 $\pm$ .005	.8845 $\pm$ .0073	.0568 $\pm$ .0023	.0099 $\pm$ .0074
-168	.031 $\pm$ .004	.9099 $\pm$ .0050	.0551 $\pm$ .0017	.0033 $\pm$ .0050
-200	.020 $\pm$ .005	.9339 $\pm$ .0051	.0443 $\pm$ .0017	.0074 $\pm$ .0050
-250	.013 $\pm$ .004	.9495 $\pm$ .0017	.0388 $\pm$ .0017	.0000 $\pm$ .0050

Table 2.9

Particle fractions in the secondary beam at the Expansion Port from the Čerenkov counter

possible for low momentum settings where the pion and electron peaks were distinguishable. For the higher settings we relied on a monte carlo calculation. The decay product component of the beam was directly proportional to the parent fraction. For the pion the only significant mode was the two-body decay into muons. However, the kaon has a number of channels not contributing to neutrino flux, but which do produce charged pions. The six principal decay modes of the kaon were included in the monte carlo calculation.

### 2.3.5 Mean momenta and widths

A Čerenkov pressure curve is a momentum transform of the beam. This is an inverse relation as shown in equation 2.2. For a given particle type, hadrons with momenta greater than the mean momentum map into pressures below the peak pressure, and vice versa. In a beam without angular dispersion:

$$2\kappa(P) = m^2 \left\langle \frac{1}{p^2} \right\rangle + \frac{2(\theta_2^4 + (\theta_1\theta_2)^2 + \theta_1^4)}{3(\theta_1^2 + \theta_2^2)} \quad (2.8)$$

where  $\langle P \rangle$  is the average pressure at peak, and  $\theta_1$  and  $\theta_2$  are the Iris angle acceptance limits (0.7mr and 1.0mr). The method was useful only for kaons and protons, since uncertainties in the Iris angle term, due to angular dispersion, become significantly more important for pions. The constant  $\kappa$  was determined from the 200GeV/c primary proton curves to be  $4.38 \pm .04 \times 10^{-8} mmHg^{-1}$ .

Agreement was seen between the momentum bite of the kaons in the beam as calculated by the beam monte carlo and as measured from the width of the kaon pressure peak. In fact, the momentum bite varied from setting to setting by no more than 0.7%. The uncertainty introduced into the flux calculation from this source was therefore negligible.

Setting	Mean $p_\pi$ GeV/c	Mean $p_K$ GeV/c	$\Delta\theta_x$ mr	$\Delta\theta_y$ mr	$\Delta p/p$ %
+120	119.5	122.4	$.16 \pm .04$	$.23 \pm .05$	10.1
+140	139.2	142.2	$.15 \pm .04$	$.21 \pm .03$	9.9
+168	166.3	169.8	$.13 \pm .03$	$.20 \pm .03$	10.0
+200	197.0	200.6	$.15 \pm .04$	$.20 \pm .02$	9.6
+250	243.8	247.0	$.16 \pm .04$	$.20 \pm .01$	9.4
-120	118.4	119.6	$.16 \pm .04$	$.23 \pm .05$	9.7
-140	137.8	138.9	$.15 \pm .04$	$.21 \pm .03$	9.4
-168	164.3	165.3	$.13 \pm .03$	$.20 \pm .03$	9.5
-200	194.0	194.6	$.15 \pm .04$	$.20 \pm .02$	9.2
-250	239.0	238.0	$.16 \pm .04$	$.20 \pm .01$	8.7

Table 2.4 Mean secondary momenta, widths and dispersions

## 2.4 Beam Dispersion and Steering

Beam profiles were routinely monitored using segmented wire ion chambers (SWICs), located in both the expansion port and the target manhole. These provided  $x$  and  $y$  projections of the beam profile at two points in the decay pipe. At each setting a scintillator scan of the beam profile was made in the expansion port. This was found to be in good agreement with the ion chamber measurements, except in the tails where some residual signal was seen in the SWICs. Combined with the known aperture of the momentum slit (4.13in x 1.50in) at the upstream end of the decay pipe, the SWIC profiles provided a measure of beam dispersion. The dispersion in the vertical plane was well determined by this method. However, the large horizontal aperture limited the precision of the measurement in the horizontal plane. Results are included in table 2.4.

Beam steering was monitored on a pulse-by-pulse basis while taking data, using split-plate ion chambers in the expansion port and target manhole. The difference over sum of the signals from the two halves of the chamber was used as a steering parameter. Vertical and horizontal split plate ratios at both locations in the decay pipe were maintained within tolerances corresponding to  $\pm 1.4$ in at Lab E. The experimenter could adjust the targeting angle of the primary proton beam if beam steering strayed outside these limits.

## 2.5 Beam Monte Carlo

A monte carlo was used to calculate the spectrum of neutrinos in both energy and position at Lab E. The calculation was divided into two parts conceptually and operationally. The first task was to produce secondary rays at the beginning of the decay pipe with characteristics matching the observed properties described above. A production model was used to generate pions, kaons, and protons at the target. These rays were then traced through the elements of the N-30 train to the momentum slit. The production spectra itself was not

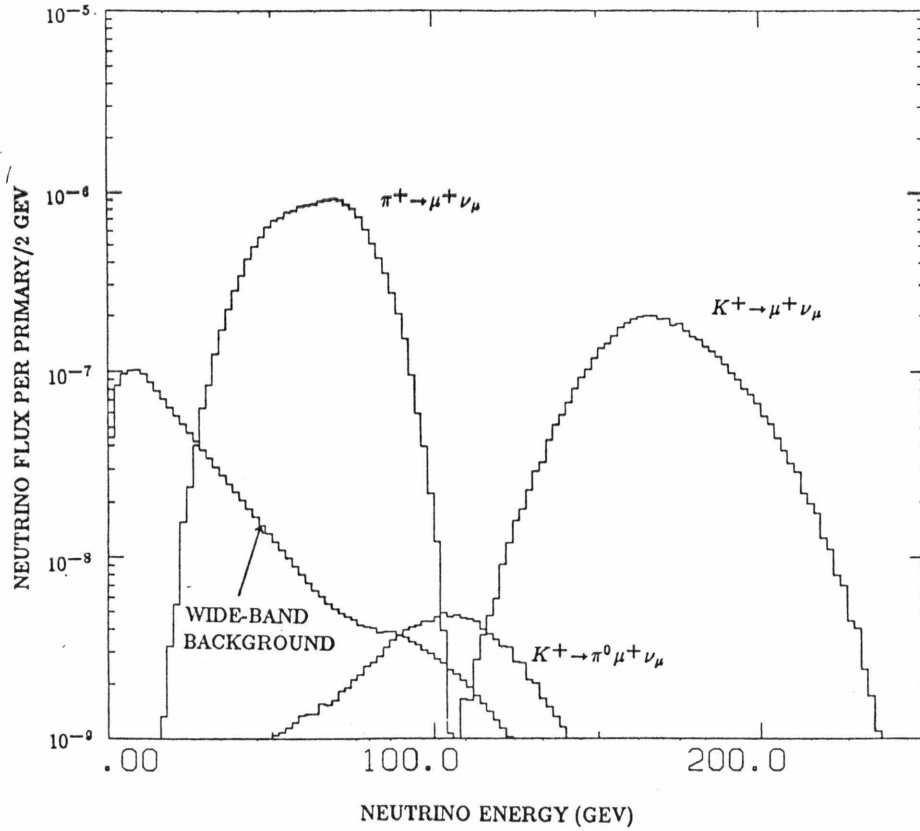


Figure 2.9

Monte Carlo calculation of neutrino flux at Lab E for 200 GeV/c secondaries

measured: only production folded against train acceptance. Furthermore, the positions of magnets and apertures on the train are only known to survey tolerances. Slight adjustments in the mean momenta, and dispersion of the secondary rays were therefore made to conform with the measurements made of these quantities.

The second stage in the calculation of fluxes was to model the decay of secondaries into neutrinos, a relatively straight-forward process. Along with the two body decay modes,  $\pi \rightarrow \mu \nu_\mu$  and  $K \rightarrow \mu \nu_\mu$  with branching ratios of 100% and 63.5% respectively, the three body decay  $K \rightarrow \pi^0 \mu \nu_\mu$  with a 3.20% branching ratio is a significant source of neutrinos in our charged current sample. (The decay channel,  $K \rightarrow \pi^0 e \nu_e$ , was an important source of background for neutral current studies.) The Monte Carlo thus produced a spectrum of neutrinos per pion or kaon at Lab E. Combined with a knowledge of the total number of lifetime pions or kaons received, this spectrum could be converted into an absolute flux. Figure 2.9 shows the calculated neutrino flux at Lab E, from the beam Monte Carlo for  $\pm 200$  GeV/c secondaries. The dichromatic nature

Setting	$k \times 10^{-11} /$ in <sup>2</sup> -primary proton	$a$ GeV	$b$ GeV	$E_0$ GeV
+120	2.14	1.18	21.01	7.36
+140	1.71	1.20	14.68	8.15
+168	1.39	0.89	21.81	8.07
+200	1.88	1.78	19.26	9.87
+250	1.48	1.32	22.97	7.50
-120	1.34	17.47	12.63	12.96
-140	1.34	17.47	12.63	12.96
-168	1.35	17.47	12.63	12.96
-200	1.46	17.47	12.63	12.96
-250	1.35	17.47	12.63	12.96

Table 2.5 Parameters for wide-band background flux

of the beam is clearly seen.

### 2.5.1 Wide-band background

Decays of secondaries before the momentum slit constituted a diffuse source of low energy neutrinos referred to as wide-band background. The energy and spatial distributions of this source of neutrinos was impossible to model, depending as it does on details of beam dumping. Instead events were recorded with protons on target but the collimator closed. Such events could then be used to make a subtraction from observed open slit events, the method used for our total cross section result [Bl82,Bl83a]. An alternative approach was to convert the observed events into a neutrino flux, using a model for the differential cross section. Wide-band flux could then be added to other flux sources. This was the technique used for the structure function results reported here. The spatial distribution was assumed to be uniform, so that the flux was just proportional to the solid angle subtended by the fiducial volume under consideration. The reconstructed energy spectrum of wide-band neutrinos, per incident proton and per unit area at Lab E, was parametrized by the model:

$$\Phi_{wb}(E) = \begin{cases} k(1 - e^{-E/a}) & E \leq E_0 \\ k(1 - e^{-E_0/a})e^{-(E-E_0)/b} & E > E_0 \end{cases} \quad (2.9)$$

Dumping for all negative settings was nearly at the same point on the train, whereas for positives various locations were used. It was therefore assumed that the energy spectrum was the same for all negative settings, but separate fits were made for the five positive settings. Results of the fits are listed in table 2.5, and the level of wide-band neutrino flux as compared with other sources is shown in figure 2.9.

## Neutrino Detector

The scale of the weak interaction requires that massive targets be used in order to obtain high statistics samples of neutrino events. The Lab E target had a mass of 680 tons, sufficient to produce but a few events per  $10^{13}$  protons on the primary target. Clearly this entire mass could not be active, and for the most part consisted of inert steel plates. However, the detector was instrumented so as to provide the information necessary to characterize a neutrino charged current event: (1) vertex position, (2) hadronic energy, (3) muon angle with respect to the incident neutrino, and (4) muon momentum. In addition, to maximize acceptance and simplify analysis, the resolution of these measurements was made as uniform as possible throughout the fiducial volume. The first three functions were performed by detectors integrated into the target, while the muon momentum was analyzed by a separate toroidal spectrometer immediately downstream.

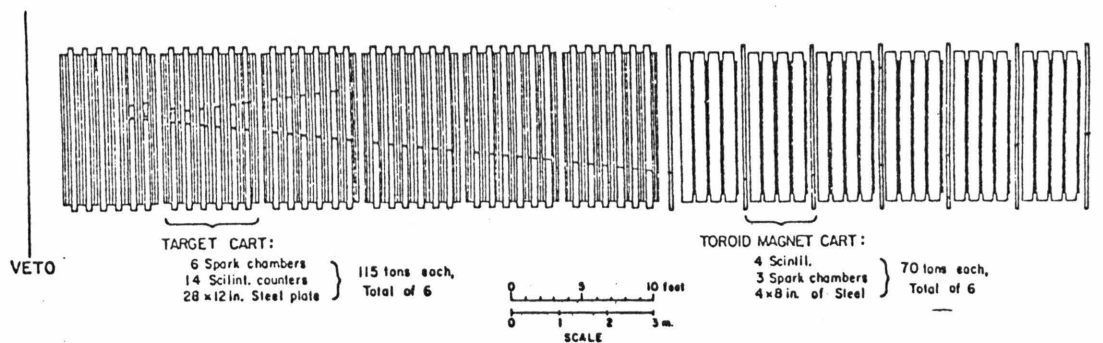


Figure 3.1 Lab E detector

### 3.1 Scintillation Counters

The hadronic energy released by the neutrino interaction was measured using a sampling calorimeter. The primary hadrons from the vertex interact in the target steel depositing energy, but also producing fast-forward going secondary pions and nucleons. These in turn interact, and a hadronic cascade develops. Interspersed in the steel are scintillation counters which sample the ionization energy of the shower. Principally this energy is in the form of **electromagnetic cascades originating from neutral pions in the hadronic shower**. The sum of the sampled energy is proportional to the total hadron energy. However, some hadronic energy is not converted to ionization energy, but is lost to nuclear binding effects. Also, some energy is badly sampled, such as low energy nucleons or alpha fragments which range out in the steel. Fluctuations in these losses result in an intrinsic resolution limit to the technique, but this limit was not reached by the relatively coarse-grained calorimeter of this experiment.

The target counters, every 10cm of steel, were 10ft×10ft×1in square acrylic tanks, filled with liquid scintillator. Along the four edges of the counter were 8 wavelength shifter bars, each 5ft in length, terminating in four RCA 6342A phototubes at the corners. Ionizing radiation passing through a counter excited a primary fluor emitting uv light. The primary emission was absorbed within approximately 1mm by a secondary fluor emitting isotropic blue light. The attenuation length at this wavelength was much longer, so the secondary light passed to the edge of the counter, where it was collected by the wavelength shifter bars. The shifter bars were acrylic doped with a third fluor, BBQ, which converted blue light into green, better matching the response of the phototubes. The air gap separating the bars from the counters caused the green light to internally reflect down the length of the bars to the phototubes at the four corners. By this means a very large area was made sensitive to ionizing radiation at an efficiency of ~12% relative to a perfectly adiabatic system of light pipes and phototubes. Nevertheless, a minimum ionizing particle produced some 16 photoelectrons in the four tubes, with about 70% response variation across the counter.

Essentially, the same technique was used for the toroid counter planes. Each scintillator plane, every 20cm of steel, was constructed of four quadrants of plastic scintillator manufactured by Polytech, 5ft square and 1.5in thick. The light collected by the shifter bars, arranged as shown in figure 3.3, was viewed by a total of 10 phototubes per plane. Approximately 8 photoelectrons were seen per quadrant, with less than 30% response variation over the surface of the counter.

The monitoring of phototube gains over the course of the experiment was accomplished using a flasher system. Light from a spark gap was passed by light fibres to a diffusing white disc at the centre of each counter. Changes in the gain of any phototube were reflected in changes in response to this stable signal.

The output signal from each phototube was used as part of the real-time trigger logic, and was recorded via ADCs for hadron calorimetry. Through a series of fan-outs, fan-ins and discriminators, shown in figure 3.4, two trigger bit levels, corresponding to one (S) and two (T) ionizing particles, along with an energy sum,  $E_n$ , were defined for each counter. These formed the basic elements of the trigger logic described in section 3.4 below.

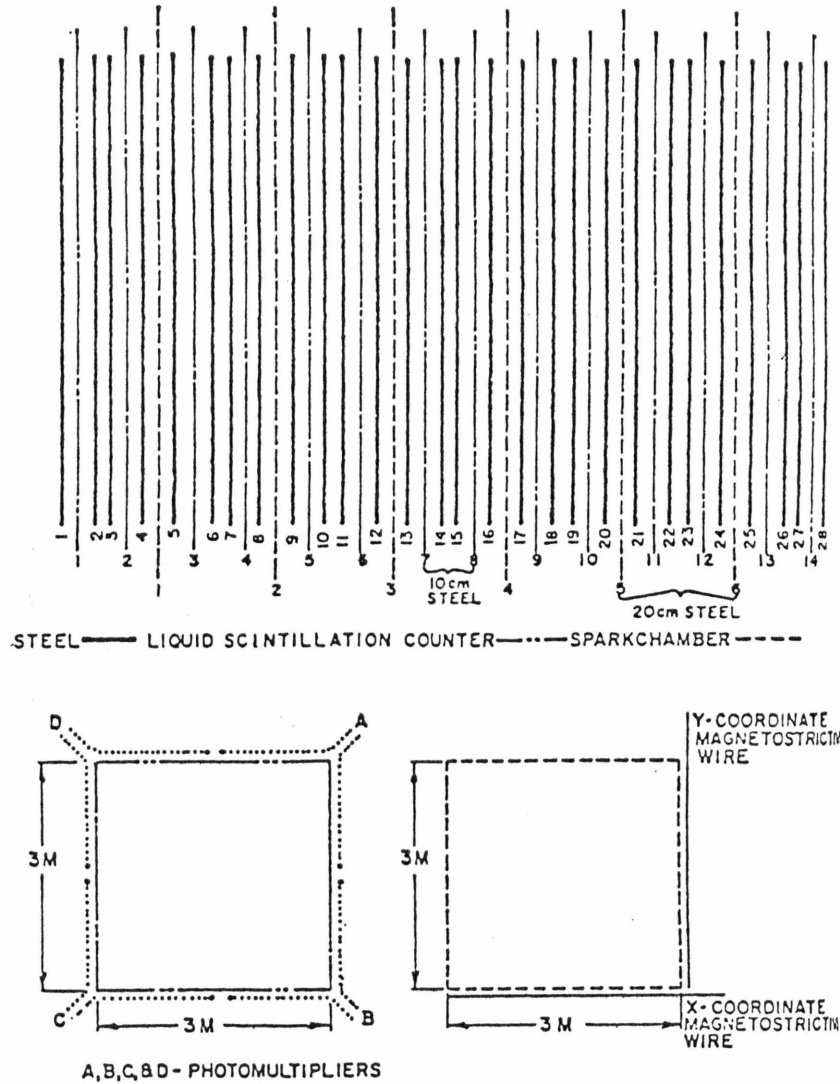


*Figure 3.2* Details of a target cart

The range of phototube signal varied from single ionizing to many times minimum in a high energy hadron shower. Historically, the dynamic range of ADCs has been limited, and so three sets of ADCs were used to digitize this large range of input signals. A 10-bit high ADC (Lecroy 2249) was used to record the sum of all signals in a plane. Single ionizing was only a few channels above pedestal, but the signals from hadron showers were at reasonable levels. For the E616 run, a 15-bit low ADC (Lecroy 2280) was available to digitize the signal

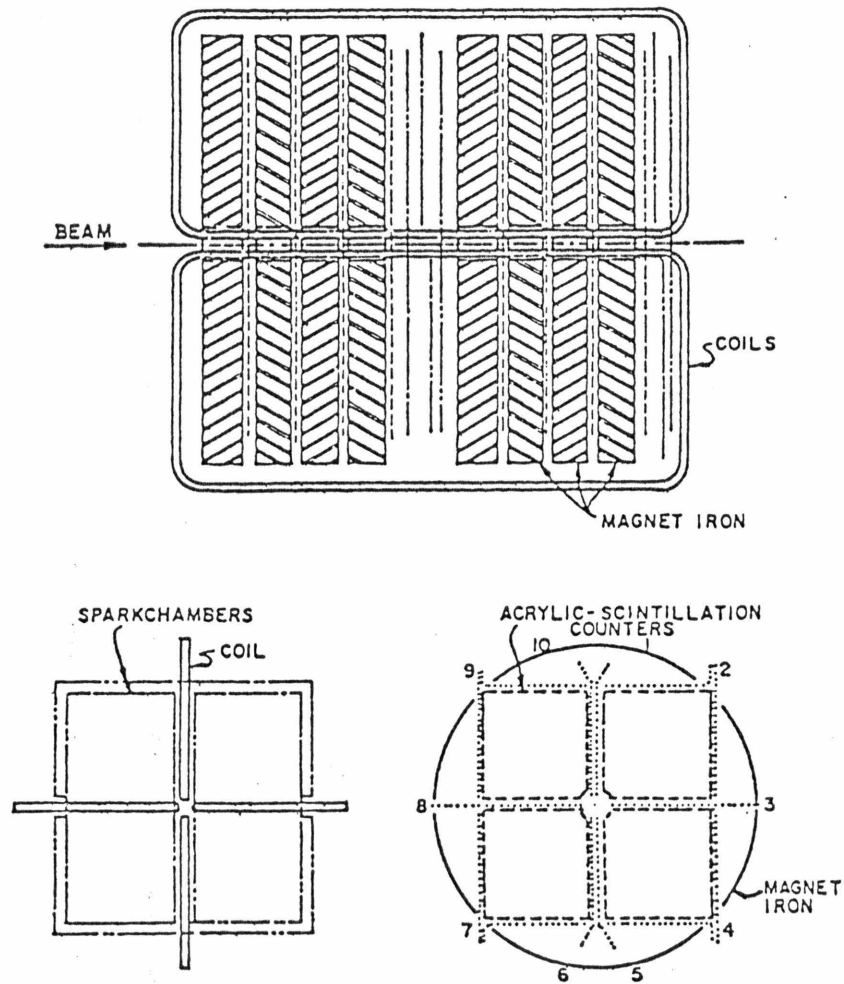


*Figure 3.9* Details of a toroid cart

from each phototube. Single ionizing was more than 100 channels above pedestal, while hadron showers were below saturation levels. In fact, the large dynamic range of these new ADCs made the highs redundant. For the small number of events for which a low ADC saturated, a superlow could be used to recover pulse height. Signals from phototubes well separated in the detector were summed and recorded by such superlow ADCs (Lecroy 2249). Presumably, only one counter in the set was likely to have a large pulse height.

### 3.2 Spark Chambers

The reconstruction of muon angle and energy was accomplished by a series of position measurements in spark chambers as the muon passed through the target and toroid. Each

target cart contained six 10ft square spark chambers, one every 20cm of steel. The toroid gaps were instrumented with a combination of 5ft $\times$ 5ft and 10ft square chambers. As shown in figures 3.2 and 3.3, a total of 78 chambers were distributed throughout the detector. The chambers were made of two 1in aluminum-clad Hexcell panels, separated by 0.5in aluminum I-beams which also provided structural support. On the interior of the Hexcell panels were bonded mylar-backed planes of 1mm spaced wires, the planes oriented at 90° to one another. A gaseous mixture of Neon-Helium (90/10) with a small amount of alcohol ( $\sim 1\%$ ) was circulated through the chambers. Following passage of an ionizing particle, the application of a  $\sim 5$ kv potential between the two wire planes of the chamber caused a breakdown of the gas, and a spark to occur at the point of particle transit.

For the target chambers the high voltage pulse was a 200ns square pulse, produced by switching to the chamber via a thyatron the energy stored on 24 $\times$ 120ft high voltage cables.

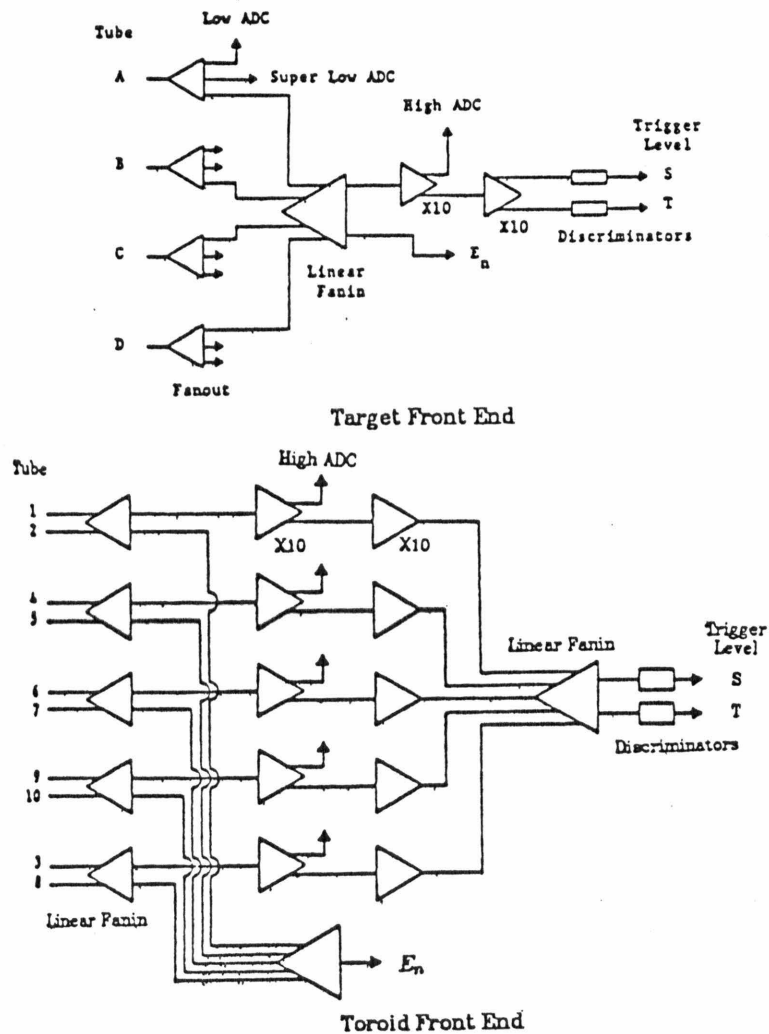


Figure 3.4 Front end logic for target and toroid counters

Such a pulse ensured good multi-spark efficiency in hadronic showers. The toroid chambers were fired with a more modest capacitor discharge system, since only one or two muon tracks were expected in the spectrometer.

The result of a discharge was an electromagnetic pulse passing down the wires of the chamber to magnetostrictive wands along two edges. An acoustic pulse, produced in the wands by the signal, traveled the length of the wand and was reconverted into a voltage signal by a transformer coil. The signal was preamplified before being sent to the readout electronics. The electronics for each wand consisted of: (1) a spark chamber interface module (SCI), for centre finding of the pulse and conversion to a logical signal, and (2) a multitime digitizer (MTD), with 20Mhz clocks to record the times of up to 16 pulses per wand relative to a common start. At fixed positions near both ends of all wands, a fiducial pulse was generated each time the chamber was fired and was likewise recorded.

The muon momentum was found by measuring the bend of the muon path in the known field of the toroidal spectrometer magnets. This field was produced by three toroidal magnets, each made up of eight 8in thick steel doughnuts, 69in in diameter, with a 10in diameter centre hole to accommodate the four sets of coils used to power the magnets. The saturated field, some 17kg over the length of the toroids, gave a transverse momentum kick of 2.45GeV/c to a particle passing the length of the spectrometer.

### 3.3 Data Acquisition

Data acquisition was through standard CAMAC, controlled and monitored through a PDP11/50. Beam line elements, including SWICs, magnet currents, collimators and the like, were monitored through the Fermilab MAC system. In addition to event records, each machine cycle (12s) pedestal, flasher, scaler and monitor records were recorded. Monitor information was recorded by the MAC system, and passed to the experiment computer at the end of a spill. Events were recorded not only during beam spills, but also during fixed length cosmic-ray gates, to enable a determination of background cosmic rays in the data sample.

Between cycles, this information was partially analyzed to provide feedback on beam and experiment operating conditions and performance. Beam steering was monitored by means of the split plate ion chambers in the expansion port and manhole. Such functions as the alignment of the Čerenkov counter could only be performed with immediate feedback on counter response variations with angle. The quality of pressure curves could also be assessed on-line. Phototube balances and pedestals, bit efficiencies and spark chamber efficiencies were calculated from a sample of analyzed events, to provide immediate warning of problems with any of the components of the Lab E detector.

Resonance extraction was used to remove protons from the main ring. Protons on the edge of the main ring beam were kicked out of the beam by an electrostatic septum, followed by a Lambertson magnet. The rate at which such extraction occurs can be controlled by the degree to which the main ring beam is blown up. For E616, two modes of operation were used: slow spill extraction over a 1s period, and fast spill with extraction over 2ms.

### 3.4 Triggers

A neutrino charged current event has a characteristic topology: a neutral incoming particle, interacting in the target fiducial volume and producing a penetrating muon and a splash of hadronic energy. The hadronic energy varies from just a recoiling nucleon in the elastic limit, up to most of the energy of the incident neutrino. The experiment ran with two triggers covering this topology. Over much of the kinematic range these were redundant, providing a means by which to check the efficiency of one trigger against the other.

The first such trigger, called a muon trigger, required a special set of fixed geometry counters to fire, as shown in figure 3.5. Essentially, a single ionizing particle had to pass through the first target cart, and partway through the toroid to trigger counters T2 and/or T3, along with no veto. The detailed logic is shown in figure 3.6. There was no hadronic energy requirement, but the muon had to have sufficient energy to reach T2. Also, due to the limited acceptance of the T2 counter, the muon angle with respect to the incident neutrino was restricted for this trigger. The T2 requirement ensured that the muon momentum could be analyzed.

The second trigger, called a penetration trigger, used information from the target counters and first ten planes of toroid counters. An event was required to have a minimum ionizing particle which penetrated at least sixteen consecutive counter planes, and to have more than 4GeV of hadronic energy, again with no veto. Although less restrictive on muon angle than the muon trigger, penetration events did have a low  $y$  cut-off due to the hadron energy threshold. Figure 3.7 is an example of a penetration trigger event, where the muon leaves the target before reaching the spectrometer.

The only element of the trigger logic common to the two triggers was the veto counter. Veto overkill, that is the overlap of the veto gate with possible good events, would deplete both triggers. A cross comparison of the two triggers of course could not measure this effect. The average veto deadtime of about 2% was measured at each setting by counting the coincidence of a trigger with the veto delayed by approximately a gate width.

The principal source of contaminating events which satisfied these triggers, was cosmic-ray muons or showers. The triggers were sufficiently restrictive so that for the 2ms fast spill gate this is not a severe problem. However, it was necessary to make these triggers more restrictive during the 1s slow spill gate, in order to keep cosmic-ray rates down to a few per second. The additional requirements were: (1) for the muon trigger, that trigger counters T3 and/or T4 fire, and (2) for the penetration trigger, that the hadron energy be greater than 10GeV. As will be shown, software cuts for the structure function analysis have been made tighter than even the slow spill requirements, and so this represents no complication to the data analysis.

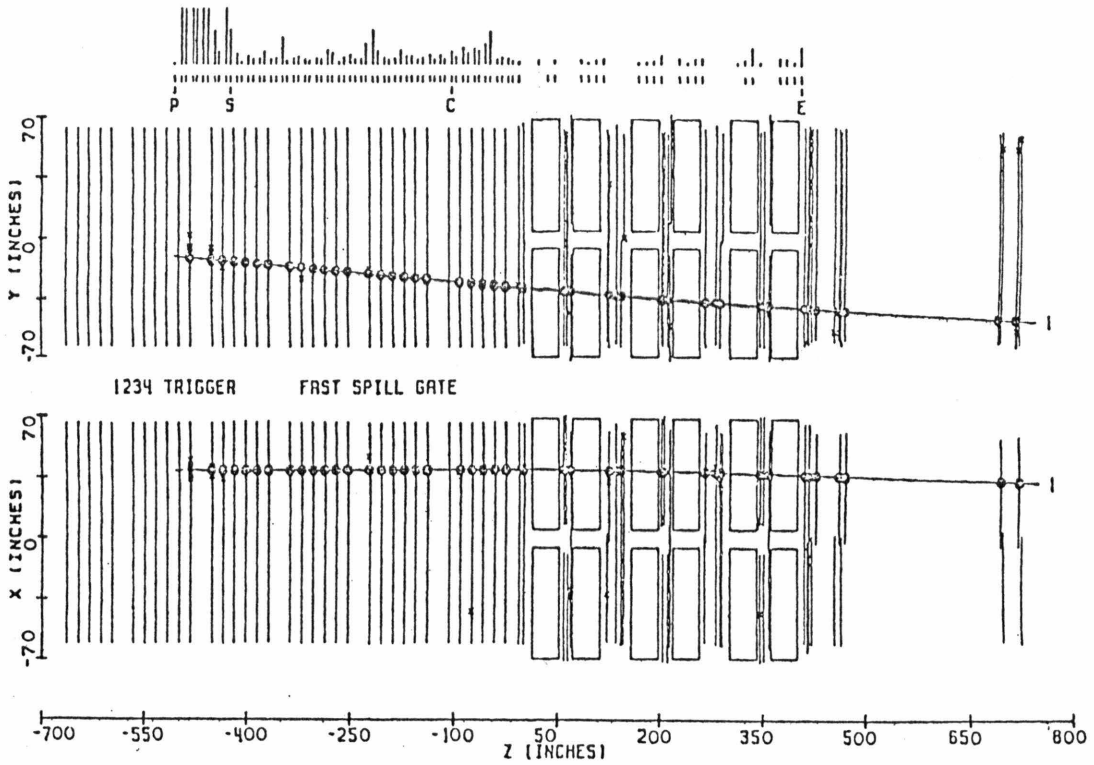


Figure 9.5 Computer reconstruction of a muon trigger event

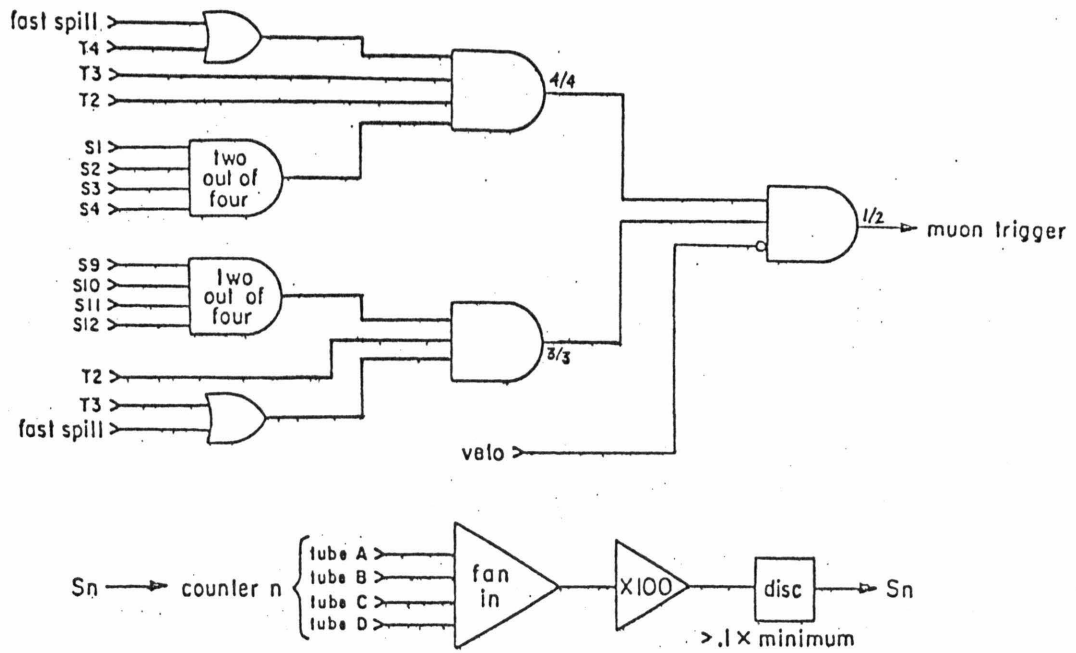


Figure 9.6 Details of the muon trigger logic

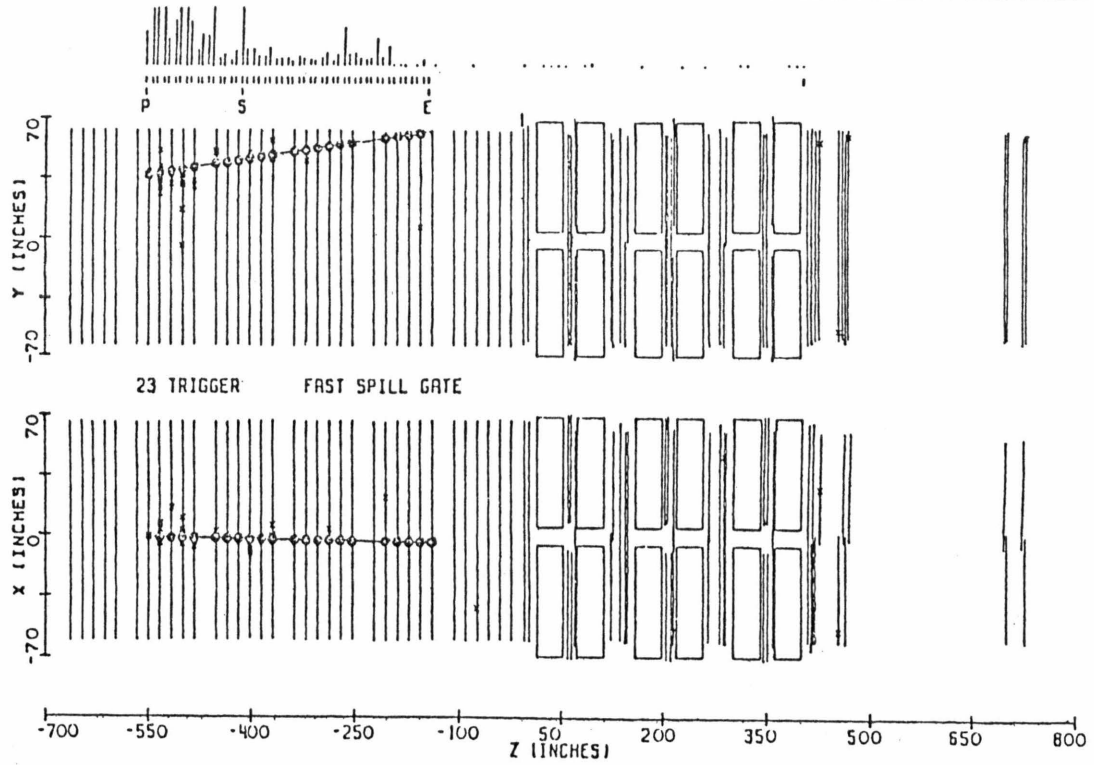


Figure 9.7 Computer reconstruction of a penetration event

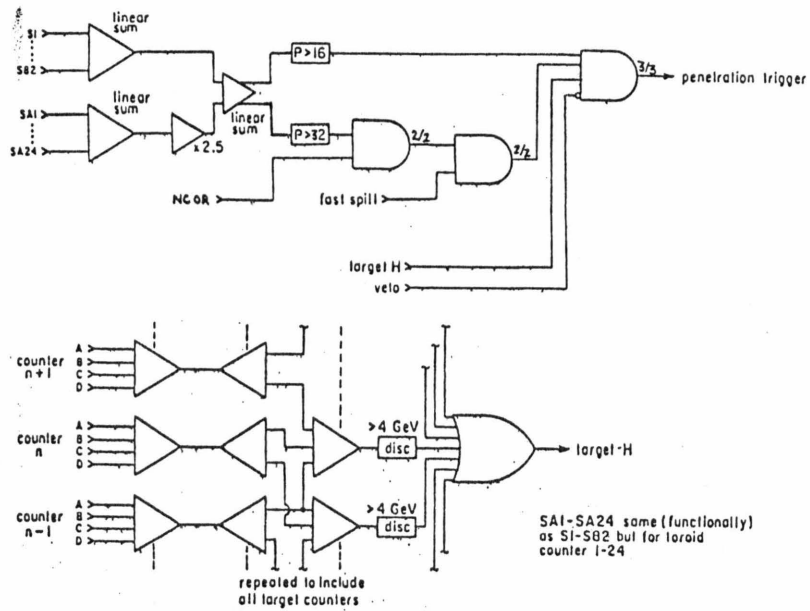


Figure 9.8 Details of the penetration trigger logic

Setting	Neuhall Toroid	Muon Triggers
-120	0.817	0.812
-140	0.821	0.824
-165	0.855	0.860
-200	0.875	0.875
-250	0.913	0.901
+120	0.694	0.717
+140	0.667	0.684
+165	0.656	0.667
+200	0.686	0.697
+250	0.709	0.724

*Table 3.1* Livetime fraction for fast spill

The experiment had a 50ms deadtime after taking an event, the time required to clear charges from the spark chambers before refring. Clearly, only one event per cycle could be recorded for the fast spill. In order that deadtime corrections not become too large, event rates for fast spill could not greatly exceed one per spill. The event rates for anti-neutrino running never exceeded this limit, and so fast spill extraction was satisfactory. For the neutrino running this was not the case, and data were taken with about equal flux in slow and fast spill extraction modes.

### 3.4.1 Livetime

Monitors were gated on either: (1) the time the signal from the toroid (BCT) was above threshold (beam gate), or (2) the beam gate in coincidence with a Lab E generated gate signifying that the detector was alive (livetime gate). On a run-by-run basis the ratio of the number of livetime to beam gated protons received on target, as measured by the toroid (BCT), was used to compute the number of livetime secondaries from the total secondaries received, as measured during the beam gate by the ion chambers. An alternative method was to determine the ratio of total muon triggers per run, extracted from scaler records, to the number of recorded muon trigger events. Since only beam associated events should be included in such a procedure, corrections for cosmic-ray contamination of the scaled and recorded muon triggers were made. Also, adjustment was made for the fact that the scaler gate was delayed by  $20\mu\text{s}$  to avoid spark chamber noise. A comparison of the two methods indicates that the rms fractional error on the livetime measurement was determined to 2.3% for neutrinos and 0.7% for anti-neutrinos. These are equivalent to an average 5% fractional error on the deadtime: therefore, the livetime error has been treated as a correlated error. Table 3.1 shows the livetime fractions for fast spill. The slow spill livetime fraction was 86.7% for all five positive settings, reflecting the dominance of the trigger rate by cosmic-ray events.

The data set used in this analysis was obtained over the period extending from June, 1979 through January, 1980. Some 800 raw data tapes were produced for off-line analysis during that time. A total of  $0.5 \times 10^{19}$  protons were received on target during useful runs, broken down between neutrinos and anti-neutrinos and among the five pairs of energy settings as shown in table 4.1. Off-line analysis was carried out on the Fermilab CDC Cybers. The analysis of monitor data has been briefly discussed in chapter 2, and it remains to describe the extraction of useful physics information from the event records.

The first step of data reduction was a sorting operation. Monitor and event records were separated, and beam steering monitors incorporated into event records. Pedestals were averaged and subtracted at this stage.

The bulk of the event analysis was divided into two subsequent steps: (1) a data cruncher, containing much of the track finding and fitting routines, and producing a partially analyzed record still retaining most of the raw detector measurements, and (2) a data summary writer, containing the final hadron energy and target track fitting routines, and producing a summary record with just a few physics variables per event. The procedures described below were for the most part incorporated into these last two analysis programs. The extraction of structure functions from the data summary files is the subject of chapter 5.

#### 4.1 Hadron Energy Determination

The hadronic energy of the charged current event was obtained by summing pulse height from counters identified as being within the region of hadron shower development. In the counters, a typical event appeared as a region of zero deposited energy (the incoming neutral neutrino), a region of large pulse height (the hadron shower containing many ionizing particles), and finally a region of single ionizing response (the outgoing muon). The counter PLACE was defined as the most upstream of a series of two counters with pulse height greater than 0.25 times minimum ionizing, signalling the abrupt transition from the neutrino segment to hadron

Setting	Primaries $\times 10^{17}$			Secondaries $\times 10^{14}$		
	Slow Spill	Fast Spill	Total	Slow Spill	Fast Spill	Total
+120	1.51	1.10	2.61	6.43	4.84	11.27
+140	1.87	1.38	3.25	8.37	6.73	15.10
+168	2.95	2.07	5.02	16.41	11.55	27.96
+200	3.53	3.01	6.54	24.44	20.68	45.12
+250	5.42	5.56	10.98	48.94	52.43	101.37
-120	0.00	1.98	1.98	0.00	2.32	2.32
-140	0.00	2.88	2.88	0.00	2.83	2.83
-168	0.00	3.79	3.79	0.00	2.70	2.70
-200	0.00	5.31	5.31	0.00	2.64	2.64
-250	0.00	11.21	11.21	0.00	2.02	2.02

Table 4.1 Protons and secondaries received in good runs

shower. (Minimum ionizing is a term defined below, but is roughly equivalent to the signal produced in the counters by a muon.) The transition between the trailing edge of the shower and the muon was less distinct. The counter SHEND marked the shower end, and was defined as the most upstream of a series of six counters with pulse height less than 3 times minimum ionizing. The total pulse height in the first six counters downstream of SHEND was found to be  $0.74 \pm 0.15$  times minimum ionizing higher than that of the next six counters. This was taken to be the average hadronic energy missed by assigning SHEND in the manner described; a correction of this amount was made on an event-by-event basis. The sum of pulse height between PLACE and SHEND was proportional to the hadronic energy,  $E_H$ , of the event. Pulse height in all counters was pedestal subtracted and converted to equivalent minimum ionizing prior to this summation. A determination of the energy equivalent of minimum ionizing allowed the calculation of  $E_H$ .

#### 4.1.1 Counter gain monitoring

The procedure was complicated somewhat by time and spatial response variations of the counters, which first had to be removed. Shifts in the gains of individual phototubes over time were monitored by the flasher system. Such shifts were corrected by the observed variation in average phototube response to the stable flasher light source. It was also supposed that the flasher could be used to balance the response of the four phototubes viewing a counter, so that a particle passing through the counter centre would produce equal amounts of light in each phototube. This was demonstrated not to be the case by mapping the response of a flasher balanced counter using a gamma-ray source. Despite the use of a diffusing white spot, the flasher illumination of the four phototubes was presumably not uniform in some counters.

Shifts in the overall counter gain were monitored using muons. The most probable value, the peak of the distribution of pulse heights from singly ionizing particles (muons), was expected [Ba75c] and observed to be independent of the energy of the traversing particle.

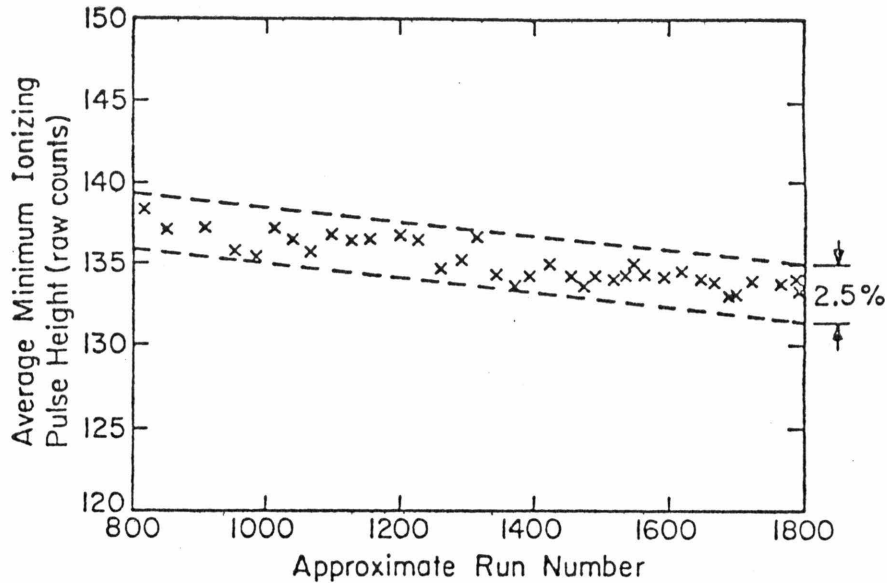


Figure 4.1 Average gain of the target counters during the run

Operationally the peak values, called minimum ionizing, were taken to be the average of the muon pulse height distribution below twice minimum ionizing. Since initially the value for minimum ionizing was unknown, this was an iterative procedure.

Over running periods of typically a few days duration, the value for minimum ionizing in each counter was obtained by averaging the response to muons passing within 30in of the detector centre. Changes in the value for that segment of running reflected gain drifts from nominal and were corrected on a counter by counter basis. Averaged over all target counters, this gain monitor showed point-to-point fluctuations of less than  $\pm 1.5\%$ , although there was observed a 2% systematic drift downwards in the response to muons over the course of the experiment (figure 4.1).

#### 4.1.2 Counter mapping

Attenuation lengths for light in the counters were of the same order as the counter dimensions. Hence, there was significant variation with shower position of the amount of light collected by any given phototube, or the sum of all four counter phototubes, for the same amount of energy deposited. This effect was removed by mapping the spatial variations using hadronic showers.

A model of the counter response was devised with four free parameters: a counter centre,  $(x_o, y_o)$ , and two attenuation lengths,  $\lambda_x$  and  $\lambda_y$ . The two attenuation lengths were used because the vertical acrylic ribs of the counter could result in different light attenuation in the vertical and horizontal directions. The counter model could be broken down into four functions representing the response of the four counter phototubes. Best values for the free parameters were obtained for each counter, using the observed fractional variation of light as seen by each phototube in hadron showers at different positions in the counters. For the  $i^{\text{th}}$  counter:

$$\chi_i^2 = \sum_{\text{events}} \sum_{j=1}^4 \frac{(p_j - N c_j(x, y))^2}{\sigma_j^2} \quad (4.1)$$

where

$$\begin{aligned} p_j &= \text{pulse height in the } j^{\text{th}} \text{ phototube} \\ c_j(x, y) &= \text{model value at the position of the shower} \\ \sigma_j &= k \sqrt{p_j} \\ k &= \text{constant related to photons per minimum ionizing} \\ N &= \frac{\sum_{j=1}^4 p_j}{\sum_{j=1}^4 c_j(x, y)} \end{aligned}$$

was minimized by varying the four parameters available. Details of the map function and fitting procedure can be found in Appendix B. Shown in figure 4.2 are equal response contours for a typical target counter.

It has been noted that the flasher system did not always succeed in properly balancing the four phototubes of a counter. The map used was inadequate to addressing this balance problem, due to strong correlations between  $(\lambda_x, \lambda_y)$  and the map centre parameters,  $(x_o, y_o)$ . In the future, the problem will be corrected by using a map with a set of three relative gains, allowing greater freedom in fitting the counter response.

An important check of the validity of the map results was to observe the variation of the map corrected mean shower pulse height for fixed energy particles incident at various positions in the target. As shown in figure 4.3, the maximum variation was found to be 3.5% for 200GeV/c pions from the target centre out to 50in, across the middle of the first two carts. Most of the observed deviation was seen beyond 40in. This was the region where the counter map would be inadequate if the four tubes were not properly balanced. Presuming that the counters in the first two target carts were representative of the rest of the target, the map correction was fractionally increased beyond 40in, reaching a maximum of 5% at 60in. The calibration measurements were then well fit by the hypothesis of no variation across the counter. A maximum of 0.40% overall systematic uncertainty in the map correction could be accommodated before the  $\chi^2$  for the fit becomes improbably small (<10%). Presumably, the map correction uncertainty was no more than twice this value.

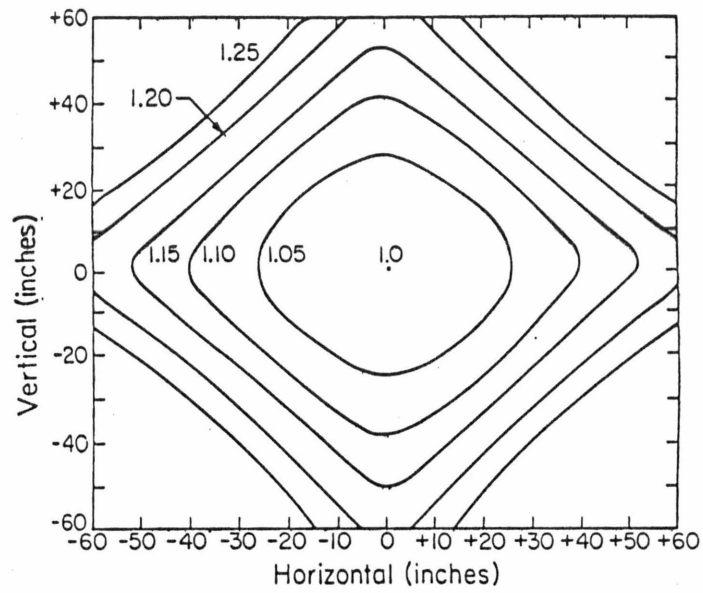


Figure 4.2 Equal response contours for a typical target counter

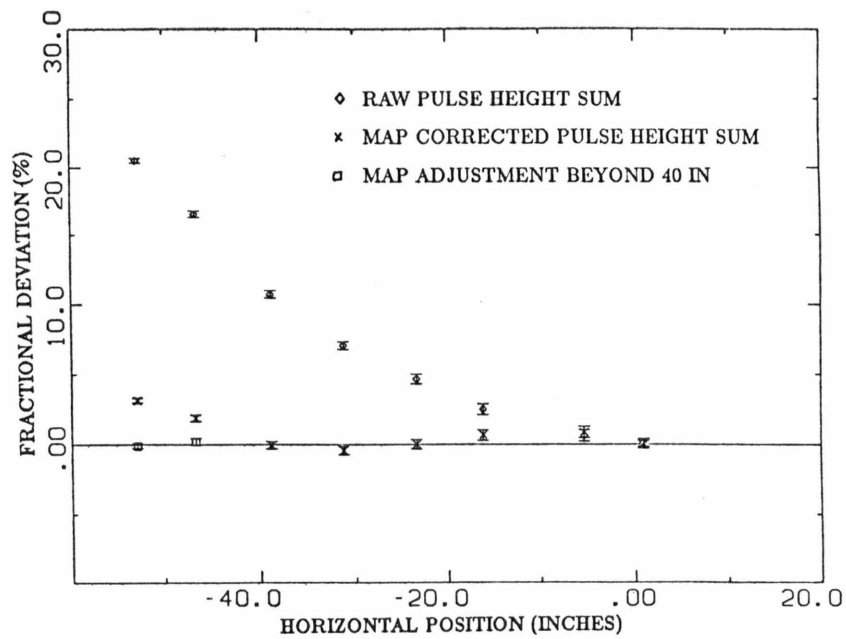


Figure 4.3

Raw and map corrected calorimeter response to 200 GeV/c pions across the second target cart

### 4.1.3 Calibration of hadron energy

After time and spatial variations in counter response were removed, a check was made of counter-to-counter gain consistency. The observed response of the target counters to some average hadronic shower should be uniform. Using a sample of penetration and neutral current events, unbiased in the  $z$  position of the vertex, the relative variation of the mean hadronic energy was observed. This in turn allowed the relative gains of the counters to be determined. Although consistent with no variation throughout the target, the correction factors shown in figure 4.4 were applied to the data.

The calorimeter was absolutely calibrated using pions from the N-5 hadronic test beam which runs along the east side of the neutrino berm at Fermilab. Data were taken in the first two target carts at beam momenta of 25, 50, 90, 200 and 250 GeV/c. All corrections described above were applied to the phototube signals. At each setting, a Poisson distribution was fit to the observed spectrum of shower pulse height sums. The deviations of the determined means from a one-parameter linear fit passing through zero are shown in figure 4.5. Minimum ionizing was found to be equivalent to  $0.2157 \pm .0006$  GeV. Figure 4.6 shows the measured resolution of the hadron energy determination as a function of the incident pion momenta. The resolution was found to be  $\delta E_H = (0.72 \pm 0.20) + (0.81 \pm 0.03)\sqrt{E_H}$ . Details of the analysis of the hadron calibration data can be found in Appendix C. On the basis of the uncertainty in the map correction and the calibration measurement, a maximum of 0.9% systematic error was assigned to the reconstructed hadron energy for neutrino events.

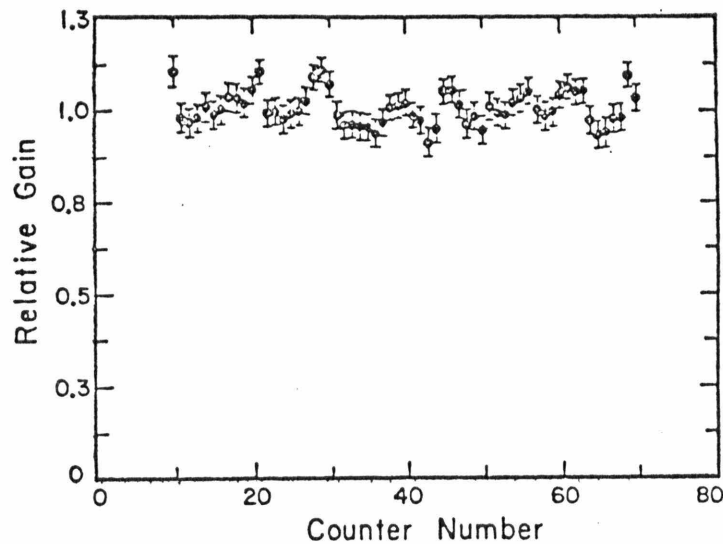


Figure 4.4 Relative counter gain through the target from hadrons

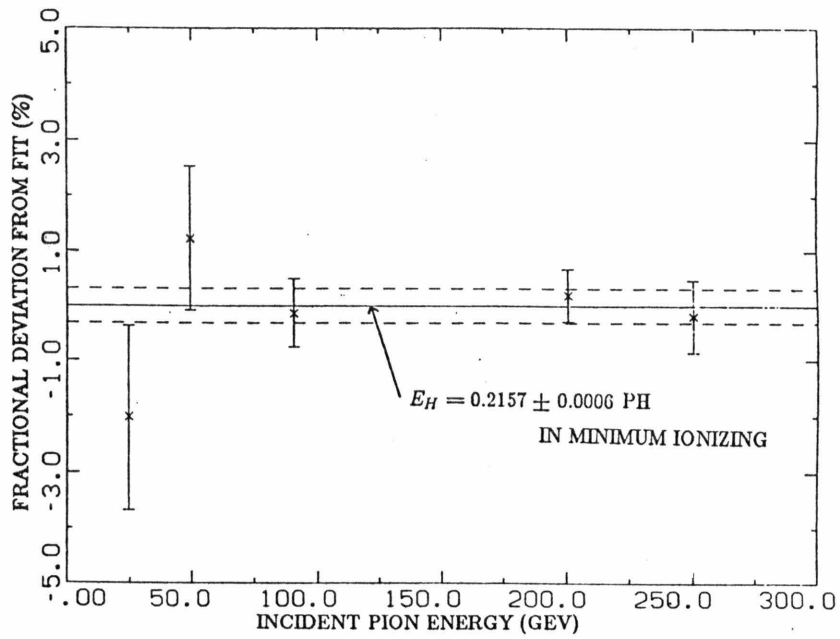


Figure 4.5 Determination of absolute calibration of minimum ionizing using a pion beam

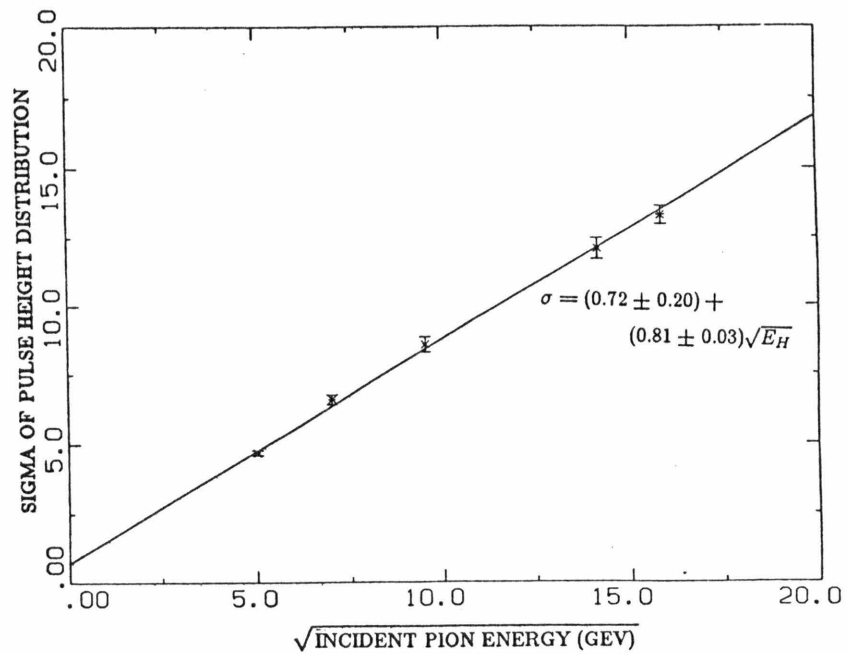


Figure 4.6 Determination of hadron energy resolution

## 4.2 Muon Parameters

### 4.2.1 Target track

The counters provided a means of identifying the  $z$  position of the interaction vertex, PLACE, as described above. The first step in the track finding procedure was to determine a crude transverse vertex position from sparks near the point of interaction. In both the horizontal and vertical planes, a linear least squares fit was made to all sparks within a gradually enlarging window, which included only the first 12 chambers immediately downstream of the interaction point.

The muon path in the unmagnetized target was a straight line except for multiple scattering effects. Hence, the sparks corresponding to the track would appear at a fixed angle,  $\theta_x$  and  $\theta_y$ , as seen from the vertex. The angular distribution of target sparks would be expected to peak in the direction of the muon, above a background of hadron shower and noise sparks. In each view, a preliminary two parameter least squares fit was made to sparks which lay within this peak. Only those sparks on each wand which deviated least from this fit were retained. Sparks were also eliminated if they were more than  $3.5\sigma$  from the position predicted by a fit to all other sparks currently then included on the target track.

The original crude determination of the transverse vertex position could cause much of the track to be missed. Therefore the procedure was iterated using the best value for the vertex position from the first pass in the second attempt. Finally, all sparks not already included on the target track, but which lay within  $2\sigma$  of the predicted track, were added to the ensemble.

### 4.2.2 Toroid track

The search for the muon track in the spectrometer was complicated by the bend of the muon in the magnetic field. However, the field was toroidal, so that to a good approximation  $\vec{B} = B_\phi(r)\vec{e}_\phi$ . Therefore, one component of angular momentum,  $L_\phi = r^2 d\phi/dz$ , was conserved. A first ensemble of toroid sparks was obtained by including spark chamber hits which occurred within some tolerance of  $L_\phi$  as determined from the upstream target track.

In general, a fit to the muon track was made by varying parameters affecting the predicted path of the muon, so as to minimize:

$$\chi^2 = \sum_i \sum_j (x_i - x_i^P) M_{ij}^{-1} (x_j - x_j^P) \quad (4.2)$$

where

$$x_i, x_i^P = \text{measured and predicted positions in the } i^{\text{th}} \text{ chamber}$$

$$M_{ij}^{-1} = \text{inverse of the error matrix}$$

If just the intrinsic resolution errors of the spark chambers,  $\sigma_o$ , are included, then both  $M = \sigma_o^2 I$  and  $M^{-1} = 1/\sigma_o^2 I$  are diagonal, and the problem reduces to minimizing the sum of

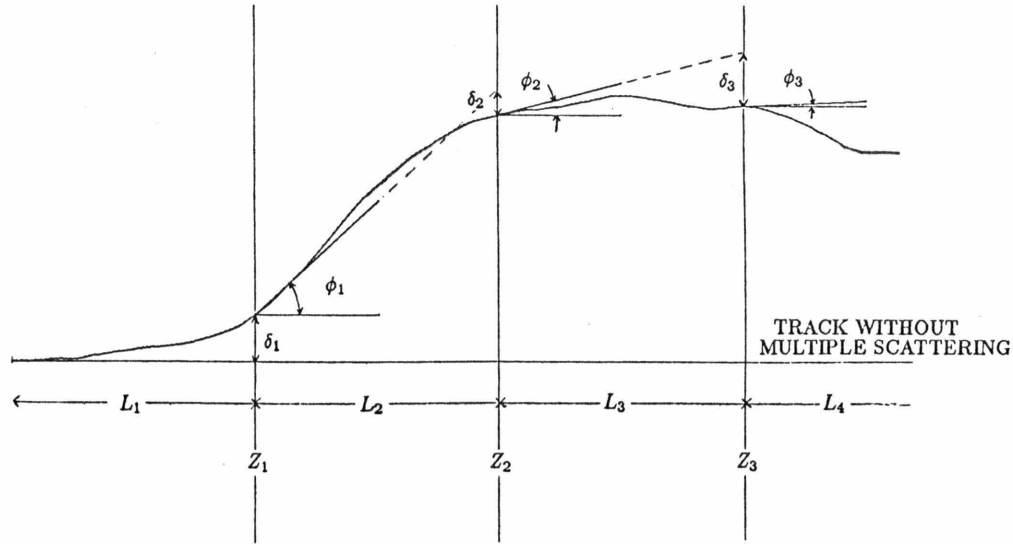


Figure 4.7 Illustration of multiple scattering error determination

squares of deviation. However, the muon undergoes multiple coulomb scattering in passing through material. Since the radiation length of steel is only 1.76cm, multiple scattering is an important effect and must be properly included in the calculation of the error matrix.

Consider a series of  $m$  measurements of a track,  $x_i$ , separated by distances  $L_i$ , as shown in figure 4.7. The standard Fermi formula gives the fundamental set of correlated errors in position and angle due to multiple scattering:

$$\begin{aligned}
 \phi_i \phi_j &= \sigma_\phi^2 \delta_{ij} \\
 \phi_i \delta_j &= \frac{L_i}{2} \sigma_\phi^2 \delta_{ij} \\
 \phi_j \delta_i &= \phi_i \delta_j \\
 \delta_i \delta_j &= \frac{L_i^2}{3} \sigma_\phi^2 \delta_{ij}
 \end{aligned} \tag{4.3}$$

where

$$\sigma_\phi = \frac{0.015}{p} \sqrt{\frac{L}{L_{rad}}}$$

From this, one can construct a full error matrix, as shown in Appendix D, and find that:

$$M_{ij} = \sum_{k=1}^i \sigma_k^2 \left( \frac{L_k^2}{3} + \frac{L_k}{2} (z_{kj} + z_{ki}) + z_{ki} z_{kj} \right) + \sigma_o^2 \delta_{ij} \quad (4.4)$$

where

$$z_{ki} = \sum_{m=k+1}^i L_m = \text{distance from } k \text{ to } i$$

Diagonal elements are increased, and off-diagonal terms, representing correlations between measurements due to multiple scattering, are introduced. This is the proper error matrix. The calculation is largely unchanged if the track passes through a magnetic field. For the fit to the toroid portion of the muon track, terms due to the errors in the determination of slope and intercept at the toroid front face, and their correlations, were added the definition of  $\chi^2$  (4.2).

An estimate of the muon momentum from the curvature of the toroid track was used to make a multiple scattering fit to the target track weighted from the toroid front face upstream. A one parameter fit to the muon momentum was then made to the toroid track using just the diagonal elements of the error matrix. During a second iteration of the fit, sparks outside errors were removed from the ensemble. It was presumed that at this point the procedure provided a good estimate of the target track slope and intercept at the toroid front face and the muon momentum. A new ensemble of toroid sparks was then obtained by including those hits which lay closest to the predicted path of the muon from this preliminary fit.

In an attempt to eliminate bad sparks from the ensemble, a new fit strategy was then invoked. A simultaneous fit was made to the target and toroid track, with free parameters being vertex position, muon angles and momentum, and multiple scattering angles at scattering centres distributed in the target and toroid steel. (Up to 12 per view in the target and 1 per half toroid per view in the spectrometer were used.) The use of multiple scattering angles at selected points distributed throughout the detector steel is an alternative method of handling errors and correlations introduced by multiple scattering. A more complete description may be found in the thesis of M.Purohit [Pu84]. Sparks with bad  $\chi^2$  were removed from the track ensemble. However, from monte carlo studies it was clear that, as implemented, this method of fitting tended to produce a biased estimate of muon momentum. Therefore, one final stage in the momentum determination was necessary: a return to the one parameter fit with inversion of the full multiple scattering error matrix in the calculation of  $\chi^2$  (4.2). Calculation of the minimum of  $\chi^2$  was iterated until successive values of the muon momentum at that minimum differed by less than 2%.

In figure 4.8 is shown the distribution of  $\sqrt{\chi^2/DF}$  from the momentum fit to muon events within the final structure function fiducial and kinematic cuts (section 4.3 below), at the +200 setting. Resolutions of 0.8mm and 2.3mm, for target and toroid spark chambers respectively, were used in the calculation of  $\chi^2$ . The observed peak of the distribution was below 1.0, indicating that the resolution error for the toroid chambers was on average somewhat better than the value used. However, there was considerable variation of the position of the peak with the number of degrees of freedom for the fit. This presumably reflects the poor alignment of a few chambers in the toroid, which affects the mean  $\chi^2$  to a greater or lesser degree depending on the ensemble of chambers included in the fit. The fact that the average resolution needed was about 2.5 times the intrinsic resolution of any single chamber was likewise a reflection of

the difficulty in aligning chambers in the toroid. The width of the observed  $\chi^2$  distribution was greater than the prediction. The shift of the peak position would also contribute to this problem, as well as the small fraction of events where the track search algorithms failed to remove all bad sparks.

The calculated resolution of  $0.11p_\mu$  on the muon momentum from the spectrometer was dominated by the contribution of multiple scattering error. The systematic error on the reconstructed momentum has been estimated at 1%. Most of this was due to the accuracy to which the magnetic field was mapped. Direct evidence was obtained from Fermilab experiment E595, which used the first two target carts and the spectrometer as part of their detector. This was an experiment to study the prompt muon signal from beam dump interactions of pions and protons. These were supplied to Lab E by the N-5 hadron beam, the same beam used for the calibration of the target calorimeters. The momentum of beam muons could be determined from the bend induced by the last beam dipole before Lab E (5E13). A set of PWCs (Proportional wire chambers) and the observed interaction point in the detector were used to define the muon track before and after the bend. A difference between this momentum and that reconstructed from the spectrometer was about 1% (two sigma).

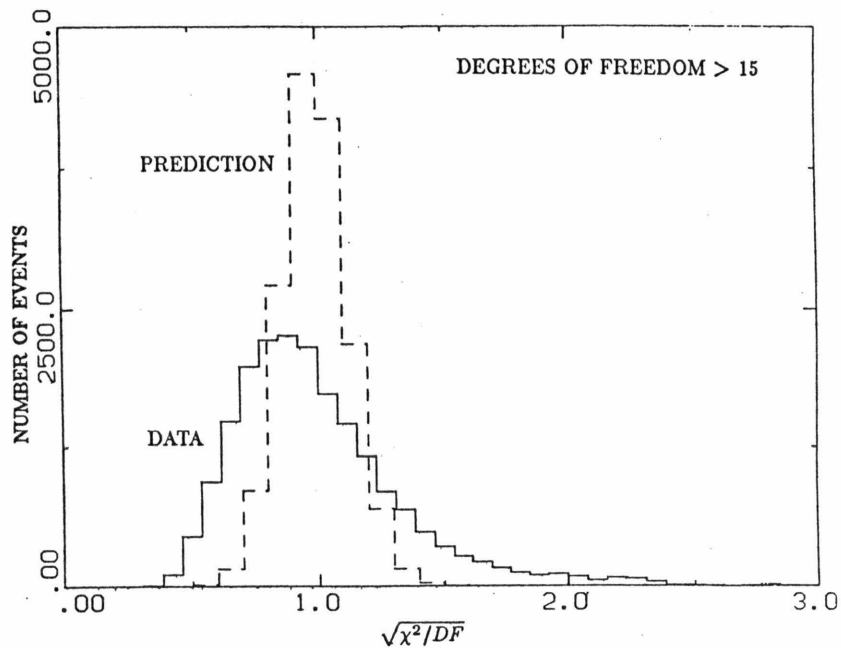


Figure 4.8

Distribution of  $\sqrt{\chi^2/DF}$  for toroid fits to muon events from the +200 setting

### 4.2.3 Event scanning

Roughly 3000 events in the data set, although passing fiducial cuts, failed to obtain an acceptable fit ( $\chi^2$  per degree of freedom greater than 9.0), through the automated procedure just described. These events were hand scanned, with sparks added or deleted as necessary, using an interactive display and fitting routine. Failures were attributable to a number of causes, including: (1) backwards going defocusing cosmic-ray muons, (2) multiple tracks in toroid or target, (3) track too short or chambers inefficient, (4) track in or near the toroid hole, (5) occasional unrecognized bad sparks, and (6) large multiple scatters in target or toroid steel. Events with defocusing tracks were removed, along with a few cosmic-ray showers, and three runs deleted where the toroid spark chamber MTDs had failed. Dimuon events have been hand scanned and analyzed in a separate investigation, and were added back into our charged current sample.

$E_\mu$ GeV	Probability of energy loss/m steel (%)					
	>1GeV	>5GeV	>10GeV	>20GeV	>30GeV	>40GeV
10.	0.92	0.01	0.00	0.00	0.00	0.00
30.	2.74	0.70	0.07	0.00	0.00	0.00
50.	3.93	1.47	0.40	0.02	0.00	0.00
70.	4.96	2.24	0.97	0.20	0.01	0.00
90.	5.52	2.55	1.18	0.46	0.14	0.01
110.	6.28	2.82	1.13	0.45	0.23	0.11
130.	7.10	3.52	1.39	0.45	0.20	0.08
150.	7.76	4.15	1.79	0.76	0.40	0.19
170.	8.15	4.81	2.46	1.04	0.65	0.29
190.	8.70	5.42	2.43	1.16	0.69	0.37
210.	9.10	5.82	2.84	1.55	1.11	0.89
230.	8.57	5.84	4.09	2.34	1.36	0.58

Table 4.2 Probability of catastrophic muon energy loss in passing through steel

### 4.2.4 Muon deep-inelastic scatters

The momentum obtained from a fit to the toroid track of the muon had to be converted to a momentum at the vertex. For the most part, this entailed the increase of the toroid fit value by the addition of ionization energy lost by the muon in passing through the steel intervening between the vertex and the toroid front face. A calculation using standard formulas for the most probable energy loss was typically sufficient to accomplish this task. However, occasionally the muon would deep inelastically scatter, colliding with a nucleus and releasing far more energy than usual. Such energy was observable in the scintillation counters as a series of counters with pulse height greater than minimum ionizing. A search was made for such splashes of energy

in the region of the detector between the end of the hadron shower and the toroid front face. Where detected, such energy was added to the muon vertex momentum along with the usual ionization formula correction. In table 4.2 can be found the observed probability for a muon to undergo a catastrophic scatter and release energy  $E_d$ .

#### 4.2.5 Best fit to muon angle

The accuracy with which the muon angle,  $\theta_\mu$ , could be determined was dominated by multiple scattering. Minimizing the length of steel intervening between the vertex and the first measurement of the muon track minimized the error in  $\theta_\mu$ . Within the hadronic shower, sparks in the chambers could be due to the muon, or any other of a myriad of forward-going ionizing particles. By projecting the fit to the muon track obtained in the unambiguous region beyond SHEND into the hadron shower, sparks within the shower due to the muon could be tentatively identified. The ratio of random sparks to good muon sparks was observed to increase as the track was extrapolated closer to the vertex. No attempt was made to project the track closer than the point at which signal to noise ratio fell below 2:1. The probability of picking up a good spark was ensured to be greater than 50% and of including a bad spark less than 10% by this requirement. The allowed extrapolation distance was a function of the hadron energy of the event, and the devised algorithm attempted to project as far as shown in table 4.3. The variation of resolution with hadronic energy, also shown in the table, simply reflects the increasing distance between the first detectable muon spark and the interaction point.

$E_H$ GeV	First chamber on muon track	$\Delta\theta_\mu$ mr
<10	1	.16 + 84.4/ $p_\mu$
10 to 25	1	.28 + 79.2/ $p_\mu$
25 to 50	2	.16 + 105.5/ $p_\mu$
50 to 100	2	.15 + 107.7/ $p_\mu$
100 to 200	3	.10 + 129.7/ $p_\mu$
>200	4	.00 + 154.8/ $p_\mu$

Table 4.3

Attempted penetration into the hadron shower by the target track search algorithm, and corresponding  $\theta_\mu$  resolution. Here, chambers are numbered downstream from the event vertex.

It is instructive to compare the angle resolution obtainable in an unmagnetized target, with relatively frequent sampling of the muon track as in the Lab E detector, with that found in a magnetized target with coarse sampling, such as the CDHS (CERN-Dortmund-Heidelberg-Saclay) neutrino detector [Ho78]. The result is a degradation of roughly a factor of three in the

measurement error on  $\theta_\mu$ . Consequently resolutions at small  $x$ , where the error on  $\theta_\mu$  dominates, are worse by a factor of three in the CDHS detector.

### 4.3 Cuts

#### 4.3.1 Monitor and steering cuts

Variations in the direction of the secondary beam are equivalent to enlarging beam dispersion in a time dependent manner, which could contribute to uncertainties in the flux of neutrinos from pion decay. Beam steering was monitored while taking data using SWICs and split-plate ion chambers in the expansion port and target manhole. As mentioned in chapter 2, the difference over sum of the two halves of the split plate signal was used as a steering parameter. Attempts were made to keep the beam position within accepted limits while taking data. Monitor and events records from a given cycle, representing about 5% of the total data sample, were removed off-line if these steering parameters were outside tolerances corresponding to  $\pm 1.4$ in at Lab E. Cycles were also removed if beam intensity dropped below acceptable levels. Whole runs were deleted if monitor or detector problems degraded the quality of the data.

Setting	Beam Gates		Cosmic-ray Gates		Total
	Slow Spill	Fast Spill	Slow Spill	Fast Spill	
+120	30007	12662	4385	3523	50577
+140	37275	25659	5150	4342	72426
+168	65373	23830	8264	6367	103834
+200	87024	33831	12429	9466	142750
+250	113574	44759	17529	14321	190183
-120	0	6689	0	2903	9592
-140	0	9430	0	4172	13602
-168	0	11950	0	6849	18799
-200	0	13809	0	9718	23527
-250	0	12557	0	11291	23848
Total	333253	195176	47757	72952	649138

Table 4.4 Events analyzed by first pass physics program

### 4.3.2 Cosmic-ray cuts

Although not a critical problem for fast spill data, the slow spill data sample was predominantly cosmic rays and not neutrino events. A number of loose cuts were devised and tested with fast spill data to eliminate these unwanted events. When the analysis of the slow spill data was undertaken, events which failed these cuts were removed from the sample before entry into the time-consuming momentum fitting routines. These cuts were: (1) vertex inside 58in in both horizontal and vertical directions, (2) no more than two interaction points determined, (3) small pulse height outside the event region, and (4) a cut on reconstructed hadron energy for penetration trigger only events at 2GeV and 7GeV respectively for fast and slow spill. More restrictive cuts were made on the final structure function data set, so that these requirements served only to save computer time by quickly eliminating a large number of cosmic-ray events.

The monitor and cosmic-ray cuts described were applied at the stage of the first pass analysis program. The number of events analyzed by the cruncher at each setting are shown in table 4.4.

### 4.3.3 Geometric and fiducial cuts

Events used in the structure function analysis must be fully reconstructed. Requiring that the event vertex lie within a target fiducial volume defined in a beam centred coordinate system by:

$$\begin{aligned} \rho_v &= \sqrt{x_v^2 + y_v^2} \leq 30in \text{ for pions} \\ |x_v| &\leq 50in \text{ and } |y_v| \leq 50in \text{ for kaons} \\ -653in &< z_v < -167in \text{ or } 80 \leq PLACE \leq 20 \text{ for all events} \end{aligned}$$

ensured that the hadronic shower was contained and hence measured. Also, within this fiducial volume the target portion of the outgoing muon track was found with high efficiency ( $99.9 \pm 0.1\%$ ), and hence  $\theta_\mu$  measured. The more restrictive transverse vertex cut on the neutrinos from pion decay was imposed because of the sensitivity of the predicted neutrino flux at large radius to uncertainties in beam dispersion and steering.

Geometric cuts on the projected target track of the muon were imposed to ensure that the muon momentum could be reconstructed and that the detector acceptance for the given event could be determined. These were:

$$\begin{aligned} \rho_F &< 69in \\ |x_{T2}| &< 55in \text{ and } |y_{T2}| < 55in \\ \lambda_H &< 0.30 \end{aligned}$$

where  $\rho_v$  is the radius of the muon at the front face of the toroid,  $(x_{T2}, y_{T2})$  is the projected position of the muon track at the T2 trigger counter, and  $\lambda_H$  is the fraction of the time that the projected muon track lies within the 10in diameter of the toroid hole. These were all defined in an apparatus centred coordinate system. A muon which satisfied these cuts entered the spectrometer. Since the magnetic field focused and the T2 cut was inside the physical dimensions of the counter, such events would satisfy the muon hardware trigger.

#### 4.3.4 Acceptance calculation

The set of geometric cuts applied to the data imply a detector acceptance which depends on the muon angles  $(\theta_\mu, \phi_\mu)$  and the vertex position  $(x_v, y_v, z_v)$ . The outgoing muon is produced uniformly in the azimuthal angle  $\phi_\mu$ , but for only some fraction  $\delta$  out of  $2\pi$  does the muon track pass the geometric cuts, and hence trigger the detector (figure 4.9). Clearly,  $\delta$  is the event acceptance.

The solid angle subtended by the spectrometer varies with the longitudinal position of the vertex, resulting in a dependence of acceptance on  $z_v$ . This effect was accounted for by averaging the acceptance of an event translated over the length of the fiducial volume.

Potentially, this  $z$  averaged acceptance could have a  $p_\mu$  dependence. Low energy muons which satisfied the muon trigger requirements, and had a vertex near the downstream end of the fiducial volume, could range-out before reaching the trigger counter T2 if the vertex were moved to the upstream end of the detector. However, such range-out events do satisfy the penetration trigger requirements. Furthermore, muon momentum can be obtained from the distance penetrated in the target steel before stopping, so these events are also fully reconstructed. Thus, by supplementing the structure function data set with penetration events which satisfied the geometric requirements of muon events, the acceptance was made  $p_\mu$  independent.

Slow spill muon events required both T2 and T3 trigger counters to fire. By scanning a sample of fast spill muon events, it was found that in all cases where the muon failed to reach T3, the muon stopped between T2 and T3. Although the slow spill muon trigger requirements would not be satisfied, these events would be included as part of the sample of penetration events pointing toward T2. It was concluded that the muon momentum could be properly reconstructed from range.

The slow spill penetration trigger required either (1) greater hadron energy ( $E_H > 10\text{GeV}$ ) or (2) greater penetration ( $>32$  counters) than the fast spill trigger. Events which pointed toward T2 and had muon energy greater than  $3\text{GeV}$  would pass the increased penetration requirement. Hence, the hadron energy threshold for both fast and slow spill events was effectively the same in the structure function data set.

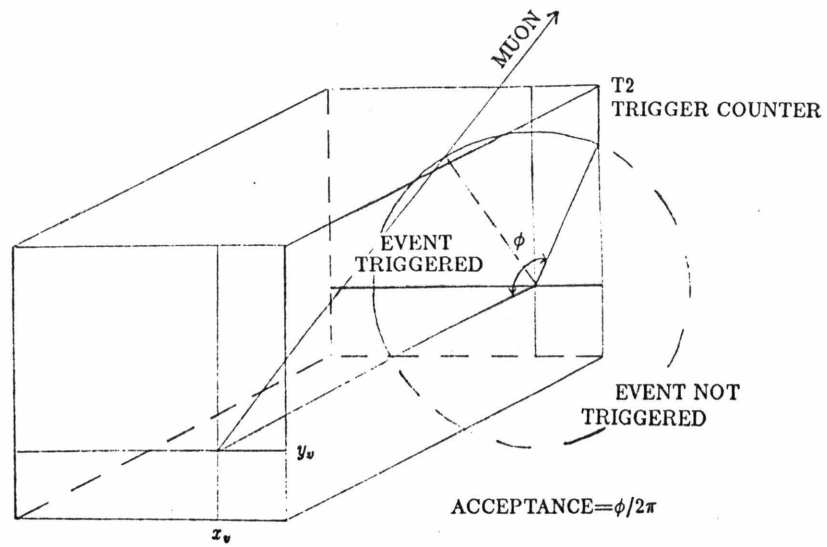


Figure 4.9 Illustration of geometric efficiency calculation

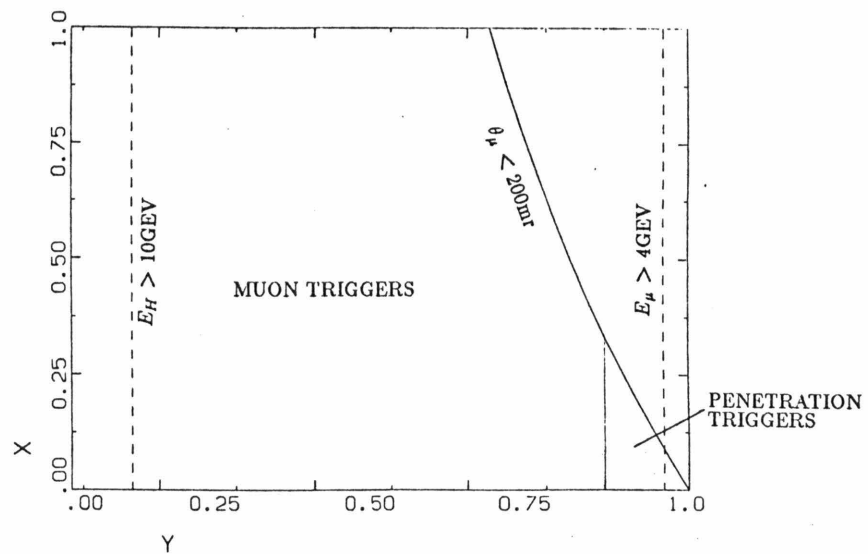


Figure 4.10 Restrictions in the  $x$ - $y$  plane due to kinematic cuts for  $E_\nu = 100 \text{ GeV}$

## 4.3.5 Kinematic cuts

Even after geometric acceptance correction, the muon trigger was not fully efficient over the entire  $x$  and  $y$  kinematic plane. An event with a vertex at the target centre, and at the most downstream end of the fiducial volume, would always fail geometric cuts if the outgoing muon had an angle  $\theta_\mu > 240\text{mr}$ ; that is, the event had zero efficiency. Also, if the muon had energy  $E_\mu < 3.8\text{GeV}$  it would fail to satisfy either charged current trigger. As noted above, the hadron energy requirement for penetration events was about  $3\text{GeV}$ . However, a more conservative cut on hadron energy was made due to uncertainties in the calibration and linearity of the calorimeter response below  $10\text{GeV}$ . A small non-linearity at low hadron energy could result in substantial systematic errors in our determination of  $x$ . The kinematic cuts applied to the events included in the structure function sample were:

$$\begin{aligned} E_H &\geq 10\text{GeV} \\ E_\mu &\geq 4\text{GeV} \\ \theta_\mu &\leq 200\text{mr} \end{aligned}$$

For a  $100\text{GeV}$  neutrino, these cuts restrict events to the region in the  $x$  and  $y$  plane shown in figure 4.10. Small angle muons from events with vertices within a radius of  $5\text{in}$  of the detector centre would pass directly down the toroid hole. The hole-time cut ( $\lambda_H$ ) would result in zero acceptance for these events. Therefore, an additional minimum angle cut was made, requiring  $\theta_\mu \geq 7.1\text{mr}$  for such events. The number of events lost due to this cut was insignificant. Table 4.5 shows the effect on the data sample of each of these kinematic cuts.

Setting	+120	+140	+168	+200	+250	Total
Muon event	10087	12552	20679	25877	32612	101807
$\theta_\mu^{max} \leq 200\text{mr}$	9992	12447	20513	25660	32347	100959
$E_H \geq 10\text{GeV}$	5569	7814	14181	18828	24996	71388
$E_\mu \geq 4\text{GeV}$	5529	7758	14068	18716	24794	70865
Fiducial cuts	3924	5905	11508	15815	21481	58633

Setting	-120	-140	-168	-200	-250	Total
Muon event	2040	2999	3328	3425	3208	15000
$\theta_\mu^{max} \leq 0.200\text{mr}$	2032	2996	3322	3418	3197	14965
$E_H \geq 10\text{GeV}$	889	1519	1870	2034	1989	8301
$E_\mu \geq 4\text{GeV}$	858	1476	1810	1957	1875	7976
Fiducial cuts	557	1065	1365	1534	1469	5990

Table 4.5 Event losses due to cuts for all settings

## 4.4 Tests of the Data

### 4.4.1 Trigger efficiencies

Due to the hadron energy requirement for the penetration trigger, the ratio of acceptance corrected muon events to penetration events, with  $\theta_\mu < 200\text{mr}$ , exhibits the fall-off as  $E_H \rightarrow 0$  shown in figure 4.11. Likewise, the spectrometer angle acceptance limit results in the decline above  $\theta_\mu = 240\text{mr}$  in figure 4.12 of the ratio of muon to penetration events. However, the two independent charged current triggers were both efficient after geometric acceptance corrections within the region:

$$\begin{aligned} E_H &> 20\text{GeV} \\ E_\mu &> 4\text{GeV} \\ \theta_\mu &< 200\text{mr} \end{aligned}$$

Within these kinematic bounds, the relative efficiency of muon and penetration triggers was found to be  $99.8 \pm 0.7\%$  for fast spill, from the ratio of the sum of acceptance weighted muon and penetration events. The procedure was unreliable for slow spill, due to contamination of high-angle penetration events by cosmic rays.

A second approach to determining trigger efficiencies excluded the complication of acceptance from the calculation. Within the kinematic limits:  $E_H > 10\text{GeV}$  (fast spill) or  $> 20\text{GeV}$  (slow spill) and  $\theta_\mu < 100\text{mr}$ , the number of penetration events which point toward the T2 trigger counter, but which do not fire a muon trigger, were determined. Some calculable fraction of these events were due to range-out before T2; the remainder represented muon trigger inefficiency. By this means, the efficiency of the muon trigger was found to be  $100. \pm 0.1\%$ . The complementary procedure, namely the number of muon triggers within these limits which failed to fire the penetration trigger, gave a penetration trigger efficiency of  $99.2 \pm 0.1\%$ .

These numbers represent efficiencies before the cut on  $\chi^2$  for the muon momentum fit. The correction for the events lost by this cut was determined in three ways. The difference in the efficiency determined with and without the cut, using either of the methods described above, could be used as the correction. Alternatively, all failed muon events were known to have final state muons with momenta  $E_\mu > 4\text{GeV}$ . The ratio of the sum of weights of failed events to all muon events within the structure function kinematic cuts also determined the required inefficiency. While this last technique was used to calculate the corrections shown in table 4.6, the three approaches produced consistent results.

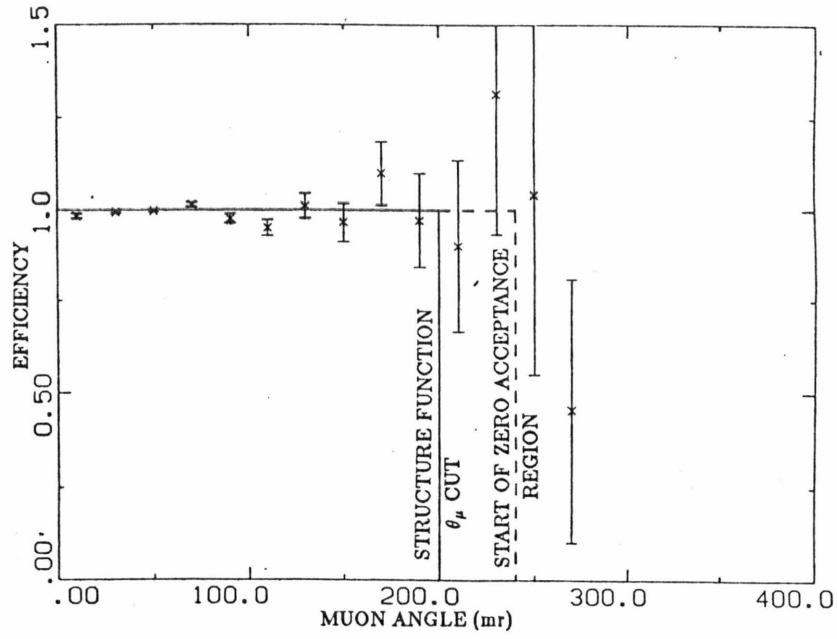


Figure 4.11 Muon trigger efficiency as a function of  $\theta_\mu$

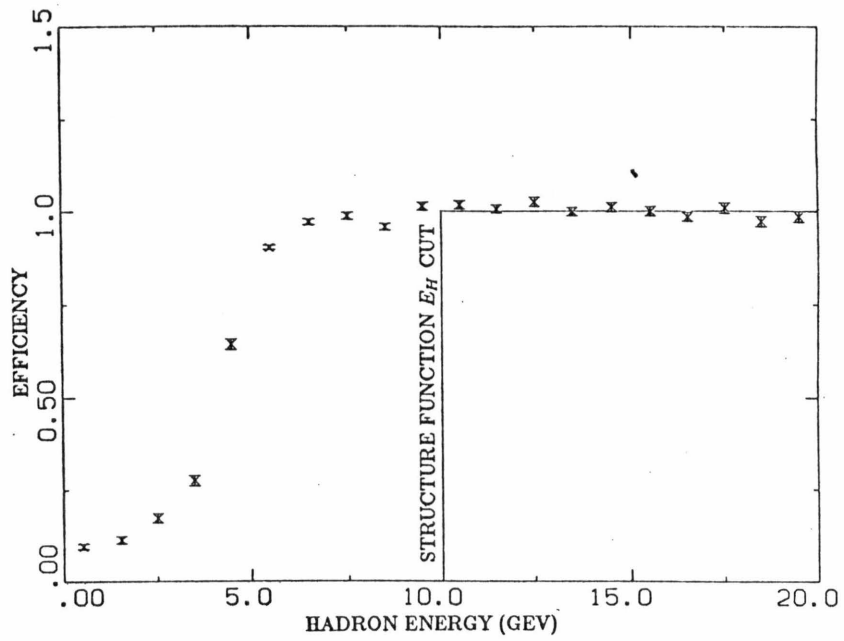


Figure 4.12 Penetration trigger efficiency as a function of  $E_H$

Setting	Positive	Negative
120	1.0059	1.0250
140	1.0123	1.0009
168	1.0265	1.0014
200	1.0169	1.0080
250	1.0072	1.0025

Table 4.6 Correction factors for losses due to toroid  $\chi^2$  failures

#### 4.4.2 Calibration check

A check of the calibration of the spectrometer and hadron calorimetry was made by comparing mean event energies as a function of  $y$ . At high  $y$  the total energy of the final state is mostly hadronic, whereas at low  $y$  it is dominated by the muon energy. Due to the muon angle cut, the limits of acceptance at high  $y$  varied with energy. Corrections were made using an event monte carlo based on our measured structure functions and flux calculations (see section 5.2.4 below). Shown in figure 4.13 for the +200 setting is the ratio of the mean observed energy to the mean energy predicted by the monte carlo, as a function of  $y$ . Included in quadrature with the statistical errors are estimated systematic errors of 1.0% on hadron energy (section 4.1.2 and 4.1.3) and 1.0% on muon energy (section 4.2.2). Both the pion and kaon mean energies are seen to be consistent with the hypothesis of  $y$ -independence. Within the noted systematic errors, this was true for all settings.

The average value for the ratio of data to monte carlo mean energy fluctuated about unity with sigmas of 1.5% and 1.0% for neutrinos from pion and kaon decay respectively. The predicted mean momenta depended directly on the mean secondary momenta from the beam monte carlo. The pion mean momenta could only be set from the energy of neutrinos from forward-going decays ( $\gamma R/z \ll 1$ ), which were directly proportional to the parent secondary energy (equation 2.1). The mean kaon energies could also be determined from the observed mean of the kaon pressure peak from the Čerenkov counter (section 2.3.5). The consistency of the two methods of measuring the mean kaon momenta indicated that a systematic error of 1% should be assigned the result. Presumably the corresponding error for pions is not much greater. In both cases, the monte carlo central momenta were smoothly adjusted to match the measurements. Therefore, the observed deviations were within expectations, given this level of systematic error on mean momenta.

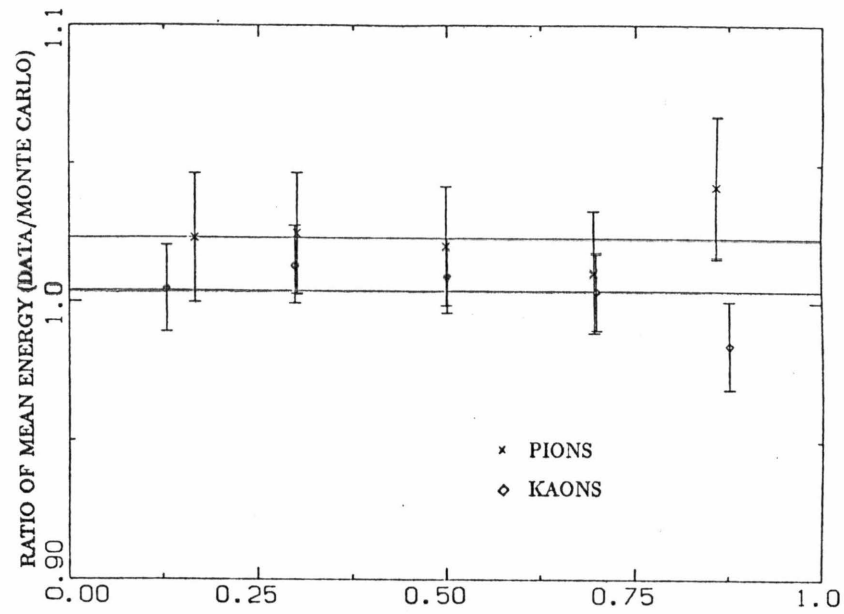


Figure 4.13 Mean energy as a function of  $y$

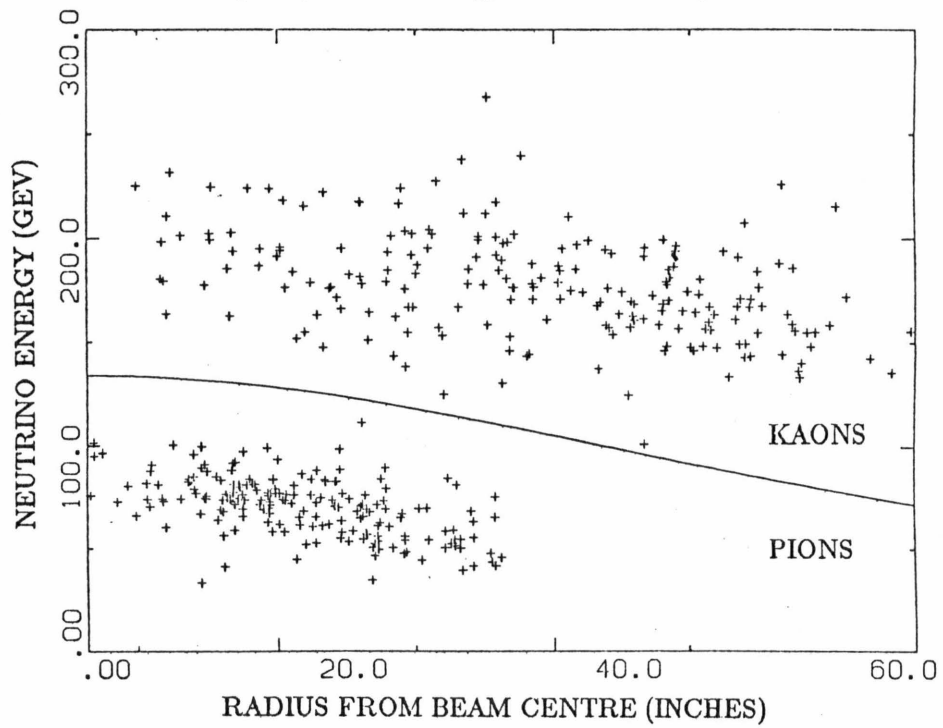


Figure 4.14

Clean separation of neutrino types in an  $E_\nu$  vs  $r$  plot for a sample of 200 GeV muon triggers

Setting	$\alpha(\text{GeV})$	$\beta(\text{in}^{-1})$
$\pm 120$	80.	0.0119
$\pm 140$	92.	0.0126
$\pm 168$	110.	0.0140
$\pm 200$	134.	0.0155
$\pm 250$	165.	0.0177

Table 4.7 Parameters for neutrino type separation

#### 4.4.3 Separation of pion and kaon neutrino events

Interactions in the target result were due to neutrinos from both pion and kaon decay, each with quite distinct energy and spatial distributions. The dichromatic nature of the neutrino source made possible an event-by-event determination of the parent secondary type. The separation was made on the basis of a function recalling the correlation between  $E_\nu$  and radius (equation 2.1):

$$E_{SEP}(r) = \frac{\alpha}{1 + (\beta r)^2} \quad (4.5)$$

where  $r$  is the radius of the event from the beam centre. If  $E_\nu < E_{SEP}(r)$  the neutrino was from a pion decay, or if  $E_\nu \geq E_{SEP}(r)$  the neutrino was from kaon decay.  $\alpha$  and  $\beta$  for the five pairs of settings are listed in table 4.7. Figure 4.14 shows the clean separation of neutrinos from pion and kaon decay in a sample of 200GeV muon events.

Beam centres for each of the settings were determined from the distribution of vertex positions for neutrinos from pion decay with  $E_\nu > 0.20E_\pi$ . It should be also noted that the beam centres of the monte carlo predicted flux distributions were calculated in an analogous fashion, and adjusted to match the data. Deviations from the target centre were small, as shown in table 4.8.

Setting	Positive		Negative	
	$x_0$ (in)	$y_0$ (in)	$x_0$ (in)	$y_0$ (in)
120	3.67	2.21	2.33	3.79
140	3.65	1.84	3.11	3.20
168	3.84	1.66	4.11	3.81
200	3.37	3.00	3.83	3.35
250	1.36	2.01	2.18	3.92

Table 4.8 Beam centres from the vertex distribution of pion events

## Extraction of Structure Functions

A sample of fully reconstructed neutrino and anti-neutrino charged current events was available within the kinematic limits and the fiducial volume described in the last chapter. The normalized flux spectrum over that same fiducial volume was calculated from properties of the secondary beam, as described in chapter 2. It remains to be shown how structure functions were extracted from this information.

### 5.1 Total Cross Sections

The probability of observing a neutrino or anti-neutrino event in a differential kinematic and fiducial volume at  $(E, x, \log Q^2)$  and  $(r, \phi)$  can be expressed as:

$$dn^{\nu(\bar{\nu})} = k \varphi_{\nu(\bar{\nu})}(E, r) A(r, \theta, \phi) \frac{d\sigma^{\nu(\bar{\nu})}}{dx d \log Q^2} dE dx d \log Q^2 dr d\phi \quad (5.1)$$

where  $k$  is the number of scattering centres in the fiducial volume,  $\varphi_{\nu(\bar{\nu})}(E, r)$  is the flux of neutrinos or anti-neutrinos, and  $A(r, \theta, \phi)$  is the acceptance of the detector for the event. The acceptance couples the spatial dependence of the flux with the kinematic dependence of the differential cross section. However, if events are weighted by one over acceptance, that is both sides of the equation 5.1 are divided by  $A(r, \theta, \phi)$ , this coupling is removed. With  $dw^{\nu(\bar{\nu})} = dn^{\nu(\bar{\nu})}/A(r, \theta, \phi)$ , the weighted event density is:

$$dw^{\nu(\bar{\nu})} = k \varphi_{\nu(\bar{\nu})}(E, r) \frac{d\sigma^{\nu(\bar{\nu})}}{dx d \log Q^2} dE dx d \log Q^2 dr d\phi \quad (5.2)$$

The probability integrated over all  $x$  and  $\log Q^2$  is proportional to the total cross section:

$$dw^{\nu(\bar{\nu})} = k \varphi_{\nu(\bar{\nu})}(E, r) \sigma^{\nu(\bar{\nu})}(E) dE dr d\phi \quad (5.3)$$

The dichromatic nature of the neutrino beam results in further simplification. Events restricted to an annulus  $(r, r + \Delta r)$  in the detector will be peaked at two distinct neutrino energies,

corresponding to neutrinos from pion and kaon decay. For each parent species:

$$\sigma^{\nu(\bar{\nu})}(E_r) = \frac{\sum w_i^{\nu(\bar{\nu})}}{k \int dE \int_r^{r+\Delta r} dr \int d\phi \varphi_{\nu(\bar{\nu})}(E, r)} \quad (5.4)$$

The fiducial volume could be divided into a series of such concentric rings. Thus, a series of paired measurements of the total cross section would be obtained as a function of neutrino energy.

In practice, the process was not quite so simple. The charged current triggers did not cover the entire kinematic range. However, for the purposes of the total cross section the accessible region was maximized by recognizing that events need not be fully determined kinematically: only separation of events into pion and kaon parent classes was necessary. Thus, penetration events were included where the muon momentum was not measured. Separation for such events was achieved on the basis of hadron energy alone, using the statistical technique described in detail in the theses of R.Blair [Bl82] and J.Lee [Le81]. Shown in figure 5.1 is the total cross section result from E616 [Bl83a]. The inner error bars represent statistical errors only, while the outer error bars include estimates of point-to-point systematic errors added in quadrature. Additional overall normalization errors of 3% and 5.5% were assigned to the neutrino and anti-neutrino cross section measurements respectively. It can be seen that generally systematic errors, which were predominantly flux errors, were greater than statistical errors.

The quark-parton model expectation is that the inclusive total cross section will rise linearly with energy. This is not modified in any essential way by QCD: the predicted level of scale breaking effects lead to cross section slopes which fall slightly with energy for neutrinos and rise slightly for anti-neutrinos. Including all sources of statistical and systematic error, the reported result  $\sigma/E$  was found to be consistent with the linearly rising hypothesis:  $\chi^2=16.9$  for 14 degrees of freedom for neutrinos, and 5.3 for 10 degrees of freedom for anti-neutrinos. The average cross section slopes were:

$$\begin{aligned} \sigma^\nu/E &= 0.669 \pm 0.003 \pm 0.024 \\ \sigma^{\bar{\nu}}/E &= 0.340 \pm 0.003 \pm 0.020 \end{aligned}$$

where the first error is statistical, and the second systematic, including the overall scale errors.

Two features of the measurements were of concern for the structure function analysis: (1) the preferred trend of  $\sigma/E$  to rise with energy for neutrinos and fall for anti-neutrinos, and (2) the large fluctuations with energy of the ratio of  $\sigma^\nu$  to  $\sigma^{\bar{\nu}}$ . If no means were found to reduce the systematic errors introduced by flux measurements, these features would significantly alter the observed scaling violations in the data, leading to large systematic errors on  $\Lambda_{QCD}$ . For the purposes of the structure function analysis, a nearly model independent procedure was devised to adjust fluxes on a setting-by-setting basis, so that the total cross section better conformed to expectations. Details concerning the method will be discussed in section 5.3 below.

Also shown in figure 5.1 are the corresponding results for  $\sigma/E$  from the CDHS collaboration at CERN [Ab83]. The absolute level of these points was normalized in the region

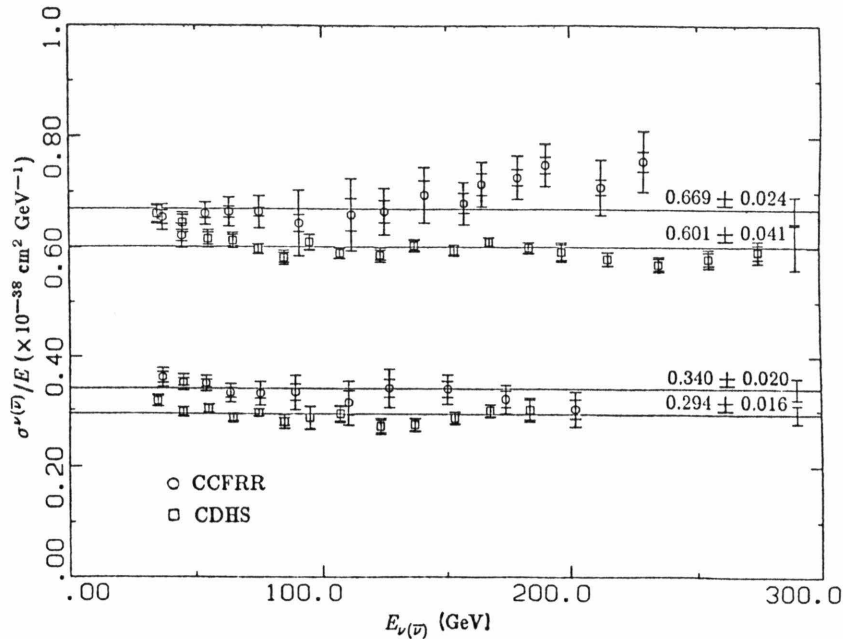


Figure 5.1 Neutrino and anti-neutrino total cross sections for CCFRR and CDHS

$30\text{GeV} < E_{\nu} < 90\text{GeV}$  to an earlier cross section measurement of  $\sigma^{\nu}/E=0.62$  and  $\sigma^{\bar{\nu}}/E=0.30$  by the same group [Gr79]. Again, the inner error bars are statistical only, while the outer error bars include point-to-point systematic errors. Average overall scale errors of 6.8% for neutrinos and 5.5% for anti-neutrinos are not shown. The average cross section slopes over the entire spanned energy region are:

$$\begin{aligned}\sigma^{\nu}/E &= 0.601 \pm 0.003 \pm 0.041 \\ \sigma^{\bar{\nu}}/E &= 0.294 \pm 0.003 \pm 0.016\end{aligned}$$

Thus, the average values of  $\sigma/E$ , as measured by the two groups, differ by 11% and 16% for neutrinos and anti-neutrinos respectively. This is somewhat outside the stated systematic errors on the measurements.

Since the CDHS detector was closer to the neutrino source, it was necessary to use only two settings of the secondary beam ( $\pm 200$  and  $+300$ ) in order to obtain neutrinos over the reported energy region. This results in a smaller contribution to point-to-point fluctuations due to uncertainties in particle fractions measurements in the secondary beam. The reported energy dependence is clearly consistent with the linear rising hypothesis of the quark-parton model, or with QCD expectations.

The total cross section is proportional to integrals of structure functions at fixed  $E_{\nu}$ . Starting with the general expression for the cross section, equation 5.12 below, and integrating

over all  $x$  and  $y$ , it can be shown that:

$$\begin{aligned}\int_0^1 F_2(x, Q^2) dx &= \frac{3}{4-R} \frac{\pi}{G^2 M} \left( \frac{\sigma^\nu}{E} + \frac{\sigma^{\bar{\nu}}}{E} \right) \\ \int_0^1 x F_3(x, Q^2) dx &= \frac{3}{2} \frac{\pi}{G^2 M} \left( \frac{\sigma^\nu}{E} - \frac{\sigma^{\bar{\nu}}}{E} \right)\end{aligned}\tag{5.5}$$

Assuming  $R = 0.1$ , and a  $\frac{1}{2}\text{SU}(3)$  symmetric strange sea (see section 5.2.1), the results for  $\sigma^{\nu(\bar{\nu})}/E$  imply:

	CCFR	CDHS
$\int_0^1 F_2(x, Q^2) dx dy$	$0.478 \pm 0.015$	$0.424 \pm 0.019$
$\int_0^1 x F_3(x, Q^2) dx dy$	$0.312 \pm 0.020$	$0.291 \pm 0.039$

The discrepancies in the total cross section measurements naturally lead to normalization differences in the integrals of structure functions, and ultimately in the extracted structure functions themselves. This is of some importance for definitive tests of quark model predictions, such as the mean quark charge test or the GLS sum rule.

## 5.2 Weighted Event Method for $F_2$ and $x F_3$

In order to obtain structure functions as a function of  $(x, \log Q^2)$ , a set of bins was defined spanning the accessible kinematic range in these variables. The binning scheme chosen is common in the literature, but also matched resolutions in  $x$  and  $Q^2$  reasonably well. The acceptance weighted mean values of  $E_H$ ,  $E_\mu$ ,  $\theta_\mu$  and  $y$ , and the average weight for each of these bins are tabulated in Appendix F. Typically, for a given  $x$  value, the low  $Q^2$  bins were populated by neutrinos from pion decay while high  $Q^2$  bins were predominantly neutrinos from kaon decay. The distribution of acceptance and the inverse of acceptance for a particular bin are shown in figure 5.2. The average weight for events from pion and kaon decay neutrinos are separately shown in table 5.1.

Setting	$\nu_\pi$	$\nu_K$	$\bar{\nu}_\pi$	$\bar{\nu}_K$
120	1.614	1.464	1.417	1.273
140	1.523	1.415	1.383	1.271
165	1.481	1.346	1.262	1.210
200	1.426	1.326	1.227	1.164
250	1.366	1.286	1.202	1.149

Table 5.1 Average weights for both neutrino types at each setting

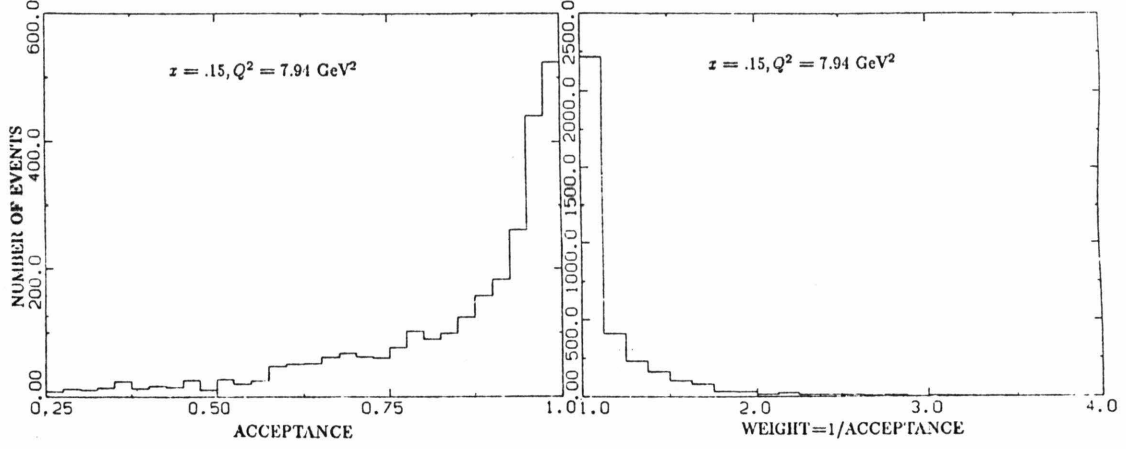


Figure 5.2 Sample acceptance and weight distribution

The weighted sum of events in a bin is related to the differential cross section. Equation 5.2 can be integrated over  $(x, \log Q^2)$  within kinematic cuts and bin limits, over  $(r, \phi)$  within the fiducial volume, and over all  $E$  to give:

$$\sum w_i^{\nu(\bar{\nu})} = k \int dE \int dx \int d \log Q^2 \frac{d\sigma^{\nu(\bar{\nu})}}{dx d \log Q^2} \Phi_{\nu(\bar{\nu})}(E) \quad (5.6)$$

Here, the integrations over the fiducial volume have been absorbed into the flux, with:

$$\Phi_{\nu(\bar{\nu})} = \int dr \int d\phi \varphi_{\nu(\bar{\nu})}(E, r) \quad (5.7)$$

Let the expectation value for a function  $\mathcal{F}(E, x, Q^2)$  be denoted as:

$$\langle \mathcal{F}(E, x, Q^2) \rangle_{\nu(\bar{\nu})} = \frac{\int dE \int dx \int d \log Q^2 \mathcal{F}(E, x, Q^2) \Phi_{\nu(\bar{\nu})}(E)}{\int dE \int dx \int d \log Q^2 \Phi_{\nu(\bar{\nu})}(E)} \quad (5.8)$$

Then, equation 5.6 can be rewritten as:

$$\frac{\sum w_i^{\nu(\bar{\nu})}}{k \int dE \int dx \int d \log Q^2 \Phi_{\nu(\bar{\nu})}} = \left\langle \frac{d\sigma^{\nu(\bar{\nu})}}{dx d \log Q^2} \right\rangle_{\nu(\bar{\nu})} \quad (5.9)$$

The most general expression for the differential cross section at high energy is in terms of three unknown structure functions:

$$\frac{d\sigma^{\nu(\bar{\nu})}}{dx d \log Q^2} = \frac{\ln 10 G^2 M E}{\pi} y \left\{ \left(1 - y - \frac{Mxy}{2E}\right) F_2^{\nu(\bar{\nu})}(x, Q^2) + \frac{y^2}{2} 2xF_1^{\nu(\bar{\nu})}(x, Q^2) \pm y\left(1 - \frac{y}{2}\right) xF_3^{\nu(\bar{\nu})}(x, Q^2) \right\} \quad (5.10)$$

Using:

$$\left(1 + \frac{Q^2}{\nu^2}\right) F_2^{\nu(\bar{\nu})}(x, Q^2) = (1 + R(x, Q^2)) 2xF_1^{\nu(\bar{\nu})}(x, Q^2) \quad (5.11)$$

this can be rewritten as:

$$\frac{d\sigma^{\nu(\bar{\nu})}}{dx d \log Q^2} = \frac{\ln 10 G^2 M E}{\pi} y \left\{ y^+ F_2^{\nu(\bar{\nu})}(x, Q^2) \pm y^- x F_3^{\nu(\bar{\nu})}(x, Q^2) \right\} \quad (5.12)$$

where:

$$y^+ = 1 - y - \frac{Mxy}{2E} + \frac{y^2}{2} \left( \frac{1 + Q^2/\nu^2}{1 + R(x, Q^2)} \right) \approx \frac{1}{2}(1 + (1 - y)^2)$$

$$y^- = \frac{1}{2}(1 - (1 - y)^2)$$

The dominance of spin  $\frac{1}{2}$  quarks in the scattering of neutrinos from nuclei is equivalent to  $R \approx 0$  [Cl79]. For the purposes of extracting  $F_2(x, Q^2)$  and  $xF_3(x, Q^2)$ , various assumptions were made concerning  $R(x, Q^2)$ , all consistent with present measurements.

Given bins sufficiently small in  $(x, \log Q^2)$ , the structure functions can be taken outside integrations and:

$$\frac{\sum w_i^{\nu(\bar{\nu})}}{\int dE \int dx \int d \log Q^2 \Phi_{\nu(\bar{\nu})}} = \frac{k \ln 10 G^2 M}{\pi} \left\{ \langle y E y^+ \rangle_{\nu(\bar{\nu})} F_2^{\nu(\bar{\nu})}(x, Q^2) \pm \langle y E y^- \rangle_{\nu(\bar{\nu})} x F_3^{\nu(\bar{\nu})}(x, Q^2) \right\} \quad (5.13)$$

If the differences in the energy spectrum of incident neutrinos and anti-neutrinos are ignored, so that  $\langle y E y^\pm \rangle_\nu = \langle y E y^\pm \rangle_{\bar{\nu}}$ , and taking  $xF_3^\nu(x, Q^2) = xF_3^{\bar{\nu}}(x, Q^2)$ , this is simply:

$$F_2(x, Q^2) = \frac{\pi}{2k \ln 10 G^2 M} \frac{1}{\langle y E y^+ \rangle} \left\{ \frac{\sum w_i^\nu}{\int \Phi_\nu} + \frac{\sum w_i^{\bar{\nu}}}{\int \Phi_{\bar{\nu}}} \right\} \quad (5.14)$$

$$xF_3(x, Q^2) = \frac{\pi}{2k \ln 10 G^2 M} \frac{1}{\langle y E y^- \rangle} \left\{ \frac{\sum w_i^\nu}{\int \Phi_\nu} - \frac{\sum w_i^{\bar{\nu}}}{\int \Phi_{\bar{\nu}}} \right\}$$

The three dimensional integrals  $\langle y E y^+ \rangle$ ,  $\langle y E y^- \rangle$ ,  $\int \Phi_\nu$ , and  $\int \Phi_{\bar{\nu}}$  can be evaluated numerically. The sum and difference of the total number of acceptance weighted neutrino and anti-neutrino events in a given bin in  $(x, \log Q^2)$ , yield  $F_2(x, Q^2)$  and  $xF_3(x, Q^2)$  respectively.

It was of course not necessary to make these simplifying assumptions, and as implemented the structure functions were extracted using:

$$\begin{aligned}
 F_2(x, Q^2) &= \frac{1}{k} \left\{ \frac{F_2(x, Q^2)}{\left\langle \frac{d\sigma^\nu}{dx d \log Q^2} \Big|_{Iron} \right\rangle_\nu + \left\langle \frac{d\sigma^{\bar{\nu}}}{dx d \log Q^2} \Big|_{Iron} \right\rangle_{\bar{\nu}}} \right\} \left\{ \frac{\sum w_i^\nu}{\int \Phi_\nu} + \frac{\sum w_i^{\bar{\nu}}}{\int \Phi_{\bar{\nu}}} \right\} \\
 xF_3(x, Q^2) &= \frac{1}{k} \left\{ \frac{xF_3(x, Q^2)}{\left\langle \frac{d\sigma^\nu}{dx d \log Q^2} \Big|_{Iron} \right\rangle_\nu - \left\langle \frac{d\sigma^{\bar{\nu}}}{dx d \log Q^2} \Big|_{Iron} \right\rangle_{\bar{\nu}}} \right\} \left\{ \frac{\sum w_i^\nu}{\int \Phi_\nu} - \frac{\sum w_i^{\bar{\nu}}}{\int \Phi_{\bar{\nu}}} \right\}
 \end{aligned} \tag{5.15}$$

The symbols  $d\sigma^{\nu(\bar{\nu})}/dx d \log Q^2 \Big|_{Iron}$  represent the cross sections for neutrinos and anti-neutrinos in an iron target. These were evaluated using the same  $F_2(x, Q^2)$  and  $xF_3(x, Q^2)$  which appear explicitly on the right hand side of equations 5.15. To begin with the structure functions were unknown: the method therefore required iteration. However, corrections were small and convergence was fast.

### 5.2.1 Corrections to isoscalar cross section

The cross section in iron can be expressed in terms of  $F_2(x, Q^2)$ ,  $xF_3(x, Q^2)$ , and a number of correction terms: (1) isoscalar corrections,  $I^{\nu(\bar{\nu})}$ , (2) strange sea corrections,  $S^{\nu(\bar{\nu})}$ , (3) corrections for slow rescaling due to the charm quark mass,  $C^{\nu(\bar{\nu})}$ , and (4) electromagnetic radiative corrections,  $R_{em}^{\nu(\bar{\nu})}$ . Thus:

$$\frac{d\sigma^{\nu(\bar{\nu})}}{dx d \log Q^2} \Big|_{Iron} = \ln 10 y \frac{d\sigma^{\nu(\bar{\nu})}}{dx dy} \Big|_{Bare} \left\{ 1 + R_{em}^{\nu(\bar{\nu})}(E, x, Q^2) \right\} \tag{5.16}$$

where:

$$\begin{aligned}
 \frac{d\sigma^{\nu(\bar{\nu})}}{dx dy} \Big|_{Bare} &= \frac{G^2 M E}{\pi} \left\{ y^+ F_2(x, Q^2) \pm y^- xF_3(x, Q^2) \right. \\
 &\quad \left. + I^{\nu(\bar{\nu})}(E, x, Q^2) + S^{\nu(\bar{\nu})}(E, x, Q^2) + C^{\nu(\bar{\nu})}(E, x, Q^2) \right\}
 \end{aligned} \tag{5.17}$$

The origin of the various correction terms is outlined below; a detailed discussion of the form of the differential cross section is included in Appendix E. Not shown is the W-Boson propagator term, which was included in the procedure for extracting structure functions.

An iron nucleus, with an excess of neutrons over protons, differs slightly from an isoscalar target. This results in the term:

$$I^{\nu(\bar{\nu})}(E, x, Q^2) = \pm(1 - 2Z/A)(u_\nu(x, Q^2) - d_\nu(x, Q^2)) \left\{ \frac{1}{(1 - y)^2} \right\} \tag{5.18}$$

where  $u_v$  and  $d_v$  are respectively the valence distributions for u and d quarks in the proton. As shown in figures 5.3 and 5.4, this correction was quite small for  $F_2$ , but was as large as 10% for  $xF_3$  at low  $Q^2$ .

If the charm content of the nucleon is taken to be negligible, then the conventional definitions of the structure functions are recovered only with the additional term:

$$S^{\nu(\bar{\nu})}(E, x, Q^2) = s(x, Q^2)(1 - (1 - y)^2) \quad (5.19)$$

where  $s$  is the strange sea in the proton. For this analysis, the strange sea was assumed to be  $\frac{1}{2}$ SU(3) symmetric, as discussed in section 5.2.2 below. Figure 5.5 shows the strange sea correction for  $F_2$ . The correction was substantial only at small  $x$ . This reflects the nature of the sea quark distribution, which is peaked at small  $x$ . In the case of  $xF_3$ , which is proportional to the difference between neutrino and anti-neutrino cross sections, the correction cancels.

The effect of a finite charm mass was properly accounted for by the use of  $\xi$ -scaling and a slow rescaling threshold factor. The components of the cross section reflecting transitions from both d and s quarks to charm were so modified. In order to restore the suppression introduced, the correction term  $C^{\nu(\bar{\nu})}(x, Q^2)$  was required. Rather than displaying this term in excruciating detail, the reader is referred to equations E.10 and E.13 for the specific form of the cross sections used in these calculations. The effect on the structure function results of a finite charm mass is shown in figures 5.6 and 5.7. Again, the correction was largest at small  $x$ . However, since Cabibbo-suppressed transitions of valence d quarks are also modified, the effect persisted at all  $x$ . The threshold effect was minimal at high energies, and hence, high  $Q^2$ : thus, the correction exhibited some  $Q^2$  dependence.

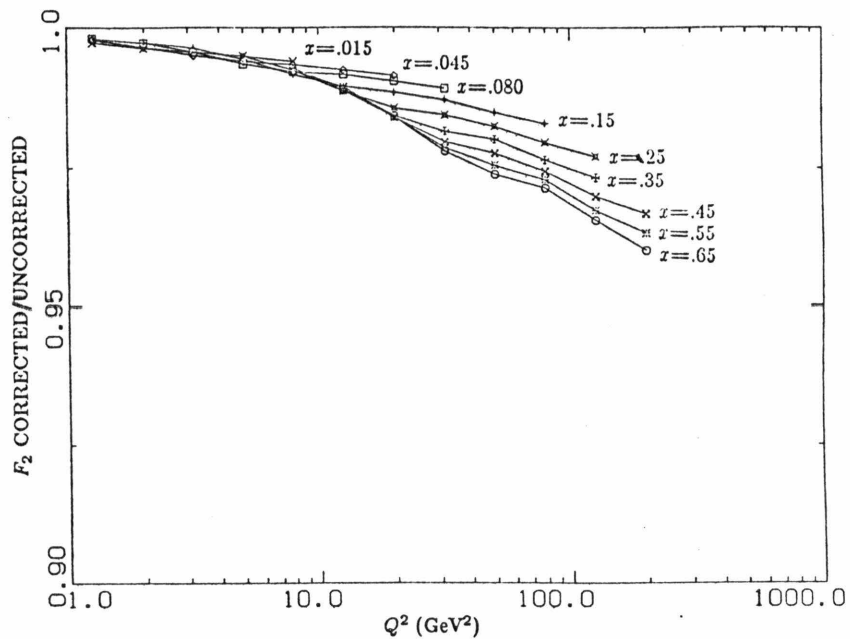


Figure 5.3 Isoscalar correction factors for  $F_2$

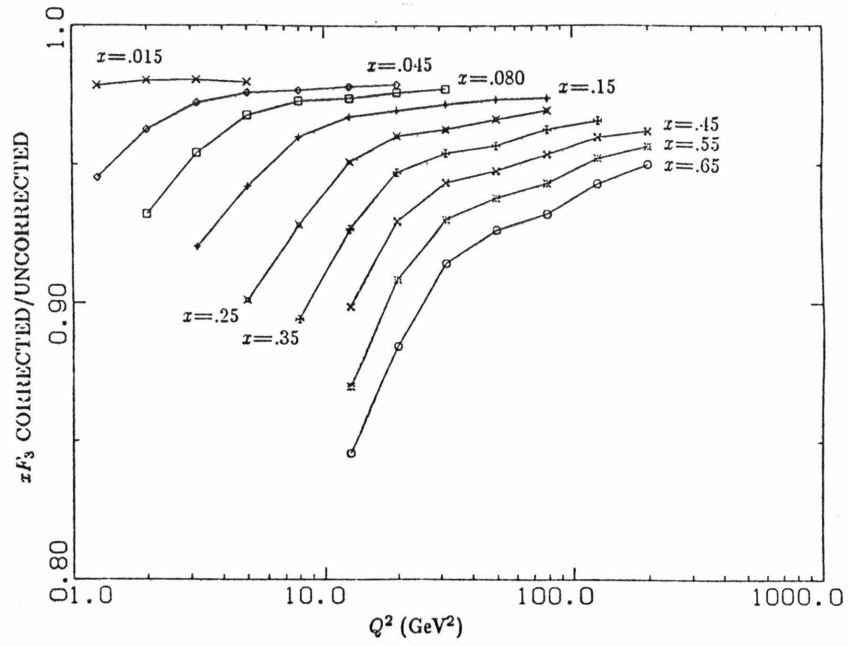


Figure 5.4 Isoscalar correction factors for  $xF_3$

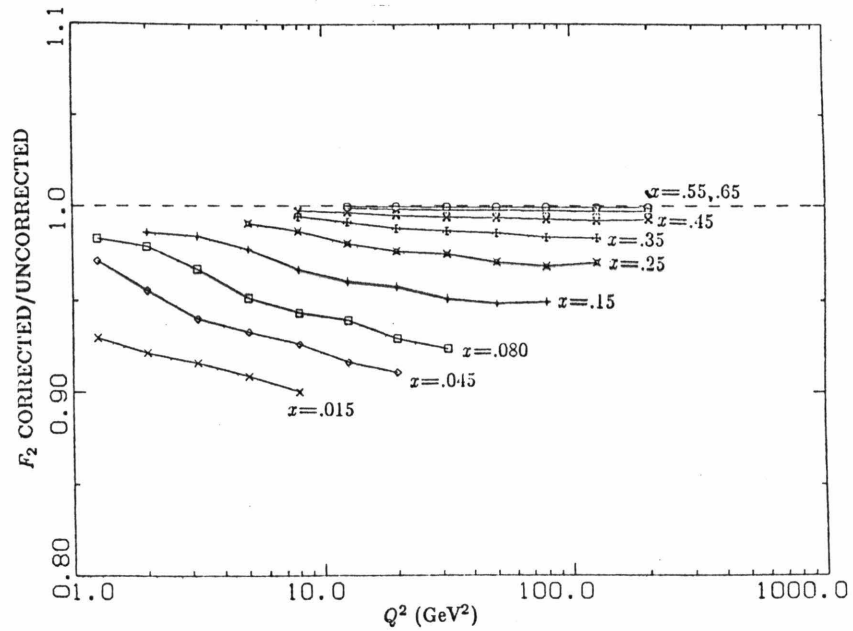


Figure 5.5 Strange sea correction factors for  $F_2$

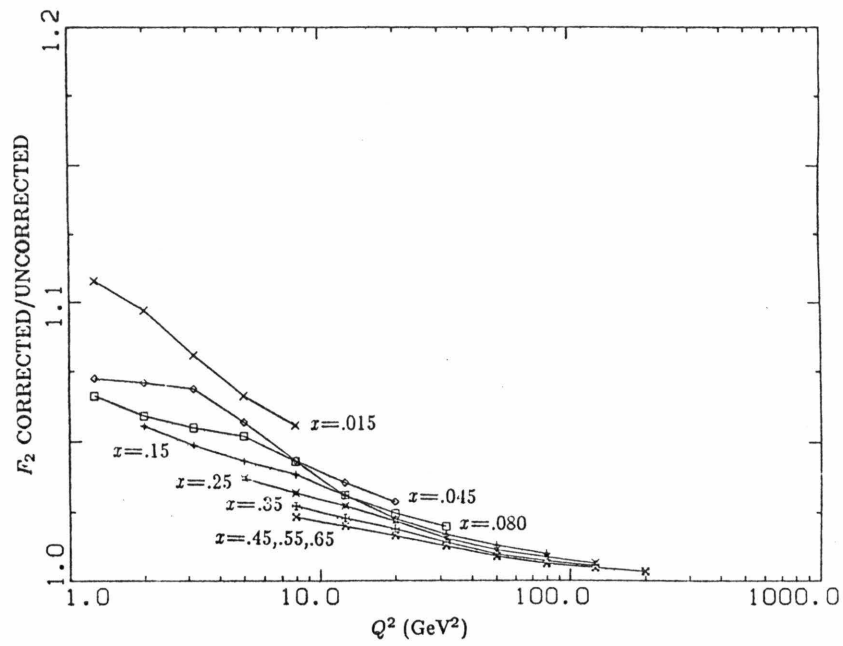


Figure 5.6 Charm mass correction factors for  $F_2$

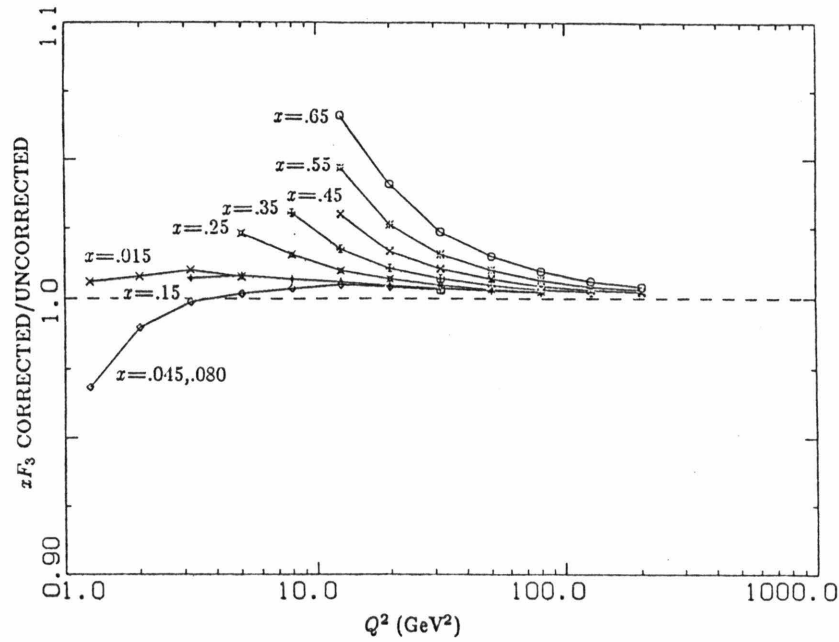
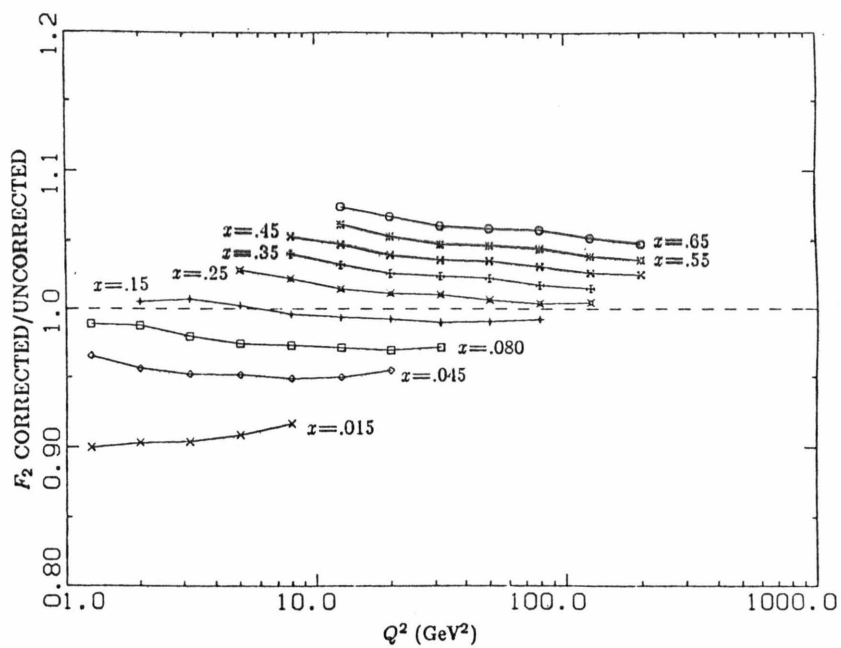
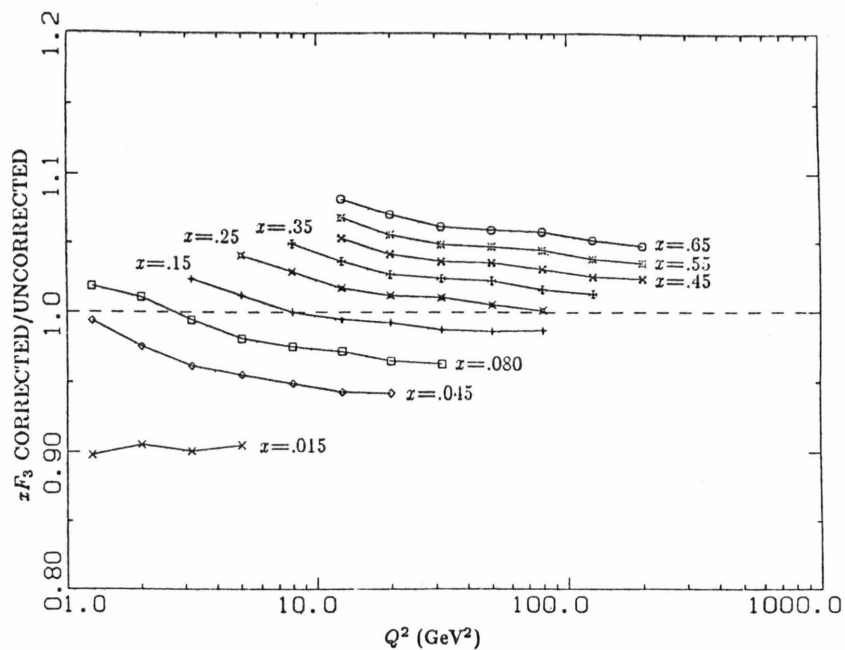


Figure 5.7 Charm mass correction factors for  $x F_3$

Figure 5.8 Radiative correction factors for  $F_2$ Figure 5.9 Radiative correction factors for  $xF_3$

Leading log radiative corrections to the lepton leg were made in the manner suggested by De Rújula and Petronzio [Ru79]. The emission of a collinear photon by the outgoing muon results in the reduction of the muon energy from  $E_\mu/z$  to  $E_\mu$ , but little change in muon angle. The migration in  $x$  and  $y$  is calculable and given by:

$$R_{em}^{\nu(\bar{\nu})}(E, x, Q^2) = \frac{\alpha_{em}}{2\pi} \ln \frac{2ME(1-y+xy)^2}{m_\mu^2} \int_0^1 dz \frac{1+z^2}{1-z} \left\{ \frac{y \Theta(z-z_{min})}{z(y+z-1)} \left[ \frac{d\sigma^{\nu(\bar{\nu})}}{dx dy} \Big|_{Bare} \right]_{x',y'} - \frac{d\sigma^{\nu(\bar{\nu})}}{dx dy} \Big|_{Bare} \right\} + O\left(\frac{\alpha_{em}^2}{2\pi}\right) \quad (5.20)$$

where:

$$\begin{aligned} x' &= xy/(z+y-1) \\ y' &= (z+y-1)/z \\ z_{min} &= 1-y+xy \end{aligned}$$

The magnitude of the radiative corrections to  $F_2$  and  $xF_3$  are shown in figures 5.8 and 5.9 respectively.

Corrections due to variations of  $F_2(x, Q^2)$  and  $xF_3(x, Q^2)$  within a bin were made implicitly by retaining the structure functions under the integral signs. These corrections were in general only a few percent, except for edge bins.

### 5.2.2 Model of $F_2$ and $xF_3$ for integrations

Quark distribution functions were obtained from fits to the data of the form proposed by Buras and Gaemers [Bu77, Bu78]. These functions represented a simple, but efficient, means of modeling the  $x$  and  $Q^2$  variation of the differential cross section for the purposes of calculating required integrals. The chosen forms were motivated by expectations of the quark-parton model and QCD. Arguments relating the pomeron and  $\rho$  Regge trajectories to the small  $x$  behavior of structure functions lead to the prediction that  $q_v(x) \sim x^{1/2}$  and  $\bar{q}(x) \sim c$  as  $x \rightarrow 0$  [Fi77, Cl79]. Correlations between elastic form factors and  $F_2$  lead to the prediction that  $q(x) \sim (1-x)^3$  as  $x \rightarrow 1$  [Dr70, We70]. Asymptotic analysis [Al82] of the Altarelli-Parisi equations confirms that  $q(x) \sim (1-x)^{\eta_q}$  as  $x \rightarrow 1$  and  $Q^2 \rightarrow \infty$ , and leads to the additional expectation that  $G(x) \sim (1-x)^{\eta_g+1}$  and  $\bar{q}(x) \sim (1-x)^{\eta_g+2}$  in the same limits. All of these predictions were incorporated in the model.

As a corollary of the fact that our target was nearly isoscalar, this experiment could not make measurements distinguishing between u and d quark  $x$  distributions. In order to establish a relationship, it was therefore necessary to make an appeal to the experimental literature. The observation in electron deep-inelastic scattering [Bo73, Fi77] that  $F_2^{en}/F_2^{ep} \rightarrow 1/4$  as  $x \rightarrow 1$ , implies that  $q(x) \sim u_v(x)$  at large  $x$ . Consistent with this result, the assumption was made that  $d_v(x) \sim u_v(x)(1-x)$ . This last represents a slight extension of the basic model proposed by Buras and Gaemers.

From asymptotic QCD, the evolution of the structure functions with  $Q^2$  can be calculated. One convenient form of these predictions is the moment equations: integrals of the Altarelli-Parisi equations over all  $x$ . Analytic expressions for the  $x$  and  $Q^2$  variation of quark distributions were devised by Buras and Gaemers, which incorporated the expectations of the parton model described above, and yet whose moments evolved as predicted by QCD.

The moment equations for the valence quark distributions are simply:

$$\langle q_v(Q^2) \rangle_{(n)} = \langle q_v(0) \rangle_{(n)} \exp[-\gamma^n s] \quad (5.21)$$

where  $\gamma^n$  are predicted by the theory (see [Bu78]), and:

$$s = \ln \frac{\ln(Q^2/\Lambda^2)}{\ln(Q_0^2/\Lambda^2)} \quad (5.22)$$

The choice of:

$$\begin{aligned} u_v(x, Q^2) &= a_v x^{\eta_1(s)} (1-x)^{\eta_2(s)} \\ d_v(x, Q^2) &= c_d(s) u_v(x, Q^2) (1-x) \end{aligned} \quad (5.23)$$

where

$$\begin{aligned} \eta_1(s) &= \eta_{10} - \eta_{11} \cdot s \\ \eta_2(s) &= \eta_{20} + \eta_{21} \cdot s \end{aligned} \quad (5.24)$$

satisfies these moment equations to high order. The parameter  $c_d$  was fixed by quark counting rules for the proton:  $\int_0^1 dx u_v(x, Q^2)/x = 2 \int_0^1 dx d_v(x, Q^2)/x$ . However, the overall normalization,  $a_v$ , was retained as a free parameter, rather than using the constraint of the GLS sum rule.

The anti-quark and gluon distributions should be peaked at small  $x$ ; hence,  $\bar{q}(x, Q^2)$  or  $G(x, Q^2)$  are well determined from the first two moments alone. A suitable choice was:

$$\begin{aligned} 2\bar{q}(x, Q^2) &= S(x, Q^2) = a_S(s) (1-x)^{\eta_S(s)} \\ G(x, Q^2) &= a_G(s) (1-x)^{\eta_G(s)} \end{aligned} \quad (5.25)$$

It can easily be seen that:

$$\begin{aligned} \eta_S(s) &= \frac{\langle S(Q^2) \rangle_2}{\langle S(Q^2) \rangle_3} - 2 \\ a_S(s) &= \langle S(Q^2) \rangle_2 (1 + \eta_S(s)) \end{aligned} \quad (5.26)$$

and likewise for the gluon parameters. The equations describing the evolution of these moments are more complicated than those for the valence quarks (5.21), but are determined by asymptotic QCD (see [Bu78] for details). Thus, the parameters required to determine this segment of the

model were the second and third moments of the anti-quark and gluon distributions at  $Q_0^2$ . The second moment of the gluons was fixed by the momentum sum rule:  $\int_0^1 F_2(x, Q^2) dx = 1 - \int_0^1 G(x, Q^2) dx$ . A reasonable choice for the gluon  $x$  dependence was  $\eta_G(0) = 5$ , which fixed the third gluon moment. The moments of the anti-quark distributions were free parameters.

Best values for the eight free parameters of the model were obtained from fits to  $2xF_1(x, Q^2)$  and  $xF_3(x, Q^2)$  extracted from our data. The structure functions were expressed in terms of quark distributions as follows:

$$\begin{aligned} xF_3(x, Q^2) &= u_v(x, Q^2) + d_v(x, Q^2) \\ 2xF_1(x, Q^2) &= \left( \frac{1 + Q^2/\nu^2}{1 + R(x, Q^2)} \right) F_2(x, Q^2) \\ &= xF_3(x, Q^2) + S(x, Q^2) \end{aligned} \quad (5.27)$$

The best values for the free parameters, under various assumptions about  $R(x, Q^2)$ , are shown in table 5.2. A  $Q_0^2 = 12.6\text{GeV}^2$  was used for all fits.

Parameter	$R = 0.1$	$R = 0.0$	$R_{QCD}$
$\Lambda$ (MeV)	210	202	247
$a_v$	1.752	1.838	1.702
$\eta_{10}$	0.413	0.438	0.408
$\eta_{11}$	0.188	0.151	0.216
$\eta_{20}$	2.333	2.285	2.225
$\eta_{21}$	1.707	1.849	1.742
$a_S(0)$	1.141	1.214	1.091
$\eta_S(0)$	6.991	6.267	6.300

Table 5.2 Parameters used in model for quark distributions

The fraction of the anti-quark distribution represented by strange quarks can be determined from events with two opposite sign muons in the final state. A charmed quark produced at the initial weak interaction vertex results in a charmed particle in the hadron shower. Such a short-lived object decays before interacting. Occasionally the decay is through a semi-leptonic channel, yielding a second muon. Due to weak selection rules, this muon would have the opposite electric charge to that from the neutrino vertex. The cross sections for such events are:

$$\begin{aligned} \frac{d\sigma^{\nu \rightarrow \mu^+ \mu^-}}{dxdy} &= \frac{G^2 ME}{\pi} B_c t_c \{ (u(\xi) + d(\xi)) \sin^2 \theta_c + 2s(\xi) \cos^2 \theta_c \} \\ \frac{d\sigma^{\bar{\nu} \rightarrow \mu^+ \mu^-}}{dxdy} &= \frac{G^2 ME}{\pi} B_c t_c \{ (\bar{u}(\xi) + \bar{d}(\xi)) \sin^2 \theta_c + 2\bar{s}(\xi) \cos^2 \theta_c \} \end{aligned} \quad (5.28)$$

where  $B_c$  is the branching ratio of charm to the muon channel. The use of the scaling variable  $\xi = x + m_c^2/2MEy$  and the threshold factor  $t_c = 1 - m_c^2/2ME\xi$  properly accounts [Ge76a,Ge76b,Ba76a] for effects of a finite charm quark mass,  $m_c$ .

A useful parametrization of the strange sea quark fraction is:

$$\lambda_s = \frac{\int_0^1 dx (s(x) + \bar{s}(x))}{\int_0^1 dx (\bar{u}(x) + \bar{d}(x))} \quad (5.29)$$

If it is assumed that the  $x$  and  $Q^2$  variation of  $s(x, Q^2)$  is the same as  $\bar{q}(x, Q^2)$ , and that  $\bar{u}(x, Q^2) = \bar{d}(x, Q^2)$ , then one obtains:

$$\begin{aligned} s(x, Q^2) = \bar{s}(x, Q^2) &= \frac{\lambda_s}{2 + \lambda_s} \bar{q}(x, Q^2) \\ \bar{u}(x, Q^2) = \bar{d}(x, Q^2) &= \frac{1}{2 + \lambda_s} \bar{q}(x, Q^2) \end{aligned} \quad (5.30)$$

The validity of this description has been confirmed in detail from the observed properties of the dimuon sample. Taking  $u(x, Q^2)$  and  $d(x, Q^2)$  from charged current data, the parameter  $\lambda_s$  can be determined from the dimuon  $x$  distributions and event rates. Our data favoured  $\lambda_s = 0.50 \pm_{-0.18}^{+0.16}$ , as shown in figure 5.10 [Ws83]. CDHS has published a determination of this same

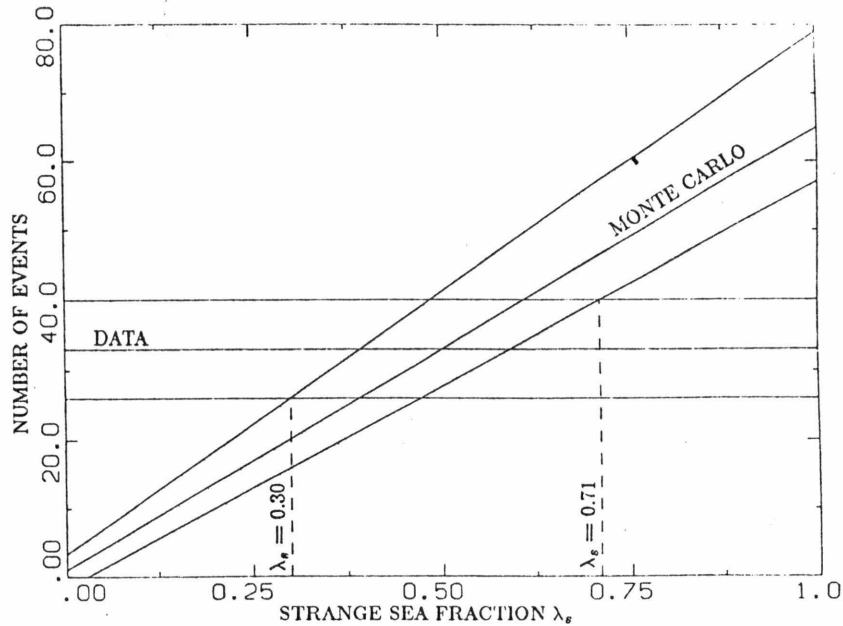


Figure 5.10 Strange sea fraction from observed number of anti-neutrino dimuon events

parameter from a high statistics sample of dimuon data obtained from wide-band neutrino and anti-neutrino running. The reported value [Ab82b] was  $\lambda_s = 0.52 \pm 0.09$ , but has substantial model dependence. Both results were obtained assuming the effective charm mass to be 1.5GeV. A 10% change in the mass was reported [Ab82b] to result in a corresponding 5% change in  $\lambda_s$ .

### 5.2.3 Quadrature technique

The beam monte carlo predicted the energy and spatial distribution of neutrinos per secondary at the Lab E detector. As has been noted above, with acceptance handled on an event-by-event basis, the integrals of flux over fiducial volume (equation 5.7) can be trivially accomplished. All neutrinos from two body decays of secondaries were included in the flux sum if:

$$\begin{aligned} \rho_\nu &= \sqrt{x_\nu^2 + y_\nu^2} \leq 30in \text{ for } \pi \rightarrow \mu\nu \\ |x_\nu| &\leq 50in \text{ and } |y_\nu| \leq 50in \text{ for } K \rightarrow \mu\nu \end{aligned}$$

Other sources of neutrino flux, representing a total of a few percent of the two body contribution, were also included: neutrinos from three body decays of kaons and wide-band background neutrinos. For these sources, the flux was first separated into that which would be classified as coming from pion or kaon decay in the event sample. The appropriate fiducial cuts were then applied, so that this flux was included only if:

$$\begin{aligned} E_\nu &< E_{SEP}(r) \text{ and } \rho_\nu \leq 30in \\ \text{or } E_\nu &> E_{SEP}(r) \text{ and } |x_\nu| \leq 50in \text{ and } |y_\nu| \leq 50in \end{aligned}$$

where  $E_{SEP}(r)$  was the same separation function used for the data (section 4.4.3). The result of this summation of flux over the fiducial volume was stored in an array of flux per secondary in 2GeV bins for each of the ten settings ( $\Phi_{\nu(\bar{\nu})}(E)$ ).

Integrals were performed by stepping through  $E_{\nu(\bar{\nu})}$  in these 2GeV bins. Within a bin, a 7 point Gaussian quadrature formula was used to integrate over  $x$ . The limits of the integration in  $\log Q^2$  were determined at each  $x$  value. If  $Q_j^2$  was the lower bin limit, then the lower and upper limits of integration were:

$$\begin{aligned} Q_{lower}^2 &= \max \left\{ \begin{array}{l} Q_j^2 \\ \frac{2MxE_H^{min}}{2E_{\nu(\bar{\nu})}^2(1 - \cos \theta_\mu^{max})} \\ \frac{1 + E_{\nu(\bar{\nu})}(1 - \cos \theta_\mu^{max})/Mx}{1} \end{array} \right. \\ Q_{upper}^2 &= \min \left\{ \begin{array}{l} Q_j^2 + \Delta Q_j^2 \\ 2Mx(E_{\nu(\bar{\nu})} - E_\mu^{min}) \end{array} \right. \end{aligned} \quad (5.31)$$

The integration in  $\log Q^2$  between these limits was accomplished using the 16 point Gaussian quadrature formula. Events with a vertex inside a radius of 5in of the apparatus centre were subject to a further  $\theta_\mu^{min}$  cut. The integration upper limit in this case was:

$$Q_{upper}^2 = \min \left\{ \begin{array}{l} Q_{upper}^2 \\ \frac{2E_\nu^2(\bar{\nu})(1 - \cos \theta_\mu^{min})}{1 + E_\nu(\bar{\nu})(1 - \cos \theta_\mu^{min})/Mx} \end{array} \right. \quad (5.32)$$

Halving the step sizes in any of these calculations had no effect on the result.

#### 5.2.4 Resolution smearing corrections

The effect of resolution smearing was calculated using an event generating monte carlo. Neutrino rays from the beam monte carlo, with the energy and spatial distribution of the dichromatic beam, were input to this program which simulated interactions in the detector. Events were thrown with the  $x$  and  $y$  distribution observed in the data. A more primitive model of the structure functions than that described in section 5.2.2 was used to parametrize the differential cross section for the event generator. The chosen form of the  $x$  dependence was similarly motivated by the need to separate the contributions of valence and sea quark distributions in the model. However, the  $Q^2$  variation was treated in a more empirical fashion, with:

$$f_i(x, Q^2) = f_i(x, Q^2 = 10) \{ (1 + \beta(x) \log(Q^2/10)) \} \quad (5.33)$$

The function,  $\beta(x) = \beta_1 - \beta_2 \sqrt{x}$ , was an *ad hoc* representation of the observed pattern of scaling violations. Such a form was better behaved as  $Q^2 \rightarrow 0$ , and therefore was more suitable for the monte carlo. The free parameters of the model were obtained from fits to our structure function results, as with the Buras-Gaemers type model. Figures 5.11 and 5.12 show observed  $x$  distribution for data obtained at the  $\pm 200$  settings, compared with the monte carlo prediction. The monte carlo can be seen to well represent the data.

Reconstructed quantities,  $E'_H$ ,  $E'_\mu$  and  $\theta'_\mu$ , were then thrown from the corresponding generated values, using the appropriate resolution functions. These were Gaussian distributions for  $E_\mu$  and  $\theta_\mu$ , with widths given by:

$$\begin{aligned} \sigma_{E_\mu} &= 0.11 \cdot E_\mu \\ \sigma_{\theta_\mu} &= \alpha + \frac{\beta}{E_\mu} \end{aligned}$$

where  $\alpha$  and  $\beta$  are given in table 4.3. The smeared  $E_H$  was thrown from a Poisson distribution, with:

$$\sigma_{E_H} = 0.72 + 0.81 \sqrt{E_H}$$

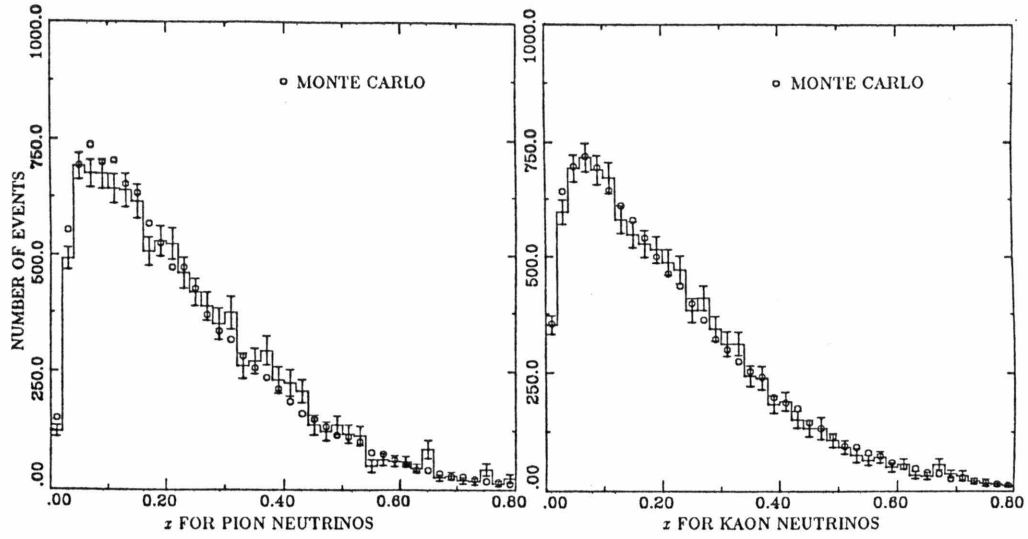


Figure 5.11 Observed and predicted  $x$  distributions at the +200 setting

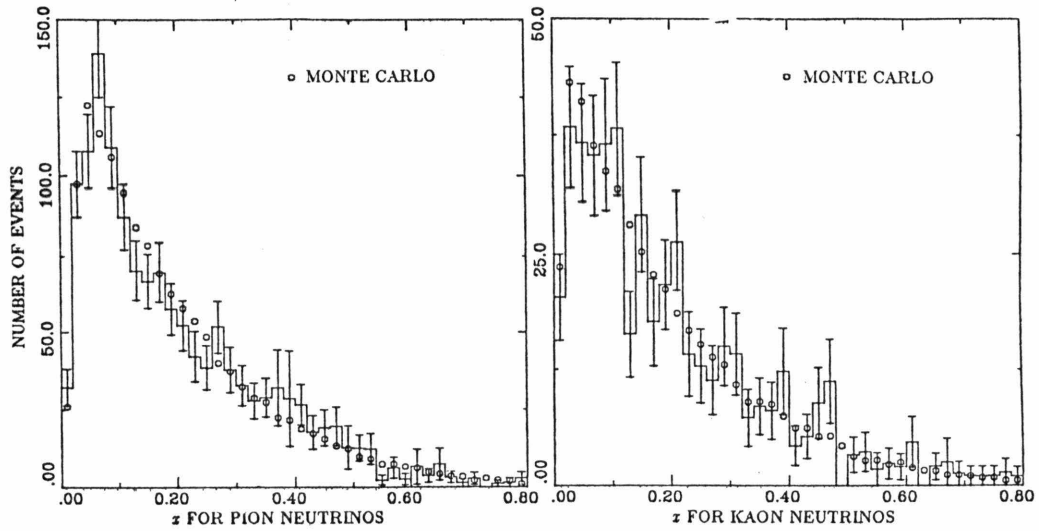


Figure 5.12 Observed and predicted  $x$  distributions at the -200 setting

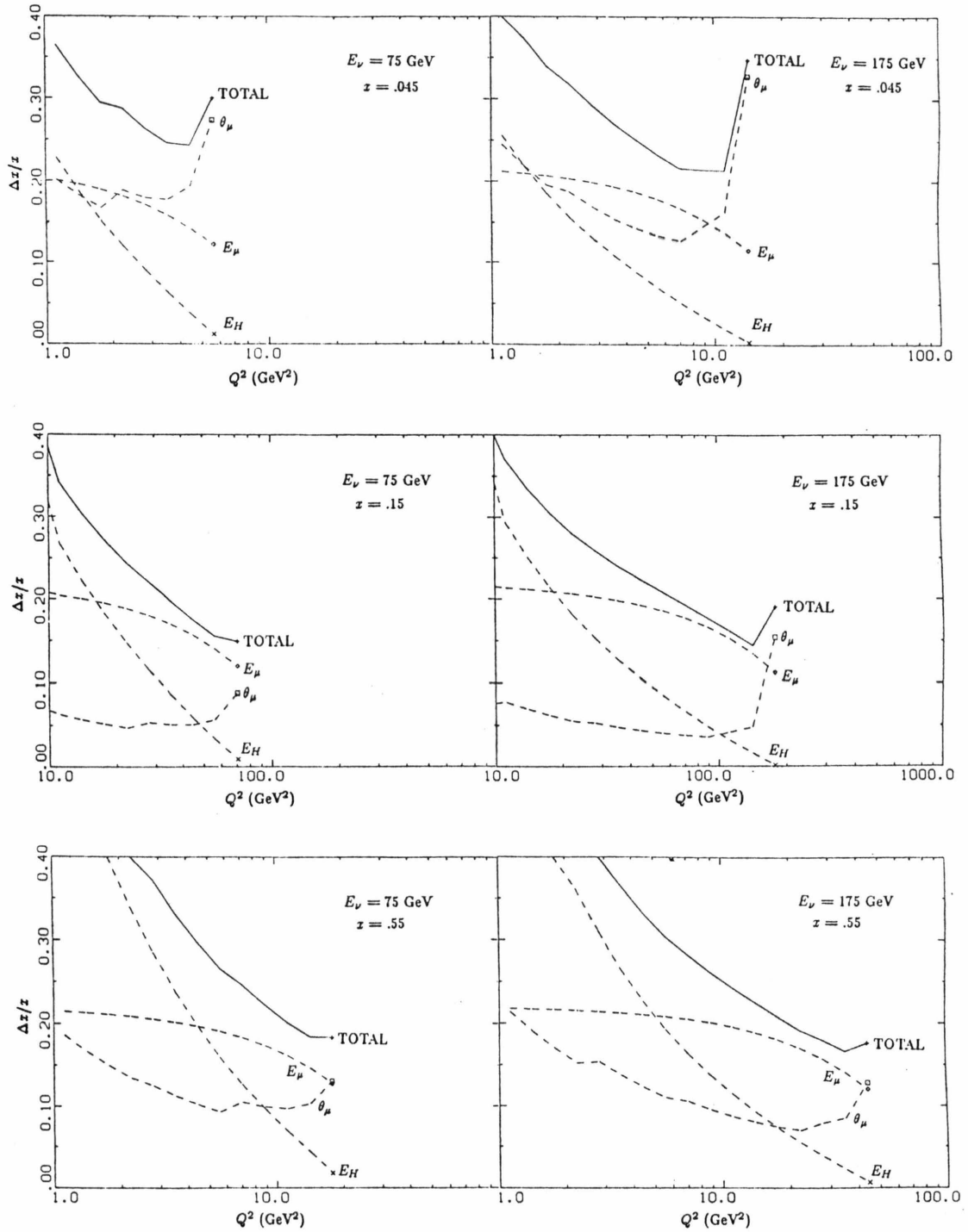


Figure 5.19 Resolutions in  $x$  for various  $x$  bins

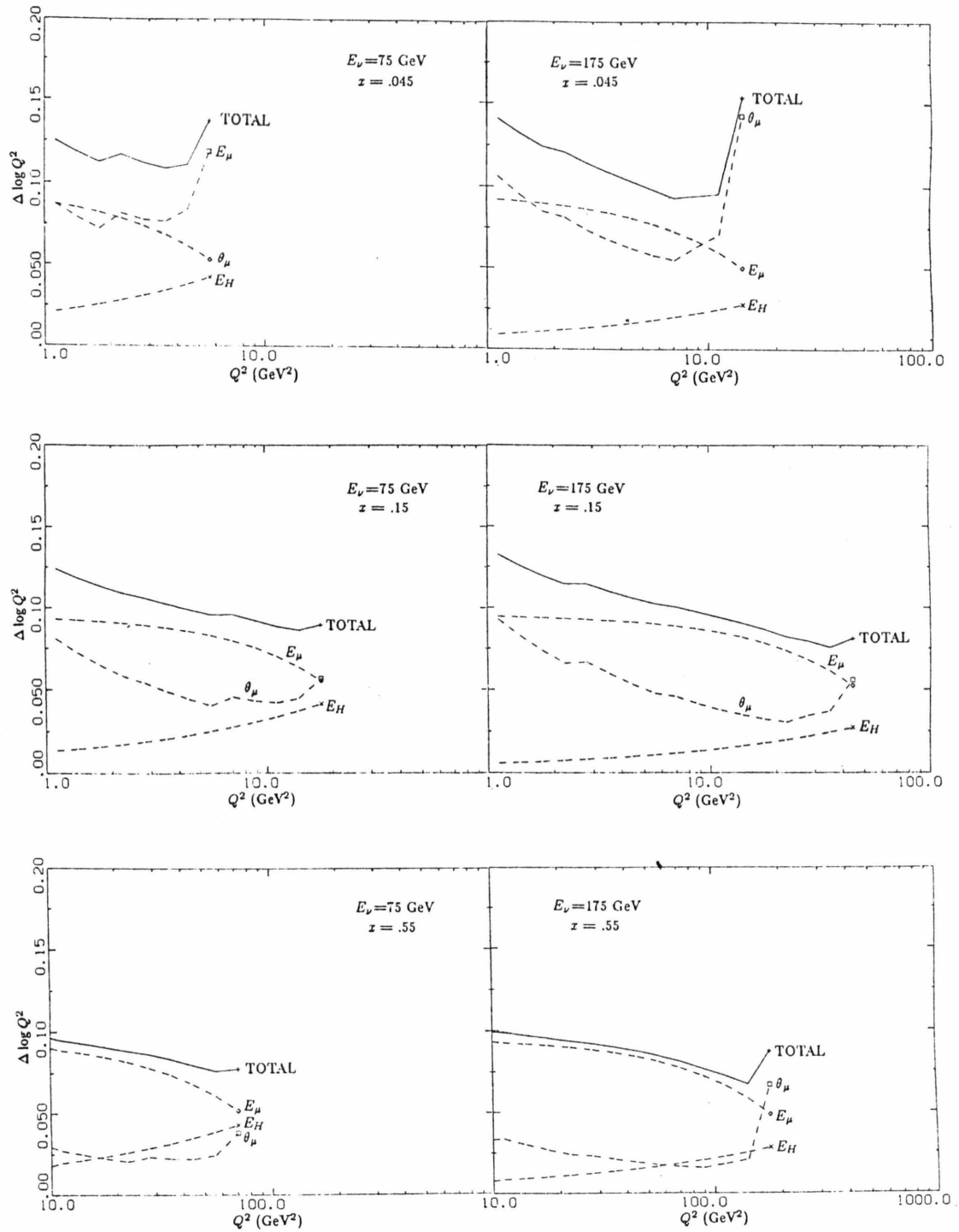


Figure 5.14 Resolutions in  $Q^2$  for various  $x$  bins

The resolution in  $x$  can readily be expressed in terms of errors on these measured quantities:

$$\left(\frac{\Delta x}{x}\right)^2 = (2-y)^2 \left(\frac{\Delta E_\mu}{E_\mu}\right)^2 + (1-y)^2 \left(\frac{\Delta E_H}{E_H}\right)^2 + 4 \left(\frac{\Delta \theta_\mu}{\theta_\mu}\right)^2 \quad (5.34)$$

At small  $x$  the error on  $\theta_\mu$  dominates the  $x$  resolution, while at large  $x$  the resolution is dominated by  $E_H$  at low  $Q^2$  and  $E_\mu$  at high  $Q^2$ . As illustrated in figure 5.13, in our detector  $x$  resolution varied from 15 to 30%, depending on  $x$  and neutrino energy. Except for the highest  $x$  bin, this was in general smaller than the bin size.

Similarly, the resolution in  $Q^2$  is given by:

$$\left(\frac{\Delta Q^2}{Q^2}\right)^2 = (2-y)^2 \left(\frac{\Delta E_\mu}{E_\mu}\right)^2 + y^2 \left(\frac{\Delta E_H}{E_H}\right)^2 + 4 \left(\frac{\Delta \theta_\mu}{\theta_\mu}\right)^2 \quad (5.35)$$

The important quantity for these considerations is  $\Delta \log Q^2$ , shown in figure 5.14. In almost all cases, the resolution was dominated by the measurement error on  $E_\mu$ . The chosen bin width in  $\log Q^2$  can be seen to be well matched to the measurement error on that quantity.

The probability distribution for deep-inelastic scatters of muons passing through the target iron was measured from the data (section 4.2.3). This distribution was used to simulate scatters within the hadron shower, which were appropriately added to  $E'_H$  and subtracted from  $E'_\mu$ , as they would be in the data. Beyond the shower, such energy losses were added back into  $E'_\mu$ , with the resolutions of a calorimetric measurement. A check was made to determine whether the muon would stop before reaching the trigger counter T2. Such events were given a fixed momentum resolution of 0.15 GeV, since momentum would be determined from range.

The observed number of events in a bin was corrected to a number without resolution smearing, by dividing by the ratio,  $R_s$ , of smeared ( $N$ ) to unsmeared ( $N'$ ) monte carlo generated events appearing in that bin. Since  $N' = N + n_{in} - n_{out}$ , the correction was just:

$$R_s = 1 - \frac{n_{out}}{N} + \frac{n_{in}}{N}$$

$$\Delta^2 R_s = \frac{1}{N} \left\{ \frac{n_{out}}{N} \left(1 - \frac{n_{out}}{N}\right) + \frac{n_{in}}{N} \left(1 + \frac{n_{in}}{N}\right) \right\} \quad (5.36)$$

where  $n_{in}$  and  $n_{out}$  are the number of events which move into and out of a bin due to smearing. In general, at least a factor of four more events are thrown at each setting than in our data set at that setting, so that  $\Delta R_s$  contributed negligibly to the final errors.

### 5.3 Flux Smoothing Procedure

As noted in section 5.1, the energy dependence of the total cross section for both neutrinos and anti-neutrinos was dominated by flux measurement systematics. The reported cross sections were consistent with the quark-parton prediction of a linear rise with energy,

but exhibited substantial fluctuation about this mean behavior, due to the magnitude of flux errors. A procedure was devised to smooth out much of this fluctuation.

If for the moment the effect of  $R$  is neglected, the structure functions  $F_2$  and  $xF_3$  extracted from any pair of neutrino and anti-neutrino secondary beam settings should be consistent, in the overlapping  $x$  and  $Q^2$  region, with the structure functions extracted from all the data. This implies that the differential cross sections constructed from the average structure functions must be consistent with the differential cross section measured at any given setting, again in the overlapping kinematic regions. The integral of this cross section, weighted by flux and within the kinematic and fiducial volume included in the structure function measurements, is just:

$$N_{\nu(\bar{\nu})}^{PRED} = \int_0^\infty dE \int_{x_{min}}^{x_{max}} dx \int_{Q_{min}^2}^{Q_{max}^2} d \log Q^2 \Phi_{\nu(\bar{\nu})}(E) \frac{d\sigma^{\nu(\bar{\nu})}}{dx d \log Q^2} \quad (5.37)$$

where  $N_{\nu(\bar{\nu})}^{PRED}$  is the predicted total number of events for the setting. The difference between  $N_{\nu(\bar{\nu})}^{PRED}$  and the observed number of events  $N_{\nu(\bar{\nu})}^{OBS}$  was presumed to originate in the flux errors: both errors on the determined secondary beam composition and run-by-run fluctuations in the ion chamber response. The ratio  $N_{\nu(\bar{\nu})}^{OBS} / N_{\nu(\bar{\nu})}^{PRED}$  was then used to adjust the flux on a setting-by-setting basis. The overall normalizations of the total cross sections were kept fixed at the reported values.

The resulting flux factors are shown in figure 5.15. The inner error bars reflect the statistical precision with which these smoothing factors could be calculated. The outer error

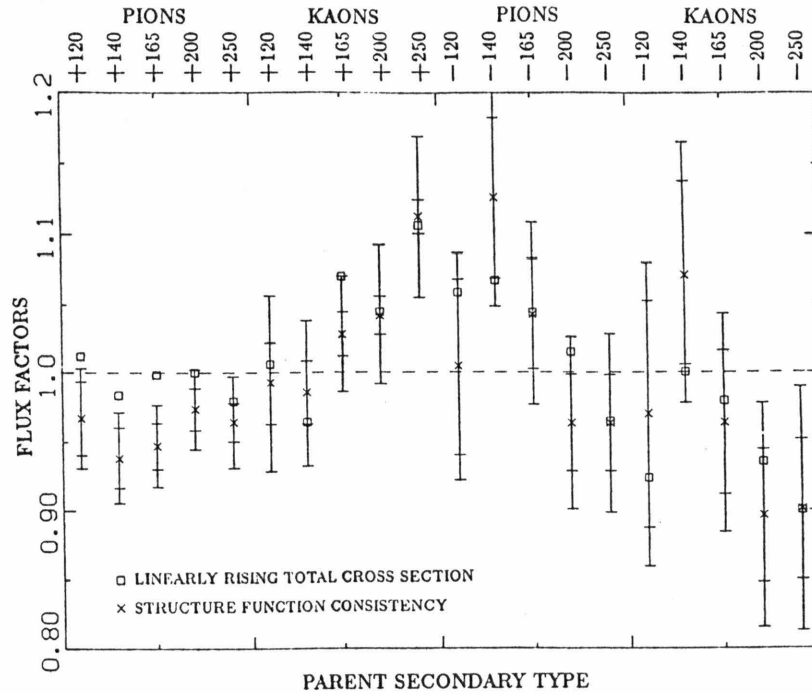


Figure 5.15 Flux smoothing factors for each setting and secondary parent type

bars include in quadrature the errors assigned to the pion and kaon Čerenkov pressure curve areas (1-2% for pions and 3-5% for kaons) and the ion chamber measurements. This last consisted for neutrinos of 2% for chamber response stability, and 1% for chamber temperature uncertainties. The corresponding numbers for anti-neutrinos were 5% and 1% respectively. Given these errors, the flux smoothing factors were consistent with unity:  $\chi^2=14.7$  for 10 degrees of freedom for neutrinos and 7.6 for 10 degrees of freedom for anti-neutrinos.

An important check of the validity of this smoothing procedure was the observed effect on the total cross section. In figures 5.16 and 5.17 are shown the 90% confidence limits for fits to the cross section slopes of the form:

$$\sigma^{\nu(\bar{\nu})}/E = \alpha + \beta \cdot E \quad (5.38)$$

For the case of our reported cross section measurements, all systematic errors were included in the calculation. For the flux smoothed case, the only errors included in addition to the statistical errors were the errors on the flux factors.

The reported cross section measurements were consistent with  $\beta = 0$ , as stated earlier (section 5.1), although the preferred value was for  $\sigma^\nu/E$  to rise with energy and  $\sigma^{\bar{\nu}}/E$  to fall. In contrast, the preferred value for the flux smoothed case lay close to the quark-parton model expectation of  $\beta = 0$ , and coincided very well with the QCD prediction. The dashed lines in figures 5.16 and 5.17 represent reasonable limits on a QCD prediction for the energy dependence of the cross section slopes. Uncertainties include the contribution of the integrated cross section below  $Q^2 = 1\text{GeV}^2$ , and assumptions about the behavior of  $R$ , particularly at low  $Q^2$ . The size of the 90% confidence ellipse was reduced, noticeably so in the neutrino case. This reflected the fact that the procedure at least partially reduced sensitivity to flux measurement systematics. However, the most important feature was the noted good agreement for the total cross section between expectation and observation.

The effect of a finite  $R$  on this smoothing procedure is to introduce an effective energy dependence into  $F_2$  extracted from different settings. This is a natural consequence of the variation of the mean neutrino energy with setting. However, the observed effect was quite small: flux smoothing factors calculated under different assumptions concerning  $R$  were the same within errors. The lack of sensitivity reflects the fact that  $R$  changes only the high  $y$  behavior of the cross section, whereas  $N_{\nu(\bar{\nu})}^{PRFD}$  was calculated by integrating over essentially all  $y$ .

As with other numerical calculations discussed in this chapter, this method required iteration. The starting values for the flux factors were taken to be unity. The corresponding structure functions were then used to calculate  $N_{\nu(\bar{\nu})}^{PRFD}$ , and hence the new flux factors. New structure functions were extracted, and the procedure repeated until convergence. However, most of the difference between unity and the final result was not dependent on the particular form of the underlying structure functions. In fact, if the  $Q^2$  dependence of the structure functions was removed, essentially the same smoothing factors would result. Again, this reflects the fact that  $N_{\nu(\bar{\nu})}^{PRFD}$  was an integral over all energies (or  $Q^2$ ), which averages out scale breaking effects. The difference in the predicted total cross section between scaling ( $\beta = 0$ ) and QCD is small.

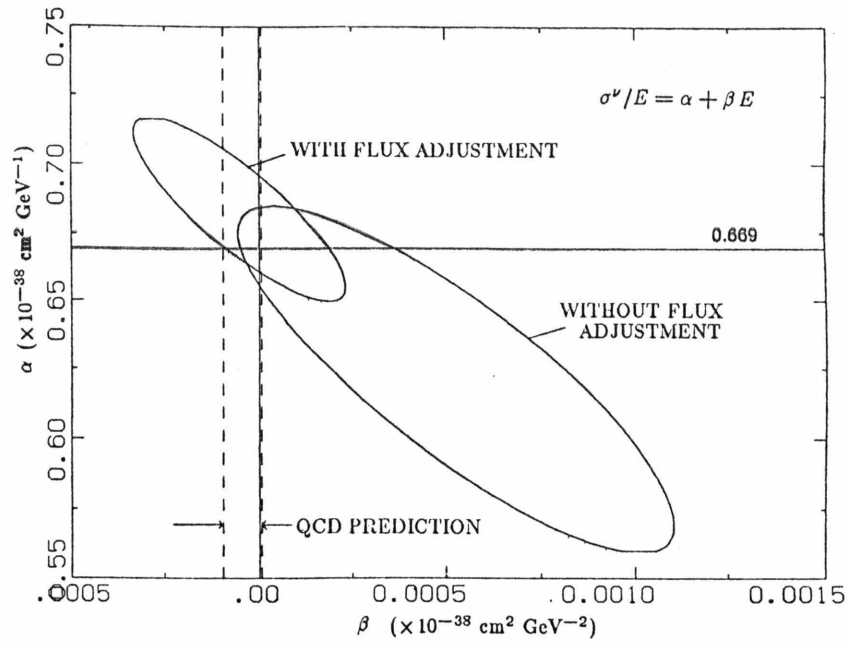


Figure 5.16 90% contour for fits to the neutrino total cross section slope

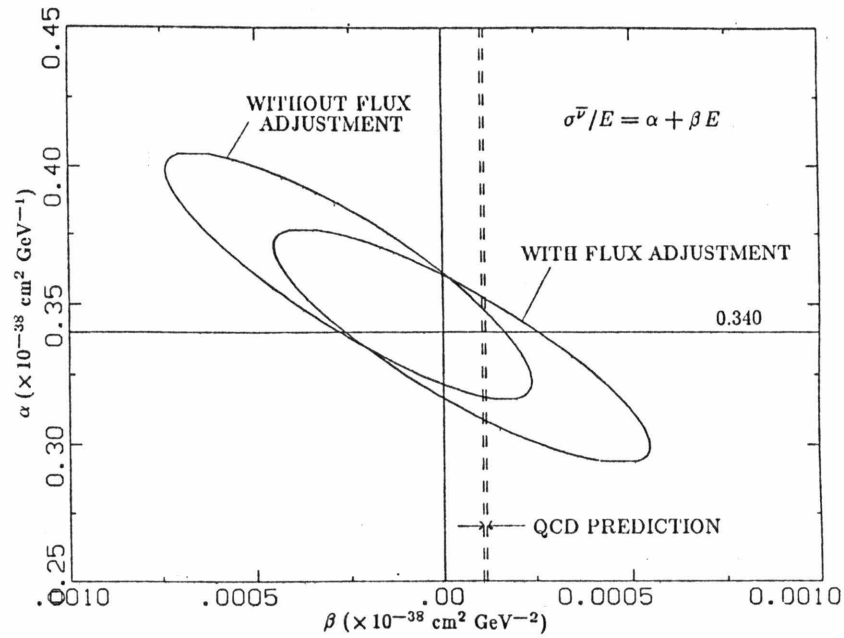


Figure 5.17 90% contour for fits to the anti-neutrino total cross section slope

An alternative approach to smoothing the total cross section might be to require a strict linear rise with energy. The flux factors necessary to achieve this end are designated as squares in figure 5.15. As expected, these points differ little from the factors derived above.

For a QCD analysis, an appropriate procedure would be to calculate the slight modification to the quark-parton prediction, and suitably adjust our measurements to match. However, the prediction relies on structure function measurements made over a restricted kinematic region. As a result, there is some uncertainty in the predicted total cross sections, becoming quite large at low energies. The chosen method did not suffer from this difficulty, as the integrations were carried out only over measured kinematic regions. Also, the method had the aesthetic appeal of using a consistency requirement, rather than a model prediction, to smooth the data.

## 5.4 Alternative Extraction Method

There are other approaches to obtaining structure functions from the data. A common method is to compare a monte carlo prediction for the number of events in a bin to the observed number. The structure functions assumed in the monte carlo are adjusted until a match with the data is achieved. Essentially, the monte carlo technique differs in that acceptance and resolution smearing are included in the calculation of predicted number of events. If smearing is corrected separately, the required integrations can be performed using standard numerical quadrature techniques. Details of the implementation of such an approach are described in the thesis of M.Purohit [Pu84], and so only an outline will be provided here.

As before, the starting point is the formal expression for the event density, equation 5.1. This can be integrated over the kinematic space,  $(E, x, \log Q^2)$  and fiducial volume,  $(r, \phi)$ , within the standard grid of  $x$  and  $\log Q^2$  bins. It can be shown from the form of the differential cross section (equation 5.10), that a linear system is obtained:

$$\begin{aligned} n_\nu &= a_\nu F_2(x, Q^2) + b_\nu x F_3(x, Q^2) + c_\nu \\ n_{\bar{\nu}} &= a_{\bar{\nu}} F_2(x, Q^2) + b_{\bar{\nu}} x F_3(x, Q^2) + c_{\bar{\nu}} \end{aligned} \quad (5.39)$$

where  $n_{\nu(\bar{\nu})}$  are the observed number of events in the bin,

$$\begin{aligned} a_{\nu(\bar{\nu})} &= k \int dE dx d \log Q^2 dr d\phi \varphi_{\nu(\bar{\nu})}(E, r) A(r, \theta, \phi) \frac{G^2 M E}{\pi} y^\pm \\ b_{\nu(\bar{\nu})} &= \pm k \int dE dx d \log Q^2 dr d\phi \varphi_{\nu(\bar{\nu})}(E, r) A(r, \theta, \phi) \frac{G^2 M E}{\pi} y^\mp \end{aligned} \quad (5.40)$$

and  $c_{\nu(\bar{\nu})}$  are integrals over the various correction terms  $I^{\nu(\bar{\nu})}$ ,  $S^{\nu(\bar{\nu})}$ ,  $R^{\nu(\bar{\nu})}$  and the like.  $F_2$  and  $x F_3$  are then found by solving this system. The effect of resolution smearing was removed by adjusting  $n_{\nu(\bar{\nu})}$ , using the same event monte carlo described in section 5.2.4 above. To summarize, this method differed in the treatment of acceptance and in the inclusion of corrections

additively rather than multiplicatively. Programming was of course quite separate. In theory, this second approach should yield structure functions with minimum possible statistical errors, although the actual improvement over the weighted event method was less than 10%.

### 5.5 Results for $F_2$ and $xF_3$ with Fixed $R$

Structure functions were extracted under three different assumptions about  $R$ . These were:  $R = 0.0$ ,  $R = 0.1$  and a so-called  $R_{QCD}$ . A brief explanation of the later is in order; for details, the reader is referred to sections 6.4 and 6.5.5.

QCD beyond leading order predicts [Fi78] a finite value for  $R$  (equation 6.17), proportional to the strong coupling constant  $\alpha_S(Q^2)$  (equation 6.13). The value can be calculated using results for  $F_2$  and assumptions about the gluon distribution. A simple model of the  $x$  and  $Q^2$  dependence of the predicted  $R$  was needed for the purposes of extracting structure functions. The  $x$  dependence of the prediction was fit at  $Q^2 = 10\text{GeV}^2$  to the form:  $a(1-x)^b$ . Neglecting contributions due to scaling violations in  $F_2$  or the gluon distribution, all of the  $Q^2$  dependence of  $R$  comes from the variation of  $\alpha_S(Q^2)$ . Therefore, the value of  $R$  at any other  $Q^2$  was obtained by:

$$R_{QCD} = a(1-x)^b \frac{\alpha_S(Q^2)}{\alpha_S(Q^2 = 10)} \quad (5.41)$$

Using the parameters for  $F_2$  and the gluon distribution listed in table 6.1 for the second order fit, a calculation of  $R$  from QCD was made. A fit to this prediction at  $Q^2 = 10\text{GeV}^2$  yielded the result:  $a = 0.14$  and  $b = 3.7$ .

The final structure function results shown in table 5.3 and 5.4 represent bin-by-bin weighted averages of the values obtained using the two extraction techniques. The value of  $F_2$  in table 5.3 was obtained using  $R_{QCD}$ . The last three columns of the table represent the absolute change in the result if the strange sea were assumed SU(3) symmetric, or if  $R = 0.0$  or  $R = 0.1$  were assumed. A W-boson mass of 80GeV was assumed in extracting the structure functions results listed in the tables. Note that bins have been eliminated from the analysis if fractional statistical error exceeded 50%, or if the smearing correction was greater than 35%.

The differences between the results obtained by the two methods were in general small, except in bins with large statistical error: the average integral over  $x$  of  $F_2$  and  $xF_3$  differed by 2% and 1% respectively. The large statistical errors on  $xF_3$  tended to exaggerate the level of the difference for this structure function. If all bins were included, the rms width of the ratio of structure functions obtained by one method to structure functions from the averaged data set was 3.0% for  $F_2$  and 8.0% for  $xF_3$ . However, if only bins with fractional statistical errors under 20% were included, the widths reduced to 2.5% and 3.0% respectively. The differences were probably statistical in origin. Fluctuations in the number of weighted versus unweighted events in a bin leads to large variations in the resulting structure functions in the case of small numbers of events. No systematic problem was thought to exist.

There was a tendency for the value of  $F_2$  in the highest  $Q^2$  bins to appear below the level anticipated from a linear extrapolation in  $\log Q^2$  from results in lower  $Q^2$  bins.

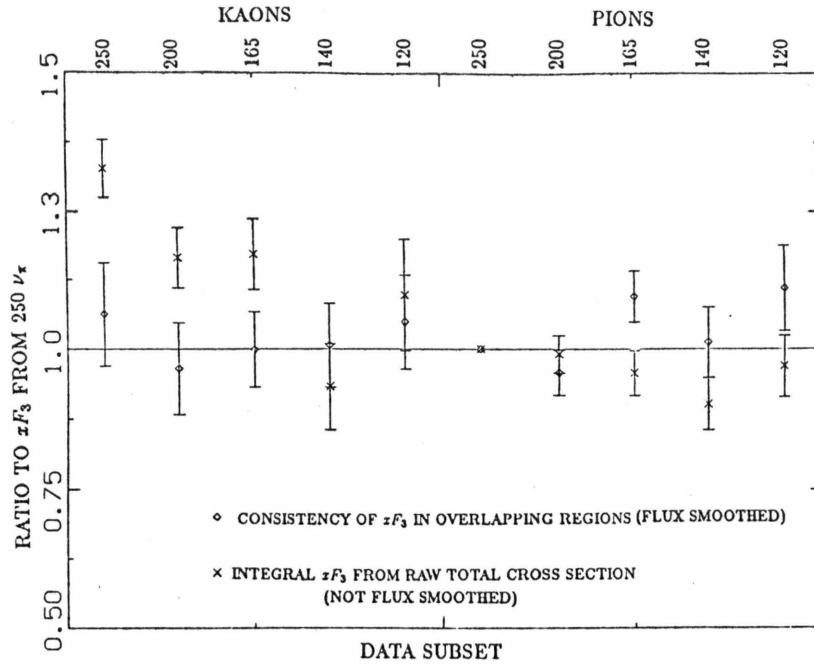


Figure 5.18 Comparison of  $xF_3$  normalization with and without flux smoothing

Possibly, this could represent an inefficiency for events with  $E_\mu < 15\text{GeV}$  and large hadron energy. However, a scan of a subset of these events revealed no evidence for such a problem.

The most direct test of the validity of the implementation of equation 5.15 was to run monte carlo events through the analysis. When this was done, it was found that the reconstructed integrals over  $x$  of  $F_2$  and  $xF_3$ , averaged over  $Q^2$ , agreed at the 0.5% level with the predicted values. The hypothesis that the generator function fit the reconstructed structure functions was checked using the standard goodness-of-fit test: the calculated  $\chi^2$  was found to be acceptable.

A further proof of the efficacy of the flux smoothing procedure was found in the consistency of  $xF_3$  obtained from different independent subsets of the data. A comparison was made of results in overlapping  $x$  and  $Q^2$  regions for each of the five pairs of secondary beam settings and two parent types. The fluctuations relative to  $xF_3$  obtained from neutrinos from pion decay at the  $\pm 250$  settings are shown in figure 5.18. For comparison, the corresponding ratios of the integral of  $xF_3$ , as computed for each subset from the total cross section result, are also shown in the figure. Errors are statistical only. The flux-smoothed structure function results are clearly consistent with unity, and exhibit less fluctuation than if raw fluxes were used. The large excursions from unity of the raw flux calculation reflect the significant nature of flux errors.

As shown in figures 6.1 and 6.2, qualitatively the  $Q^2$  dependence was consistent with QCD; namely, the structure functions rose at small  $x$  with  $Q^2$  and fell at large  $x$ . Quantitative statements on this and other features of the data which can be tested against theory are reserved for chapter 6.

$Q^2$	$x$	$F_2$	$\Delta_{stat}$	$\Delta_{sys}$	SU(3)	$R = 0.1$	$R = 0.0$
1.26	.015	1.287	.051	.021	.016	-.032	-.078
2.00		1.343	.059	.022	.000	-.034	-.091
3.16		1.537	.084	.024	-.019	-.036	-.109
5.01		1.402	.116	.023	-.035	-.030	-.109
7.94		1.584	.269	.026	-.058	-.031	-.148
1.26	.045	1.134	.050	.019	.027	-.001	-.015
2.00		1.359	.047	.022	.014	-.009	-.037
3.16		1.363	.044	.021	-.003	-.016	-.062
5.01		1.545	.059	.023	-.021	-.017	-.082
7.94		1.662	.081	.025	-.041	-.015	-.095
12.6		1.531	.113	.023	-.055	-.010	-.110
20.0	1.071	.197	.018	-.047	-.002	-.091	
1.26	.080	1.244	.128	.021	.035	-.001	-.002
2.00		1.445	.055	.024	.029	.002	-.009
3.16		1.487	.046	.023	.012	-.001	-.024
5.01		1.464	.044	.022	-.006	-.004	-.048
7.94		1.545	.051	.022	-.022	-.002	-.066
12.6		1.591	.068	.023	-.037	.002	-.070
20.0		1.576	.090	.023	-.052	.008	-.089
31.6		1.228	.166	.020	-.048	.014	-.085
2.00		.150	1.183	.109	.020	.026	.003
3.16	1.180		.036	.019	.019	.003	.001
5.01	1.280		.028	.020	.010	.003	-.009
7.94	1.235		.025	.018	-.003	.006	-.022
12.6	1.232		.028	.018	-.013	.010	-.032
20.0	1.292		.036	.019	-.021	.015	-.036
31.6	1.270		.046	.019	-.030	.021	-.044
50.1	1.161		.075	.019	-.032	.030	-.051
79.4	.889		.251	.016	-.025	.031	-.045
5.01	.250	1.026	.039	.020	.013	.002	.002
7.94		.985	.026	.019	.007	.004	-.002
12.6		.933	.024	.017	.000	.009	-.007
20.0		.923	.026	.017	-.005	.015	-.012

$Q^2$	$x$	$F_2$	$\Delta_{stat}$	$\Delta_{sys}$	SU(3)	$R = 0.1$	$R = 0.0$
31.6	.250	.952	.033	.018	-.009	.018	-.014
50.1		.840	.034	.016	-.012	.022	-.016
79.4		.747	.053	.015	-.013	.029	-.019
126.		.568	.279	.012	-.010	.027	-.017
7.94	.350	.676	.027	.019	.005	.001	.001
12.6		.649	.023	.017	.002	.004	-.001
20.0		.638	.024	.016	.000	.009	-.003
31.6		.627	.027	.016	-.002	.012	-.004
50.1		.587	.028	.016	-.003	.014	-.004
79.4		.597	.037	.015	-.005	.022	-.007
126.		.684	.076	.018	-.006	.034	-.010
7.94	.450	.498	.041	.019	.003	-.001	.001
12.6		.419	.020	.017	.001	.001	.000
20.0		.395	.019	.015	.001	.004	.000
31.6		.382	.020	.014	.000	.007	-.001
50.1		.347	.021	.013	-.001	.007	-.001
79.4		.375	.026	.014	-.001	.011	-.002
126.		.279	.028	.010	-.001	.013	-.002
200.		.290	.132	.010	-.001	.018	-.002
12.6	.550	.241	.017	.014	.001	.000	.000
20.0		.231	.016	.013	.000	.002	.000
31.6		.206	.014	.011	.000	.003	.000
50.1		.198	.018	.011	.000	.004	.000
79.4		.199	.020	.011	.000	.005	.000
126.		.150	.019	.008	.000	.006	.000
200.		.120	.040	.006	.000	.007	.000
12.6	.650	.150	.018	.013	.000	.000	.000
20.0		.120	.010	.011	.000	.001	.000
31.6		.138	.015	.012	.000	.001	.000
50.1		.111	.015	.010	.000	.002	.000
79.4		.098	.016	.008	.000	.002	.000
126.		.092	.014	.007	.000	.003	.000
200.		.068	.020	.005	.000	.003	.000

Table 5.9

Averaged  $F_2$  obtained under various assumptions about  $R$  and the strange sea (Propagator included with  $m_W = 80\text{GeV}$ ). Systematic errors are diagonal elements only and do not include an overall scale error of 3.1%.

$Q^2$	$x$	$xF_3$	$\Delta_{stat}$	$\Delta_{sys}$
1.26	.015	.165	.058	.012
2.00		.366	.056	.021
3.16		.303	.076	.017
5.01		.431	.106	.025
1.26	.045	.440	.143	.055
2.00		.620	.089	.049
3.16		.608	.062	.032
5.01		.508	.072	.023
7.94		.693	.094	.033
12.6		.646	.116	.028
20.0		.631	.182	.026
2.00		.080	.615	.182
3.16	.769		.103	.054
5.01	.666		.070	.031
7.94	.655		.069	.025
12.6	.781		.085	.031
20.0	.771		.098	.028
31.6	.662		.162	.022
3.16	.150		.732	.135
5.01		.689	.073	.043
7.94		.879	.046	.036
12.6		.855	.042	.027
20.0		.790	.049	.024
31.6		.847	.055	.025
50.1		.799	.080	.021
79.4		.704	.239	.018
5.01	.250	.623	.161	.052
7.94		.794	.076	.045
12.6		.797	.048	.029
20.0		.770	.042	.023
31.6		.799	.050	.023
50.1		.747	.042	.020
79.4		.650	.057	.016
7.94		.350	.584	.108
12.6	.553		.060	.027
20.0	.469		.047	.017
31.6	.512		.048	.017
50.1	.563		.041	.019
79.4	.500		.045	.014
126.	.266		.083	.007

$Q^2$	$x$	$xF_3$	$\Delta_{stat}$	$\Delta_{sys}$
12.6	.450	.452	.068	.029
20.0		.306	.043	.015
31.6		.319	.038	.014
50.1		.340	.036	.015
79.4		.317	.037	.013
126.		.303	.032	.011
200.		.302	.139	.011
12.6		.550	.218	.071
20.0	.168		.044	.012
31.6	.209		.029	.013
50.1	.171		.033	.011
79.4	.169		.031	.010
126.	.170		.024	.009
200.	.130		.044	.007
12.6	.650		.163	.080
20.0		.171	.033	.018
31.6		.122	.039	.012
50.1		.072	.030	.007
79.4		.058	.028	.005
126.		.099	.018	.003
200.		.076	.023	.006

Table 5.4

Averaged  $xF_3$  obtained assuming  $R_{QCD}$  (Propagator included with  $m_W = 80\text{GeV}$ ). Systematic errors are diagonal elements only and do not include an overall scale error of 3.1%.

## 5.6 Systematic Errors

There were a number of sources of systematic errors on the structure functions. These included: (1) errors on flux measurements, (2) systematic uncertainties in  $E_H$  and  $E_\mu$ , (3) differences between the results of the two extraction techniques, and (4) errors on smearing corrections. Shown in table 5.3 and 5.4 are the diagonal elements of the systematic error matrix. These are useful only in illustrating the relative level of systematic and statistical errors. For all bins, the latter exceeded the former. Global fits, such as those for QCD, were made with proper point-to-point correlations.

Consider the flux uncertainties first. Much of the error contributing to setting-to-setting fluctuations was removed using the procedure described in section 5.3 above. The residual error, reflecting the total number of events at each setting, represented the precision with which the flux adjustments could be made. In addition, there were correlated and

Source	$\nu$ flux error (%)	$\bar{\nu}$ flux error (%)	Common flux error (%)
Ion chamber calibration			1.5
Calibration connection to data			2.0
Veto deadtime			0.5
$\chi^2$ correction			0.5
Livetime			1.7
Neutrino energy			1.0
Ion chamber temperature	1.0	1.0	
Proton fraction	1.0		
$(\nu/\bar{\nu})$ ion chamber connection		3.0	
Total	1.4	3.2	3.1

Table 5.5 Sources of overall flux error

uncorrelated overall errors for neutrinos and anti-neutrinos. The sources of these scale errors have been discussed at various points in the text, but are collected here for convenience in table 5.5. The total uncorrelated error on flux was 1.4% for neutrinos and 3.2% for anti-neutrinos. The shape of the extracted structure functions was directly affected by these uncertainties in the relative neutrino to anti-neutrino normalization. The total correlated scale error of 3.1% was of significance for the quark model tests.

The method used to study contributions of these flux errors to errors on the structure functions was typical of all our studies of systematic errors. The simplest representation of the expression for extraction of structure functions (equation 5.15) is in each  $x$  and  $Q^2$  bin:

$$f_i(x, Q^2) = \left\{ \frac{\frac{n_\nu^{OBS}}{\int \Phi_\nu} \pm \frac{n_{\bar{\nu}}^{OBS}}{\int \Phi_{\bar{\nu}}}}{\frac{n_\nu^{PRED}}{\int \Phi_\nu} \pm \frac{n_{\bar{\nu}}^{PRED}}{\int \Phi_{\bar{\nu}}}} \right\} f_i(x, Q^2) \quad (5.42)$$

where  $f_i(x, Q^2)$  corresponds to  $F_2(x, Q^2)$  and  $xF_3(x, Q^2)$  respectively. Since the level of systematic error was small compared with statistical errors, it would be difficult to separate the effect of the two sources if examined in combination. It was more appropriate to consider the effect of systematic errors on an infinite statistics sample.

Equivalent to this,  $n_{\nu(\bar{\nu})}^{PRED}$  could be used in both the numerator and denominator of equation 5.42. This trivially yields  $f_i(x, Q^2)$  unless sources of systematic error are appropriately added. For the study of flux errors, the variant used was:

$$f_i(x, Q^2) = \left\{ \frac{\frac{n_\nu^{OBS}}{f_\nu \int \Phi_\nu} \pm \frac{n_{\bar{\nu}}^{OBS}}{f_{\bar{\nu}} \int \Phi_{\bar{\nu}}}}{\frac{n_\nu^{PRED}}{\int \Phi_\nu} \pm \frac{n_{\bar{\nu}}^{PRED}}{\int \Phi_{\bar{\nu}}}} \right\} f_i(x, Q^2) \quad (5.43)$$

An ensemble of twenty experiments was constructed by calculating structure functions with factors  $f_\nu$  and  $f_{\bar{\nu}}$  randomly thrown from Gaussian distributions with mean unity, and sigmas corresponding to the noted systematic flux errors. Thus, for the overall level errors,  $f_\nu$  and  $f_{\bar{\nu}}$  were obtained from distributions with sigmas of 1.6% and 3.2% respectively. For the errors on the flux factors, uncorrelated values for  $f_\nu$  or  $f_{\bar{\nu}}$  were thrown for each setting, with the widths matching respective errors. The sigma in each bin of the distribution of structure function values for the ensemble of experiments was taken as the diagonal element of the error matrix. Typically, these errors were small for  $F_2$ , but varied from 5-7% for  $xF_3$  in the lowest  $Q^2$  bin to 1-2% in the highest  $Q^2$  bin at each  $x$  value. Clearly, the error contributed to each of the parameters of a global fit could be determined from the width of the distribution of parameter values from fits to the ensemble of experiments. This would properly account for correlations among errors.

This method was easily adapted to study the error introduced by beam dispersion. The quantities  $n_{\nu(\bar{\nu})}^{PRED}$  in the numerator of equation 5.42 were calculated not with the nominal beam dispersions, but with all dispersions increased by one standard deviation. From a comparison of monte carlo prediction with measurement, the dispersion error appeared to be well correlated from setting to setting. Given this observation, there was no need to generate an ensemble of experiments in order to study the problem. Typically the contribution of this source of error was a few percent for bins containing events from pion decay neutrinos. For bins consisting mostly of neutrinos from kaon decay the contribution was negligible. If in fact the dispersion error was not correlated from setting-to-setting, studies showed that the error introduced was approximately random and less than 1%. The actual situation probably lies between these two extreme assumptions.

The analysis of systematic errors due to uncertainties in the calibration of muon (1.5%) and of hadron (0.5%) energies was similarly accomplished. Here, the quantities  $n_{\nu(\bar{\nu})}^{PRED}$  in the numerator were calculated with the cross section evaluated not at  $(x, y, Q^2)$ , but at  $(x', y', Q^{2'})$ . It is a simple matter to show that for  $E'_H = E_H(1 + \delta_H)$  and  $E'_\mu = E_\mu$ :

$$\begin{aligned} x' &= x \left( \frac{1 + \delta_H y}{1 + \delta_H} \right) \\ y' &= y \left( \frac{1 + \delta_H}{1 + \delta_H y} \right) \\ Q^{2'} &= Q^2 (1 + \delta_H y) \end{aligned} \tag{5.44}$$

and for  $E'_H = E_H$  and  $E'_\mu = E_\mu(1 + \delta_\mu)$ :

$$\begin{aligned} x' &= x(1 + \delta_\mu(1 - y))(1 + \delta_\mu) \\ y' &= \frac{y}{1 + \delta_\mu(1 - y)} \\ Q^{2'} &= Q^2(1 + \delta_\mu(1 - y))(1 + \delta_\mu) \end{aligned} \tag{5.45}$$

Again, all errors were considered correlated, so that an ensemble of experiments was not needed. It should be noted that systematic shifts of  $E_\mu$  effectively enter as the square of the deviation

at moderate to high  $y$ . In contrast, for  $E_H$  the effect is proportional to  $\delta_H$  and decreases to zero at high  $y$ . In both cases, the systematic uncertainty was magnified at large  $x$  by the  $(1-x)^{-1}$  behavior of  $df_i/dx$  over  $f_i$ . The calibration error on  $E_\mu$  resulted in systematic uncertainties as large as 8% in the highest  $x$  bins. In general, the error from  $E_H$  was considerably smaller.

A simple check was made of these calculations. From the mean value of  $y$  in each bin (see Appendix F), the shift in  $x$  and  $Q^2$  could be calculated. The ratio of the structure function at the bin centre to the value at this shifted position gave the systematic error due to  $E_H$  or  $E_\mu$ . This simple calculation agreed with the more elaborate technique.

The systematic errors on the smearing corrections were examined in a somewhat less than rigorous fashion. The parameters of the structure function model and the resolution functions of the event monte carlo were varied within reasonable limits. However, this was not an exhaustive study. The observed changes in the smearing corrections were smaller than the statistical precision with which corrections were calculated. This would imply that the systematic uncertainty in the smearing corrections was less than 10% of the statistical error in any bin. In the sense that the statistical errors on the smearing corrections were added in quadrature with those from the data, systematic uncertainties in the smearing corrections have been properly included.

## 5.7 Extraction of $R$

The method devised to simultaneously obtain  $2xF_1$ ,  $R$  and  $xF_3$  from the data was a two-step process. First, the differential cross section,  $d\sigma^{\nu(\bar{\nu})}/dxdy$ , was found in bins of  $x$ ,  $y$  and  $\nu = E_H$ . The method used was basically an extension of the approach described above for extraction of structure functions. The second step was a one or two parameter fit to the  $y$  dependence of these cross sections.

Analogous to the expression for extracting structure functions (equation 5.15), in each bin in  $(x, y, E_H)$  the relationship between observed events and the differential cross section (equation 5.9) can be rewritten as:

$$\frac{1}{E} \frac{d\sigma^{\nu(\bar{\nu})}}{dxdy} = \frac{\frac{1}{E} \frac{d\sigma^{\nu(\bar{\nu})}}{dxdy}}{\left\langle \frac{1}{E} \frac{d\sigma^{\nu(\bar{\nu})}}{dxdy} \Big|_{Iron} \right\rangle_{\nu(\bar{\nu})}} \frac{\sum w_i^{\nu(\bar{\nu})}}{k \int dE \int dx \int dy \Phi_{\nu(\bar{\nu})}(E)} \quad (5.46)$$

where integrations are implicitly within bin limits and kinematic cuts. On the right-hand side, the cross section in iron is  $d\sigma^{\nu(\bar{\nu})}/dxdy|_{Iron}$  (equation 5.16), and  $d\sigma^{\nu(\bar{\nu})}/dxdy$  is the bare isoscalar cross section (equation 5.17), evaluated with  $xF_3^\nu = xF_3^{\bar{\nu}} = q - \bar{q}$ . The necessary isoscalar, strange sea, charmed mass and radiative corrections to the differential cross section are thus accomplished. Within each bin the sum of neutrino and anti-neutrino cross sections is:

$$2xF_1(x, Q^2) \left\{ (1-y)(1+R(x, Q^2)) + \frac{y^2}{2} \right\} = \frac{\pi}{G^2 ME} \left\{ \frac{d\sigma^\nu}{dxdy} + \frac{d\sigma^{\bar{\nu}}}{dxdy} \right\} \quad (5.47)$$

Using:

$$\epsilon(y) = \frac{2(1-y)}{1+(1-y)^2} \quad (5.48)$$

this can be written as:

$$2xF_1(x, Q^2)\{1 + \epsilon(y)R(x, Q^2)\} = \frac{1}{1+(1-y)^2} \frac{2\pi}{G^2 ME} \left\{ \frac{d\sigma^\nu}{dx dy} + \frac{d\sigma^{\bar{\nu}}}{dx dy} \right\} \quad (5.49)$$

A two parameter linear fit for  $2xF_1$  and  $F_L = 2xF_1 \cdot R$  to the  $y$  distribution in each  $x$  and  $E_H$  bin can be converted into a measurement of  $2xF_1$  and  $R$ . Likewise,  $xF_3$  can be found by using:

$$xF_3(x, Q^2) = \frac{1}{1-(1-y)^2} \frac{2\pi}{G^2 ME} \left\{ \frac{d\sigma^\nu}{dx dy} - \frac{d\sigma^{\bar{\nu}}}{dx dy} \right\} \quad (5.50)$$

Examples of  $y$  distribution fits are shown in figure 5.19. To cover a large range in polarization  $\epsilon$ , and in particular to obtain points below  $\epsilon = 0.5$ , requires data at large  $y > 0.70$ . This limits the useful range in  $\nu = E_h$  over which results can be obtained without large systematic errors.

### 5.7.1 Results for $R = \sigma_L/\sigma_T$

In table 5.6 are recorded the values for  $2xF_1$ ,  $F_L$  and  $R$  obtained in the manner described. If the error on the sum of neutrino and anti-neutrino differential cross sections exceeded 50%, that bin was removed from the analysis. Bins in  $(x, \nu)$  were discarded if the minimum polarization was greater than 0.70, or if the number of available measurements in  $y$  fell below four. This ensured a reasonable range in  $\epsilon$  over which the two parameter fit was to be made. Comparison of these results with expectations and with the values assumed for  $R$  in section 5.5 will be made in section 6.5.5.

Note, that the form of the fit in  $y$  was optimal for extracting  $R$  and  $2xF_1$ . The error on  $F_2 = 2xF_1 + F_L$  could be reduced by reworking equation 5.47 in terms of  $F_2$  and  $R$ . However, the dependence on  $R$  would enter as a coefficient of a  $y^2$  term, requiring good measurements at even higher  $y$  values than the chosen technique.

Not listed are the values for  $xF_3$ , which can be found both by the method of section 5.2 and as in equation 5.50, independent of the assumption for  $R$ . The two techniques yield the same average value for  $xF_3$  within 1%, confirming the validity of the implementation of the  $R$  extraction code. Reconstruction of monte carlo data produces a value for  $R$  within errors of the generator value,  $R = 0.1$ .

One observation should be made with regard to the measurements obtained in the  $x = 0.15$  bin. Only when all settings were combined did the value rise to the reported large values. Separate results from different pairs of neutrino and anti-neutrino settings were more consistent with expectations. This was an indication that some setting-to-setting systematic errors were important, at least for this particular bin.

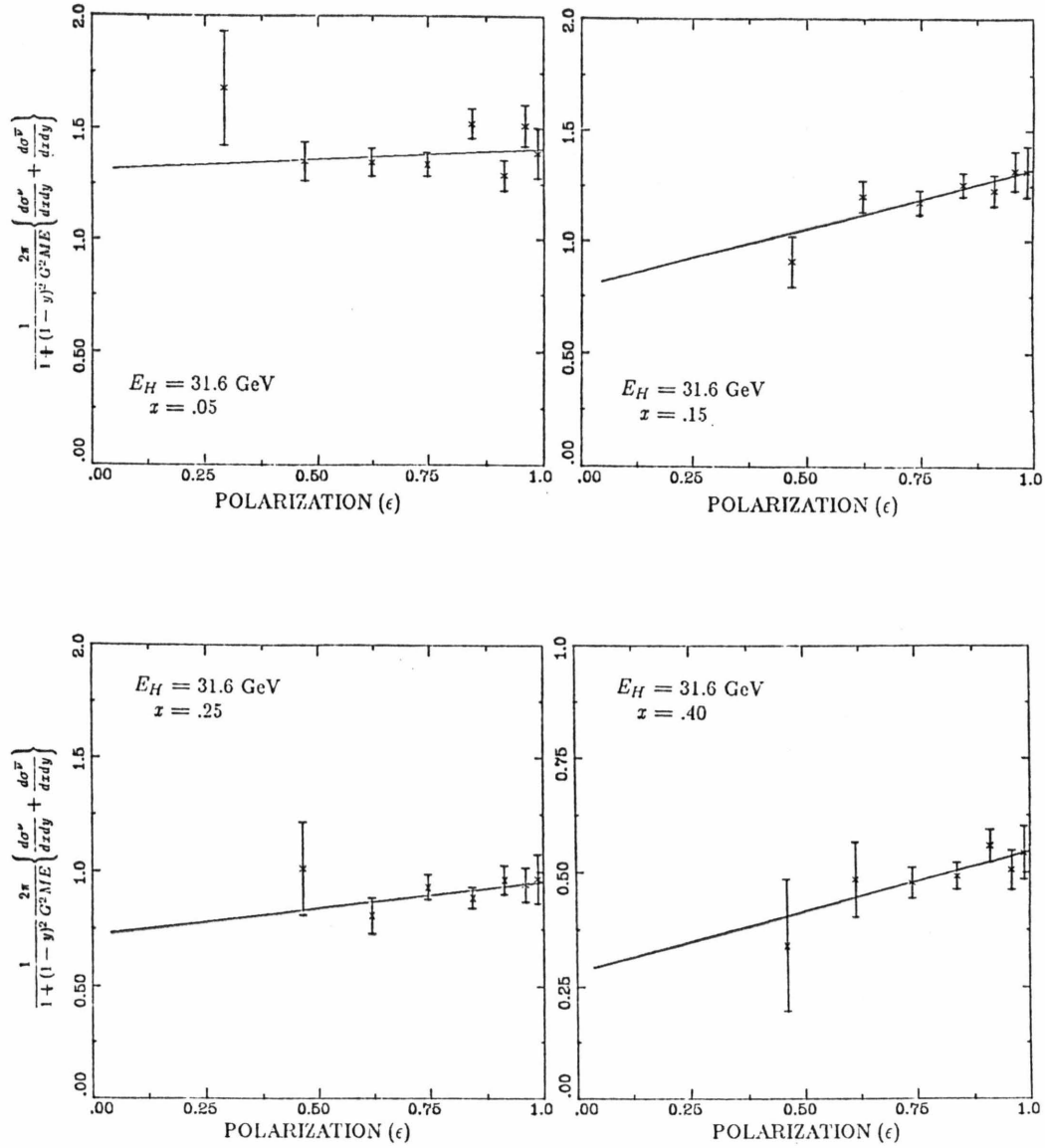


Figure 5.19 Examples of fits to the  $y$  variation of the sum of differential cross sections

$E_H$ (GeV)	$Q^2$ (GeV <sup>2</sup> )	$x$	$2xF_1$	$F_L$	$R$
20.0	1.88	.050	$1.078 \pm .275$	$0.157 \pm .413$	$0.145 \pm .322$
31.6	2.97		$1.314 \pm .133$	$0.096 \pm .215$	$0.073 \pm .136$
50.1	4.70		$1.014 \pm .086$	$0.259 \pm .156$	$0.255 \pm .149$
79.4	7.46		$1.479 \pm .111$	$0.026 \pm .203$	$0.018 \pm .116$
126.	11.8		$1.425 \pm .121$	$0.230 \pm .275$	$0.161 \pm .186$
20.0	5.63	.150	$0.676 \pm .363$	$0.600 \pm .542$	$0.887 \pm 1.069$
31.6	8.90		$0.788 \pm .161$	$0.535 \pm .256$	$0.678 \pm .389$
50.1	14.1		$0.968 \pm .117$	$0.363 \pm .201$	$0.375 \pm .212$
79.4	22.4		$0.911 \pm .143$	$0.616 \pm .260$	$0.676 \pm .341$
126.	35.5		$1.155 \pm .161$	$-0.055 \pm .336$	$-0.048 \pm .249$
20.0	9.39	.250	$0.876 \pm .387$	$0.133 \pm .574$	$0.152 \pm .550$
31.6	14.8		$0.721 \pm .186$	$0.234 \pm .186$	$0.324 \pm .394$
50.1	23.5		$0.754 \pm .151$	$0.191 \pm .151$	$0.253 \pm .305$
79.4	37.3		$0.930 \pm .176$	$-0.045 \pm .176$	$-0.048 \pm .248$
126.	59.1		$0.652 \pm .154$	$0.282 \pm .154$	$0.432 \pm .512$
31.6	23.7	.400	$0.282 \pm .134$	$0.264 \pm .134$	$0.934 \pm 1.001$
50.1	37.6		$0.517 \pm .103$	$-0.043 \pm .103$	$-0.084 \pm .233$
79.4	59.6		$0.335 \pm .094$	$0.147 \pm .094$	$0.439 \pm .497$
126.	94.6		$0.447 \pm .107$	$-0.025 \pm .107$	$-0.056 \pm .391$
50.1	56.4	.600	$0.175 \pm .091$	$-0.045 \pm .091$	$-0.260 \pm .472$
79.4	89.5		$0.056 \pm .080$	$0.123 \pm .080$	$2.187 \pm 4.991$
126.	142.		$0.097 \pm .036$	$0.009 \pm .036$	$0.094 \pm .601$

Table 5.6 Results for  $2xF_1$  and  $R$ 

Much of the emphasis in the analysis efforts described in this thesis has been confined to the extraction and study of structure functions under fixed assumptions about  $R$ . As a consequence, no studies of the systematic errors on these results for  $R$  and  $2xF_1$  have been undertaken as yet. This will presumably be accomplished by future graduate students, working with higher statistics samples of charged current events.

## Quark-Parton Model and QCD Results

The structure functions obtained by the methods detailed above are compared with both experimental and theoretical expectations in this final chapter. Much of the structure function effort was the work of this author and M.Purohit. The emphasis in the physics discussions included here is on our results for  $F_2$ . Corresponding and complementary analyses for  $xF_3$  are described in detail in the thesis of M.Purohit [Pu84]. Only salient features of these last discussions will be presented here in the interest of completeness.

### 6.1 Comparisons with Existing Neutrino Results

This is not the first experiment to extract structure functions from neutrino and anti-neutrino charged current data. The consistency of our measurements with published results will first be examined. Of particular interest are the high statistics data from the CDHS collaboration [Ab83]. These are reported for the same kinematic range as covered by this experiment, with comparable statistics. Other relevant results are from BEBC-Gargamelle [Bo78] and CHARM [Pa81] at CERN, and HPWFOR [He81] at Fermilab. All results from neutrino experiments discussed in this chapter have been appropriately adjusted where necessary for the effect of the W-Boson propagator.

The comparisons were made with a view to addressing three aspects of the results: (1) normalization, (2)  $x$  dependence of structure functions at fixed  $Q^2$ , and (3)  $Q^2$  dependence. To achieve this end, the various data sets were to be interpolated to common  $x$  and  $Q^2$  points. If necessary in  $x$ , this was accomplished by linearly interpolating the two nearest  $x$  bins to the required  $x$  value. The  $Q^2$  variation of these points was then fit to the form:

$$f_i(x, Q^2) = f_i^0(x) \{1 + \beta(x) \log(Q^2/10)\} \quad (6.1)$$

where  $f_i$  was either  $F_2$  or  $xF_3$ , and  $f_i^0(x)$  was the value of the structure function at  $Q^2 = 10\text{GeV}^2$ . The motivation for such a form is the expectation from QCD that scaling violations will be logarithmic in  $Q^2$ .

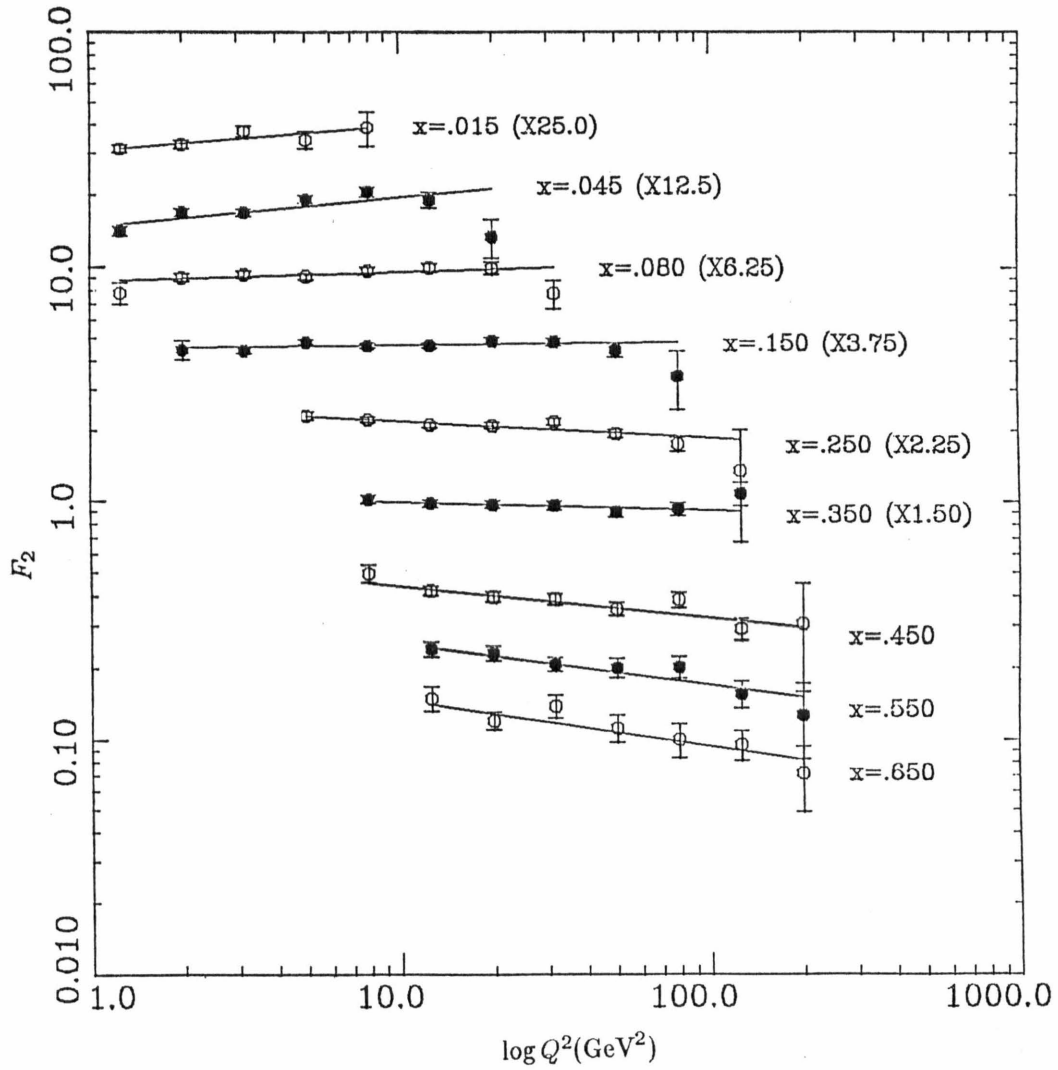


Figure 6.1  $F_2(x, Q^2)$  from this experiment (CCFR) with linear fits in  $\log Q^2$

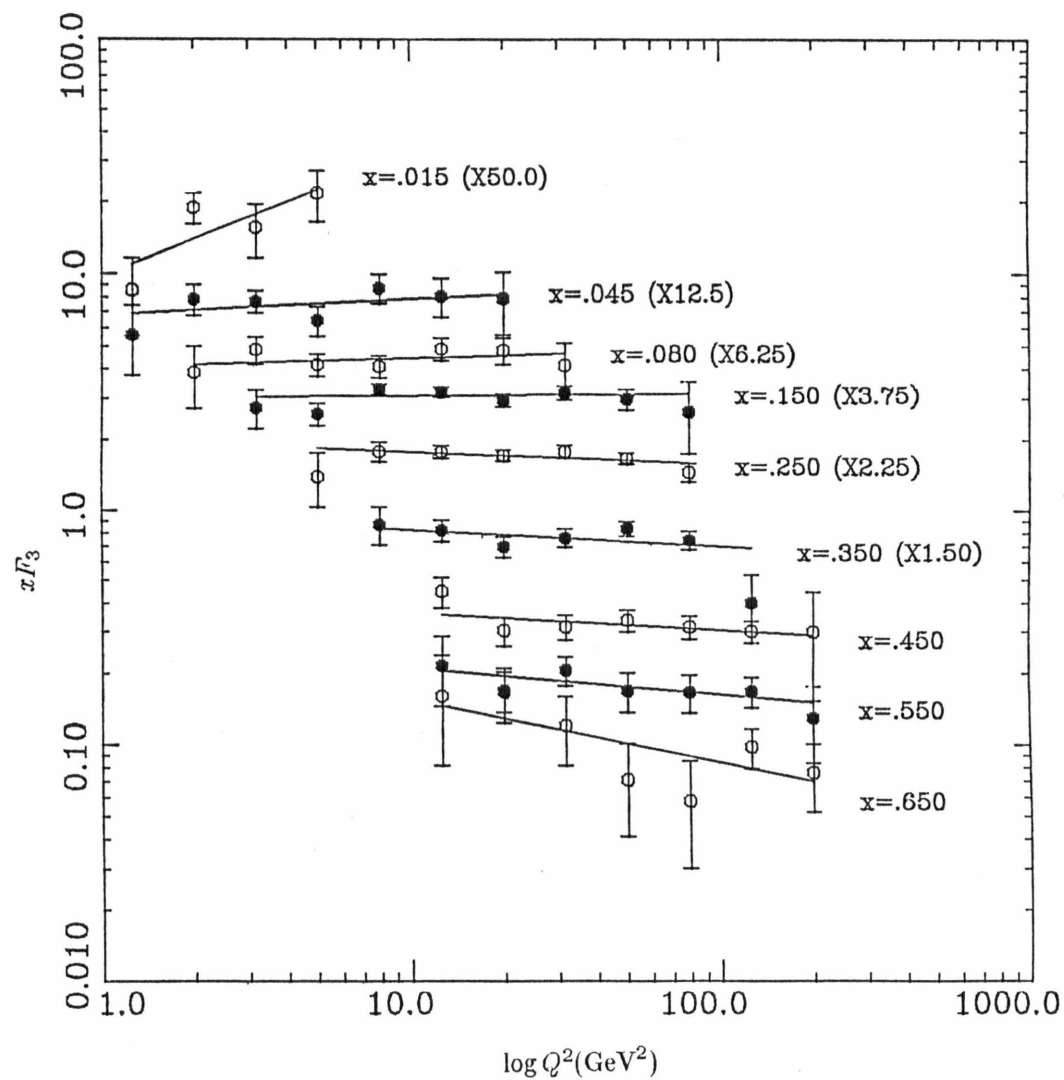


Figure 6.2  $xF_3(x, Q^2)$  from this experiment (CCFRR) with linear fits in  $\log Q^2$

Examples of fits to our data are shown in figures 6.1 and 6.2 for  $F_2$  and  $xF_3$  respectively. These illustrate the degree to which the data conforms to this functional form. It can be seen that for the most part the fitted value of the structure function at  $Q^2 = 10\text{GeV}^2$  represents an interpolation of the data, rather than an extrapolation, except in the lowest and highest  $x$  bins.

In figure 6.3 are shown the values of the parameter  $\beta$  obtained from fits to reported data without interpolation in  $x$ . The fits were limited in  $Q^2$  to the region above the lowest  $Q^2$  bin reported by this experiment. The  $Q^2$  behavior of data so eliminated could differ from that in the region of concern, due to the effect of higher-twist terms which decrease with inverse powers of  $Q^2$ , rather than logarithmically. Results from BEBC-GGM are not shown, as the statistical precision of this data in the overlap region was limited. The conclusion to be drawn from the figure is that the  $Q^2$  variation of the considered data sets is consistent, although at high  $x$  the scaling violations in the HPWFOR result are generally larger.

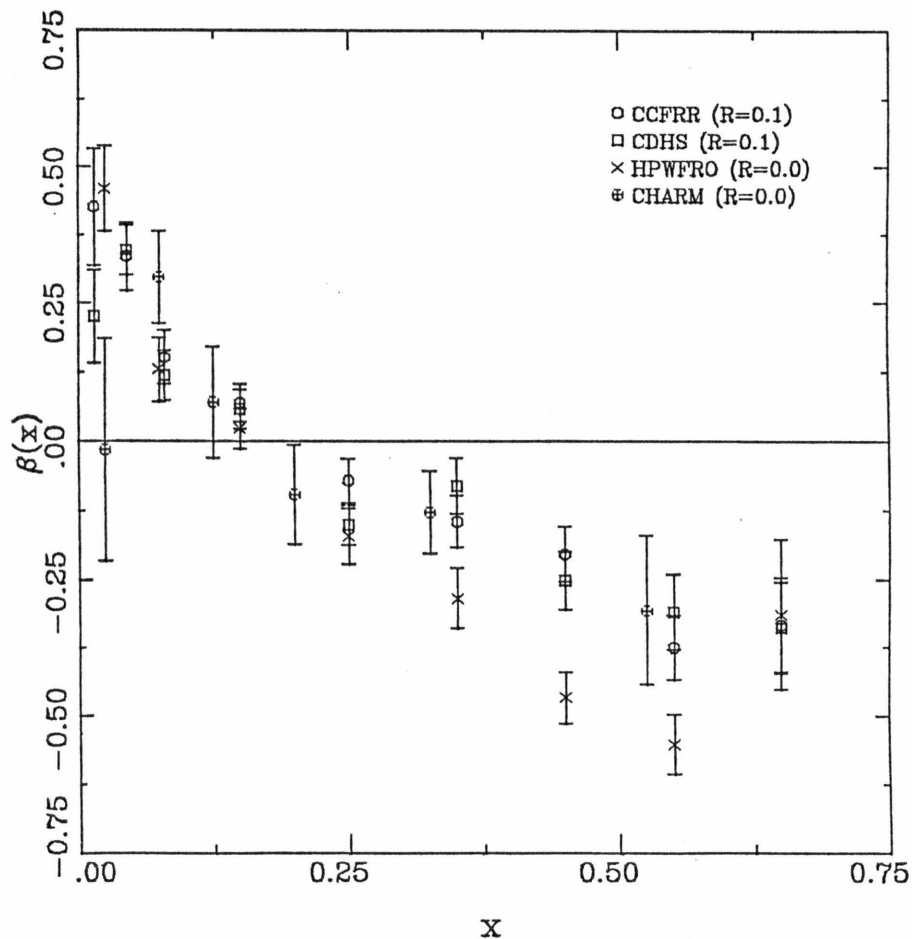


Figure 6.3 Values of  $(d \log F_2 / d \log Q^2) / F_2$  at  $Q^2 = 10\text{GeV}^2$  for various experiments

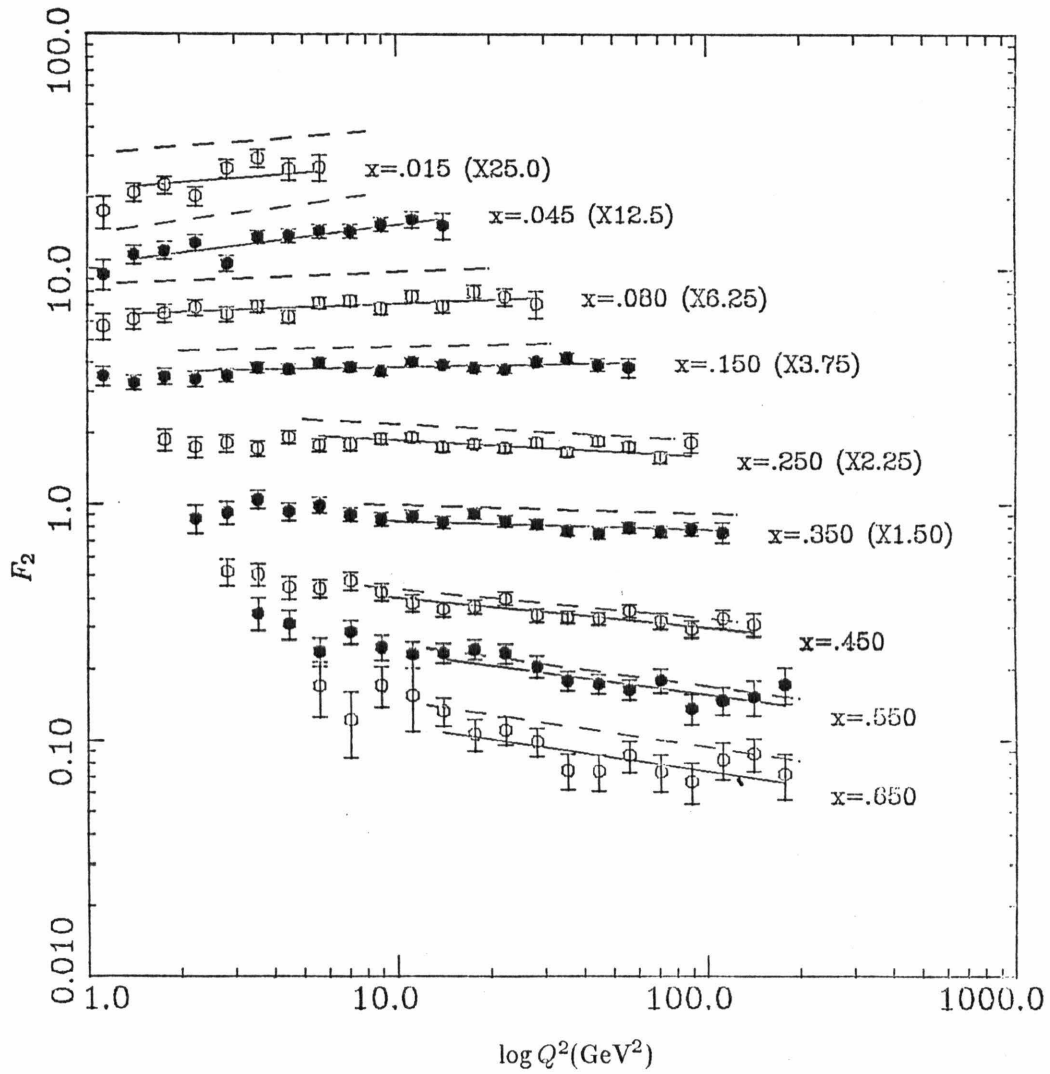


Figure 6.4

$F_2(x, Q^2)$  from the CDHS collaboration. Solid lines are fits to CDHS using slopes from our data. Dashed lines are corresponding fits to CCFRR.  $R = 0.1$  was assumed for both sets of data.

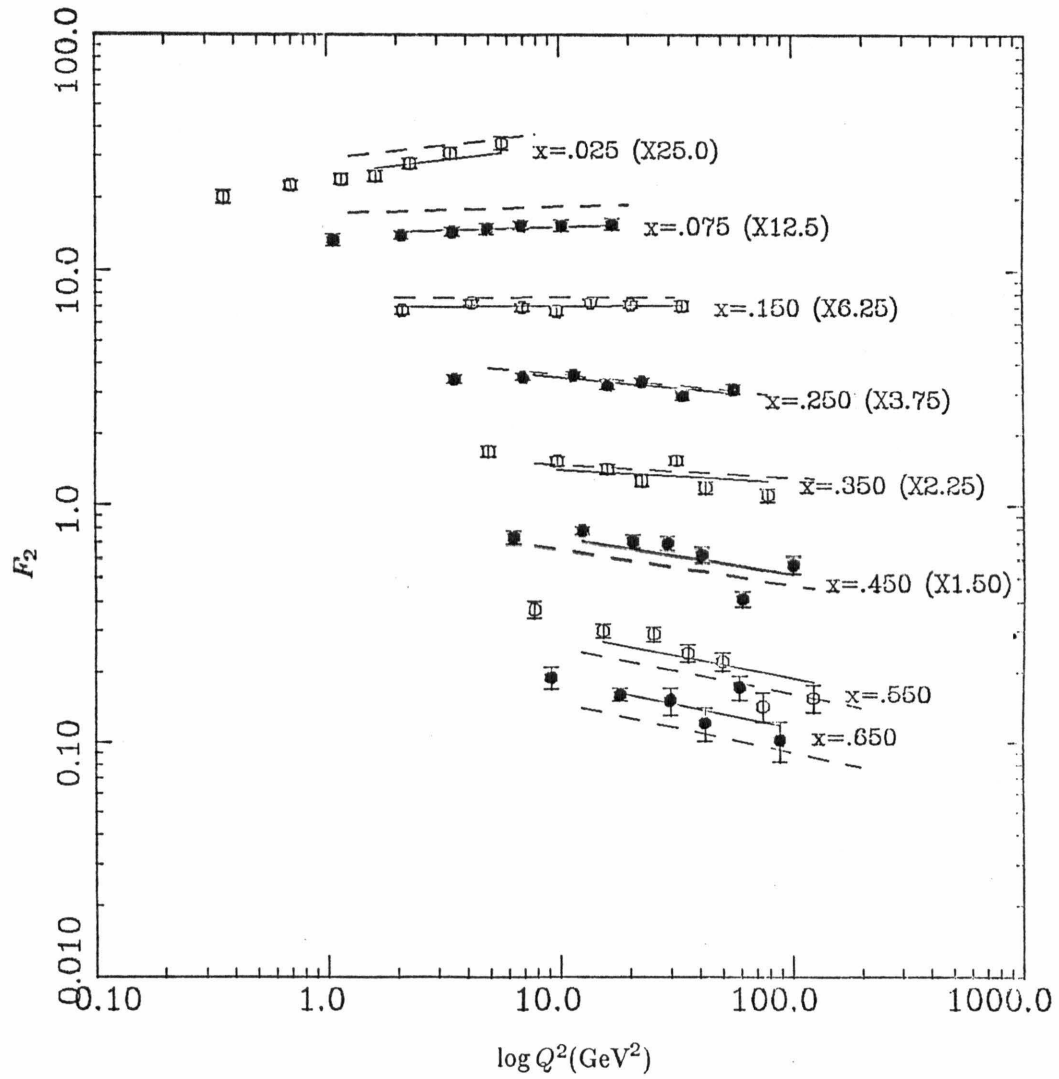


Figure 6.5

$F_2(x, Q^2)$  from the HPWFOR collaboration. Solid lines are fits to HPWFOR using slopes from our data. Dashed lines are corresponding fits to CCFRR.  $R = 0.0$  was assumed for both sets of data.

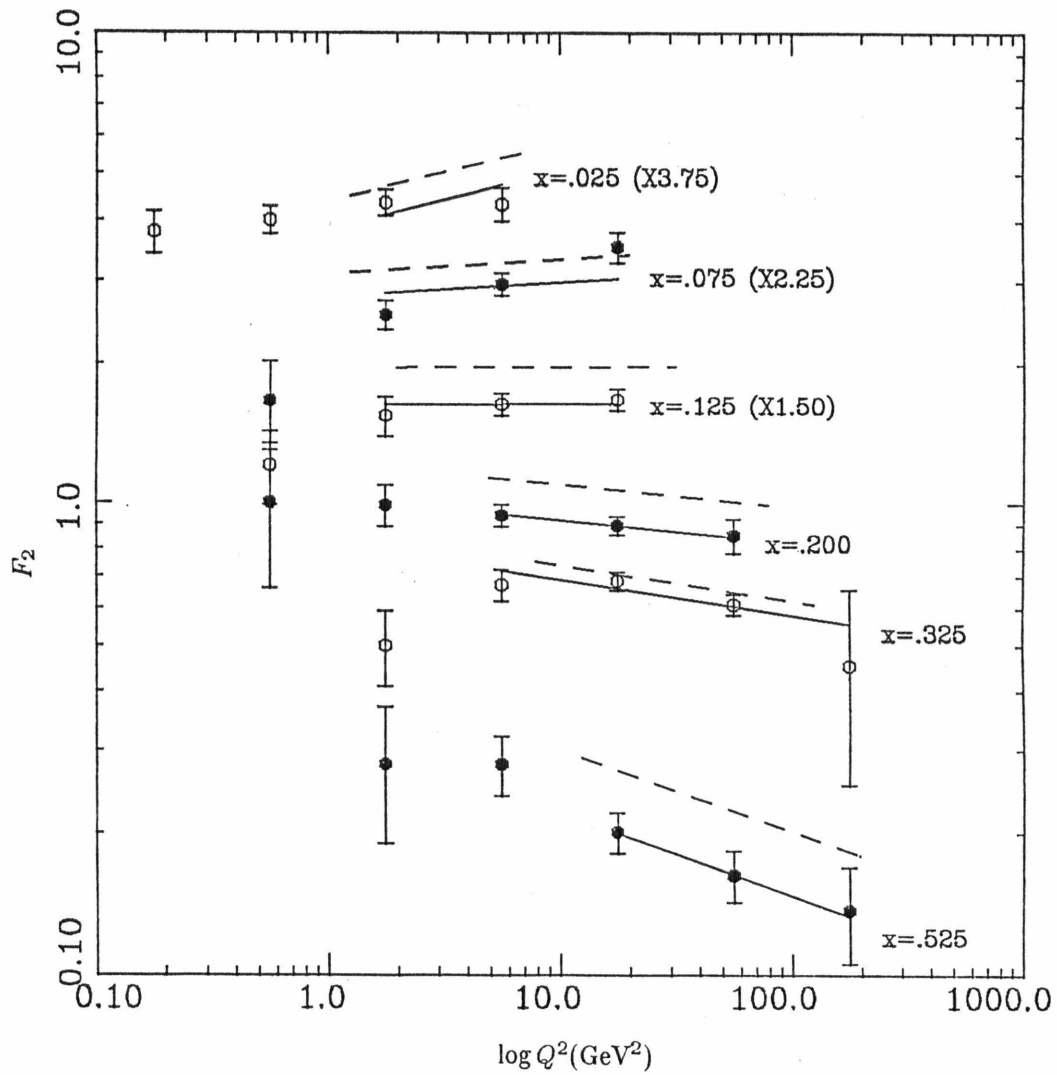


Figure 6.6

$F_2(x, Q^2)$  from the CHARM collaboration. Solid lines are fits to CHARM using slopes from our data. Dashed lines are corresponding fits to CCFRR.  $R = 0.0$  was assumed for both sets of data.

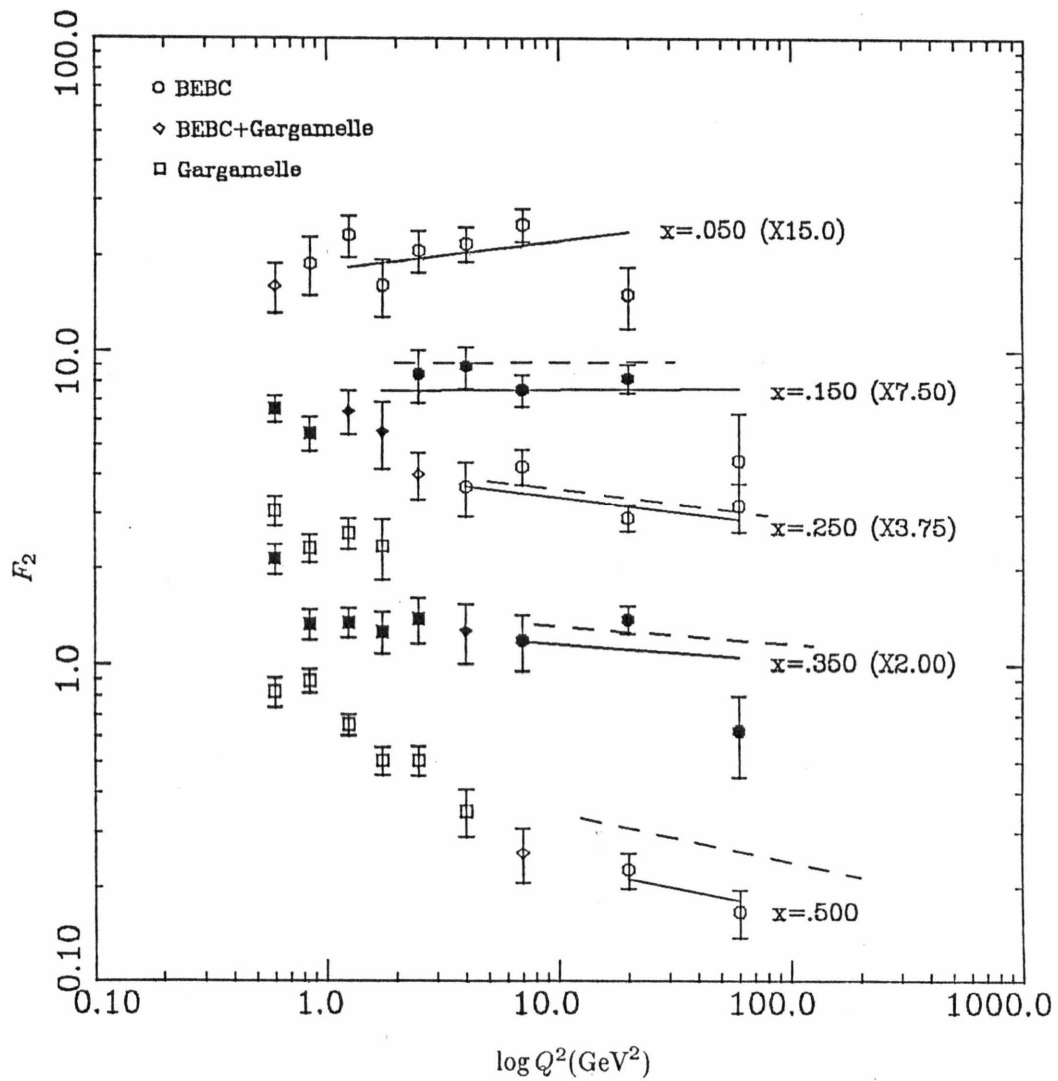


Figure 6.7

$F_2(x, Q^2)$  from the BEBC-GGM collaboration. Solid lines are fits to BEBC-GGM using slopes from our data. Dashed lines are corresponding fits to CCFRR.  $R = 0.0$  was assumed for both sets of data.

Given this conclusion, the normalization and  $x$  dependence differences among the various results were investigated using the value of  $\beta$  obtained from our data in each  $x$  bin. Equation 6.1 then becomes a one parameter fit for the comparison data set. Within the limits of the stated assumption, the values of ratio of  $F_2$  at  $Q^2 = 10\text{GeV}^2$  from the two experiments under consideration therefore had smaller errors. The efficacy of the procedure is illustrated by examining figures 6.4 through 6.7. These show the logarithmic variation in  $Q^2$  of  $F_2$  for each of the other data sets. The solid lines in the figures are the best fits to  $F_2(x, Q^2 = 10\text{GeV}^2)$  using  $\beta$  from our data. The dashed lines are the best fit to our data, with the actual points removed for clarity of presentation. The chosen technique can be seen to fit the various data sets reasonably well. There is a hint in the Gargamelle data, shown in figure 6.7, that at large  $x$  the  $Q^2$  dependence below  $Q^2 = 10\text{GeV}^2$  differs significantly from that measured by this experiment. This observation is confirmed by reported measurements of  $F_2$  from SLAC [Bo79] discussed below.

Figure 6.8 shows the fit values of  $F_2$  at  $Q^2 = 10\text{GeV}^2$  from both our data and CDHS. Part of the discrepancy between the results reflects the difference in the reported total cross sections. On this basis, one would expect the integrals to differ by 10%, somewhat outside the estimated normalization errors of 4.1% for  $F_2$  from this experiment and 6% for that from CDHS. In order to connect the normalization of structure functions to a pre-assigned total cross section level, it would be necessary to estimate the integrals of structure functions in unmeasured regions. Disagreements at the few percent level might be anticipated. However, the integrals in fact differ by a total of 19%. The origin of the additional discrepancy is not understood. Our structure function measurements, given reasonable extrapolations of their behavior outside the measured region, have been found to reproduce the reported total cross section measurement to within  $\pm 2\%$ . Also, the integral over all  $x$  of structure functions averaged over  $Q^2$  was 0.482 for  $F_2$  and 0.324 for  $x F_3$  (with zero charm mass and  $1/2$  SU(3) symmetric strange sea). These are within 1% and 4% respectively of the predicted values from the total cross section (section 5.1). The results calculated from the total cross section are averages of structure function integrals at fixed  $E_{\nu(\bar{\nu})}$ , and do not strictly correspond to  $Q^2$ -averaged integrals of structure function measurements. Therefore, this represents reasonable agreement.

Irrespective of these overall normalization difficulties, there is considerable difference in the reported  $x$  dependence of  $F_2$ . This is most easily seen in figure 6.9, which shows the ratio at  $Q^2 = 10\text{GeV}^2$  of  $F_2$  from CDHS to  $F_2$  reported here. The dashed line represents the average ratio expected from the total cross section values. The CDHS result was reported under the assumption of a zero charm quark mass. The effect on the ratio has been estimated to vary from 5% at small  $x$  to 2% at large  $x$ , but is not sufficient to account for the discrepancy. The squares in the figure show the necessary level of adjustment for each  $x$  bin. The differences between the two results are outside statistical errors, and exhibit a clear systematic trend. In general, our result for  $F_2$  is more strongly peaked at small  $x$  than that from CDHS. Except in the highest  $x$  bins, the systematic errors in the two results have been estimated to be small. The ratio of neutrino to anti-neutrino total cross sections used in the two analyses was not sufficiently different to contribute significantly to a shape difference. Therefore, the origin of the difficulty is not understood either. However, the reader is reminded that the resolution of our measurements at small  $x$  was about three times better than that of CDHS.

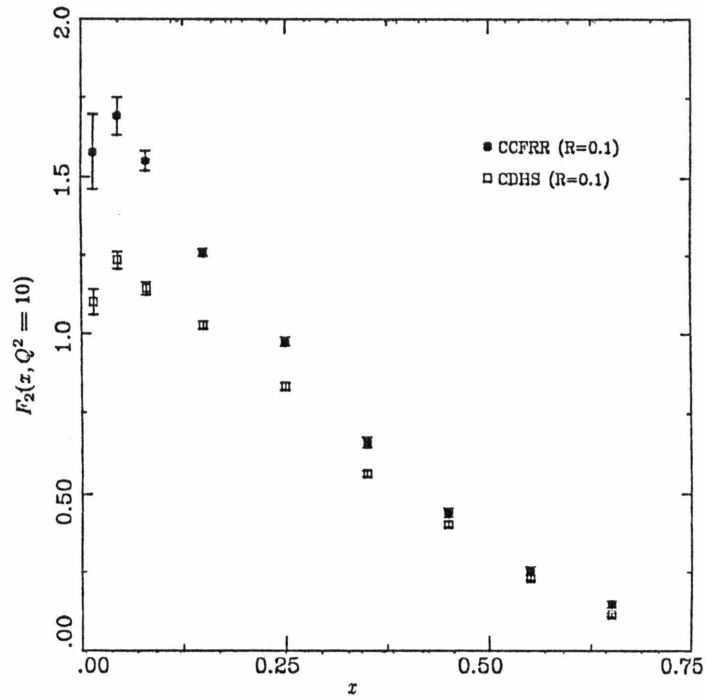


Figure 6.8 Fit values of  $F_2$  at  $Q^2 = 10\text{GeV}^2$  for CCFRR and CDHS assuming  $R = 0.1$

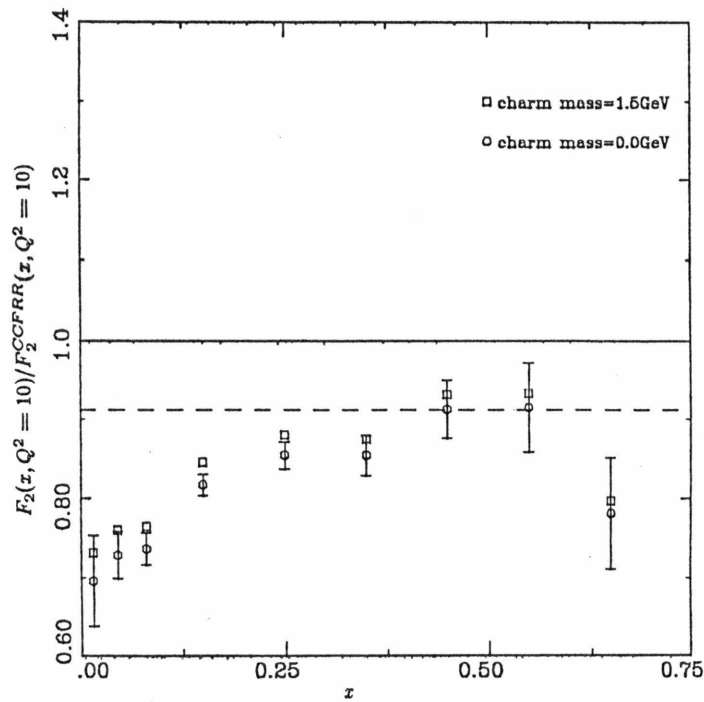


Figure 6.9 Ratio of  $F_2$  at  $Q^2 = 10\text{GeV}^2$  for CCFRR and CDHS assuming  $R = 0.0$

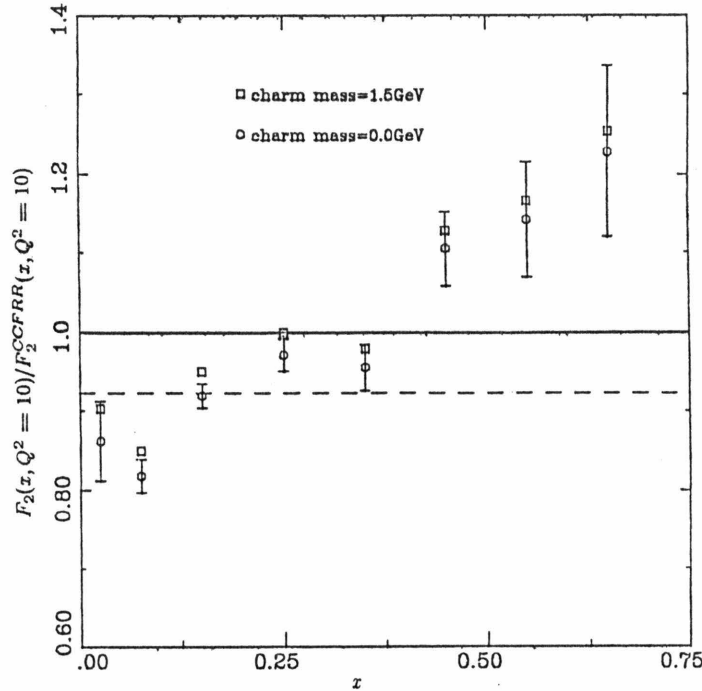


Figure 6.10 Ratio of  $F_2$  at  $Q^2 = 10\text{GeV}^2$  for CCFRR and HPWFOR assuming  $R = 0.0$

This same analysis has been repeated in comparing our result for  $F_2$  with that from HPWFOR. Figure 6.10 shows the ratio of  $F_2$  at  $Q^2 = 10\text{GeV}^2$  from the two experiments. Results under the assumption that  $R = 0.0$  were used for both groups. The dashed line in the figure is the expected ratio from the total cross sections. The squares represent the adjustment required for a finite charm mass ( $1.5\text{GeV}$ ). Despite the obvious differences at large  $x$ , the ratio of integrals of  $F_2$  was not in serious disagreement with the predicted ratio from the total cross section. It should be noted that in the case of the HPWFOR result, the total cross sections used were not measured but represented the world average at the time of the experiment. Ignoring the level difference, the shape of the HPWFOR result matches well the CDHS result except at large  $x$ . The effect of the different assumptions made about  $R$  by the two groups is appreciable only below  $x = 0.2$ , and does not change this conclusion. Therefore, the observation that our result for  $F_2$  is more strongly peaked at small  $x$  is true in comparison with HPWFOR. The difference between our measurement and that of HPWFOR could originate in at least two sources: (1) the HPWFOR result was obtained in a wide-band beam, which suggests that systematic errors in neutrino flux could be a contributing factor to the discrepancy, and (2) the HPWFOR target was scintillator (2/3) and iron (1/3), so that nuclear Fermi motion corrections could explain part of the large  $x$  difference. In this last connection, the reader is referred to section 6.2 for a discussion of the observation in charged lepton scattering experiments of target-dependent differences in the shape of  $F_2(x)$ .

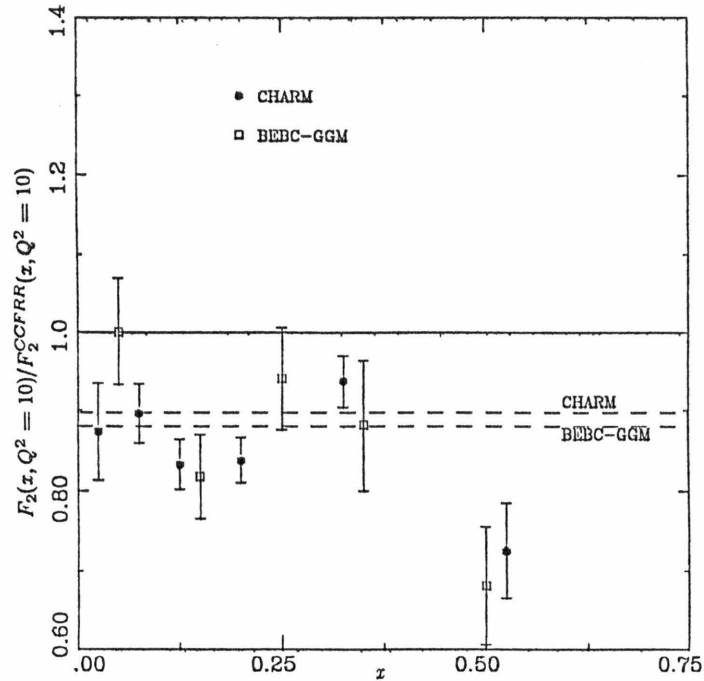


Figure 6.11

Ratio of  $F_2$  at  $Q^2 = 10\text{GeV}^2$  for CCFRR and CHARM and BEBC-GGM assuming  $R = 0.0$

Finally, consider the comparison of our results with those from CHARM and BEBC-Gargamelle. Figure 6.11 shows the ratio of  $F_2$  from these experiments to our result at  $Q^2 = 10\text{GeV}^2$ . Appropriately, our  $R = 0.0$  measurement was used for this comparison. Limited statistics in the overlapping  $Q^2$  regions, particularly for the BEBC result, make definitive conclusions impossible. However, there is reasonable agreement between the observed level differences and the expectation from total cross section predictions. Except at high  $x$ , the  $x$  dependence of the CHARM result agrees with our measurement. Again, the target material for CHARM was marble and not iron, so the agreement is perhaps fortuitous. For the BEBC-GGM results the target was variously liquid freon or a liquid Ne-H<sub>2</sub> mix.

These observations can be summarized as: (1) there are systematic discrepancies in the  $x$  dependence of  $F_2$  from the various experiments, and (2) the normalization differences among the experiments for the most part reflect the different total cross section measurements used by the groups, and hence flux normalization errors. It should be noted that there is some additional level discrepancy in comparison with CDHS, perhaps due to some difficulty with resolution corrections in conjunction with uncertainties in the values of structure functions outside kinematically accessible regions. Despite these differences in the  $x$  dependence of  $F_2$ , the  $Q^2$  variation observed in the data is quite similar, as indicated by the agreement in values of  $d \ln F_2 / d \ln Q^2$ .

## 6.2 Mean Square Quark Charge Test

In the quark-parton model the structure functions are interpreted in terms of quark densities within the nucleon. Let  $q_i(x)dx$  be the probability density in momentum space of the  $i^{\text{th}}$  quark with fraction  $x$  of the nucleon momentum. Then:

$$\begin{aligned} 2xF_1(x) = F_2(x) &= \sum_i (q_i(x) + \bar{q}_i(x)) \\ xF_3(x) &= \sum_i (q_i(x) - \bar{q}_i(x)) \end{aligned} \quad (6.2)$$

Neglecting thresholds introduced by finite quark masses, the coupling of the weak force to quarks is flavour independent. On the other hand, coupling to the electromagnetic force is proportional to  $e_{q_i}^2$ . Structure functions extracted from electron or muon scattering from the nucleon reflect this fact. In the quark-parton model:

$$2xF_1^{l\pm}(x) = F_2^{l\pm} = \sum_i e_{q_i}^2 (q_i + \bar{q}_i) \quad (6.3)$$

( $xF_3$  is not measurable in parity-conserving electromagnetic interactions.)

$F_2$  as measured by muon scattering from protons and neutrons is:

$$\begin{aligned} F_2^{\mu p}(x) &= \frac{4}{9}(u_p(x) + \bar{u}_p(x)) + \frac{1}{9}(d_p(x) + \bar{d}_p(x)) + \\ &\quad \frac{1}{9}(s_p(x) + \bar{s}_p(x)) + \frac{4}{9}(c_p(x) + \bar{c}_p(x)) \\ F_2^{\mu n}(x) &= \frac{4}{9}(u_n(x) + \bar{u}_n(x)) + \frac{1}{9}(d_n(x) + \bar{d}_n(x)) + \\ &\quad \frac{1}{9}(s_n(x) + \bar{s}_n(x)) + \frac{4}{9}(c_n(x) + \bar{c}_n(x)) \end{aligned} \quad (6.4)$$

Now, assume the usual isospin symmetry:  $u_p(x) = d_n(x)$  and  $d_p(x) = u_n(x)$ , and that for sea quarks  $q_p(x) = q_n(x)$ . Then for an isoscalar target:

$$F_2^{\mu N}(x) = \frac{5}{18} \left\{ 1 - \frac{3(s(x) - c(x)) + (\bar{s}(x) - \bar{c}(x))}{q(x) + \bar{q}(x)} \right\} \sum_i (q_i(x) + \bar{q}_i(x)) \quad (6.5)$$

Thus  $F_2^{\mu N}$  is related in this model by the mean square quark charge (5/18) to  $F_2^{\nu N}$ .

The European Muon Collaboration (EMC) has published [Au81b] a high statistics measurement of  $F_2$  from inclusive deep-inelastic muon-scattering data in iron. This data has been used along with corresponding results for neutrino scattering in iron to test the quark-parton model prediction. For this test the structure functions have been compared as a function of  $x$  at a fixed  $Q^2$ . The same technique described in section 6.1 was used to accomplish this end. The EMC data were first interpolated to the same  $x$  values as the comparison neutrino

data set. A linear fit in  $\log Q^2$  was made to the interpolated points:

$$F_2^{\mu N}(x, Q^2) = F_2^{\mu N}(x, Q^2 = 10) \{1 + \beta_{EMC}(x) \log(Q^2/10)\} \quad (6.6)$$

Since the EMC data had the greatest statistical precision, the comparison data sets were interpolated to the  $Q^2 = 10\text{GeV}^2$ , using the best fit to the  $Q^2$  variation of the EMC data:

$$F_2^{\nu N}(x, Q^2) = F_2^{\nu N}(x, Q^2 = 10) \{1 + \beta_{EMC}(x) \log(Q^2/10)\} \quad (6.7)$$

A predicted value for the neutrino result at  $Q^2 = 10\text{GeV}^2$  was made using  $F_2^{\mu N}$  and equation 6.5.

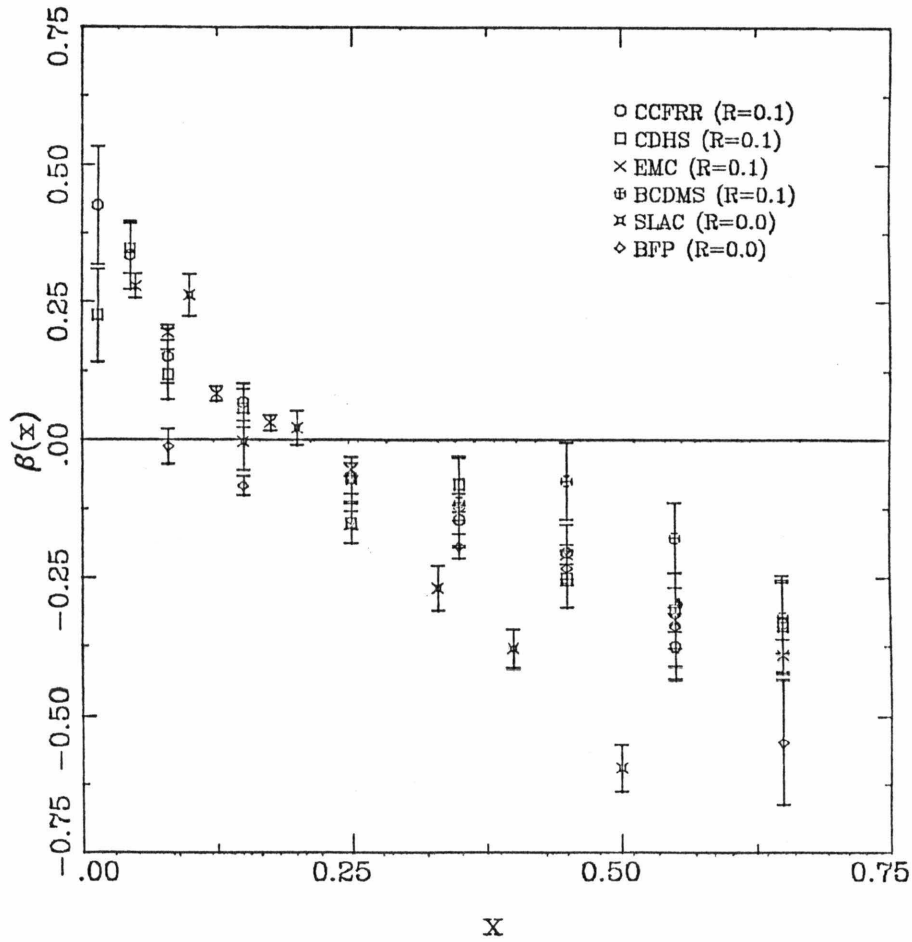


Figure 6.12

Values of  $dF_2/d\log Q^2$  normalized by  $F_2$  at  $Q^2 = 10\text{GeV}^2$  for various neutrino and charged lepton experiments

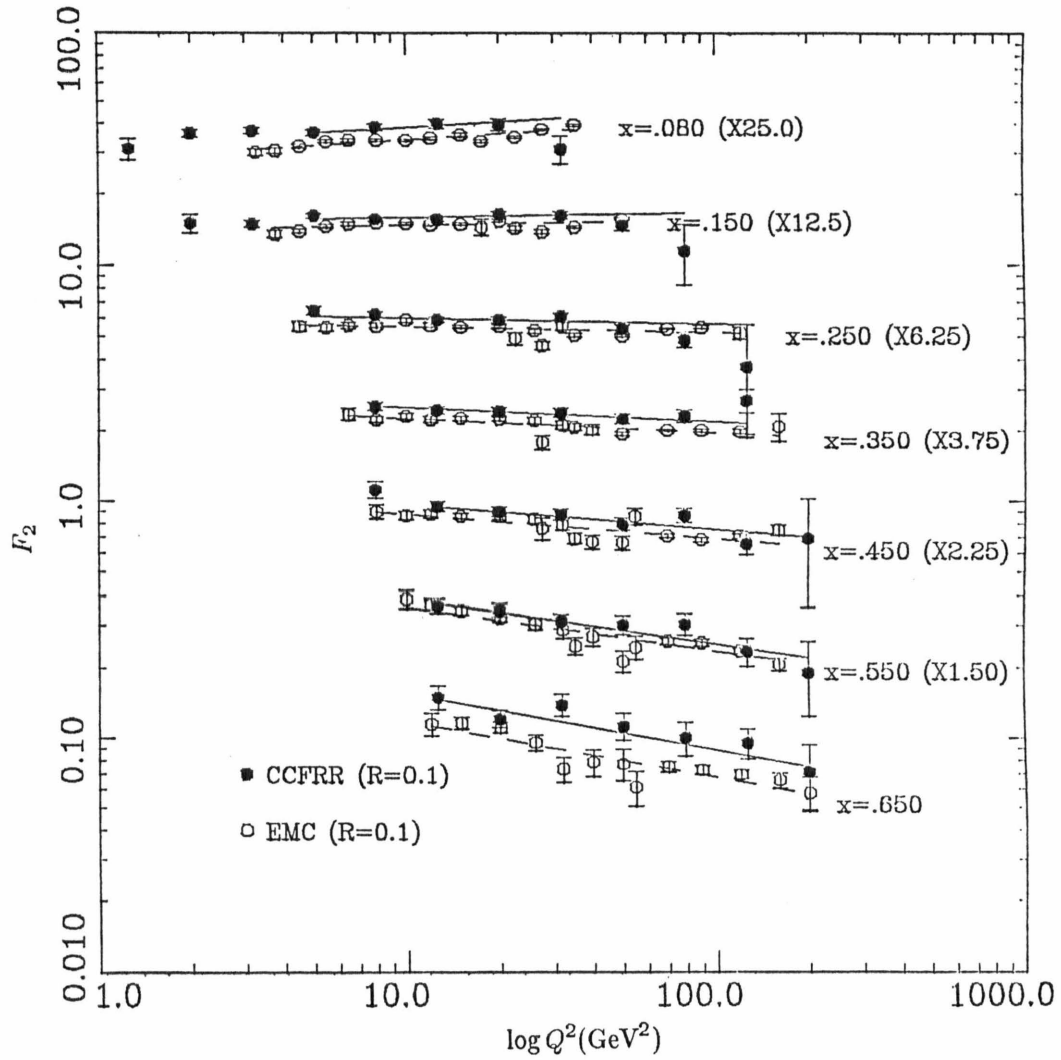


Figure 6.19

$F_2(x, Q^2)$  from this experiment and EMC. Solid lines are fits to our data using slopes from EMC. Dashed lines are corresponding fits to EMC.  $R = 0.1$  was assumed for both sets of data.

The procedure is justified, as in the case of the comparison of neutrino experiments in section 6.1, by the agreement in the level of observed scaling violations found in the various data sets. A measure of this agreement is shown in figure 6.12: the fit values of  $\beta$  from neutrino and charged lepton measurements of  $F_2$ . Shown in the figure are both fits to our result and that of CDHS, along with those from EMC ( $\mu$ -iron) [Au81b], BFP ( $\mu$ -iron) [Me83], BCDMS ( $\mu$ -carbon) [Bo81] and SLAC ( $e$ - $D_2$ ) [Bo79]. Except for the SLAC data, the fits were made in overlapping  $Q^2$  regions, and are in reasonably good agreement. The SLAC measurements were at lower  $Q^2$ , and significantly differ from the other results at large  $x$ . Thus, the hint of larger  $Q^2$  variation in the BEBC-GGM data at small  $W^2$  and large  $x$  is also seen in the SLAC data.

An example of a fit of the form given in equations 6.6 and 6.7 is shown in figure 6.13. The dashed line in the figure is the best fit to the EMC data. The solid line is the result of a one parameter fit to our data using  $\beta_{EMC}(x)$ . The ratio of  $F_2^{\nu N}$  from this experiment to the predicted value from  $F_2^{EMC}$  is shown in figure 6.14. The inner error bars represent statistical errors only, while the outer error bars include in quadrature estimates of point-to-point systematic errors. Additional overall scale errors of 4.1% for our result and 3% for that from EMC are not shown. The small correction for the strange sea was made using the measured  $x$  dependence of  $\bar{q}(x, Q^2)$  from our data. It was assumed that  $c(x) = \bar{c}(x) = 0$  within the nucleon. As shown in the figure,  $x$  dependent changes at the few percent level could be made in the ratio by changing the fraction of the sea assumed to be represented by strange quarks (nominally 1/2 SU(3)), or the correction for slow rescaling due to finite charm quark

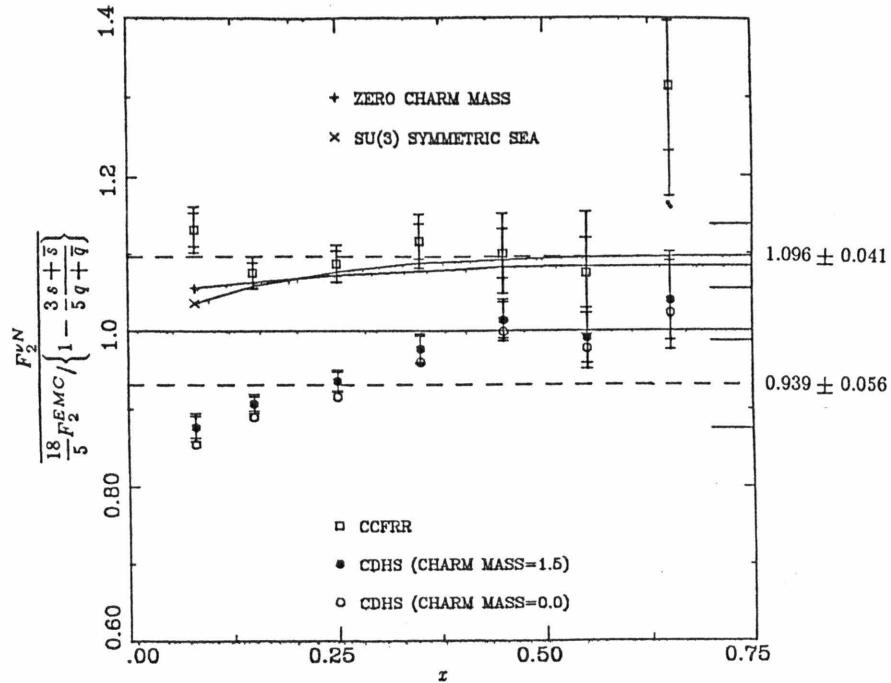


Figure 6.14 Mean square quark charge test: neutrino results for  $F_2$  compared with EMC

$m_c=1.5\text{GeV}$ ). These uncertainties do not modify significantly the conclusions to be drawn from the figure. It can be seen that our result lies on average 9.5% above the predicted value, but shows little  $x$  dependence. The level difference is somewhat outside the quoted systematic scale errors.

There is some evidence that systematic uncertainties in the normalization of the EMC result have been underestimated. Comparisons of published results for  $F_2$  from charged lepton scattering in  $H_2$  have been made by Smadja [Sm81] for SLAC [Bo79] and EMC [Au81a], and by Sciulli and Fisk [Fi82] for CHIO [Go79] and EMC. Reproduced in figure 6.15 is the ratio of  $F_2$  from the three experiments. It was concluded that there existed a discrepancy in the normalization of the three experiments outside estimated scale errors. On average the measurements from SLAC and CHIO were respectively 10% and 8% higher than EMC. Recently, other results for  $F_2$  from iron have been presented by the BPF muon experiment [Cl83]. This group found that the EMC result was systematically lower by 5% in comparison with their measurement of  $F_2$ . This suggests that the EMC results from both  $H_2$  and iron targets should be raised by  $5 \pm 5\%$  to accommodate the incompatibility among charged lepton results. Reasonable agreement between the EMC measurement and our result using the quark model relation (equation 6.5) would then be observed.

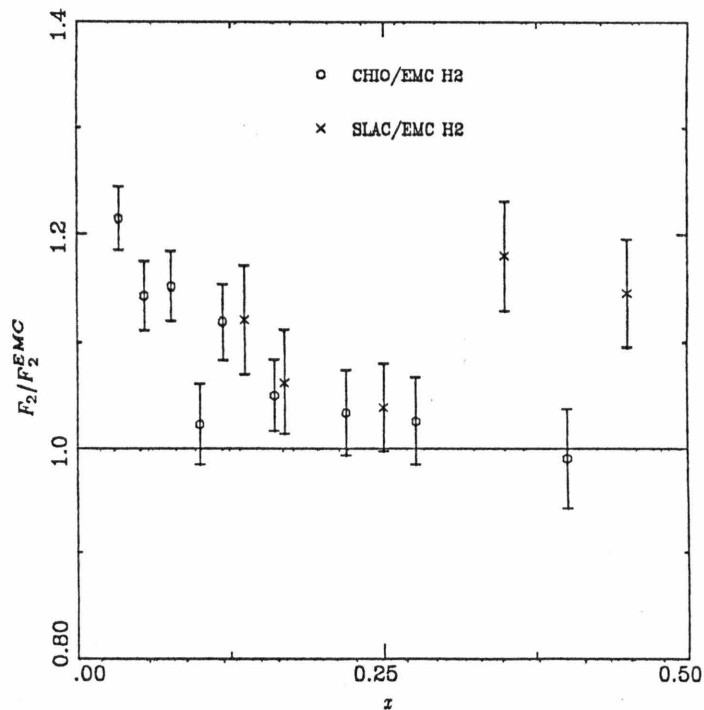


Figure 6.15 Comparison of charged lepton results for  $F_2$  ([Sm81] and [Fi82])

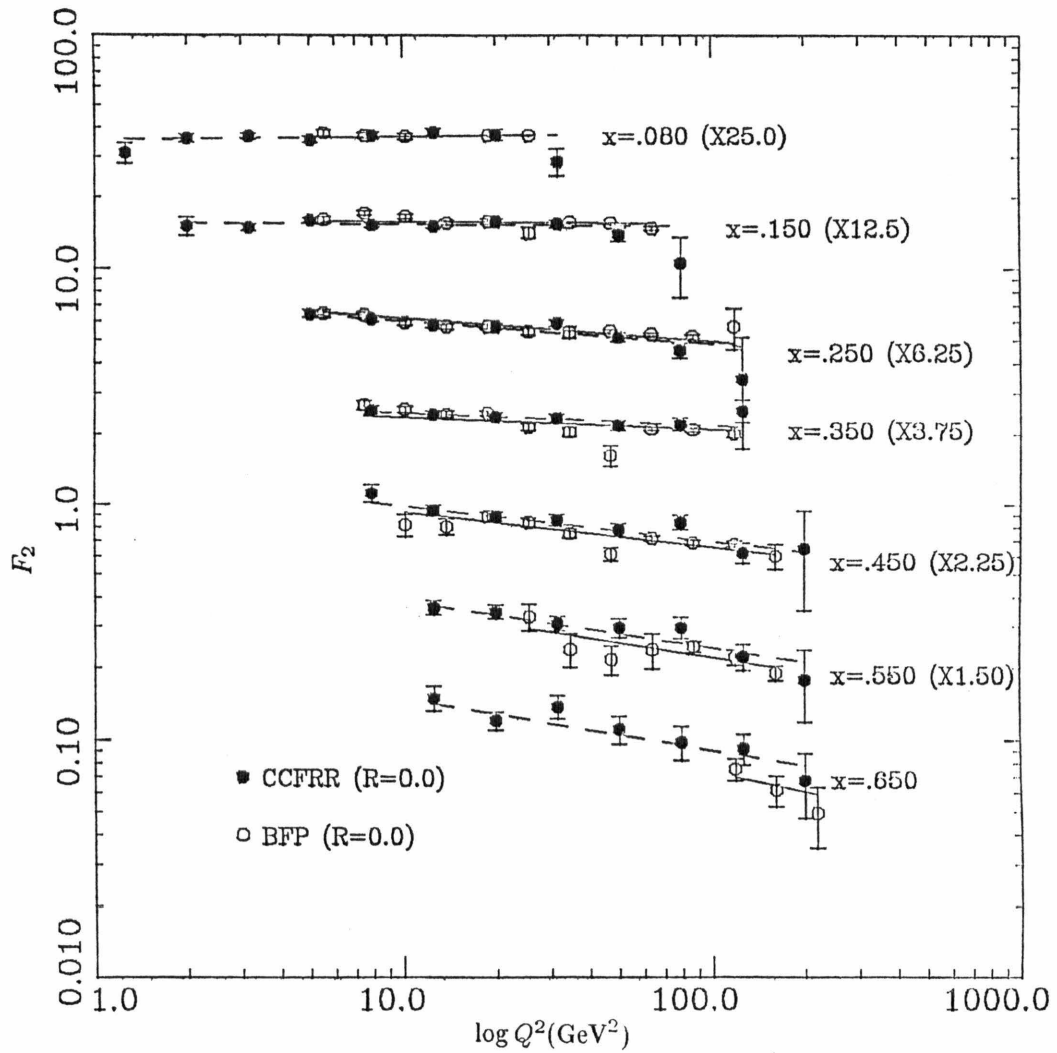


Figure 6.16

$F_2(x, Q^2)$  from this experiment and BFP. Solid lines are fits to BFP using slopes from our data. Dashed lines are corresponding fits to CCFRR.  $R = 0.0$  was assumed for both sets of data.

The relation can also be tested using the published neutrino results from the CDHS collaboration. This comparison is shown in figure 6.14. Here the ratio exhibits an  $x$  dependence, with the CDHS measurement on average 10% below the predicted value. Again, the level difference is outside the combined systematics of the two experiments. If the CDHS result was adjusted for a finite charm mass, the average difference would be reduced to 6%. However, the disagreement at small  $x$  would remain. Since the  $x$  dependence of our result is seen to agree well with that of EMC, the comparison reflects on the earlier observation of disagreement between our measurements and those from CDHS. Other authors have pointed out the low  $x$  discrepancy between EMC and CDHS [De83].

The same procedure can be repeated in comparing our results with those from the BFP muon experiment [Me83]. In this case, the values of  $\beta$  from fits to our data were used to constrain the fit to the muon data. The two data sets, along with the fits obtained, are shown in figure 6.16. The ratio of the values of  $F_2$  at  $Q^2 = 10\text{GeV}^2$  is shown as a function of  $x$  in figure 6.17. Clearly, there is good agreement between  $F_2$  from this experiment and the BFP measurement of  $F_2$  adjusted by the quark-parton model factor of 18/5. The scale error for the BFP measurement was reported to be 3% [Cl83].

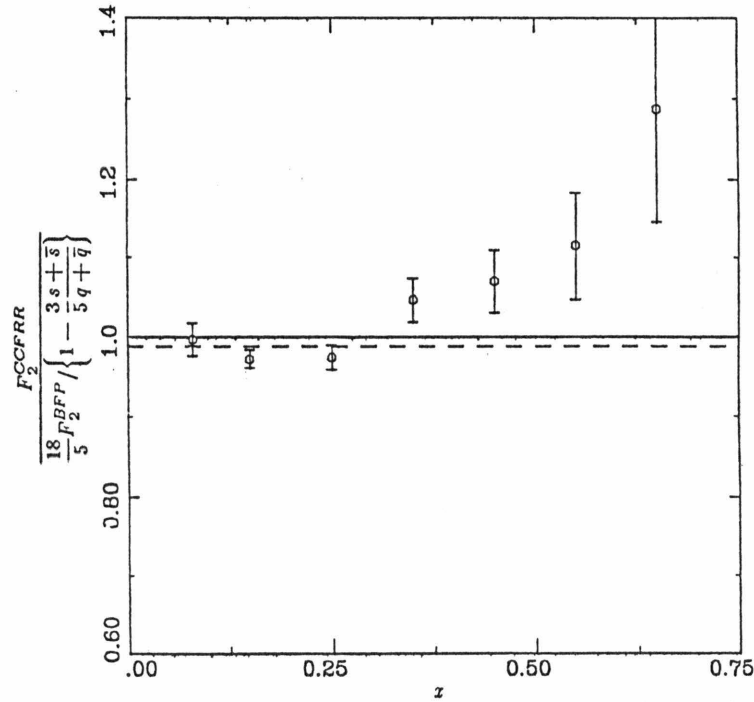


Figure 6.17 Mean square quark charge test:  $F_2$  from CCFRR compared with BFP muon results

Before examining the comparison between our results and those from SLAC, a short digression is in order to remind the reader of recent unexpected developments in the field. The ratio of  $F_2$  from iron to  $F_2$  from  $D_2$  has been found to exhibit a strong  $x$  dependence not explainable in terms of Fermi motion corrections. In fact, the effect is in a direction opposite to that expected from Fermi motion smearing. The phenomenon has been observed both in muon scattering by the EMC collaboration [Au83] and in electron scattering at SLAC [Bo83a]. Figure 6.18 reproduces the ratio observed by the two collaborations. The good agreement between the two measurements, despite the large difference in mean  $Q^2$  for the experiments, indicates that the effect has little  $Q^2$  dependence above  $Q^2$ 's of a few  $\text{GeV}^2$ . The explanation for the difference in the intrinsic shape of quark distributions in iron and deuterium is thought to lie in large distance, low  $Q^2$  effects, uncalculable using perturbative QCD. Quark distributions within a nucleon are apparently distorted by the presence of other nucleons within the nucleus. Recent bag model calculations [Ja83] suggest that distortions can occur by mechanisms such as six quark collective states. These observations invalidate previous QCD fits which combined raw measurements of structure functions obtained from different targets, but not fits made to data internal to one target or properly adjusted data from different targets.

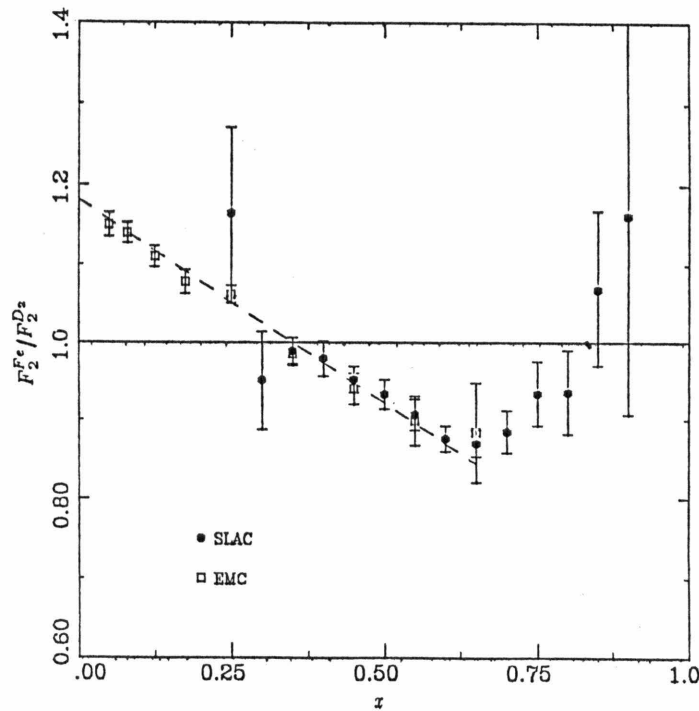


Figure 6.18 Ratio of  $F_2^{Fe}/F_2^{D_2}$  from EMC [Au83] and SLAC [Bo83a]

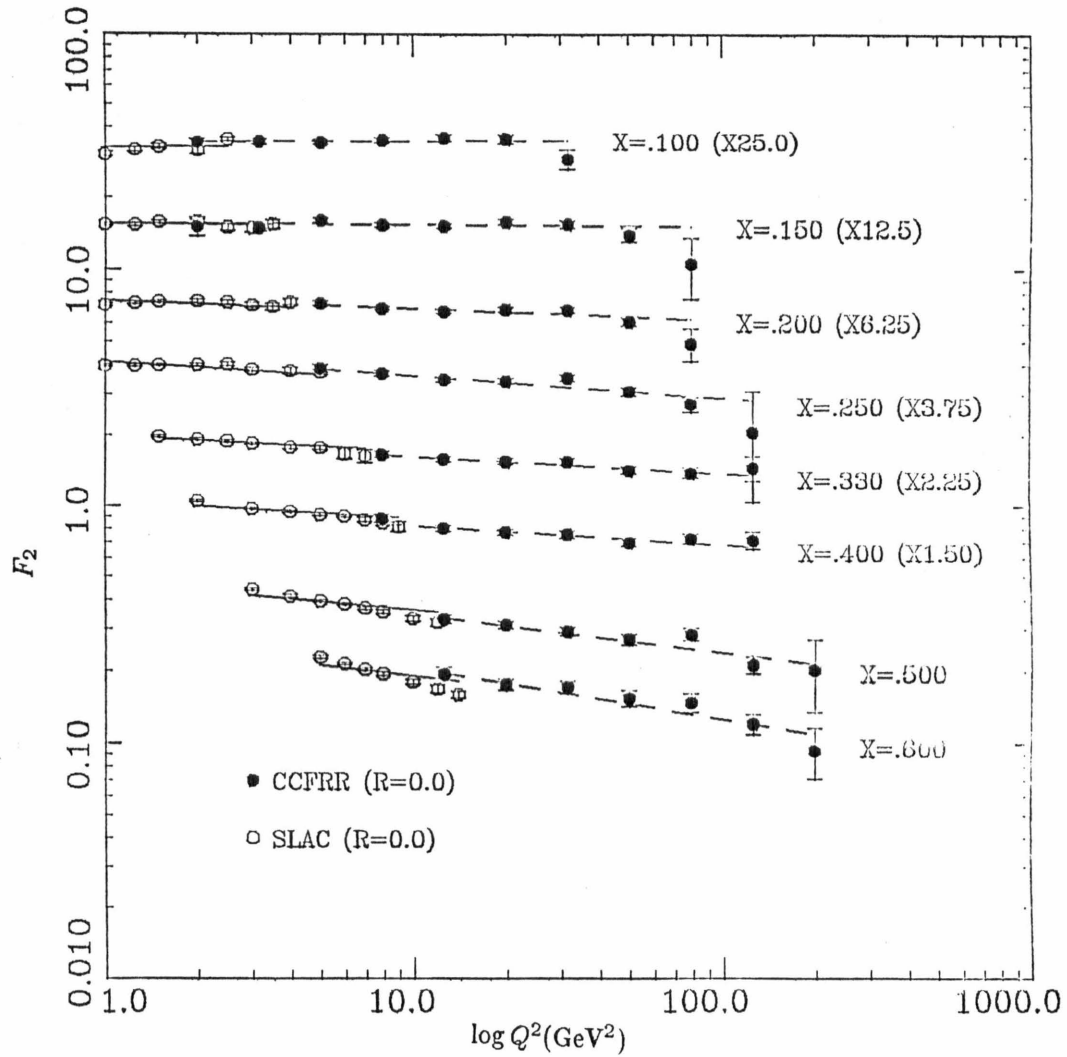


Figure 6.19

$F_2(x, Q^2)$  from this experiment and SLAC. Solid lines are fits to SLAC using slopes from our data. Dashed lines are corresponding fits to CCFRR.  $R = 0.0$  was assumed for both sets of data.

In order to compare the shape and normalization of the SLAC data within our own measurements, it was necessary to make suitable adjustments to the  $x$  dependence of the SLAC deuterium results. This adjustment was based on the EMC measurement [Au83] of:

$$F_2^{F\epsilon}/F_2^{D_2} = 1.182 - 0.52 \cdot x \quad (6.8)$$

Below  $x = 0.65$ , this clearly fits the SLAC measurements as well. Adjustments were also needed to account for the fact that the SLAC data were analyzed in terms of  $2xF_1$  and  $F_2$ , with no fixed assumption about  $R$ . This makes comparisons with experiments which do assume values for  $R$  more difficult. The method used by SLAC to obtain structure functions [Bo79] was similar in spirit to that described in section 5.7. In fixed bins of  $x$  and  $Q^2$ , the differential cross section was measured at various angles,  $\theta_e$ , or photon polarizations ( $\epsilon$ ). A two parameter linear fit was then made, with  $2xF_1$  proportional to the intercept and  $F_2$  proportional to the value at  $\epsilon = 1.0$ . Experiments which assume  $R$  fix the slope of this fit. Without the full correlation matrix, such a one parameter fit cannot be reconstructed from the published data. However, if  $R = 0.0$  is assumed, only the diagonal elements of the matrix are needed. Under this assumption,  $F_2$  is the weighted average of the published results for  $F_2$  and  $2xF_1$ . Appropriately, our results assuming  $R = 0.0$  were compared with the SLAC results so adjusted.

There was almost no overlap in the  $Q^2$  range covered by the two experiments. The requirement that only common  $Q^2$  regions be considered was therefore removed. Fits were made both with and without the constraint of using  $\beta$  determined from our data. An example

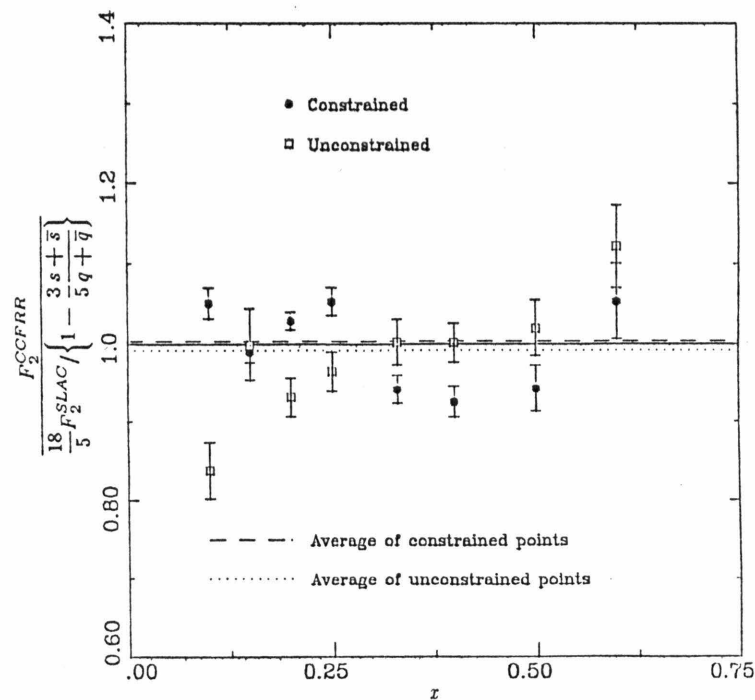


Figure 6.20 Mean square quark charge test:  $F_2$  from CCFRR compared with SLAC electron results

of a fit including the  $Q^2$  constraint is shown in figure 6.19. The observed ratio of  $F_2$  at  $Q^2 = 10\text{GeV}^2$  is shown in figure 6.20. As expected from the discussion of the consistency of SLAC and EMC results from  $H_2$ , our measurement can be seen to be in good agreement with the adjusted SLAC results.

A common feature of these comparisons of our measurements of  $F_2$  with both neutrino and charged lepton-scattering results is the tendency for the last  $x$  bin (0.65) to lie above expectations. The predominant systematic error in this bin was calibration uncertainties in the measurements of  $E_\mu$  and to a lesser extent  $E_H$ . The implication is that the muon energy measurement was systematically high. However, as illustrated in figure 6.14, the estimated systematic errors assigned the measurements in that bin were sufficient to accommodate the discrepancy.

To summarize these observations: (1) the  $x$  dependence of our measurement of  $F_2$  is consistent with comparable measurements from charged lepton scattering in contrast with the disagreement among neutrino experiments, and (2) the mean square quark charge test is confirmed at the 10% level. The agreement among the results from SLAC, BFP and this experiment is well within errors. There is evidence that the normalization uncertainty assigned the EMC result is underestimated. If so, the level discrepancy between EMC and our result is understood. Finally, the scaling violations seen in measurements of  $F_2$  in the  $Q^2$  range covered by this experiment are similar for both neutrino and charged lepton experiments.

### 6.3 Gross-Llewellyn Smith Sum Rule

Another result which is sensitive to absolute normalization is the Gross-Llewellyn Smith (GLS) sum rule [Gr69]. Under the usual assumption of isospin symmetry,  $u_p = d_n$  and  $d_p = u_n$ , the net electric charge of protons and neutrons can be expressed in terms of integrals over quark number densities:

$$\begin{aligned} \int_0^1 \frac{dx}{x} \left\{ \frac{2}{3}(u(x) - \bar{u}(x)) - \frac{1}{3}(d(x) - \bar{d}(x)) \right\} &= 1 \\ \int_0^1 \frac{dx}{x} \left\{ \frac{2}{3}(d(x) - \bar{d}(x)) - \frac{1}{3}(u(x) - \bar{u}(x)) \right\} &= 0 \end{aligned} \quad (6.9)$$

Thus

$$\begin{aligned} \int_0^1 \frac{dx}{x} (u(x) - \bar{u}(x)) &= 2 \\ \int_0^1 \frac{dx}{x} (d(x) - \bar{d}(x)) &= 1 \end{aligned} \quad (6.10)$$

Furthermore, the nucleon has net strangeness zero, so:

$$\int_0^1 \frac{dx}{x} (s(x) - \bar{s}(x)) = 0 \quad (6.11)$$

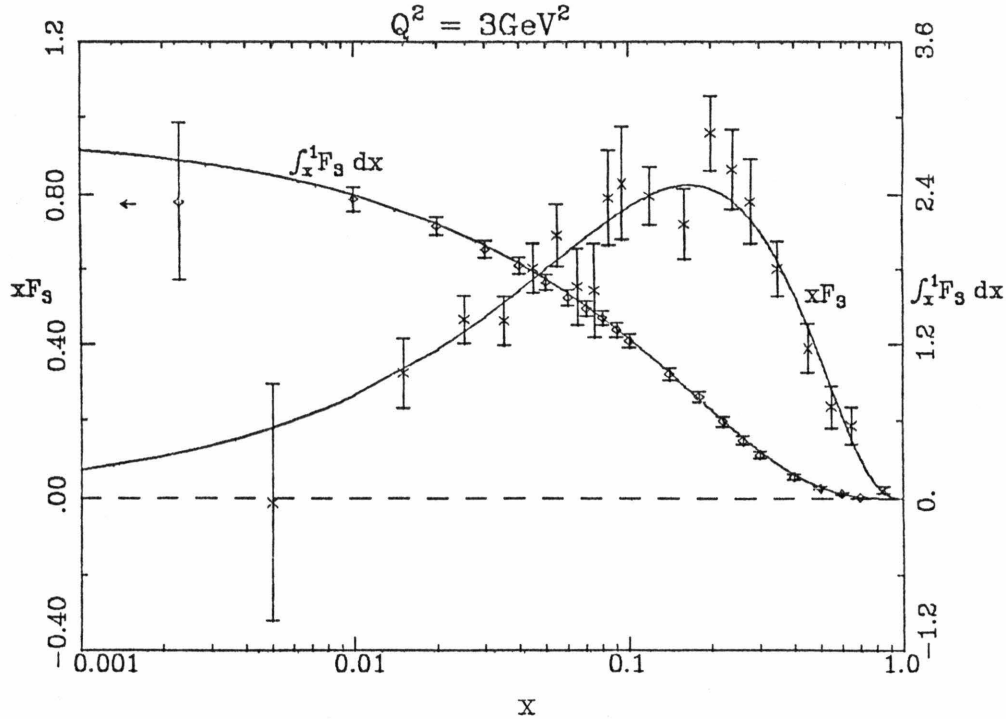


Figure 6.21  $xF_3$  and  $\int_0^x F_3 dx$  at  $Q^2 = 3\text{GeV}^2$  with global fit  $xF_3(x) = Ax^\alpha(1-x)^\beta$

Combining these results, it can be seen that the quark-parton model result for the GLS sum rule is:

$$\int_0^1 \frac{dx}{x} xF_3(x, Q^2) = \int_0^1 \frac{dx}{x} (q(x) - \bar{q}(x)) = 3 \left( 1 - \frac{\alpha_S(Q^2)}{\pi} \right) \quad (6.12)$$

Equation 6.12 includes the correction due to QCD beyond the leading log approximation.

Summarized here are results for the GLS sum rule reported by M.Purohit [Pu84]. The experimental measurement of the integral of  $F_3$  receives important contributions from the small  $x$  region. In fact, roughly half the integral comes from  $x$  below 0.06. The excellent small  $x$  resolution of this experiment allows us to make a nearly model independent measurement. However, the reported result is necessarily at low  $Q^2$ , since the accessible  $Q^2$  range at small  $x$  was limited. The technique used was to divide the integral into two portions. Above  $x = 0.06$ ,  $xF_3/x$  was numerically integrated. Below this point,  $xF_3$  was extracted in six bins of width 0.01, and fit to the form  $Ax^\alpha$ . The best value for  $\alpha$  was  $0.58 \pm 0.18$ . This is consistent with the expectation [Fi77] that  $xF_3$  behaves like  $\sqrt{x}$  as  $x \rightarrow 0$ . The result for the GLS sum rule was  $2.79 \pm .28 \pm .14$  at  $Q^2 = 3\text{GeV}^2$ , where the first error is statistical and the second the scale uncertainty for  $xF_3$ . A more model dependent fit of the form  $Ax^\alpha(1-x)^\beta$  yielded a consistent value of  $2.83 \pm .15$ , with  $\beta = 0.58 \pm .06$ . These results indicate that  $\Lambda_{QCD} < 600\text{MeV}$ . Figure 6.21 shows the  $x$  dependence of both  $xF_3$  and the integrated value of  $F_3$  at  $Q^2 = 3\text{GeV}^2$ .

## 6.4 QCD Formalism

A brief summary of the perturbative QCD description of deep-inelastic scattering processes is presented here. The reader interested in a more complete and rigorous discussion is referred to the extensive literature on the subject, such as review articles by Altarelli [Al82] or Field [Fi78,Fi79]. For QCD beyond leading order the work of Curci, Furmanski and Petronzio [Cu80,Fu82] has been useful.

Quantum Chromodynamics (QCD) is the most promising field theoretic description of the strong interaction. Formally, QCD is a non-Abelian gauge theory based on the SU(3) (colour) group [Po73,Gr73]. In this description, forces among coloured quarks are mediated by the exchange of massless vector gluons. The exchanged particles are also coloured and therefore self-coupling. The coupling between quarks and gluons,  $\alpha_S(Q^2)$ , decreases logarithmically with increasing momentum transfer,  $Q^2$ : the theory is asymptotically free. In leading order:

$$\begin{aligned}\alpha_S(Q^2) &= \frac{4\pi}{\beta_0 \ln Q^2/\Lambda^2} \\ \beta_0 &= 11 - \frac{2}{3}N_f\end{aligned}\tag{6.13}$$

where  $N_f$  is the number of quark flavours, and  $\Lambda$  is the QCD scale parameter, related to the renormalization point. This implies that high  $Q^2$  elements of processes are calculable using perturbation theory and Feynman rules derived from the quantized QCD lagrangian. However, those elements of the process involving low  $Q^2$  cannot be so addressed. Suitable division of problems into high and low  $Q^2$  parts is a necessary precursor to solution in terms of QCD.

For the deep-inelastic scattering problem, this division has been made in analogy to the quark-parton model. Structure functions are calculated by convoluting parton densities with parton-current cross sections. The validity of such a procedure rests on the assumption that partons within the nucleon have limited  $k_\perp$  and are quasi-free. The quark-parton interaction is therefore a high  $Q^2$  process: modifications to the pointlike cross section are significant and calculable. In lowest order, this is handled by absorbing the leading-log corrections to the cross section into the definition of the parton density: the parton density becomes effectively  $Q^2$  dependent. As the current probes the nucleon with larger  $Q^2$ , quarks are resolved into quark plus anti-quark pairs, or quark plus gluon. Thus the evolution of quark densities with  $Q^2$  can be described. The aspect of the problem which is not calculable is the intrinsic distribution of quarks within the nucleon: this depends on long range and low  $Q^2$  interactions among constituent quarks. Also, distortions observed in intrinsic quark distributions due to the nuclear environment in which the quark is found cannot at present be predicted.

The Altarelli-Parisi equations [Al77] represent a quantitative statement of the solution to the deep-inelastic scattering problem:

$$\begin{aligned}
\frac{dF_2(x, Q^2)}{d \ln Q^2} &= \frac{\alpha_S(Q^2)}{2\pi} \left\{ P_{qq}^{(0)}(x) \otimes F_2(x, Q^2) + 2N_f P_{qG}^{(0)}(x) \otimes G(x, Q^2) \right\} \\
\frac{dG(x, Q^2)}{d \ln Q^2} &= \frac{\alpha_S(Q^2)}{2\pi} \left\{ P_{Gq}^{(0)}(x) \otimes F_2(x, Q^2) + P_{GG}^{(0)}(x) \otimes G(x, Q^2) \right\} \\
\frac{dx F_3(x, Q^2)}{d \ln Q^2} &= \frac{\alpha_S(Q^2)}{2\pi} P_{qq}^{(0)}(x) \otimes x F_3(x, Q^2)
\end{aligned} \tag{6.14}$$

where

$$f(x) \otimes g(x) = \int_x^1 \frac{dz}{z} f\left(\frac{x}{z}\right) g(x) \tag{6.15}$$

The splitting functions,  $P_{ij}^{(0)}(z)$ , describe the probability of finding a parton  $i$  with momentum  $z$  produced by a parent parton  $j$ . These probabilities are completely determined by the theory:

$$\begin{aligned}
P_{qq}^{(0)}(z) &= \frac{4}{3} \left\{ \frac{1+z^2}{(1-z)_+} + \frac{3}{2} \delta(z-1) \right\} \\
P_{qG}^{(0)}(z) &= \frac{1}{2} \{ z^2 + (1-z)^2 \} \\
P_{Gq}^{(0)}(z) &= \frac{4}{3} \left\{ \frac{1+(1-z)^2}{z} \right\} \\
P_{GG}^{(0)}(z) &= 6 \left\{ \frac{z}{(1-z)_+} + \frac{1-z}{z} + z(1-z) + \frac{33-2N_f}{36} \delta(z-1) \right\}
\end{aligned} \tag{6.16}$$

where  $(1-z)_+^{-1}$  is defined by

$$\int_x^1 dz \frac{h(z)}{(1-z)_+} = h(z=1) \ln(1-x) + \int_x^1 dz \frac{h(z) - h(z=1)}{1-z}$$

The evolution of the singlet distribution,  $F_2$ , can be seen to receive contributions from two terms: (1) quark bremsstrahlung and (2) pair production from the unknown gluon distribution,  $G(x, Q^2)$ . The gluon distribution itself evolves with  $Q^2$ . Thus, a coupled set of integral-differential equations simultaneously describe the evolution of  $F_2$  and  $G$ . The evolution of the non-singlet combination of quark densities,  $x F_3$ , has a more simple description. Here the contribution of gluon pair production to quark and anti-quark sea distributions cancels, leaving just the quark bremsstrahlung term.

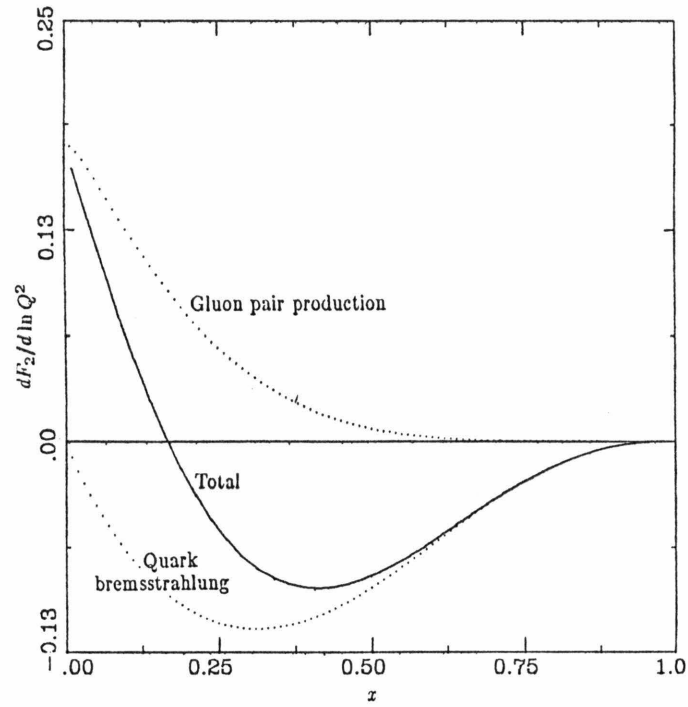


Figure 6.22 QCD prediction for  $dF_2/d \ln Q^2$  at  $Q^2 = 5 \text{ GeV}^2$  using nominal structure functions

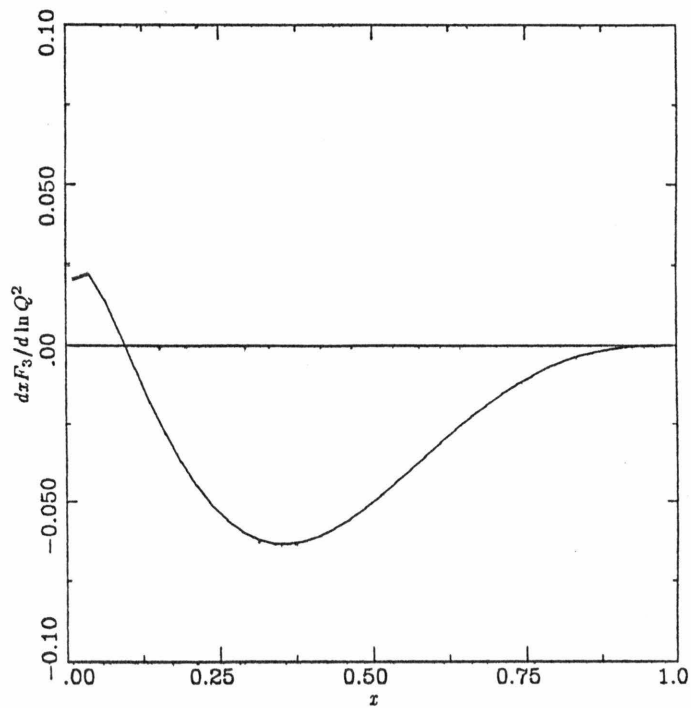


Figure 6.23 QCD prediction for  $dx F_3/d \ln Q^2$  at  $Q^2 = 5 \text{ GeV}^2$  using nominal structure functions

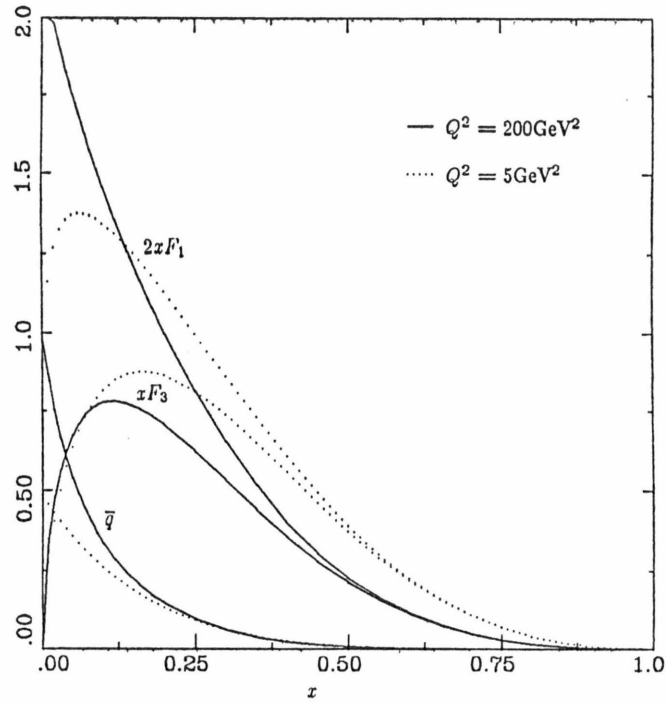


Figure 6.24 Quark distributions at  $Q^2 = 5 \text{ GeV}^2$  and  $200 \text{ GeV}^2$  using nominal structure functions

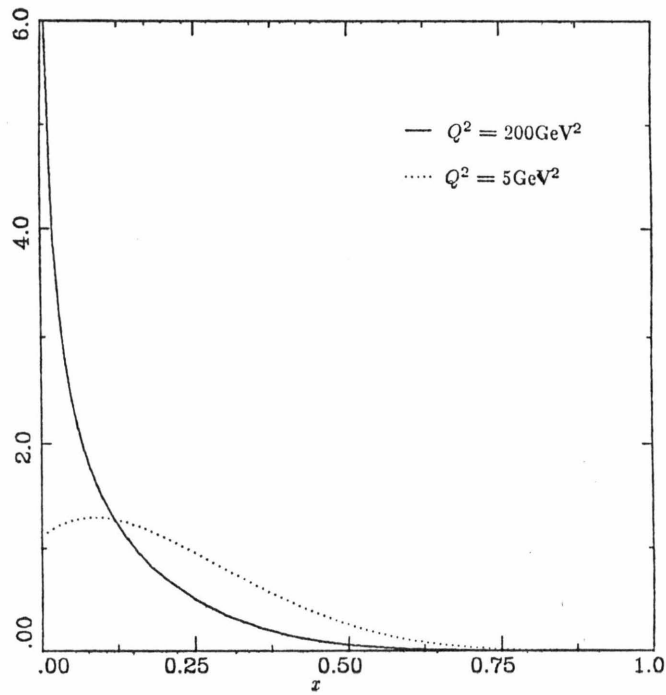


Figure 6.25 Gluon distributions at  $Q^2 = 5 \text{ GeV}^2$  and  $200 \text{ GeV}^2$  using nominal structure functions

In figure 6.22, a typical example of the predicted variation of  $dF_2/d \ln Q^2$  with  $x$  is shown, with the level of contribution from quark bremsstrahlung and gluon pair production separately indicated. In this particular example, for  $x > 0.15$  the losses due to quark radiation exceed gains from gluon pair production. For  $x < 0.15$  the second process contributes more than the first. The observed pattern of scaling violations in  $F_2$  conforms to these expectations. As can be seen in figure 6.1,  $F_2$  at small  $x$  increases with  $Q^2$ , and at large  $x$  decreases. Figure 6.23 shows the corresponding variation with  $x$  of  $dx F_3/d \ln Q^2$ , which receives contributions only from quark bremsstrahlung.

Another useful way of illustrating the features induced in parton distributions by QCD scaling violations is to compare distributions at two different values of  $Q^2$ . In figure 6.24 and 6.25 are shown typical values for  $2xF_1 = q + \bar{q}$ ,  $x F_3 = q - \bar{q}$ ,  $\bar{q}$  and the gluon distribution at  $Q^2 = 5\text{GeV}^2$  and  $Q^2 = 200\text{GeV}^2$ . The migration of valence quarks to smaller  $x$  is clearly evident in  $x F_3$ . The increase in the sea quark distributions at small  $x$  due to gluon pair production results in the corresponding increase of  $F_2$  at small  $x$ . Along with losses at high  $x$  from pair production, the gluon distribution rises sharply at small  $x$  due to quark bremsstrahlung.

Calculations of the next-to-leading order corrections to the Altarelli-Parisi equations have recently been made (see [Fu82] for the long list of contributors to this work). Presuming the perturbation series to be convergent, these calculations offer a more accurate prediction of the processes under consideration. For example, calculations beyond the leading order lead to predictions for a finite value for  $F_L = F_2 - 2xF_1$  or  $R$ , proportional to  $\alpha_s(Q^2)$ :

$$\begin{aligned} F_L &= \frac{\alpha_s(Q^2)}{2\pi} \int_x^1 \frac{dy}{y^3} \left\{ \frac{8}{3} F_2(y, Q^2) + \frac{40}{9} y G(y, Q^2) \left(1 - \frac{x}{y}\right) \right\} \\ R &= \frac{F_L}{2xF_1} \end{aligned} \quad (6.17)$$

Neglecting  $Q^2$  variation in the quark and gluon distributions,  $F_L$  should decrease logarithmically with  $Q^2$ . Also, it is evident that  $F_L$  should be large at small  $x$  and small at large  $x$ .

There is an additional consideration. The strong coupling constant is a solution to the renormalization group equations. In leading order the most general solution is:

$$\alpha_s(Q^2) = \frac{4\pi}{\beta_0(\ln Q^2/\Lambda^2 + c)} = \frac{4\pi}{\beta_0 \ln Q^2/\Lambda^2} + O(\alpha_s^2) \quad (6.18)$$

where  $\beta_0$  is given in equation 6.13. The constant  $c$  is equivalent to  $O(\alpha_s^2)$  corrections to the leading order expression, and can in general differ from process to process. Only by including next-to-leading order effects will the value of  $\Lambda$  be the same from different processes. This implicitly assumes that  $O(\alpha_s^3)$  corrections are small.

Beyond leading order, several renormalization schemes appear in the literature; commonly the  $\overline{\text{MS}}$  scheme is used which minimizes the  $O(\alpha_s^2)$  corrections to the evolution equations. There is a further ambiguity in the precise factorization of structure functions into parton densities and parton-current cross sections. One approach is to evolve universal parton densities

according to:

$$\begin{aligned}
\frac{dq(x, Q^2)}{d \ln Q^2} &= \frac{\alpha_S(Q^2)}{2\pi} \{P_{qq}(x) \otimes q(x, Q^2) + P_{q\bar{q}}(x) \otimes \bar{q}(x, Q^2) \\
&\quad + P_{qG}(x) \otimes G(x, Q^2)\} \\
\frac{d\bar{q}(x, Q^2)}{d \ln Q^2} &= \frac{\alpha_S(Q^2)}{2\pi} \{P_{\bar{q}q}(x) \otimes q(x, Q^2) + P_{\bar{q}\bar{q}}(x) \otimes \bar{q}(x, Q^2) \\
&\quad + P_{\bar{q}G}(x) \otimes G(x, Q^2)\} \\
\frac{dG(x, Q^2)}{d \ln Q^2} &= \frac{\alpha_S(Q^2)}{2\pi} \{P_{Gq}(x) \otimes q(x, Q^2) + P_{G\bar{q}}(x) \otimes \bar{q}(x, Q^2) \\
&\quad + P_{GG}(x) \otimes G(x, Q^2)\}
\end{aligned} \tag{6.19}$$

Here the splitting functions  $P_{ij}$  include the first order terms of equation 6.16 plus  $O(\alpha_S)$  corrections:

$$P_{ij} = P_{ij}^{(0)}(x) + \frac{\alpha_S(Q^2)}{2\pi} P_{ij}^{(1)}(x) \tag{6.20}$$

The structure functions obtained from specific deep-inelastic scattering processes are constructed by convoluting these universal parton densities with the corresponding short distance cross section (coefficient functions) calculated to  $O(\alpha_S)$ :

$$F_i(x, Q^2) = \sum_j C_j^i(x) \otimes q_j(x, Q^2) + C_G^i(x) \otimes G(x, Q^2) \tag{6.21}$$

The form of the splitting functions and coefficient functions can be found in the literature [Cu80, Fu82]. Of course, as in first order, there is no contribution from the gluons to the evolution of  $xF_3$ . However, QCD beyond the leading order predicts a difference between  $2xF_1$  and  $F_2$ , as manifested in the formalism by different coefficient functions for  $2xF_1$  and  $F_2$ . This two-step method was the approach adopted in a program written by Duke [De83] and later supplied for our use. Charge and momentum sum rules in these universal parton densities are preserved to all orders.

Alternatively, the definition of parton densities can be fixed to some specific process. A common choice is to preserve the Adler sum rule to all orders:

$$\int_0^1 \frac{dx}{x} \{F_2^{\nu n} - F_2^{\nu p}\} = 2 \tag{6.22}$$

Evolution of structure functions is accomplished directly, using an appropriately modified set of splitting functions. The virtue of this second approach is computational simplicity. The program used and supplied by Barnett [Ab80] for next-to-leading order fits to  $xF_3$  uses this one-step method. The observable structure functions are of course the same in either method; how they are parametrized in terms of parton distributions is ambiguous.

For completeness, it should be mentioned that there are processes and effects at low  $Q^2$  and low  $W^2$  which can contribute scaling violations to the data decreasing with inverse

powers of  $Q^2$ . These include (1) scattering from di-quark or multi-quark components of the nucleon wave function, (2) the intrinsic  $k_\perp$  distributions of quarks leading to finite values of  $R$ , (3) quark mass thresholds and (4) target mass corrections. In a global view of existing data, it is evident that at high  $x$  there is a considerable difference between the amount of scaling violation observed in low  $Q^2$  experiments, such as SLAC [Bo79], and the more recent higher  $Q^2$  results. This was noted in section 6.2 above. The difference cannot be accommodated in a global QCD fit, but does suggest significant higher-twist contributions to scaling violations at small  $W^2$  [Ei81]. This region was not included in any of the QCD fits described below.

### 6.5 QCD Fits

Several methods exist for comparing data with QCD predictions. One particularly simple form is the moment equations for the non-singlet distribution:

$$M_n(Q^2) = \int_0^1 \frac{dx}{x} x^n F_3(x, Q^2) \quad (6.23)$$

In this case, the convolution integral for  $xF_3$  (equation 6.14) reduces to a simple product, so that:

$$\frac{d \ln M_n(Q^2)}{d \ln Q^2} = \frac{\alpha_S(Q^2)}{2\pi} a_n \quad (6.24)$$

where  $a_n$  is the  $n^{\text{th}}$  moment of the splitting function,  $P_{qq}^{(0)}(z)$ . Ratios of moments are predicted to vary linearly with slopes fixed by the theory. From equation 6.24, it can be shown that the moments decrease in inverse powers of  $\ln Q^2/\Lambda^2$ , which also can be tested. A summary of results from other experiments using these techniques can be found in the review by Söding and Wolf [So81]. The principal limitation of such methods is that in order to compute the moments, substantial extrapolation outside the measured  $x$  region is necessary.

An alternative method has been suggested by Buras and Gaemers [Bu77, Bu78]. Simple analytic expressions for quark distributions were constructed, which represented approximate solutions to the Altarelli-Parisi equations. For the valence quarks, the distributions reproduced the expected scaling violations of the first 12 moments to within 2%. The sea and gluon distributions were less well modeled. However, efficient numerical integration of the equations using a computer allows the use of a less restrictive model, with hardly any more difficulty.

These data therefore have been fit to QCD predictions for parton distributions directly evolved using numerical integration. As noted in section 6.4, programs have been provided by Barnett [Ab80] and Duke [De83] to accomplish this end. The strategy employed is to start with a suitable general functional form for the quark distributions at some  $Q_0^2$ , and evolve to all other required  $Q^2$ . The parameter  $\Lambda$ , through the strong coupling constant  $\alpha_S(Q^2)$ , controls the amount of scaling violation predicted. The virtue of the technique lies in directly comparing prediction with measurement in accessible kinematic regions.

The various functional forms assumed for the behavior of  $G$ ,  $F_2$  and  $xF_3$  at  $Q_0^2$  were:

$$\begin{aligned} G(x, Q_0^2) &= a_G(1-x)^{c_G}(1+\gamma_G x) \\ F_2(x, Q_0^2) &= a_2(1-x)^{c_2}(1+\gamma_2 x) \\ xF_3(x, Q_0^2) &= a_3x^{b_3}(1-x)^{c_3}(1+\gamma_3 x) \end{aligned} \tag{6.25}$$

The motivation for these particular choices is much the same as that described in relation to the calculational model used for integrations necessary for structure function extraction (section 5.2.2). Along with  $\Lambda$ , appropriate subsets of these parameters were varied until a minimum  $\chi^2$  was obtained.

Several subtle limitations of this approach have been reported [De83]. First, the amount of scaling violation induced in the data by the essentially unmeasured region above  $x = 0.65$  is substantial, and depends on the functional form assumed for the behavior of the quark distributions in this region. Second, there is an inconsistency between the usual prescriptions for making target mass corrections: the use of Nachtmann moments [Na73] and the Georgi-Politzer [Ge76a, Ge76b] convolution integrals in momentum space. To address this last difficulty, fits were restricted to the region  $Q^2 > 5\text{GeV}^2$  and  $W^2 > 10\text{GeV}^2$ , as these authors have recommended.

The relative statistical precision with which  $F_2$  is measured would seem to offer the best opportunity for testing QCD. However, the evolution of  $F_2$  is complicated by coupling to the evolution of the gluon distribution. The form of  $G$  is not directly probed by the deep-inelastic processes considered here. Hence, fits to singlet combinations of quark distributions contain additional free parameters. The nature of the contribution of the gluon distribution to scaling violations in  $F_2$  is not well constrained by  $F_2$  alone. It is difficult to decouple the correlation between  $\Lambda$  and parameters of the gluon distribution.

This can be seen in figure 6.22. The values of  $F_2$  imply through the quark bremsstrahlung term a  $\Lambda$  dependent expectation for the level of scaling violation in the data. In fits to  $F_2$  alone, the deviations in the  $x$  dependence of these scaling violations from this expectation are all that determine the gluon distribution. The integral of  $G$  is normally fixed by the momentum sum rule (equation 6.26 below), but the distribution in  $x$  needs to be determined. If the fraction of gluons at large  $x$  were increased, for example by decreasing  $c_g$ , the same values for  $dF_2/d\ln Q^2$  could be obtained by increasing  $\Lambda$ . Thereby, the contributions from the quark bremsstrahlung term would be increased to offset the increased component of the scaling violations due to the gluon term. Clearly, distortions in the predicted  $x$  dependence of  $dF_2/d\ln Q^2$  would result. However, there is relatively little correlation between small and large  $x$  behavior embodied in the functional form used for the gluons. It is unreasonable, and in fact undesirable, to expect that the fitted form of the gluons at small  $x$  should strongly limit the behavior of  $G$  at large  $x$ . Therefore, it is beyond the statistical power of the present measurements of  $F_2$  alone to well constrain the fraction of gluons at large  $x$ .

Alternatively, fits to  $xF_3$  could be used to determine  $\Lambda$ . Since the evolution of this structure function does not depend on the gluon distribution, potentially a unique opportunity exists to make a measurement of  $\Lambda$  with minimum assumption. From the experimental point

	Leading Order $R = 0.0$	Second Order(MS) $R = R_{QCD}$
$\Lambda$	$360 \pm 100\text{MeV}$	$340 \pm 110\text{MeV}$
$a_2$	$1.525 \pm .086$	$1.808 \pm .092$
$c_2$	$2.85 \pm .16$	$3.36 \pm .15$
$\gamma_2$	$1.87 \pm .56$	$2.14 \pm .57$
$\chi^2$	45.5 for 39 DF	45.5 for 39 DF

Table 6.1

Best values for free parameters obtained in fits to  $F_2$  with  $c_G = 4.6$  and  $\gamma_G = 9.0$

of view,  $xF_3$  is also attractive since extraction is nearly independent of the value of  $R$  and assumptions about the strange sea. However, the data are statistically less precise than  $F_2$ , and the resulting best values for  $\Lambda$  have large errors.

### 6.5.1 $F_2$ analysis

Fits were made to  $F_2$  in the region  $Q^2 > 5\text{GeV}^2$  and  $W^2 > 10\text{GeV}^2$ , where target mass, higher-twist and quark mass threshold corrections should be small. Data below  $x = 0.1$  are eliminated in an attempt to limit reliance on uncertain assumptions about the strange sea. The normalization of the gluon distribution at  $Q_0^2 = 5\text{GeV}^2$  was obtained from the momentum sum rule:

$$\int_0^1 G(x, Q^2) dx = 1 - \int_0^1 F_2(x, Q^2) dx \quad (6.26)$$

As expected, fits using  $F_2$  alone were unable to significantly constrain the other gluon parameters. These parameters were therefore fixed to reasonable values:  $c_G = 4.6$  and  $\gamma_G = 9.0$ . Target mass corrections were made following the prescription of Georgi and Politzer [Ge76a, Ge76b]. Due to the  $Q^2$  and  $W^2$  restrictions noted above, these corrections resulted in changes in  $\Lambda$  of less than 15MeV.

The best values for the free parameters from a leading order fit to  $F_2$  (extracted with  $R = 0.0$ ) are listed in Table 6.1, along with associated statistical errors. Figure 6.26 shows the variation of  $\chi^2$  with  $\Lambda_{LO}$  for this fit, with minimum at  $\Lambda = 360\text{MeV}$ . The horizontal lines correspond to one standard deviation and the 90% confidence limit. The corresponding result for a second order fit to  $F_2$  (extracted with  $R = R_{QCD}$ ) is shown in figure 6.27. The best values for the free parameters from this fit are listed in the second column of table 6.1. The fit was equally good, and the value of  $\Lambda$  was 20MeV smaller than that obtained in the leading order case. The results for  $F_2$  assuming  $R = R_{QCD}$ , together with the second order QCD fit are shown in figure 6.28.

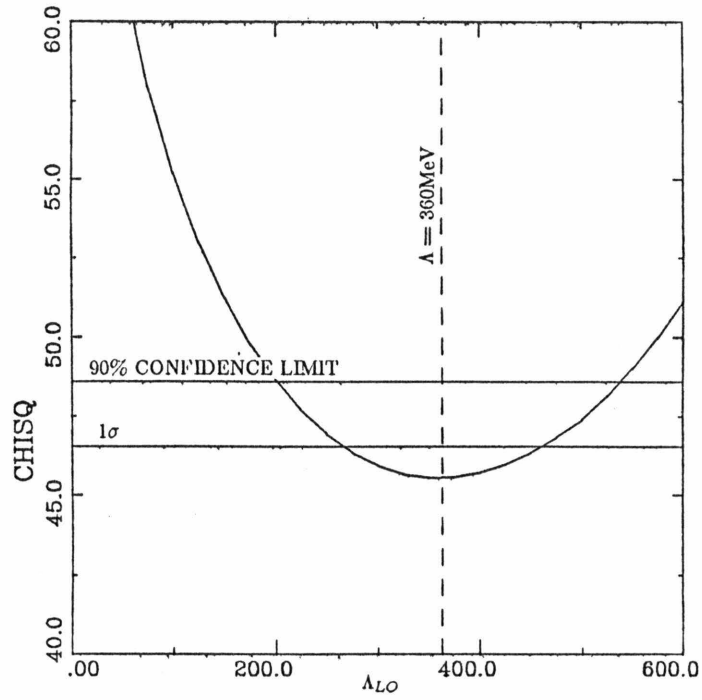


Figure 6.26  $\chi^2$  as a function of  $\Lambda_{LO}$  for fit to  $F_2$  ( $R = 0.0$ )

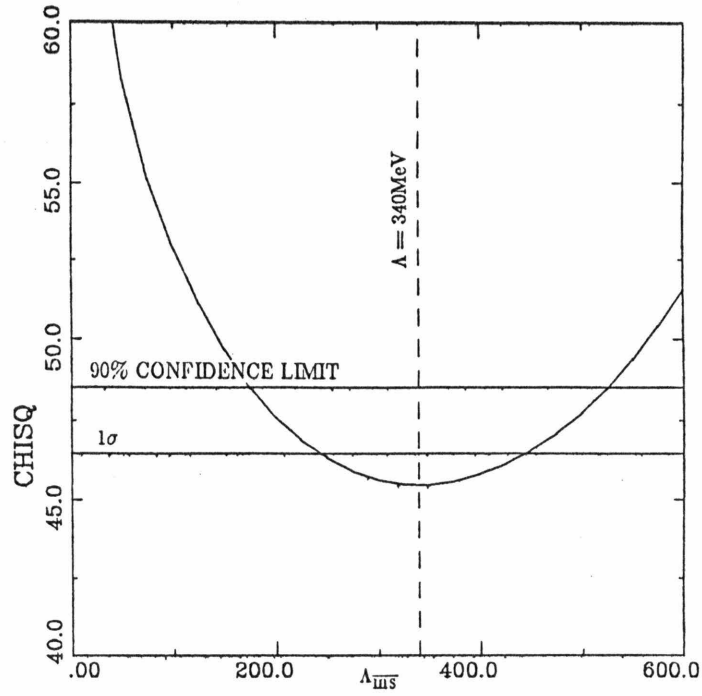


Figure 6.27  $\chi^2$  as a function of  $\Lambda_{\overline{MS}}$  for fit to  $F_2$  ( $R = R_{QCD}$ )

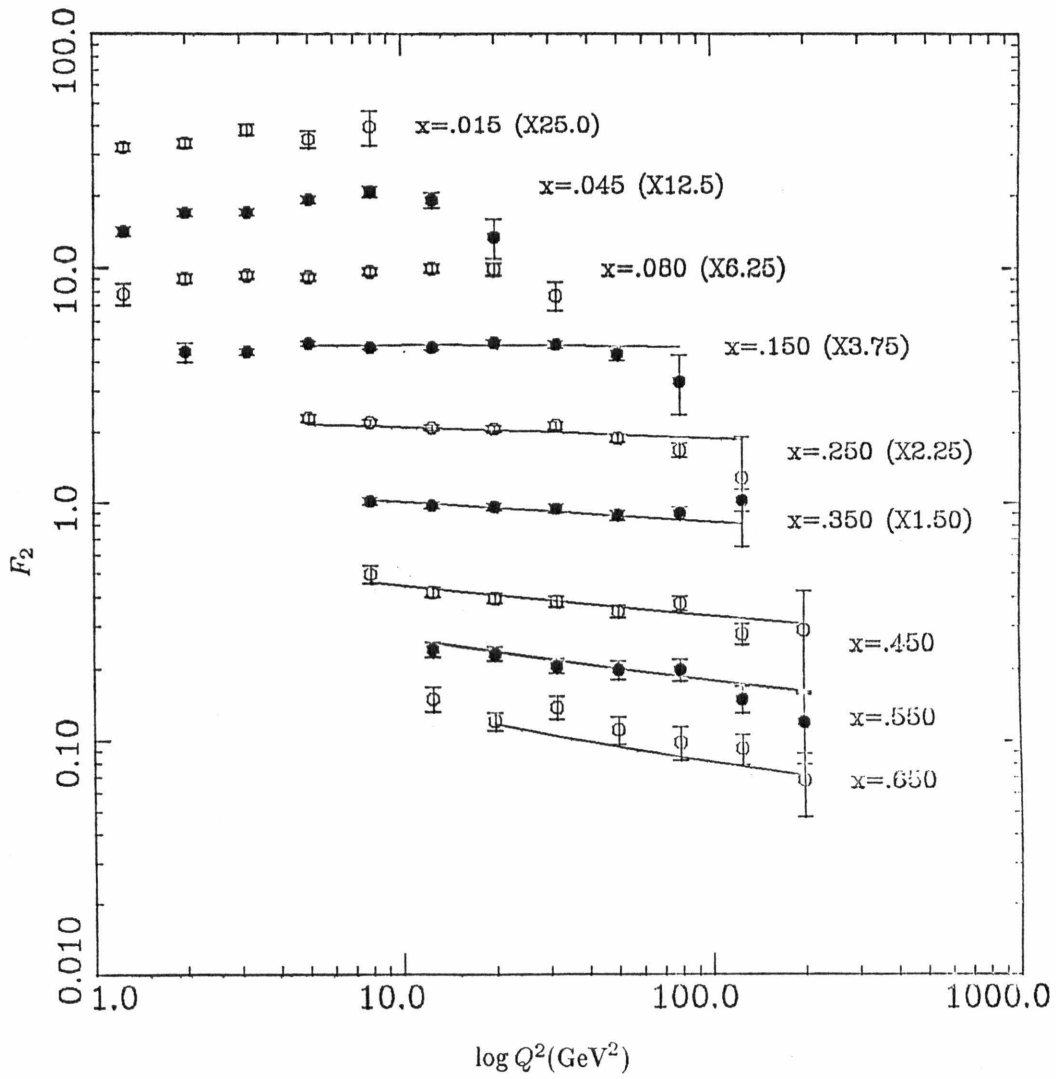


Figure 6.28  $F_2$  ( $R = R_{QCD}$ ) with second order QCD fit

It is well known [Ab82a,De83] that the fitted value of  $\Lambda$  is strongly correlated with the parameters characterizing the gluon distribution. The variation of the value obtained for  $\Lambda$  with changes in the assumed values for the parameters of the gluon distribution has been studied. The correlation between  $\Lambda_{LO}$  and  $c_G$ , for various values of  $\gamma_G$ , is shown in figure 6.29 for the leading order fit described above ( $R = 0.0$ ). Figure 6.30 shows the correlations observed for the second order fit ( $R = R_{QCD}$ ). The quark-parton model and asymptotic QCD [Al82] predict that the gluon distribution behaves at large  $x$  like  $(1-x)^{c_3+1}$ . The large  $x$  behavior of both  $xF_3$  and  $F_2$  suggest that  $c_3 \sim 3$ . It is reasonable to expect that the gluon parameters lie within the limits:  $4 \leq c_G \leq 8$  and  $\gamma_G \geq 0$ . The rms contribution to the uncertainty in the determined value of  $\Lambda$  was found to be about  $\pm 50\text{MeV}$ , if all values of the gluon parameters within the noted limits were equally probable.

The best value of  $\Lambda_{LO}$  also depended on  $R$ . The level of sensitivity is shown in table 6.2, where the results obtained for  $\Lambda$  under various assumed values for  $R$  are listed. The same gluon distribution noted above was used in all cases. The value of  $\Lambda_{LO}$  increased by  $160\text{MeV}$  in changing  $R$  from 0.1 to 0.0. Structure functions extracted with a value of  $R$  as predicted by second order QCD (equation 6.17) lie roughly midway between the  $R = 0$  and  $R = 0.1$  results.

The predicted value of  $R$  depends on both  $F_2$  and the gluon distribution. The correlation between  $\Lambda$  and the gluon parameters shown in figure 6.30 does not take this fact into account. The shift in  $\Lambda$  was observed for two extreme assumptions about the gluon distribution: ( $c_G = 3, \gamma_G = 1000$ ) and ( $c_G = 8, \gamma_G = 0$ ). The change produced was in a direction to reduce the sensitivity to the gluon distribution: at ( $c_G = 3, \gamma_G = 1000$ ) the value of  $\Lambda$  shifted down by  $30\text{MeV}$  and at ( $c_G = 8, \gamma_G = 0$ ) the value shifted up by  $30\text{MeV}$ . Hence, if properly included, the effect of using a predicted value for  $R_{QCD}$  would reduce the maximum range of variation induced in  $\Lambda$  by variations in the assumed gluon distribution. Most of the shift was found to be due to changes in the  $x$  dependence of  $R$  resulting from different gluon distributions. The effect on  $\Lambda$  of changing the amount of scaling violation in  $R$  was found to be negligible.

Considerable variation in the best value for  $\Lambda$  also arises from changing assumptions about the strange sea. If the strange sea were full rather than half  $SU(3)$  symmetric,  $\Lambda$  would increase by  $70\text{MeV}$ . The uncertainty in our measurement of the strange sea fraction,  $\lambda_s = 0.5 \pm_{.18}^{.16}$ , implies the assignment of a  $\pm 25\text{MeV}$  uncertainty to  $\Lambda$  from this source. Furthermore, the effect of changing the charm quark mass used in slow rescaling was also significant. If the effective charm mass were raised to  $1.8\text{GeV}^2$ , and  $\lambda_s$  in correspondence increased to 0.55, the value of  $\Lambda$  was found to fall by  $25\text{MeV}$ . Conversely, a mass of  $1.2\text{GeV}$  and fraction  $\lambda_s$  produced a rise of  $25\text{MeV}$ . Reasonable variation of the assumptions about the strange sea therefore led to uncertainties in  $\Lambda$  of about  $\pm 35\text{MeV}$ .

	$\Lambda_{LO}$	$\Lambda_{\overline{MS}}$
$R = 0.0$	$360 \pm 100\text{MeV}$	$390 \pm 110\text{MeV}$
$R = 0.1$	$200 \pm 90\text{MeV}$	$230 \pm 100\text{MeV}$
$R_{QCD}$	$300 \pm 100\text{MeV}$	$340 \pm 110\text{MeV}$

Table 6.2 Variation of the best value of  $\Lambda$  with the assumed  $R$

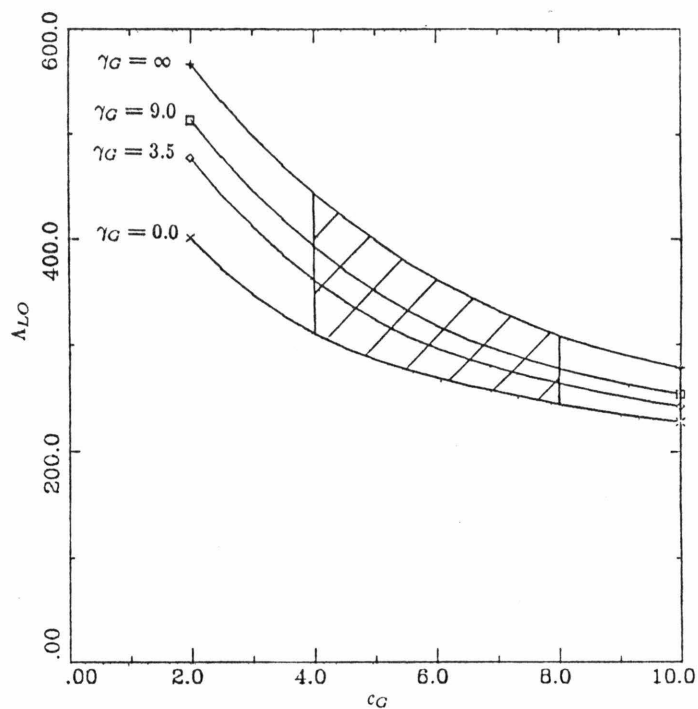


Figure 6.29 Correlation between  $\Lambda_{LO}$  and  $c_G$  for fits to  $F_2$  ( $R = 0.0$ )

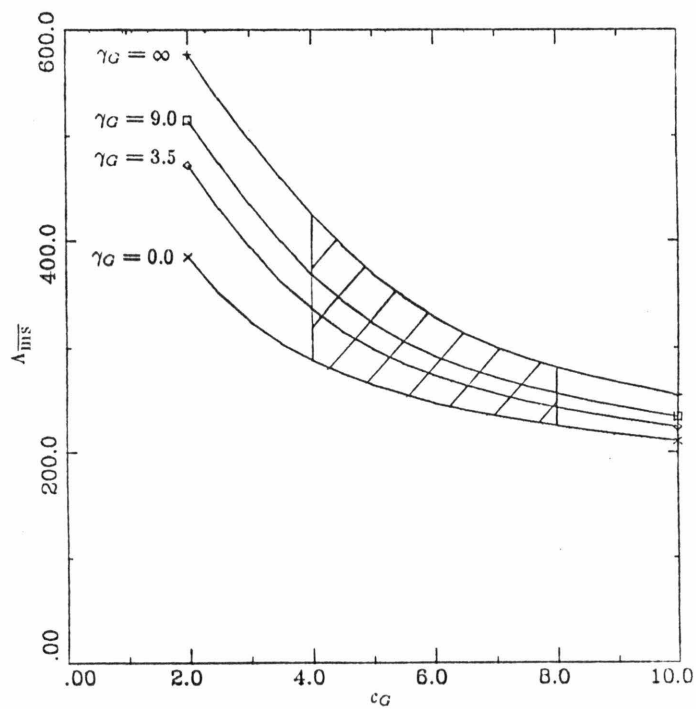


Figure 6.30 Correlation between  $\Lambda_{\overline{MS}}$  and  $c_G$  for fits to  $F_2$  ( $R = R_{QCD}$ )

Source of error	Change in $\Lambda_{LO}$
Gluon distribution	$\pm 50\text{MeV}$
Strange sea	$\pm 35\text{MeV}$
Flux smoothing	$\pm 25\text{MeV}$
Flux level	$\pm 30\text{MeV}$
Secondary beam dispersion	$\pm 10\text{MeV}$
Hadron energy calibration	$\pm 15\text{MeV}$
Muon energy calibration	$\pm 15\text{MeV}$
Total (excluding gluon contribution)	$\pm 57\text{MeV}$

Table 6.3 Approximate systematic errors on  $\Lambda_{LO}$  from fits to  $F_2$ 

	$\bar{R} = 0.1$	$R = 0.0$	$R = R_{QCD}$
$W^2 > 10\text{GeV}^2$	$200 \pm 90\text{MeV}$	$360 \pm 100\text{MeV}$	$300 \pm 100\text{MeV}$
$W^2 > 20\text{GeV}^2$	$180 \pm 130\text{MeV}$	$410 \pm 150\text{MeV}$	$310 \pm 140\text{MeV}$
$W^2 > 30\text{GeV}^2$	$250 \pm 210\text{MeV}$	$520 \pm 230\text{MeV}$	$410 \pm 200\text{MeV}$

Table 6.4 Best values for  $\Lambda_{LO}$  as a function of the  $W^2$  cut

The uncertainty contributed by systematic measurement errors has also been evaluated. For each of the partially correlated sources of systematic error, such as the normalization errors, an ensemble of twenty experiments was randomly thrown as described in section 5.6. The resulting values for  $F_2$  from each of these pseudo experiments were fit using the same procedure described above. The rms of the distribution of fit values for each of the parameters was taken as the systematic error on that parameter due to the source under consideration. The systematic error on  $\Lambda_{LO}$ , due to normalization errors and the flux smoothing procedure, was thereby determined to be  $\pm 40\text{MeV}$  for  $F_2$ .

For completely correlated sources of error, such as the calibration error on  $E_\mu$ , a fit was made to the values of  $F_2$  shifted by an amount corresponding to a one sigma variation of the particular source of systematic error. Consistent with the remarks made in section 5.6, the contribution of uncertainties in secondary beam dispersion was evaluated by shifting the dispersion at all settings by one sigma. This represented the extreme case. If instead a large component of the uncertainty was not correlated from setting-to-setting, the error due to dispersion would be smaller. Collected in table 6.3 are estimates of systematic errors on  $\Lambda$  due to various measurement errors. As expected, these are considerably smaller than statistical errors.

The effect of raising the  $W^2$  cut was studied. Systematic changes in the fit value of  $\Lambda$  as a function of the  $W^2$  cut have been observed in other data sets [Ba82b]. This has been interpreted as possible evidence for substantial contributions by higher-twist terms to the scaling violations in these data. As shown in table 6.4, there is a systematic trend observable in our data also. However, the changes are well within errors and are in a direction opposite to that seen in fits to the CDHS and EMC results for  $F_2$ .

### 6.5.2 Comparison with results from other experiments

Comparisons of results for  $\Lambda$  from  $F_2$  are complicated by the many different assumptions made by the various experiments in both extracting the structure function and in making the QCD fits. Different assumptions about  $R$ , and for neutrino experiments about the strange sea, have been shown to induce large changes in the value of  $\Lambda$ . The results are also sensitive to assumptions about the gluon distribution. This includes the use by some groups of the non-singlet evolution equation for fits to  $F_2$  above some  $x$  value: implicitly, the effect of the gluons is assumed to be negligible above that  $x$ .

Despite these complications, it is clear that results from deep-inelastic experiments in the  $Q^2$  range covered by this experiment are consistent. This conclusion is in part drawn from the literature, such as studies by Duke [De83]. It can also be illustrated by the specific examples. Where possible, for the comparisons listed in table 6.5, our  $F_2$  results were fit under the same assumptions about the gluon distribution and  $R$  as the particular experiment under consideration. The one exception was the result attributed to the CDHS collaboration. This value was obtained using the program supplied by Duke [De83] to fit published data [Ab83] from that group. Differences between pairs of results can be seen to lie within statistical errors. The agreement was not unexpected, given the similar behavior among the experiments of  $d \ln F_2 / d \ln Q^2$  noted earlier. This is not to say that  $\Lambda$  is well determined: the mean value from the ensemble of experiments can vary considerably depending on the choice for the gluon distribution or  $R$ .

This agreement among current results is in contrast with the historical trend in reported results for  $\Lambda$ . Fits to measurements of  $F_2$  in lower  $Q^2$  ranges produce distinctly higher values for  $\Lambda$  [Fi82]. QCD alone would have difficulty accommodating both high and low  $Q^2$  data, possibly due to higher-twist contributions at these lower  $Q^2$ 's [Ei81, Ba82b].

### 6.5.3 $F_2$ analysis with $\bar{q}$

To obtain the results reported above, it was necessary to assume a reasonable form for the gluon distribution: a less than satisfying procedure. Analysis of  $F_2$  alone cannot simultaneously constrain the width of the gluon distribution and determine  $\Lambda$ . However, a measurement of the anti-quark distribution,  $\bar{q}(x, Q^2)$ , could be used to limit the fraction of

Experiment	Gluon distribution ( $c_G, \gamma_G$ )	$R$	$\Lambda$ (MeV)	$\Lambda_{CCFR}$ (MeV)
CDHS	(4.6, 9.0)	0.1	$240 \pm 70$	$200 \pm 90$
CHARM [Jo82]	(4.6, 0.0)	0.0	$290 \pm 90$	$240 \pm 70$
EMC [Au82a]	(5.9, 9.0)	0.0	$200 \pm 30$	$300 \pm 90$
BFP [Cl83]	(5.0, 0.0)	0.0	$230 \pm 80$	$280 \pm 90$

Table 6.5 Comparison of current measurements of  $\Lambda_{LO}$  from  $F_2$  QCD fits

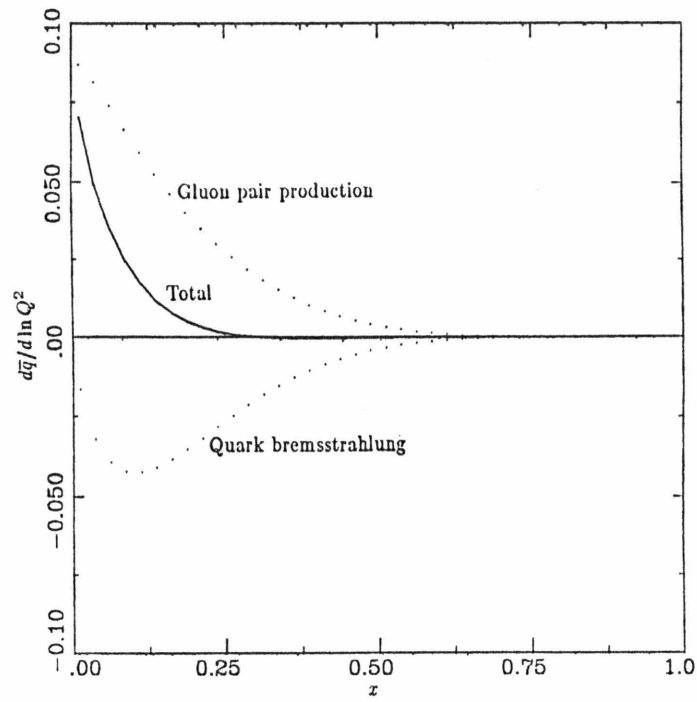


Figure 6.31 QCD prediction for  $d\bar{q}/d\ln Q^2$  at  $Q^2 = 5\text{GeV}^2$

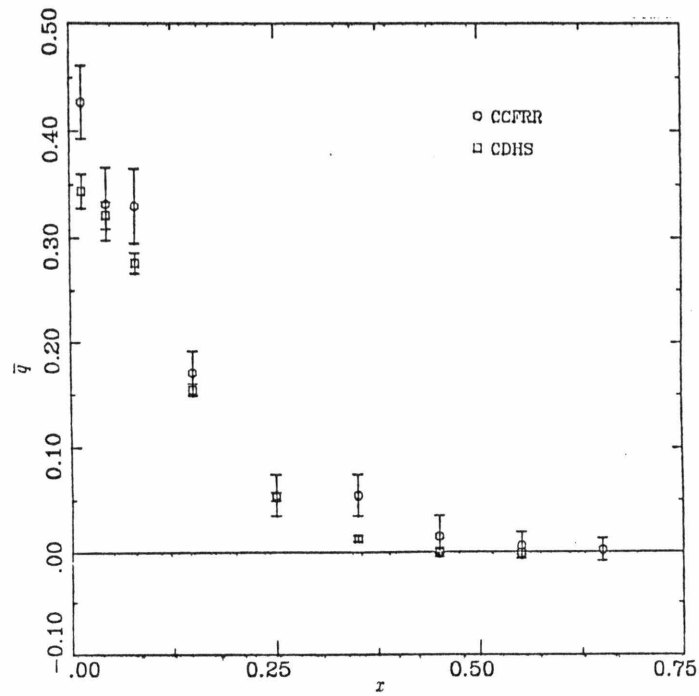


Figure 6.32 Observed average  $\bar{q}$  distribution for CCFRR and CDHS [Ab83]

gluons at large  $x$ . The evolution of  $\bar{q}(x, Q^2)$  is given by:

$$\frac{d\bar{q}(x, Q^2)}{d \ln Q^2} = \frac{\alpha_S(Q^2)}{2\pi} \left\{ P_{q\bar{q}}^{(0)}(x) \otimes \bar{q}(x, Q^2) + N_f P_{qG}^{(0)} \otimes G(x, Q^2) \right\} \quad (6.27)$$

where the  $P_{ij}^{(0)}(z)$  are the same splitting functions appearing in equation 6.16. It is the fact that the  $\bar{q}$  distribution is strongly peaked at small  $x$  which leads directly to the constraint of the gluon distribution at high  $x$ : above some  $x$  value, a null result for  $\bar{q}$  implies that the gluon term  $P_{qG}^{(0)}(x) \otimes G(x, Q^2)$  must also be small. Figure 6.31 shows the contribution to scaling violations in  $\bar{q}$  from both gluon pair production and anti-quark bremsstrahlung.

One way of measuring the anti-quark distribution is to use the difference between  $2xF_1$  and  $xF_3$ :

$$\bar{q} = \frac{1}{2}(2xF_1 - xF_3) \quad (6.28)$$

where  $2xF_1$  is obtained from  $F_2$  using the same value for  $R$  as used in the extraction of  $F_2$ :

$$2xF_1 = \left( \frac{1 + Q^2/\nu^2}{1 + R} \right) F_2 \quad (6.29)$$

The result shown in figure 6.32 for  $\bar{q}$  averaged over  $Q^2$  was obtained in this manner ( $R = R_{QCD}$  assumed). However, the measurement was not sufficiently precise to constrain the gluons.

The CDHS collaboration has published a high statistics determination of  $\bar{q}$ , from a large sample of wide-band anti-neutrino events [Ab83]. These measurements, averaged over  $Q^2$ , are also shown in figure 6.32. Our result can be seen to be consistent at large  $x$ , although with considerably larger errors. The technique used by the CDHS group to obtain this result was based on the fact that the anti-neutrino cross section at large  $y$  is due mostly to scattering from anti-quarks. From the form of the cross section shown in equation 1.16, at high  $y$  the quark contribution is clearly suppressed by a  $(1 - y)^2$  factor, but the anti-quark component is not. Such measurements are particularly suited to the CDHS detector [Ho78], which has good acceptance at high  $y$ .

It has been remarked [De83] that the values for  $\bar{q}$  so obtained are sensitive to radiative corrections and assumptions about  $R$  and the strange sea. Furthermore, there are substantial normalization and  $x$  dependence differences between the structure functions obtained by CDHS and this group. However, the near zero result above  $x = 0.30$  cannot be seriously affected by any of these uncertainties. On the basis of this argument, simultaneous fits were made to  $\bar{q}$  from CDHS above  $x = 0.30$  and  $F_2$  from this experiment. Additional parameters were introduced to describe the anti-quark distribution at  $Q_0^2$ :

$$\bar{q} = a_s(1 - x)^c \quad (6.30)$$

Cuts in  $Q^2$  and  $W^2$  were retained, but the restrictions in  $x$  were relaxed to include data above  $x = 0.04$ .

$\Lambda_{LO}$	$240 \pm 100\text{MeV}$	$250 \pm 80\text{MeV}$
$a_2$	$2.85 \pm .15$	$2.84 \pm .13$
$c_2$	$1.621 \pm .090$	$1.602 \pm .070$
$\gamma_2$	$1.49 \pm .42$	$1.53 \pm .38$
$a_s$	$0.025 \pm .028$	$0.054 \pm .057$
$c_s$	$3.61 \pm 1.62$	$c_G + 1$
$c_G$	$5.55 \pm 1.43$	$5.17 \pm .14$
$\gamma_G$	$8.5 \pm 8.6$	$9.00 \pm .59$
$\chi^2$	80.1 for 79 DF	78.5 for 80 DF

Table 6.6

Best values for free parameters obtained in fits to  $F_2$  ( $R = R_{QCD}$ ) and  $\bar{q}$  from CDHS [Ab83]

Two approaches to fitting  $F_2$  and  $\bar{q}$  were made. In the first attempts, both  $a_s$  and  $c_s$  were retained as free parameters. However, in using this method it was found that only one of the gluon parameters ( $c_G$ ) could be well determined. Partly, this resulted from the use of two parameters to fit an essentially null result. Additional fits were therefore made retaining as variable the level of anti-quarks beyond  $x = 0.30$ , but fixing:

$$c_s = c_G + 1 \quad (6.31)$$

The relationship between gluon and anti-quark behavior at large  $x$  embodied in equation 6.31 is predicted by an asymptotic analysis of the Altarelli-Parisi equations [Al82] in the limit  $Q^2 \approx$ . The values for the free parameters resulting from these fits are listed in table 6.6. Only the leading order QCD evolution equations were used, with no target mass corrections.

The observed values of  $\Lambda$  listed in table 6.6 are somewhat lower than those reported in section 6.5.1. This is mostly due to the relaxation of the lower  $x$  limit to include all data above  $x = 0.04$ . The result without target mass corrections and using the standard assumed gluon distribution was  $\Lambda = 260 \pm 90\text{MeV}$ .

The main purpose of this exercise was to measure the gluon distribution. In comparing our results with those of CDHS [Ab83], it has been noted that (1) the integrals of  $F_2$  differ by about 19%, and (2) the  $x$  dependence of  $F_2$  exhibits differences at the level of 10%. These observations imply that the integral of the gluon distribution is 19% smaller in our case. The common constraint of the  $\bar{q}$  result from CDHS above  $x = 0.30$  forces the behavior of  $G$  at large  $x$  to be similar. Consequently, the behavior at small  $x$  is quite dissimilar. A comparison of the fit values of  $F_2$  and  $G$  at  $Q_0^2$  is shown in figure 6.33. The value reported for  $\Lambda$  by the CDHS collaboration [Ab83] was  $290 \pm 30\text{MeV}$ . Despite the difference in the fitted gluon distribution, the results for  $\Lambda$  agree within errors.

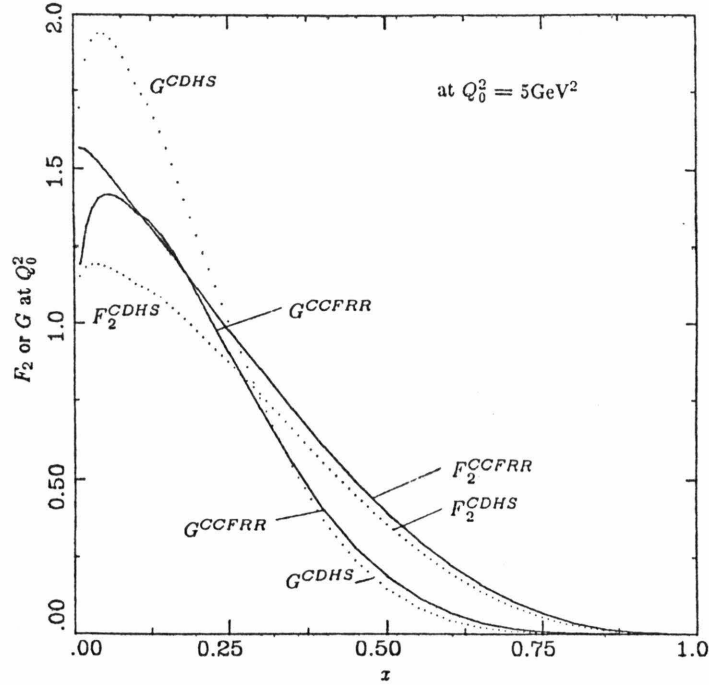


Figure 6.99 Comparison of QCD fits for  $F_2$  and  $G$  for CCFRR and CDHS [Ab82a,Ab83]

#### 6.5.4 $xF_3$ analysis

QCD fits to  $xF_3$  were made to those results with  $Q^2 > 5\text{GeV}^2$ ,  $W^2 > 10\text{GeV}^2$  and  $0.04 < x < 0.70$ . These restrictions excluded regions where non-perturbative effects are expected to be large. The functional form used for  $xF_3$  at  $Q_0^2 = 12.6\text{GeV}^2$  was as shown in equation 6.25 above. The GLS sum rule (equation 6.12) was not used to constrain the normalization, but the parameter  $\gamma_3$  was fixed to be zero. Target mass corrections were not made.

Results using the two available programs [Ab80,De83] agreed in leading order. The 90% CL limit on  $\Lambda$  is  $.2 < \Lambda_{LO} < 420\text{MeV}$ . The best values for the various parameters are listed in table 6.7. The evolution equations (6.14) depend non-linearly on  $\Lambda$ . Therefore, given the large statistical errors on  $xF_3$ , a more appropriate measure of the scaling violations was found to be  $\alpha_S$ . The value of  $\int F_3 dx = 2.70 \pm .15$  obtained was consistent with the more model independent result discussed in section 6.3. The reduced statistical error was due to the constraint of point-to-point correlations imposed by the global model.

The same non-singlet analysis was repeated using the standard technique [De83] of replacing the experimental values of  $xF_3$  for  $x > 0.4$  with those of  $F_2$ . This implicitly assumes a vanishing sea and small  $R$  in the high  $x$  region, or equivalently that  $xF_3 = F_2$  above  $x = 0.4$ . The results of such a fit is also listed in table 6.7. It should be noted that for both non-singlet

	$xF_3$ only	$xF_3, x < 0.4$ $F_2, x > 0.4$
$\Lambda$	$90^{+160}_{-80}$ MeV	$270^{+110}_{-100}$ MeV
$\alpha_S(Q^2 = 12.6\text{GeV}^2)$	$0.204 \pm 0.079$	$0.291 \pm 0.047$
$a_3$	$4.34 \pm 0.24$	$4.29 \pm 0.22$
$b_3$	$0.672 \pm 0.058$	$0.635 \pm 0.049$
$c_3$	$3.29 \pm 0.24$	$2.90 \pm 0.13$
$\chi^2$	44.2 for 39 DF	50.0 for 46 DF

Table 6.7 Non-singlet fits to  $xF_3$  or  $xF_3$  and  $F_2$ 

Method	$\Lambda$ (MeV)	$\alpha_S(Q^2 = 12.6\text{GeV}^2)$
Leading Order	$90^{+160}_{-80}$	$.204 \pm .079$
$\overline{\text{MS}}$ [Ab80]	$120^{+200}_{-110}$	$.176 \pm .062$
$\overline{\text{MS}}$ [De83]	$190^{+270}_{-160}$	$.201 \pm .070$

Table 6.8  $\Lambda$  and  $\alpha_S$  resulting from first and second ( $\overline{\text{MS}}$ ) order fits

fits, the hypothesis of no QCD scale breaking ( $\alpha_S = 0$  or  $\Lambda = 0$ ) was poor:  $\chi^2$  was 52.7 for 45 degrees of freedom using  $xF_3$  alone and 100.6 for 47 degrees of freedom using the combination of  $xF_3$  and  $F_2$ . In both cases, the  $\chi^2$  for the best fit was acceptable using statistical errors only.

The systematic errors on these results have been investigated using the same technique described in section 6.5.1 for  $F_2$ . In all cases, the uncertainties in  $\alpha_S$  (or  $\Lambda$ ) represented by systematic errors were smaller than statistical errors. It should be noted that the shape of  $xF_3$  is sensitive to relative uncertainties in the neutrino and anti-neutrino fluxes: precision flux measurements are necessary in order to keep this source of error small.

Finally, these fits have also been made in second order using both programs. In contrast with the agreement between the results of leading-order fits, the results shown in table 6.8 exhibit significant differences in the values of  $\Lambda$  obtained in second order. As was noted in section 6.4, the programs differ in that Barnett [Ab80] uses the one-step version of the second order equations, while Duke [De83] uses the two-step method. However, in principle similar values for  $\Lambda_{\overline{\text{MS}}}$  should be obtained. It has been suggested [Ow83] that if a more general functional form for  $xF_3$  were used, the discrepancy would disappear. Experimentally, the data did not support the use of additional parameters, since  $\chi^2$  changed by less than one when  $\gamma_3$  was allowed to vary. The two results did coincide within errors.

### 6.5.5 Comments on $R$

QCD beyond the leading order predicts a value for  $R$  which falls rapidly with  $x$ , and decreases logarithmically with  $Q^2$ . The value depends on  $F_2$  and  $G$ , as shown in equation 6.17, where  $R = F_L/2xF_1$ . A calculation of the prediction was made by modifying the program

for QCD evolution supplied by Duke [De83]. This involved suitably changing the coefficient functions used for  $F_2$  into those necessary for  $2xF_1$  [Fu82].  $\Lambda$  and the parameters used for  $F_2$  and  $G$  were assigned the values listed in table 6.1 for the fit beyond leading order.

The result is shown as a function of  $x$  in figure 6.34, along with our measurements (section 5.7). The data were consistent with expectations, although the errors were quite large. The  $\chi^2$  for the fit to the prediction shown was 5.0 for 5 degrees of freedom. The alternative assumptions made in the structure function analysis,  $R = 0.0$  and  $R = 0.1$ , also were consistent with the measurements. The fit to the  $R = 0.1$  hypothesis was actually slightly better than to  $R = R_{QCD}$ :  $\chi^2 = 3.8$  for 5 degrees of freedom. The  $R = 0.0$  case was somewhat improbable ( $\chi^2 = 9.8$  for 5 degrees of freedom), due to the finite value observed in the two smallest  $x$  bins. Given such large errors, no significant  $Q^2$  variation could be noted, as shown in figure 6.35.

There have been several other attempts to measure  $R$ : also shown in the two figures are results from the CDHS collaboration [Ab81]. The error bars are smaller, particularly at large  $x$ , due to the better high  $y$  acceptance of the CDHS detector. However, the measurements are not any more conclusive with regard to testing the QCD prediction. The average result,  $R = 0.10 \pm 0.025 \pm 0.06$ , is somewhat at variance with the hypothesis  $R = 0.0$ . The finite values are mostly clustered at small  $x$ , while the large  $x$  results would easily overlap zero if systematic errors were included. The EMC collaboration has reported [Au82b] an average result of  $R = 0.00 \pm 0.035 \pm 0.095$  for data with an average  $\nu = 100\text{GeV}$ . They concluded that these results were also consistent with a QCD prediction.

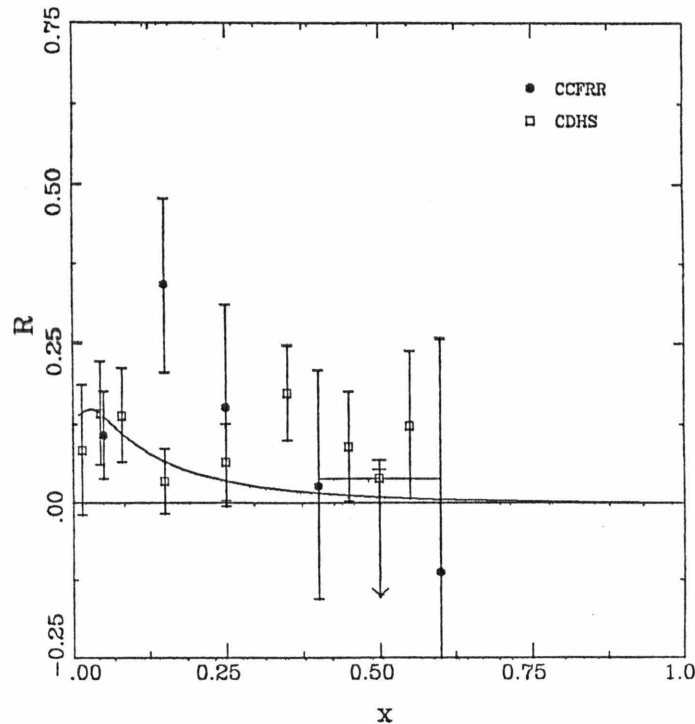


Figure 6.34 Results for  $R$  as a function of  $x$ , with QCD prediction

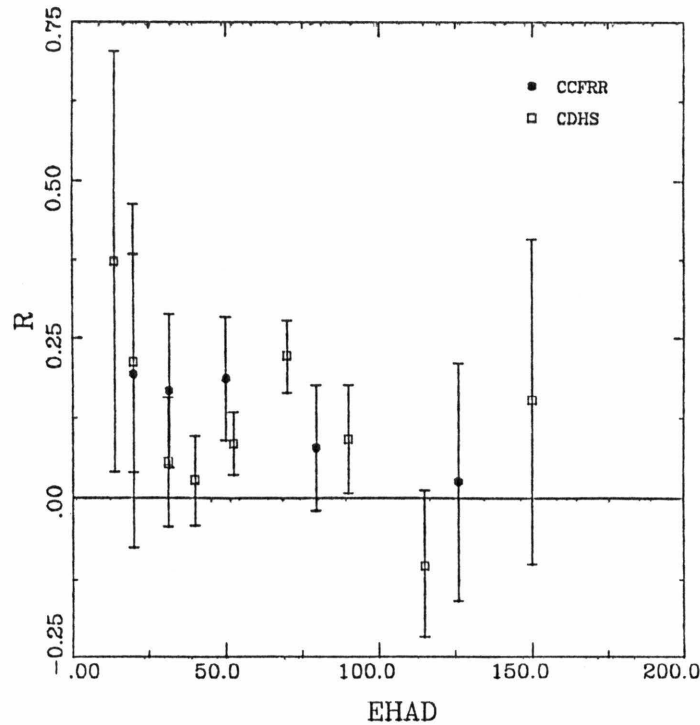


Figure 6.95 Results for  $R$  as a function of  $E_H$

On the basis of results from this experiment, and published data in similar  $Q^2$  from other experiments, none of the three hypotheses used in extracting structure functions can be ruled out. There is a slight hint that  $R$  has an  $x$  dependence, with a finite value at small  $x$ . For the purposes of QCD, the preferred structure function results are those obtained using a value for  $R$  consistent with the theory.

## 6.6 Conclusions and the Future

A high statistics sample of neutrino-nucleon scattering data has been obtained using the Lab E detector at Fermilab (experiment E616). Care was taken to understand both the detector and the neutrino in painstaking detail. In so doing, the systematic uncertainties in these results have been minimized. The structure functions  $F_2$  and  $xF_3$  extracted from the data have been analyzed in terms of the quark-parton model and QCD. From these studies it is concluded that:

- (1) Inconsistencies among results from the various neutrino experiments exist outside difficulties with overall normalization. The scale errors presumably reflect problems with overall flux measurements, but differences in the  $x$  dependence of structure functions imply more subtle problems.

(2) The quark-parton model comparison of  $F_2(x)$  with the analogous structure function measured in muon scattering by the EMC collaboration [Au81b] shows a level difference of about 10%, probably due to systematic normalization differences among experiments. The  $x$  dependence of the two structure functions is very similar. The difference between our measurements and those published by SLAC [Bo79] or the BFP collaboration [Me83,C183] are within systematic errors.

(3) The pattern of scaling violations observed in measurements of  $F_2$  was consistent with that in comparable published results from both neutrino and muon scattering experiments.

(4) Measurement of the GLS sum rule [Pu84] gives

$$\int_0^1 F_3 dx = 2.79 \pm .28 \pm .13$$

consistent with the quark-parton model and QCD with  $\Lambda < 600\text{MeV}$ .

(5) Fits to  $F_2$  in leading order and second order give, with statistical and estimates of systematic errors:

$$\begin{aligned}\Lambda_{LO}^{F_2} &= 360 \pm 90 \pm 60\text{MeV} (R = 0.0) \\ \Lambda_{\overline{\text{MS}}}^{F_2} &= 340 \pm 100 \pm 60\text{MeV} (R = R_{QCD})\end{aligned}$$

for a particular choice of gluon distribution. Variations of the parameters in the gluon distribution over reasonable limits indicate an additional rms uncertainty in  $\Lambda$  of approximately 50MeV. Also, the assumed value of  $R$  can introduce large variations in the best value for  $\Lambda$ . Other sources of systematic error, such as flux uncertainties, were smaller than the statistical error. The result for  $\Lambda$  is consistent with other measurements from deep-inelastic scattering.

(6) Fits to  $F_2$  from this experiment and  $\bar{q}$  from CDHS [Ab83] allow a determination of  $\Lambda$  and the form of the gluon distribution. The result obtained for the gluon distribution differs substantially at small  $x$  from that reported by the CDHS collaboration. This fact is a direct consequence of differences in the  $x$  dependence of  $F_2$  noted in item (1). The constraint of the  $\bar{q}$  measurement leads to similar large  $x$  behavior in the two results.

(7) A fit to  $xF_3$  in leading order, gives with statistical and estimated systematic errors [Pu84]:

$$\Lambda_{LO}^{xF_3} = 90_{-80}^{+160} {}_{-70}^{+120}\text{MeV}$$

Second order fits [Ab80,De83] to  $xF_3$  give somewhat different values of  $\Lambda$ , although  $\alpha_S(Q_0^2 = 12.6\text{GeV}^2)$  are not so strikingly different. The value obtained using the program obtained from

Duke [De83] was  $190 \pm_{160}^{270}$  MeV. Both results were consistent with the values for  $\Lambda$  obtained from  $F_2$ . Again, systematic errors were found to be smaller than the statistical errors for these fits.

It is evident that, for the purposes of testing QCD hypotheses, the results reported here are statistically limited. A factor of five more data could easily be accommodated before the level of systematic error would become comparable. This conclusion is based on ignoring the uncertainties in the  $F_2$  result due to the gluon distribution or  $R$ . Presumably, these quantities are of interest as well as a determination of  $\Lambda$ . The direct strategy of obtaining a well-constrained measurement of  $\Lambda$  from  $xF_3$ , and using  $F_2$  to measure the gluon distribution, could be employed if the measurement of  $xF_3$  were sufficiently precise.

With the upgraded Lab E detector [Bl80], the limitation of only one event per 50ms will be removed. A large sample of events obtained in wide-band running at the Tevatron, normalized to these or future dichromatic results, would represent a logical way of increasing the size of the data sample in the kinematic region covered by this experiment.

Finally, approved running in the dichromatic beam at the Tevatron [Bl80] offers the opportunity of increasing the maximum available  $Q^2$  by about a factor of three. The test of whether structure functions at these high  $Q^2$ 's represent logarithmic extrapolations of present measurements will be definitive for QCD.

## List of Collaborators on E616

The following people and institutions contributed to the data taking or analysis of Fermilab experiment E616:

D.B.MacFarlane, M.V.Purohit, R.E.Blair,<sup>a</sup> Y.K.Chu,  
B.N.Jin,<sup>b</sup> R.L.Messner,<sup>c</sup> J.Ludwig,<sup>d</sup> D.B.Novikoff,<sup>e</sup>

**California Institute of Technology, Pasadena, CA 91125**

P.S.Auchincloss, F.J.Sciulli, M.H.Shaevitz

**Columbia University, New York, NY 10027**

H.E.Fisk, Y.Fukishima,<sup>f</sup> Q.A.Kerns, T.Kondo,<sup>f</sup> P.A.Rapidis,  
S.L.Segler, R.J.Stefanski, D.E.Theriot, D.D.Yovanovitch

**Fermi National Accelerator Laboratory, Batavia, IL 60510**

A.Bodek, R.N.Coleman,<sup>g</sup> W.L.Marsh<sup>g</sup>

**University of Rochester, Rochester, NY 14627**

O.D.Fackler, K.A.Jenkins

**Rockefeller University, New York, NY 10021**

- 
- <sup>a</sup> Columbia University, New York, NY 10027
  - <sup>b</sup> Institute for High Energy Physics, Peking, P.R. China
  - <sup>c</sup> SLAC, Stanford, CA 94305
  - <sup>d</sup> Albert Ludwigs University, Freiburg, F.R. Germany
  - <sup>e</sup> Hughes Aircraft Co., El Segundo, CA 90245
  - <sup>f</sup> National Laboratory for High Energy Physics, Tsukuba-gun, Ibaraki-ken 305, Japan
  - <sup>g</sup> Fermi National Accelerator Laboratory, Batavia, IL 60510

Appendix B  
Target Counter Maps

The response function for each of the four counter tubes was divided into three parts: (1) exponential attenuation in the counter from the light source to the edge of the counter, (2) transmission across the air gap to the light bar and (3) exponential attenuation in the light bar. The transmission across the air gap was calculated by integrating the average transmission coefficient for parallel and perpendicular polarized electric fields:

$$I_t(\varphi) = \int_{-\theta_{cr}}^{\theta_{cr}} I_t(\theta, \varphi) d\theta \quad (\text{B.1})$$

where  $\theta$  is the angle out of the counter plane, and  $\varphi$  is the polar angle in the plane of the counter. The limits of integration were the angles at which total internal reflection occurred,  $\pm\theta_{cr}$ . The function  $I_t(\varphi)$  was found to be well approximated by a step function between the limits  $\varphi = \varphi_{cr}$  and  $\varphi = -\varphi_{cr}$ , where again  $\varphi_{cr}$  is the critical angle. For each light bar and its reflection, the extent of the region for which transmission could occur was determined, given the constraints of geometry and the requirement that  $\varphi < \varphi_{cr}$ . Figure B.1 illustrates this procedure for a typical topology. If the lower and upper limits in  $\varphi$  are designated  $\varphi_1$  and  $\varphi_2$  respectively, then the mean value of  $\cos \varphi$  is:

$$\overline{\cos \varphi} = \frac{\int_{\varphi_1}^{\varphi_2} \cos \varphi d\varphi}{\int_{\varphi_1}^{\varphi_2} d\varphi} \quad (\text{B.2})$$

The distance from the source to the bar at this mean cosine was used to determine the attenuation of light passing from the source to the light bar. In practice, as indicated in the figure, the allowed region for each light bar was divided into three portions in order to improve the fit.

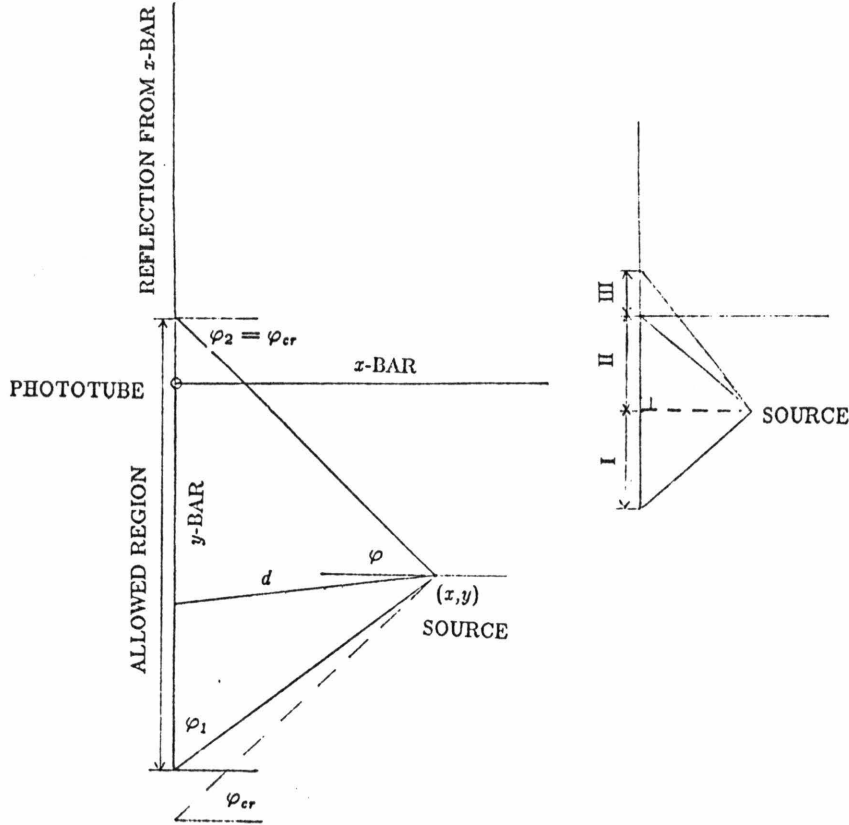


Figure B.1 Typical geometry for collecting light from a source within a counter

The map function for each tube represented the sum of contributions from two light bars ( $i$ ), each with three segments ( $j$ ):

$$c_k(x, y) = \sum_{i=1}^2 \left\{ \sum_{j=1}^3 \int_{\varphi_1(j)}^{\varphi_1(j)} d\varphi \exp \left[ -\frac{(x_{ij} - x_0)^2}{\lambda_x^2} - \frac{(y_{ij} - y_0)^2}{\lambda_y^2} \right] \right\} \cdot \left\{ \sum_{j=1}^3 \Delta\varphi_j \exp \left[ -\frac{L_j}{\lambda_{bar}} \right] \right\} \quad (\text{B.3})$$

The quantities  $x_{ij}$  and  $y_{ij}$  are the  $x$  and  $y$  distances from the source to the calculated mean position on the  $j^{\text{th}}$  segment of the  $i^{\text{th}}$  light bar. The distance from the mean position to the phototube is denoted by  $L_j$ . Thus, the model had five free parameters:  $(x_0, y_0)$ , the counter balance point,  $(\lambda_x, \lambda_y)$ , the attenuation lengths in  $x$  and  $y$ , and  $\lambda_{bar}$ , the attenuation length in the light bars.

The best values of the map parameters were obtained using hadron showers from neutrino events. For this purpose the absolute level of response was unimportant and in fact varied greatly among the chosen ensemble of showers. Instead, on a counter-by-counter basis the variation with shower position of the fraction of light collected by each of the four counter phototubes was used in fitting for the parameters.

For a particular counter, an event was included in the fit if the following constraints were satisfied:

- (1) a muon or penetration trigger fired
- (2) a good target track was obtained for the muon, and hence the vertex was well known
- (3) the vertex lay within a radius of 50in of the apparatus centre
- (4) the counter was among the first four counters in the shower, that is was close to the vertex
- (5) the pulse height in any phototube was more than two times minimum, and the sum of the four tubes was greater than ten times minimum
- (6) the left-right asymmetry of the four tubes was within 30% of zero.

These criteria eliminated cosmic-ray showers, and ensured adequate photostatistics. The values of map parameters were obtained by minimizing for this ensemble of events ( $i$ ):

$$\chi^2 = \sum_{\text{events}} \sum_{j=1}^4 \frac{(p_j - N_i c_j(x_i, y_i))^2}{\sigma_j^2} \quad (\text{B.4})$$

where:

$$p_j \text{ was the observed pulse height in the } i^{\text{th}} \text{ low}$$

$$N_i = \sum_j p_j / \sum_j c_j \text{ was a normalization factor}$$

$$c_j \text{ was the map-predicted pulse height at } x_i, y_i$$

$$\sigma_j = 0.25\sqrt{p_j} \text{ was the error due to photostatistics}$$

Note that the calculation of  $\sigma_j$  was in error, since the contribution from the normalization condition was ignored. Future efforts should include this term. It was found that  $\chi^2$  was insensitive to the value of the attenuation length in the light bars, which was thereafter fixed to be 115in. Since a target track was required, no data were available for mapping the first ten counters: therefore, the average values for the map parameters were used instead.

One additional point should be reiterated here. The procedure described assumes the response of the four phototubes to be balanced: light at the counter centre produces equal response in all tubes. If this were not true, the available range of variation of the balance parameters is limited by strong coupling to the attenuation lengths  $\lambda_x$  and  $\lambda_y$ . It has been determined from mapping the counters with sources that the flasher system did not always properly balance the phototube response. Therefore, a more suitable approach was devised for subsequent efforts to map the counters,  $c'_k(x, y)$ . An attenuation length for the counter ( $\lambda$ ) and three balance coefficients were used instead of two attenuation lengths and a balance point:

$$c'_k(x, y) = f_k c_k(x, y)$$

$$\sum_{k=1}^4 f_k = 4 \quad (\text{B.5})$$

---

The inability of the original map to adequately correct counter planes which were not properly balanced is thought to be the origin of the few percent rise beyond 40in of the map-corrected calibration results shown in figure 4.3.

## Hadron Calibration

The response of the calorimeter was calibrated using pions brought to Lab E by means of the N-5 hadron test beam. This beam ran along the east side of the Neutrino area berm, providing pions or muons with a  $\Delta p/p$  of about 1%. The target and toroid of the Lab E detector are segmented, which allowed us to move the first two target carts into the beam. Data were taken at 25, 50, 90, 200 and 250 GeV/c, near the centre of the detector.

The transverse vertex position for each event was taken to be the average of the shower spark positions in the target. Beam centres  $(x_0, y_0)$  for each setting were determined from the mean of the distribution of this vertex. The counter pulse heights were map corrected, with the position in the  $i^{\text{th}}$  counter calculated from the nominal beam centre and direction:

$$\begin{aligned}x_i &= x_0 + 0.03(z_i - z_0) \\y_i &= y_0\end{aligned}\tag{C.1}$$

The quantity  $z_0$  was the position of the upstream end of the second target cart. Since the showers were near the target centre these corrections were small. Cuts were applied to the data to eliminate events due to muons (1) a vertex cut:  $(x - x_0)^2 + (y - y_0)^2 \leq 1.75\text{in}$ , and (2) a hadron energy requirement of more than 10 GeV.

The same techniques used to find the beginning and end of the hadron shower in the charged current analysis (section 4.1) were used for the calibration data. However, the algorithm for finding the longitudinal position of the vertex assumed a neutral incoming particle. As a result, for a charged pion the vertex was always at the upstream end of the second target cart. An average correction of 0.8 times minimum ionizing was necessary to account for events which actually interacted further downstream. The average energy lost due to a misidentified shower end has been found to be of almost equal amount, but in the opposite direction. Therefore, the net correction was taken to be zero.

Beam momenta were determined from recorded currents of two dipole magnets in the N-5 beam line: 5E01 and 5W09 in enclosures 101 and 109 respectively. However, the momenta

Pion Momentum	$x_0$ inches	$y_0$ inches	Mean shower sum (minimums)	Sigma
$25.21 \pm .39$	-0.20	-0.24	$114.56 \pm 0.56$	$21.77 \pm 0.40$
$48.99 \pm .60$	-0.13	-0.21	$229.92 \pm 1.12$	$30.56 \pm 0.82$
$90.63 \pm .42$	-0.50	-0.37	$419.52 \pm 1.73$	$39.65 \pm 1.31$
$200.0 \pm .83$	-0.27	-0.26	$928.62 \pm 2.36$	$55.99 \pm 1.76$
$250.5 \pm 1.6$	0.10	0.06	$1158.9 \pm 2.20$	$61.58 \pm 1.53$

*Table C.1* Mean shower sums and sigmas for the calibration data

so found were not quite consistent. Therefore, the average of the two measurements was used, with the error taken to be half the difference. Ultimately, the absolute calibrations of these currents were measured by E595, an active beam dump experiment using part of the Lab E detector [Bo82,Ri83]. This group found the momentum of each incoming hadron from the bend induced by the final dipole magnet before Lab E, 5E13. PWCs upstream and the target spark chambers downstream provided a measurement of the track position before and after the magnet. The reported accuracy of the upstream tagging system was 0.5% [Bo82].

The sum of map-corrected shower pulse height at each setting was fit using a Poisson distribution, as suggested by Barish, et al. [Ba75c]. The resulting values for the mean shower pulse height and distribution width are listed in table C.1. These were used to obtain the calibration constant and resolution function reported in section 4.1.

## Multiple Scattering Error Matrix

A charged particle passing through a uniform material of length  $L$ , undergoes a shift in angle,  $\phi$ , and displacement,  $\delta$ , as illustrated in figure 4.7. The probability distribution for such scatters is described by the Fermi formula:

$$p(\phi, \delta) = N \exp \left\{ -\frac{2}{\sigma^2} \left[ \phi^2 - \frac{3\phi\delta}{L} + \frac{3\delta^2}{L^2} \right] \right\} \quad D.1$$

where:

$$\sigma^2 = \left( \frac{0.015}{p} \right)^2 \frac{L}{L_{RAD}} \left( 1 + \frac{1}{9} \log \frac{L}{L_{RAD}} \right) \quad D.2$$

From this we infer that:

$$\begin{aligned} \chi^2 &= \frac{4}{\sigma^2} \left\{ \phi^2 - \frac{3\phi\delta}{L} + \frac{3\delta^2}{L^2} \right\} \\ &= \phi^2 M_{11}^{-1} + 2\phi\delta M_{12}^{-1} + \delta^2 M_{22}^{-1} \end{aligned} \quad D.3$$

where  $M^{-1}$  is the inverse of the error matrix. The elements of  $M^{-1}$  can be identified and the inversion carried out to obtain the fundamental correlation matrix for multiple scattering:

$$M = \sigma^2 \begin{pmatrix} 1 & L/2 \\ L/2 & L^2/3 \end{pmatrix} \quad D.4$$

If there are  $m$  such slabs of material, then scatters in the  $i^{th}$  slab are independent of scatters in the  $j^{th}$  slab, so that:

$$\begin{aligned} \phi_i \phi_j &= \sigma_i^2 \delta_{ij} \\ \phi_i \delta_j &= \delta_i \phi_j = \frac{L_i}{2} \sigma_i^2 \delta_{ij} \\ \delta_i \delta_j &= \frac{L_i^2}{3} \sigma_i^2 \delta_{ij} \end{aligned} \quad D.5$$

Displacements after each slab of material are:

$$\begin{aligned}
 \Delta_1 &= \delta_1 \\
 \Delta_2 &= \Delta_1 + L_2\phi_1 + \delta_2 \\
 &= (\delta_1 + \delta_2) + L_2\phi_1 \\
 \Delta_3 &= \Delta_2 + L_3(\phi_1 + \phi_2) + \delta_3 \\
 &= (\delta_1 + \delta_2 + \delta_3) + L_3(\phi_1 + \phi_2) + L_2\phi_1 \\
 &\cdot \\
 &\cdot \\
 \Delta_i &= \sum_{k=1}^i \delta_k + \sum_{k=1}^{i-1} \phi_k \sum_{m=k+1}^i L_m \\
 &= \sum_{k=1}^i (\delta_k + \phi_k d_{ki})
 \end{aligned} \tag{D.6}$$

where  $d_{ki} = \sum_{m=k+1}^i L_m$ , and using the fact that  $d_{ii} = 0$ . Then:

$$\Delta_i \Delta_j = \sum_{k=1}^i \sum_{l=1}^j (\delta_k + \phi_k d_{ki})(\delta_l + \phi_l d_{lj}) \tag{D.7}$$

Consider only the case  $i \leq j$ , since  $\Delta_i \Delta_j = \Delta_j \Delta_i$ . Using the results of equation D.6, one obtains:

$$\Delta_i \Delta_j = \sum_{k=1}^i \sigma_k^2 \left\{ \frac{L_k^2}{3} + \frac{L_k}{2} (d_{kj} + d_{ki}) + d_{ki} d_{kj} \right\} \tag{D.8}$$

This is the multiple scattering error matrix used in fitting the muon toroid track, and referred to in Section 4.2.2.

## Quark Model Predictions for Cross Sections

Cross sections for neutrinos and anti-neutrinos from protons and neutrons can be constructed from the quark cross sections detailed in Table 1.3. Assume that:

$$\begin{aligned}
 u_p(x) &= d_n(x) = u(x) \\
 d_p(x) &= u_n(x) = d(x) \\
 \bar{u}_p(x) &= \bar{d}_n(x) = \bar{d}_p(x) = \bar{u}_n(x)
 \end{aligned}
 \tag{E.1}$$

One obtains:

$$\begin{aligned}
 \frac{d\sigma^{\nu p}}{dx dy} &= \frac{2G^2 ME}{\pi} \left\{ d(x) \cos^2 \theta_c + d(\xi) t_c \sin^2 \theta_c + s(\xi) t_c \cos^2 \theta_c + s(x) \sin^2 \theta_c \right. \\
 &\quad \left. + (\bar{u}(x) + \bar{c}(x))(1 - y)^2 \right\}
 \end{aligned}
 \tag{E.2}$$

where the significance of the finite charm mass,  $m_c$ , is taken into account by the use of  $\xi$ -scaling and threshold factor,  $t_c$ :

$$\begin{aligned}
 \xi &= x + \frac{m_c^2}{2MEy} \\
 t_c &= 1 - \frac{M_c^2}{2ME\xi}
 \end{aligned}
 \tag{E.3}$$

Contributions to the cross section by such transitions to a charm quark are limited to the kinematic region:

$$\begin{aligned}
 \frac{m_c^2}{2ME} &< \xi < 1 \\
 \frac{m_c^2}{2ME\xi} &< y < 1
 \end{aligned}
 \tag{E.4}$$

Likewise:

$$\frac{d\sigma^{\nu n}}{dxdy} = \frac{2G^2 ME}{\pi} \left\{ u(x) \cos^2 \theta_c + u(\xi) t_c \sin^2 \theta_c + s(\xi) t_c \cos^2 \theta_c + s(x) \sin^2 \theta_c \right. \\ \left. + (\bar{d}(x) + \bar{c}(x))(1-y)^2 \right\} \quad (\text{E.5})$$

$$\frac{d\sigma^{\bar{\nu} p}}{dxdy} = \frac{2G^2 ME}{\pi} \left\{ \bar{d}(x) \cos^2 \theta_c + \bar{d}(\xi) t_c \sin^2 \theta_c + \bar{s}(\xi) t_c \cos^2 \theta_c + \bar{s}(x) \sin^2 \theta_c \right. \\ \left. + (u(x) + c(x))(1-y)^2 \right\} \quad (\text{E.6})$$

$$\frac{d\sigma^{\bar{\nu} n}}{dxdy} = \frac{2G^2 ME}{\pi} \left\{ \bar{u}(x) \cos^2 \theta_c + \bar{u}(\xi) t_c \sin^2 \theta_c + \bar{s}(\xi) t_c \cos^2 \theta_c + \bar{s}(x) \sin^2 \theta_c \right. \\ \left. + (d(x) + c(x))(1-y)^2 \right\} \quad (\text{E.7})$$

An iron nucleus contains  $Z$  protons and  $A - Z$  neutrons, and so the cross section for neutrinos in iron is:

$$\frac{d\sigma^\nu}{dxdy} = \frac{Z}{A} \frac{d\sigma^{\nu p}}{dxdy} + \left(1 - \frac{Z}{A}\right) \frac{d\sigma^{\nu n}}{dxdy} \quad (\text{E.8})$$

Note that:

$$\frac{Z}{A} d(x) + \left(1 - \frac{Z}{A}\right) u(x) = \frac{1}{2}(u(x) + d(x)) + \frac{1}{2}\left(1 - \frac{2Z}{A}\right)(u(x) - d(x)) \quad (\text{E.9})$$

Hence:

$$\frac{d\sigma^\nu}{dxdy} = \frac{G^2 ME}{\pi} \left\{ (u(x) + d(x)) \cos^2 \theta_c + (u(\xi) + d(\xi)) t_c \sin^2 \theta_c + 2s(\xi) t_c \cos^2 \theta_c + 2s(x) \sin^2 \theta_c \right. \\ \left. + (\bar{u}(x) + \bar{d}(x) + 2\bar{c}(x))(1-y)^2 \right. \\ \left. + \left(1 - \frac{2Z}{A}\right)(u(x) - d(x)) \cos^2 \theta_c \right. \\ \left. + \left(1 - \frac{2Z}{A}\right)(u(\xi) - d(\xi)) t_c \sin^2 \theta_c \right\} \quad (\text{E.10})$$

Likewise for anti-neutrinos in iron:

$$\frac{d\sigma^{\bar{\nu}}}{dxdy} = \frac{Z}{A} \frac{d\sigma^{\bar{\nu} p}}{dxdy} + \left(1 - \frac{Z}{A}\right) \frac{d\sigma^{\bar{\nu} n}}{dxdy} \quad (\text{E.11})$$

Again:

$$\frac{Z}{A} u(x) + \left(1 - \frac{Z}{A}\right) d(x) = \frac{1}{2}(u(x) + d(x)) - \frac{1}{2}\left(1 - \frac{2Z}{A}\right)(u(x) - d(x)) \quad (\text{E.12})$$

Hence:

$$\begin{aligned} \frac{d\sigma^{\bar{\nu}}}{dx dy} = \frac{G^2 ME}{\pi} \left\{ (\bar{u}(x) + \bar{d}(x)) \cos^2 \theta_c + (\bar{u}(\xi) + \bar{d}(\xi)) t_c \sin^2 \theta_c + 2\bar{s}(\xi) t_c \cos^2 \theta_c + 2\bar{s}(x) \sin^2 \theta_c \right. \\ \left. + (u(x) + d(x) + 2c(x))(1-y)^2 \right. \\ \left. - \left(1 - \frac{2Z}{A}\right)(u(x) - d(x))(1-y)^2 \right\} \end{aligned} \quad (\text{E.13})$$

If the charm mass is neglected, these neutrino and anti-neutrino cross sections become:

$$\begin{aligned} \frac{d\sigma^{\nu}}{dx dy} = \frac{G^2 ME}{\pi} \left\{ u(x) + d(x) + 2s(x) + (\bar{u}(x) + \bar{d}(x) + 2\bar{c}(x))(1-y)^2 \right. \\ \left. + \left(1 - \frac{2Z}{A}\right)(u(x) - d(x)) \right\} \end{aligned} \quad (\text{E.14})$$

$$\begin{aligned} \frac{d\sigma^{\bar{\nu}}}{dx dy} = \frac{G^2 ME}{\pi} \left\{ \bar{u}(x) + \bar{d}(x) + 2\bar{s}(x) + (u(x) + d(x) + 2c(x))(1-y)^2 \right. \\ \left. - \left(1 - \frac{2Z}{A}\right)(u(x) - d(x))(1-y)^2 \right\} \end{aligned} \quad (\text{E.15})$$

Let these expressions be rewritten in terms of quark and anti-quark distributions:

$$\begin{aligned} q(x) &= u(x) + d(x) + s(x) + c(x) \\ \bar{q}(x) &= \bar{u}(x) + \bar{d}(x) + \bar{s}(x) + \bar{c}(x) \end{aligned} \quad (\text{E.16})$$

Then:

$$\begin{aligned} \frac{d\sigma^{\nu}}{dx dy} = \frac{G^2 ME}{\pi} \left\{ q(x) + s(x) - c(x) + (\bar{q}(x) + \bar{c}(x) - \bar{s}(x))(1-y)^2 \right. \\ \left. + \left(1 - \frac{2Z}{A}\right)(u(x) - d(x)) \right\} \end{aligned} \quad (\text{E.17})$$

$$\begin{aligned} \frac{d\sigma^{\bar{\nu}}}{dx dy} = \frac{G^2 ME}{\pi} \left\{ \bar{q}(x) + \bar{s}(x) - \bar{c}(x) + (q(x) + c(x) - s(x))(1-y)^2 \right. \\ \left. - \left(1 - \frac{2Z}{A}\right)(u(x) - d(x))(1-y)^2 \right\} \end{aligned} \quad (\text{E.18})$$

Now:

$$\begin{aligned} F_2(x) &= q(x) + \bar{q}(x) \\ xF_3(x) &= q(x) - \bar{q}(x) \end{aligned} \quad (\text{E.19})$$

If we assume  $s(x) = \bar{s}(x)$  and  $c(x) = \bar{c}(x)$ , then an expression for the cross sections in terms of the standard definitions of the structure functions is obtained, and may be directly compared with equation 5.17:

$$\frac{d\sigma^\nu}{dx dy} = \frac{G^2 ME}{\pi} \left\{ y^+ F_2(x) + y^- x F_3(x) + (s(x) - c(x))(1 - (1 - y)^2) + \left(1 - \frac{2Z}{A}\right)(u(x) - d(x)) \right\} \quad (\text{E.20})$$

$$\frac{d\sigma^{\bar{\nu}}}{dx dy} = \frac{G^2 ME}{\pi} \left\{ y^+ F_2(x) - y^- x F_3(x) + (s(x) - c(x))(1 - (1 - y)^2) - \left(1 - \frac{2Z}{A}\right)(u(x) - d(x))(1 - y)^2 \right\} \quad (\text{E.21})$$

where:

$$\begin{aligned} y^+ &= \frac{1}{2}(1 + (1 - y)^2) \\ y^- &= \frac{1}{2}(1 - (1 - y)^2) \end{aligned} \quad (\text{E.22})$$

## Characteristics of Binned Data

Mean values in each structure function bin for various relevant kinematic quantities are given in tables F.1 and F.2. The symbols:  $\bar{E}_H$ ,  $\bar{E}_\mu$ ,  $\bar{\theta}_\mu$  and  $\bar{y}$ , represent the one over acceptance-weighted average values of  $E_H$ ,  $E_\mu$ ,  $\theta_\mu$  and  $y$  for the  $n$  events appearing in the bin. The average total energy is  $\bar{E}_{\nu(\bar{\nu})} = \bar{E}_H + \bar{E}_\mu$ . The average weight is given in the column designated  $\bar{w}$ .

$Q^2$	$x$	$n$	$\bar{w}$	$\bar{E}_H$ (GeV)	$\bar{E}_\mu$ (GeV)	$\bar{\theta}_\mu$ (mr)	$\bar{y}$
1.26	.015	169	$1.077 \pm .009$	$41.5 \pm 1.6$	$41.2 \pm 2.5$	$27.8 \pm 1.3$	$.543 \pm .015$
2.00		110	$1.073 \pm .010$	$57.8 \pm 2.5$	$42.0 \pm 3.1$	$31.5 \pm 1.7$	$.617 \pm .017$
3.16		75	$1.069 \pm .014$	$86.4 \pm 3.3$	$48.0 \pm 4.1$	$30.8 \pm 2.0$	$.673 \pm .021$
5.01		24	$1.119 \pm .041$	$110.9 \pm 4.0$	$47.0 \pm 7.2$	$33.7 \pm 3.2$	$.729 \pm .030$
7.94		8	$1.110 \pm .078$	$145.9 \pm 7.3$	$52.7 \pm 15.0$	$41.9 \pm 9.1$	$.764 \pm .059$
1.26		.045	145	$1.072 \pm .019$	$16.6 \pm 0.3$	$54.4 \pm 3.1$	$26.5 \pm 1.7$
2.00	195		$1.082 \pm .009$	$25.2 \pm 0.4$	$40.9 \pm 2.2$	$36.5 \pm 1.3$	$.439 \pm .011$
3.16	187		$1.086 \pm .013$	$38.5 \pm 0.6$	$44.6 \pm 2.8$	$42.2 \pm 1.7$	$.533 \pm .013$
5.01	140		$1.178 \pm .032$	$58.6 \pm 1.1$	$47.5 \pm 3.5$	$51.8 \pm 2.6$	$.630 \pm .016$
7.94	65		$1.257 \pm .058$	$89.7 \pm 2.5$	$53.6 \pm 4.5$	$48.2 \pm 3.6$	$.664 \pm .022$
12.6	23		$1.183 \pm .055$	$134.7 \pm 5.7$	$50.5 \pm 6.7$	$45.9 \pm 4.3$	$.738 \pm .029$
20.0	3		$1.447 \pm .226$	$157.8 \pm 3.2$	$19.3 \pm 5.0$	$79.4 \pm 10.7$	$.894 \pm .024$
1.26	.080		39	$1.070 \pm .019$	$11.2 \pm 0.1$	$53.5 \pm 5.3$	$27.6 \pm 2.6$
2.00		199	$1.090 \pm .022$	$14.4 \pm 0.2$	$50.4 \pm 2.3$	$34.8 \pm 1.7$	$.272 \pm .009$
3.16		254	$1.130 \pm .039$	$21.8 \pm 0.2$	$47.2 \pm 2.2$	$46.5 \pm 2.1$	$.387 \pm .010$
5.01		256	$1.263 \pm .055$	$34.5 \pm 0.4$	$40.2 \pm 2.1$	$64.2 \pm 2.3$	$.545 \pm .011$
7.94		182	$1.277 \pm .054$	$52.9 \pm 0.6$	$44.5 \pm 2.5$	$65.5 \pm 2.7$	$.611 \pm .013$
12.6		80	$1.336 \pm .075$	$78.9 \pm 1.2$	$45.9 \pm 3.5$	$63.9 \pm 3.5$	$.675 \pm .015$
20.0		37	$1.288 \pm .065$	$125.0 \pm 3.1$	$53.2 \pm 4.8$	$56.3 \pm 3.8$	$.717 \pm .020$
31.6		4	$1.403 \pm .239$	$174.2 \pm 8.8$	$33.8 \pm 7.5$	$74.1 \pm 9.6$	$.845 \pm .026$

$Q^2$	$x$	$n$	$\bar{w}$	$\bar{E}_H$ (GeV)	$\bar{E}_\mu$ (GeV)	$\bar{\theta}_\mu$ (mr)	$\bar{y}$
2.00	.150	37	1.080 ± .016	11.2 ± 0.1	48.7 ± 4.4	34.7 ± 2.6	.219 ± .014
3.16		267	1.065 ± .005	13.4 ± 0.1	57.2 ± 2.0	35.7 ± 0.9	.224 ± .005
5.01		489	1.108 ± .013	19.4 ± 0.2	51.2 ± 1.5	47.8 ± 1.0	.321 ± .006
7.94		398	1.225 ± .027	30.8 ± 0.3	49.5 ± 1.8	62.5 ± 1.5	.450 ± .008
12.6		266	1.359 ± .043	45.7 ± 0.6	53.0 ± 2.1	68.6 ± 2.0	.523 ± .009
20.0		156	1.386 ± .056	70.8 ± 1.2	61.8 ± 2.8	65.6 ± 2.5	.574 ± .012
31.6		59	1.473 ± .114	108.9 ± 2.6	63.0 ± 4.6	70.8 ± 4.1	.662 ± .018
50.1		11	2.208 ± .457	155.0 ± 6.8	29.4 ± 4.7	114.3 ± 7.7	.846 ± .021
3.16	.250	2	1.092 ± .014	10.3 ± 0.1	29.6 ± 1.3	57.7 ± 2.4	.258 ± .010
5.01		197	1.115 ± .020	12.1 ± 0.1	52.9 ± 2.3	49.4 ± 1.6	.222 ± .006
7.94		288	1.170 ± .019	17.8 ± 0.2	54.3 ± 2.1	58.1 ± 1.4	.294 ± .006
12.6		230	1.324 ± .042	27.4 ± 0.3	51.0 ± 2.2	74.4 ± 2.0	.407 ± .008
20.0		146	1.435 ± .086	42.2 ± 0.6	57.7 ± 3.0	80.7 ± 3.0	.489 ± .012
31.6		72	1.562 ± .147	68.4 ± 1.2	67.5 ± 4.4	82.5 ± 4.5	.556 ± .018
50.1		25	1.437 ± .130	107.1 ± 3.4	72.4 ± 5.4	70.1 ± 4.9	.610 ± .022
79.4		5	1.779 ± .358	143.0 ± 4.8	45.1 ± 6.8	100.0 ± 8.4	.769 ± .025
5.01	.350	8	1.146 ± .087	10.5 ± 0.1	51.9 ± 11.3	54.7 ± 7.0	.203 ± .023
7.94		142	1.121 ± .018	12.9 ± 0.1	64.4 ± 3.3	51.1 ± 1.7	.202 ± .006
12.6		159	1.250 ± .036	19.7 ± 0.2	56.2 ± 2.6	68.6 ± 2.1	.304 ± .008
20.0		135	1.600 ± .127	29.7 ± 0.3	51.3 ± 2.8	94.3 ± 3.3	.437 ± .011
31.6		65	1.958 ± .261	48.3 ± 0.6	57.2 ± 4.2	102.9 ± 4.7	.530 ± .016
50.1		25	1.421 ± .121	76.4 ± 2.2	83.5 ± 5.4	69.0 ± 4.8	.498 ± .020
79.4		11	1.815 ± .360	118.7 ± 4.8	62.7 ± 7.0	95.6 ± 8.3	.667 ± .031
126.		4	2.531 ± .385	167.2 ± 7.5	43.4 ± 5.3	116.8 ± 6.5	.794 ± .023
7.94	.450	48	1.122 ± .029	11.3 ± 0.1	57.7 ± 4.4	56.0 ± 2.7	.187 ± .008
12.6		89	1.276 ± .066	14.8 ± 0.2	58.4 ± 3.7	69.8 ± 3.1	.245 ± .009
20.0		87	1.439 ± .070	24.4 ± 0.3	61.6 ± 3.8	79.0 ± 3.0	.335 ± .011
31.6		49	2.004 ± .222	35.7 ± 0.5	57.1 ± 4.3	102.4 ± 4.6	.453 ± .015
50.1		23	1.743 ± .135	58.0 ± 1.2	81.1 ± 7.0	78.5 ± 5.0	.455 ± .021
79.4		13	1.675 ± .164	97.3 ± 3.0	77.9 ± 6.2	84.1 ± 5.3	.567 ± .022
7.94	.550	2	1.113 ± .031	10.2 ± 0.1	42.9 ± 2.5	66.3 ± 3.2	.192 ± .009
12.6		46	1.360 ± .098	12.4 ± 0.2	57.8 ± 4.7	73.2 ± 4.5	.220 ± .012
20.0		45	1.582 ± .120	19.8 ± 0.3	54.4 ± 4.6	88.9 ± 4.2	.315 ± .013
31.6		27	1.685 ± .173	29.7 ± 0.7	63.5 ± 7.6	93.0 ± 5.5	.377 ± .020
50.1		14	1.802 ± .667	46.4 ± 1.2	92.8 ± 14.0	100.8 ± 12.9	.431 ± .040
79.4		7	1.748 ± .202	75.3 ± 1.9	89.6 ± 9.6	79.8 ± 7.6	.476 ± .033

$Q^2$	$x$	$n$	$\bar{w}$	$\bar{E}_H$ (GeV)	$\bar{E}_\mu$ (GeV)	$\bar{\theta}_\mu$ (mr)	$\bar{y}$
12.6	.650	17	$1.318 \pm .121$	$11.6 \pm 0.2$	$57.7 \pm 8.4$	$73.3 \pm 6.1$	$.199 \pm .015$
20.0		19	$1.301 \pm .148$	$15.8 \pm 0.3$	$60.3 \pm 5.8$	$76.8 \pm 6.4$	$.235 \pm .017$
31.6		16	$2.635 \pm .719$	$27.2 \pm 0.7$	$41.0 \pm 4.5$	$134.4 \pm 7.8$	$.447 \pm .022$
50.1		11	$2.323 \pm .475$	$39.3 \pm 0.7$	$61.5 \pm 8.0$	$107.6 \pm 8.3$	$.438 \pm .027$
79.4		6	$2.104 \pm .395$	$66.3 \pm 1.6$	$70.1 \pm 8.4$	$102.3 \pm 8.8$	$.509 \pm .030$
12.6	.850	7	$1.397 \pm .088$	$10.9 \pm 0.2$	$64.6 \pm 15.7$	$74.3 \pm 9.0$	$.184 \pm .021$
20.0		35	$1.476 \pm .122$	$14.0 \pm 0.3$	$62.7 \pm 5.8$	$83.7 \pm 4.8$	$.220 \pm .012$
31.6		16	$2.086 \pm .621$	$20.1 \pm 0.3$	$65.4 \pm 10.3$	$118.0 \pm 11.0$	$.333 \pm .027$
50.1		11	$1.563 \pm .155$	$31.1 \pm 1.1$	$79.4 \pm 10.7$	$85.9 \pm 6.7$	$.313 \pm .020$
79.4		6	$1.182 \pm .063$	$53.7 \pm 1.7$	$122.6 \pm 14.8$	$64.1 \pm 6.4$	$.319 \pm .024$

Table F.1 Mean values of kinematic variables for anti-neutrino events

$Q^2$	$x$	$n$	$\bar{w}$	$\bar{E}_H$ (GeV)	$\bar{E}_\mu$ (GeV)	$\bar{\theta}_\mu$ (mr)	$\bar{y}$
1.26	.015	941	$1.054 \pm .003$	$52.1 \pm 1.1$	$58.9 \pm 1.6$	$23.1 \pm 0.5$	$.520 \pm .007$
2.00		915	$1.064 \pm .004$	$65.8 \pm 1.1$	$59.4 \pm 1.6$	$27.0 \pm 0.6$	$.580 \pm .007$
3.16		733	$1.101 \pm .008$	$91.1 \pm 1.2$	$58.9 \pm 1.6$	$29.1 \pm 0.7$	$.644 \pm .007$
5.01		464	$1.129 \pm .011$	$123.1 \pm 1.3$	$50.4 \pm 1.5$	$31.7 \pm 0.8$	$.726 \pm .007$
7.94		206	$1.204 \pm .023$	$161.2 \pm 1.7$	$38.2 \pm 1.6$	$40.3 \pm 1.3$	$.816 \pm .007$
12.6		17	$1.198 \pm .069$	$209.5 \pm 4.3$	$23.2 \pm 3.4$	$53.3 \pm 4.3$	$.902 \pm .013$
1.26	.045	674	$1.062 \pm .005$	$16.2 \pm 0.1$	$64.3 \pm 1.9$	$22.5 \pm 0.5$	$.260 \pm .005$
2.00		1117	$1.075 \pm .004$	$25.8 \pm 0.2$	$58.5 \pm 1.5$	$31.9 \pm 0.6$	$.394 \pm .005$
3.16		1391	$1.116 \pm .008$	$39.1 \pm 0.2$	$55.3 \pm 1.3$	$41.8 \pm 0.7$	$.510 \pm .005$
5.01		1260	$1.154 \pm .010$	$60.0 \pm 0.4$	$61.3 \pm 1.3$	$44.0 \pm 0.8$	$.575 \pm .006$
7.94		1101	$1.188 \pm .011$	$96.4 \pm 0.6$	$62.5 \pm 1.1$	$39.3 \pm 0.7$	$.639 \pm .005$
12.6		644	$1.261 \pm .016$	$137.6 \pm 1.0$	$47.4 \pm 1.1$	$48.0 \pm 0.9$	$.755 \pm .005$
20.0		122	$1.322 \pm .037$	$182.6 \pm 1.8$	$33.7 \pm 1.9$	$61.1 \pm 1.8$	$.850 \pm .007$
1.26	.080	133	$1.044 \pm .004$	$11.3 \pm 0.1$	$71.3 \pm 4.6$	$22.0 \pm 0.9$	$.183 \pm .007$
2.00		882	$1.067 \pm .004$	$14.7 \pm 0.1$	$68.4 \pm 1.6$	$27.4 \pm 0.5$	$.233 \pm .004$
3.16		1464	$1.093 \pm .008$	$22.3 \pm 0.1$	$58.9 \pm 1.2$	$39.3 \pm 0.6$	$.354 \pm .004$
5.01		1773	$1.187 \pm .013$	$34.7 \pm 0.1$	$55.3 \pm 1.1$	$53.8 \pm 0.8$	$.489 \pm .005$
7.94		1671	$1.271 \pm .019$	$53.5 \pm 0.2$	$56.2 \pm 1.1$	$61.8 \pm 1.0$	$.577 \pm .005$
12.6		1349	$1.293 \pm .022$	$86.0 \pm 0.4$	$65.3 \pm 1.0$	$52.3 \pm 0.9$	$.613 \pm .004$
20.0		996	$1.423 \pm .022$	$130.2 \pm 0.6$	$47.4 \pm 0.8$	$62.9 \pm 0.9$	$.748 \pm .004$
31.6		229	$1.554 \pm .052$	$177.4 \pm 1.4$	$32.2 \pm 1.3$	$80.8 \pm 1.7$	$.852 \pm .005$
50.1		5	$1.340 \pm .166$	$237.3 \pm 5.2$	$29.6 \pm 5.5$	$80.6 \pm 8.0$	$.890 \pm .019$

$Q^2$	$x$	$n$	$\bar{w}$	$\bar{E}_H$ (GeV)	$\bar{E}_\mu$ (GeV)	$\bar{\theta}_\mu$ (mr)	$\bar{y}$	
2.00	.150	186	$1.059 \pm .009$	$11.0 \pm 0.1$	$64.4 \pm 3.4$	$29.8 \pm 1.2$	$.189 \pm .006$	
3.16		1369	$1.070 \pm .003$	$13.6 \pm 0.1$	$65.1 \pm 1.2$	$35.3 \pm 0.5$	$.223 \pm .003$	
5.01		2681	$1.120 \pm .006$	$19.9 \pm 0.1$	$62.1 \pm 0.9$	$46.4 \pm 0.5$	$.313 \pm .003$	
7.94		3461	$1.249 \pm .011$	$31.3 \pm 0.1$	$56.8 \pm 0.8$	$63.1 \pm 0.6$	$.446 \pm .003$	
12.6		3239	$1.418 \pm .021$	$46.7 \pm 0.2$	$58.0 \pm 0.8$	$74.8 \pm 0.7$	$.536 \pm .003$	
20.0		2639	$1.470 \pm .022$	$73.9 \pm 0.3$	$64.6 \pm 0.7$	$69.5 \pm 0.7$	$.586 \pm .003$	
31.6		2080	$1.548 \pm .023$	$114.2 \pm 0.5$	$56.9 \pm 0.7$	$74.4 \pm 0.7$	$.689 \pm .003$	
50.1		818	$1.750 \pm .040$	$157.7 \pm 0.7$	$41.6 \pm 0.7$	$93.7 \pm 1.0$	$.798 \pm .003$	
79.4		55	$2.051 \pm .166$	$208.2 \pm 1.6$	$29.4 \pm 1.5$	$110.9 \pm 2.8$	$.879 \pm .005$	
3.16		.250	11	$1.067 \pm .025$	$10.2 \pm 0.0$	$63.4 \pm 9.0$	$35.9 \pm 5.4$	$.165 \pm .021$
5.01	931		$1.099 \pm .007$	$12.2 \pm 0.0$	$69.5 \pm 1.6$	$43.6 \pm 0.7$	$.199 \pm .003$	
7.94	1859		$1.186 \pm .010$	$18.1 \pm 0.1$	$62.8 \pm 1.1$	$57.6 \pm 0.7$	$.289 \pm .003$	
12.6	2272		$1.403 \pm .020$	$28.4 \pm 0.1$	$57.9 \pm 0.9$	$76.6 \pm 0.8$	$.417 \pm .003$	
20.0	2096		$1.585 \pm .027$	$43.7 \pm 0.1$	$60.3 \pm 0.9$	$85.1 \pm 0.8$	$.504 \pm .003$	
31.6	1740		$1.644 \pm .036$	$69.5 \pm 0.2$	$69.7 \pm 0.9$	$81.3 \pm 0.9$	$.557 \pm .003$	
50.1	1370		$1.638 \pm .024$	$108.9 \pm 0.4$	$64.5 \pm 0.8$	$80.4 \pm 0.8$	$.649 \pm .003$	
79.4	549		$1.951 \pm .058$	$156.3 \pm 0.7$	$46.2 \pm 0.8$	$104.7 \pm 1.2$	$.780 \pm .003$	
126.	25		$3.135 \pm .346$	$205.7 \pm 2.2$	$28.4 \pm 1.3$	$133.5 \pm 2.6$	$.879 \pm .005$	
5.01	.350		40	$1.123 \pm .030$	$10.4 \pm 0.0$	$64.5 \pm 6.7$	$47.3 \pm 3.3$	$.177 \pm .011$
7.94		842	$1.148 \pm .014$	$13.0 \pm 0.1$	$67.5 \pm 1.5$	$53.5 \pm 0.9$	$.208 \pm .003$	
12.6		1187	$1.323 \pm .020$	$19.9 \pm 0.1$	$63.7 \pm 1.3$	$71.2 \pm 1.0$	$.309 \pm .004$	
20.0		1240	$1.628 \pm .039$	$31.4 \pm 0.1$	$59.5 \pm 1.1$	$90.6 \pm 1.1$	$.431 \pm .004$	
31.6		1109	$1.901 \pm .064$	$49.4 \pm 0.2$	$61.0 \pm 1.1$	$101.4 \pm 1.2$	$.527 \pm .004$	
50.1		905	$1.779 \pm .055$	$77.7 \pm 0.3$	$72.6 \pm 1.1$	$88.5 \pm 1.2$	$.560 \pm .004$	
79.4		708	$1.872 \pm .037$	$122.3 \pm 0.5$	$62.4 \pm 0.9$	$94.4 \pm 0.9$	$.675 \pm .003$	
126.		167	$2.472 \pm .148$	$177.3 \pm 1.1$	$43.2 \pm 1.1$	$124.8 \pm 1.9$	$.807 \pm .004$	
7.94		.450	203	$1.174 \pm .032$	$11.0 \pm 0.0$	$68.1 \pm 3.3$	$57.2 \pm 2.0$	$.184 \pm .006$
12.6			631	$1.298 \pm .021$	$15.4 \pm 0.1$	$64.7 \pm 1.8$	$69.3 \pm 1.2$	$.248 \pm .004$
20.0	691		$1.498 \pm .036$	$24.6 \pm 0.1$	$66.0 \pm 1.6$	$83.2 \pm 1.3$	$.343 \pm .004$	
31.6	629		$1.844 \pm .068$	$38.7 \pm 0.2$	$64.2 \pm 1.5$	$99.3 \pm 1.5$	$.454 \pm .005$	
50.1	528		$1.837 \pm .067$	$59.5 \pm 0.3$	$76.3 \pm 1.6$	$92.5 \pm 1.5$	$.495 \pm .005$	
79.4	491		$1.787 \pm .043$	$94.9 \pm 0.5$	$77.4 \pm 1.3$	$89.0 \pm 1.2$	$.574 \pm .004$	
126.	211		$2.543 \pm .136$	$144.6 \pm 0.9$	$50.5 \pm 1.2$	$125.5 \pm 1.7$	$.751 \pm .004$	
200.	17		$2.904 \pm .325$	$204.1 \pm 1.9$	$45.3 \pm 2.3$	$129.7 \pm 3.3$	$.820 \pm .008$	

$Q^2$	$x$	$n$	$\bar{w}$	$\bar{E}_H$ (GeV)	$\bar{E}_\mu$ (GeV)	$\bar{\theta}_\mu$ (mr)	$\bar{y}$
7.94	.550	6	$1.101 \pm .053$	$10.1 \pm 0.0$	$50.0 \pm 3.8$	$59.1 \pm 4.3$	$.173 \pm .011$
12.6		304	$1.222 \pm .019$	$12.9 \pm 0.1$	$67.0 \pm 2.5$	$64.9 \pm 1.5$	$.202 \pm .004$
20.0		347	$1.478 \pm .060$	$20.1 \pm 0.1$	$65.9 \pm 2.4$	$83.5 \pm 1.9$	$.295 \pm .006$
31.6		348	$1.744 \pm .074$	$31.3 \pm 0.2$	$68.9 \pm 2.3$	$95.9 \pm 1.9$	$.387 \pm .006$
50.1		278	$1.831 \pm .081$	$49.0 \pm 0.3$	$80.4 \pm 2.3$	$91.3 \pm 2.0$	$.436 \pm .007$
79.4		256	$1.703 \pm .060$	$79.4 \pm 0.5$	$90.5 \pm 2.1$	$85.4 \pm 1.7$	$.497 \pm .006$
126.		169	$2.142 \pm .105$	$123.5 \pm 1.0$	$69.0 \pm 1.8$	$110.3 \pm 2.0$	$.657 \pm .006$
200.		23	$3.693 \pm .360$	$176.4 \pm 1.9$	$42.9 \pm 1.6$	$144.3 \pm 2.6$	$.806 \pm .006$
12.6	.650	108	$1.182 \pm .025$	$11.7 \pm 0.1$	$78.7 \pm 4.6$	$59.0 \pm 2.4$	$.165 \pm .006$
20.0		215	$1.415 \pm .053$	$16.8 \pm 0.1$	$69.9 \pm 3.0$	$79.0 \pm 2.2$	$.246 \pm .006$
31.6		200	$1.714 \pm .091$	$25.6 \pm 0.2$	$70.7 \pm 3.0$	$94.8 \pm 2.5$	$.335 \pm .007$
50.1		141	$1.860 \pm .149$	$40.0 \pm 0.3$	$79.9 \pm 3.4$	$97.1 \pm 3.0$	$.397 \pm .010$
79.4		110	$2.064 \pm .139$	$66.1 \pm 0.6$	$82.0 \pm 3.3$	$100.8 \pm 2.9$	$.492 \pm .010$
126.		108	$2.020 \pm .120$	$103.5 \pm 0.9$	$82.4 \pm 2.6$	$101.9 \pm 2.4$	$.577 \pm .008$
200.		33	$2.752 \pm .321$	$153.6 \pm 2.2$	$61.6 \pm 3.1$	$130.0 \pm 3.7$	$.722 \pm .010$
12.6		.850	26	$1.161 \pm .042$	$10.8 \pm 0.1$	$88.9 \pm 9.9$	$53.6 \pm 4.4$
20.0	191		$1.379 \pm .043$	$13.6 \pm 0.1$	$74.9 \pm 3.4$	$75.6 \pm 2.2$	$.199 \pm .005$
31.6	187		$1.539 \pm .072$	$21.4 \pm 0.2$	$79.5 \pm 3.0$	$84.2 \pm 2.5$	$.262 \pm .007$
50.1	146		$1.880 \pm .121$	$34.4 \pm 0.3$	$87.6 \pm 3.7$	$95.6 \pm 2.9$	$.348 \pm .009$
79.4	102		$1.873 \pm .174$	$53.1 \pm 0.6$	$93.3 \pm 4.3$	$98.4 \pm 3.4$	$.417 \pm .011$
126.	95		$1.873 \pm .111$	$86.2 \pm 1.1$	$97.7 \pm 3.5$	$96.3 \pm 2.7$	$.495 \pm .010$
200.	50		$2.557 \pm .230$	$130.0 \pm 1.7$	$73.6 \pm 3.1$	$125.9 \pm 3.3$	$.650 \pm .011$

Table F.2 Mean value of kinematic variables for neutrino events

## List of References

- Ab80 L.F.Abbott and R.M.Barnett, *Ann.Phys.*, **125**, 276 (1980).
- Ab81 H.Abromowicz, et al., *Phys.Lett.*, **107B**, 141 (1981).
- Ab82a H.Abromowicz, et al., *Z.Phys.*, **C12**, 289 (1982).
- Ab82b H.Abromowicz, et al., *Z.Phys.*, **C15**, 19 (1982).
- Ab83 H.Abromowicz, et al., *Z.Phys.*, **C17**, 283 (1983).
- Al77 G.Altarelli and S.Parisi, *Nucl.Phys.*, **B126**, 298 (1977).
- Al82 G.Altarelli, *Phys.Reports*, **81**, 1 (1982).
- Au74a J.J.Aubert, et al., *Phys.Rev.Lett.*, **33**, 1404 (1974).
- Au74b J.-E.Augustin, et al., *Phys.Rev.Lett.*, **33**, 1406 (1974).
- Au81a J.J.Aubert, et al., *Phys.Lett.*, **105B**, 315 (1981).
- Au81b J.J.Aubert, et al., *Phys.Lett.*, **105B**, 322 (1981).
- Au82a J.J.Aubert, et al., *Phys.Lett.*, **114B**, 291 (1982).
- Au82b J.J.Aubert, et al., *Phys.Lett.*, **121B**, 1983 (1982).
- Au83 J.J.Aubert, et al., *Phys.Lett.*, **123B**, 275 (1983).
- Ba75a B.Barish, et al., *Phys.Rev.Lett.*, **34**, 538 (1975).
- Ba75b B.Barish, et al., *Phys.Rev.Lett.*, **35**, 1316 (1975).
- Ba75c B.Barish, et al., *Nucl.Instr.Meth.*, **130**, 49 (1975).
- Ba76a R.Barbieri, J.Ellis, M.K.Gaillard and G.G.Ross, *Nucl.Phys.*, **B117**, 50 (1976).
- Ba76b B.Barish, et al., *Phys.Rev.Lett.*, **36**, 939 (1976).
- Ba77a B.Barish, et al., *Phys.Rev.Lett.*, **38**, 577 (1977).
- Ba77b B.Barish, et al., *Phys.Rev.Lett.*, **39**, 981 (1977).
- Ba77c B.Barish, et al., *Phys.Rev.Lett.*, **39**, 1595 (1977).

- Ba77d B.Barish, et al., *Phys.Rev.Lett.*, **39**, 741 (1977).
- Ba78a B.Barish, et al., *Phys.Rev.Lett.*, **40**, 1414 (1978).
- Ba78b B.Barish, et al., *IEEE Transactions on Nuclear Science*, **NS-25**, 532 (1978).
- Ba82a R.M.Barnett and D.Schlatter, *Phys.Lett.*, **112B**, 475 (1982).
- Ba82b R.M.Barnett, *Phys.Rev.Lett.*, **48**, 1657 (1982).
- Bj69 J.D.Bjorken and E.A.Paschos, *Phys.Rev.*, **185**, 1975 (1969).
- Bl80 R.Blair et al., "Neutrino Physics at the Tevatron", Fermilab-Proposal-E652, (1980).
- Bl82 R.Blair, "A Total Cross Section and Y Distribution Measurement for Muon Type Neutrinos and Antineutrinos on Iron", Ph.D.Thesis (unpublished), Caltech (1982).
- Bl83a R.Blair et al., *Phys.Rev.Lett*, **51**, 343 (1983).
- Bl83b R.Blair, et al., "A Monitoring and Calibration System for Neutrino Flux Measurement in a High Energy Dichromatic Neutrino Beam", Nevis Preprint (1983), Fermilab-Pub-83/26-Exp. To be submitted to *Nucl.Instr.Meth*.
- Bo73 A.Bodek, et al., *Phys.Rev.Lett.*, **30**, 1087 (1973).
- Bo79 A.Bodek, et al., *Phys.Rev.*, **D20**, 1471 (1979).
- Bo78 P.C.Bosetti, et al., *Nucl.Phys.*, **B142**, 1 (1978).
- Bo81 D.Bollini, et al., *Phys.Lett.*, **104B**, 403 (1981).
- Bo82 A.Bodek, et al., *Phys.Lett.*, **113B**, 77, (1982).
- Bo83a A.Bodek, et al., *Phys.Rev.Lett.*, **50**, 1431, (1983).
- Bo83b A.Bodek et al., *Z.Phys.*, **C18**, 289 (1983).
- Bu77 A.Buras, *Nucl.Phys.*, **B125**, 125 (1977).
- Bu78 A.Buras and K.J.F.Gaemers, *Nucl.Phys.*, **B132**, 249 (1978).
- Ca63 N.Cabibbo, *Phys.Rev.Lett*, **10**, 531 (1963).
- Ca69 C.Callan and D.Gross, *Phys.Rev.Lett.*, **22**, 156 (1969).
- Cl83 A.R.Clark, et al., "Measurement of the Nucleon Structure Function in Iron Using 215 and 93 GeV Muons", Preprint LBL-16286 (1983). Contributed to *1983 International Symposium on Lepton and Photon Interactions at High Energies*, Cornell, N.Y.
- Cl79 F.Close, *An Introduction to Quarks and Partons*, Academic Press, New York, N.Y. (1979).
- Co73 E.Commins, *Weak Interactions*, McGraw-Hill, New York, N.Y. (1973).
- Cu80 G.Curci, W.Furmanski and R.Petronzio, *Nucl.Phys.*, **B175**, 27 (1980).
- De83 A.Devoto. D.W.Duke, J.F.Owens and R.G.Roberts, *Phys.Rev.*, **D27**, 508, (1983).
- Dr70 S.D.Drell and T.M.Yan, *Phys.Rev.Lett.*, **24**, 181 (1970).

- Ed76a D.Edwards and F.Sciulli, "A Second Generation Narrow Band Neutrino Beam", Fermilab TM-660 (1976).
- Ed76b D.Edwards, S.Mori and S.Pruss, "350 GeV/c Dichromatic Neutrino Target Train", Fermilab TM-810 (1976).
- Ei81 F.Eisele, et al. *Proc.Neutrino '81 Conf.*, High-Energy Physics Group, Univ. of Hawaii, Honolulu, 297 (1981).
- Fe34 E.Fermi, *Z.Phys.*, **88**, 161 (1934).
- Fe58 R.Feynman and M.Gell-Mann, *Phys.Rev.*, **109**, 193 (1958).
- Fe69 R.Feynman, *Phys.Rev.Lett.*, **109**, 1415 (1969).
- Fe72 R.Feynman, *Photon-Hadron Interactions*, W.A.Benjamin, Reading, Mass., (1972).
- Fi77 R.Field and R.P.Feynman, *Phys.Rev.* **D15**, 2590 (1977).
- Fi78 R.Field, Caltech Preprint 68-696 (1978)
- Fi79 R.Field, Caltech Preprint 68-739 (1979)
- Fi82 H.E.Fisk and F.Sciulli, *Ann.Rev.Nucl.Part.Sci.*, **32**, 499 (1982).
- Fu82 W.Furmanski and R.Petronzio, *Z.Phys.*, **c11**, 293, (1982).
- Ge64 M.Gell-Mann, *Phys.Lett.*, **8**, 214 (1964).
- Ge76a H.Georgi and H.D.Politzer, *Phys.Rev.Lett.*, **36**, 1281 (1976).
- Ge76b H.Georgi and H.D.Politzer, *Phys.Rev.* **D14**, 1829 (1976).
- Gl70 S.L.Glashow, J.Iliopoulos and L.Maiani, *Phys.Rev.*, **D2**, 1285 (1970).
- Go79 B.A.Gordon, et al., *Phys.Rev.*, **D20**, 2645, (1979).
- Gr79 J.G.H.de Groot, et al., *Z.Phys.*, **C1**, 143 (1979).
- Gr69 D.J.Gross and C.H.Llewellyn Smith, *Nucl.Phys.*, **B14**, 337 (1969).
- Gr73 D.J.Gross and F.Wilczek, *Phys.Rev.Lett.*, **30**, 1343, (1973).
- Ha83 C.Haber, et al., "A Search for Inclusive Oscillations of Muon Neutrinos in the Mass Range,  $20 < \Delta m^2 < 900 \text{eV}^2$ ", Nevis preprint R1290. Contributed paper to EPS meeting, Brighton, England (1983).
- He77 S.W.Herb, et al., *Phys.Rev.Lett.*, **39**, 252 (1977).
- He81 S.M.Heagy, et al., *Phys.Rev.*, **D23**, 1045, (1981).
- Ho78 M.Holder, et al., *Nucl.Instr.Meth.*, **148**, 235 (1978).
- Ja83 R.L.Jaffe, *Phys.Rev.Lett.*, **50**, 228, (1983).
- Jo77 L.W.Jones, *Rev.Mod.Phys.*, **69**, 717 (1977).
- Jo82 M.Jonker, et al., *Phys.Lett.*, **109B**, 133 (1982).
- Ko73 M.Kobayashi and K.Kaskawa, *Prog.Theor.Phys.*, **49**, 652 (1973).

- La77 G.La Rue, et al., *Phys.Rev.Lett.*, **38**, 1011 (1977).
- La79 G.La Rue, et al., *Phys.Rev.Lett.*, **42**, 142 (1979).
- La81 G.La Rue, et al., *Phys.Rev.Lett.*, **46**, 967 (1981).
- Ly80 L.Lyons, Oxford Preprint NP-38/80 (1980).
- Le56 T.Lee and C.Yang, *Phys.Rev.*, **104**, 254 (1959).
- Le81 J.Lee, "Measurement of  $\nu N$  Charged Current Cross Sections from  $E_\nu = 25$  GeV to  $E_\nu = 260$  GeV", Ph.D.Thesis (unpublished), Caltech (1981).
- Me83 P.Meyers, Private communication.
- Na73 O.Nachtmann, *Nucl.Phys.*, **63**, 237 (1973).
- Ow83 J.Owens, Private communication.
- Pa81 J.K.Panman, "A Study of Inclusive Neutrino Interactions in a Marble Target", Ph.D.Thesis (unpublished), NIKHEF, Amsterdam, The Netherlands (1981).
- Pa33 W.Pauli, *Septieme Conseil de Physique Solvay 1933*, Gauthier-Villars, Paris, 324 (1934)
- Pe69 D.H.Perkins, *Topical Conference on Weak Interactions*, CERN, 1 (1969).
- Po73 D.Politzer, *Phys.Rev.Lett.*, **30**, 1346 (1973).
- Po59 B.Pontecorvo, *Soviet Phys. JETP*, **4**, 1148 (1959).
- Po67 B.Pontecorvo, *Soviet Phys. JETP*, **53**, 1717 (1967).
- Pu84 M.V.Purohit, "Nucleon Structure Functions from  $\nu_\mu$ -Fe Interactions and a Study of the Valence Quark Distribution", Ph.D.Thesis (unpublished), Caltech (1984).
- Re59 F.Reines and C.Cowan, *Phys.Rev.*, **113**, 273 (1959).
- Ri83 J.L.Ritchie, et al., *Phys.Lett.*, **126B**, 499, (1983).
- Ro82 M.Roos, et al., "Review of Particle Properties", *Phys.Lett.*, **111B**, 1 (1982).
- Ru79 A.de Rújula and R.Petronzio, *Nucl.Phys.*, **B154**, 394 (1979).
- Sa68 A.Salam, *Elementary Particle Theory*, 367, Almqvist and Wiksell, Stockholm (1968).
- Sc60 M.Schwartz, *Phys.Rev.Lett.*, **4**, 306, (1960).
- Sm81 G.Smadja, *Proc.Int.Symp.Leptons Photons High Energies*, ed. W.Pfeil, Univ.Bonn Phys.Inst., 444 (1981).
- Sm83 W.Smith, Private communication (1983). Publication in preparation.
- So81 P.Söding and G.Wolf, *Ann.Rev.Nucl.Part.Sci.*, **31**, 231 (1981).
- St78 H.Stredde, "Mechanical Design of the 350 GeV/c Dichromatic Train", Fermilab TM-810 (1978).
- We67 S.Weinberg, *Phys.Rev.Lett.*, **19**, 1264 (1967).

- 
- We70 G.B.West, *Phys.Rev.Lett.*, **24**, 1206 (1970).  
Wu57 C.S.Wu, et al., *Phys.Rev.*, **105**, 1413 (1957).  
Ze64 G.Zweig, CERN preprints TH401 and TH412 (1964).